THE EFFECT OF THERMAL LOAD CONFIGURATIONS ON PASSIVE CHILLED BEAM PERFORMANCE

A Dissertation

by

IAN CARL NELSON

Submitted to the Office of Graduate Studies of
Texas A&M University
in partial fulfillment of the requirements for the degree of

DOCTOR OF PHILOSOPHY

Approved by:

Co-Chairs of Committee,	Charles Culp
	David Claridge
Committee Members,	Andrew Duggleby
	Dennis O'Neal
Head of Department,	Jerald Caton

December 2012

Major Subject: Mechanical Engineering

ABSTRACT

This dissertation presents the findings of a study to quantify the effect of heat source configurations on the performance of passive chilled beams. Experiments in a thermally controlled test room were conducted using thermal manikins as heat sources cooled with a 0.6 m by 2.4 m beam. The thermal manikins were arranged in a symmetric and an asymmetric configuration and tested over a range of input power to simulate a low-to-high load heat distribution of an indoor space. A computational fluid dynamics (CFD) model was developed in Star CCM+ v6.06 and used for further analysis of the flow field and to predict additional spatial arrangements of the beam, interior dimensions, and heat source configurations. The CFD model implemented a calculation for the beam cooling capacity to predict the beam performance based on the room thermal conditions.

The experimental data revealed an average reduction of 15 % in the passive beam cooling capacity for the asymmetrically configured thermal manikins compared to the symmetric arrangement. The CFD model was validated with the experimental data and predicted the asymmetric heat source beam performance reduction to be 17 %. The reduction in performance based on the heat source arrangement was found with analysis of the CFD simulations to be a result of the above-beam air velocity field. The unbalanced thermal manikin configuration generated an unbalanced flow condition at the inlet of the beam that resulted in the room air circumventing the inlet of the passive beam, as compared to the inlet velocity field of the symmetric configuration.

Additional configurations were investigated with the CFD model to include the beam position, floor area, ceiling height, and thermal manikin arrangements. The simulation results were analyzed by comparing the efficiency of beam performance using the beam cooling capacity calculation for each scenario. The predictions of additional configurations found that the efficiency increased when the beam was perpendicular to a group of heat sources and the changes in beam performance with heat source configurations was not affected by the interior dimensions of the space. However, the resulting thermal conditions in the occupied zone for the beam positions of highest efficiency may negatively impact the thermal comfort of occupants.

DEDICATION

To Courtney, my best friend and forever companion. And to my parents for their ever-steady support.

ACKNOWLEDGEMENTS

I would like to express my sincere gratitude to my advisor, Dr. Culp. Over the past five years, he has been a guide and mentor to me in my academic and professional development. His commitment to support me as a graduate assistant researcher for the duration of my studies enabled me to pursue this project and finish it. From our time together, I learned to be a better engineer, investigator, analyzer, writer, communicator and leader. I would also like to recognize my committee members, Dr. Claridge, Dr. Duggleby and Dr. O'Neal for their wise input and direction that increased the quality of this study.

I am grateful to the engineers at Price who supported me in the experimental data collection and allowed me to conduct this study in their laboratory. Specifically I would like to thank Julian Rimmer, who was enthusiastic about helping when I approached him with the project concept. I would also like to thank Brad Tully and Tom Epp for their help and assistance in the scheduling, experimental setup, data collection and overall interest in seeing the success of this work.

Finally, my family and friends provided me support and counsel, helping me to find the resolve to continue working through setbacks and believe that the hard work would soon lead to the completion of this project.

NOMENCLATURE

A	area (m^2)
b	characteristic length scale (m)
c	speed of sound ($m \cdot s^{-1}$)
c_p	specific heat capacity ($kJ \cdot kg^{-1} \cdot K^{-1}$)
C	coefficient of porous inertial resistance; transport equation coefficient
C_{bc}	coefficient of beam cooling
C_c	plume parameter
C_M	coefficient of dilatation dissipation
C_μ	empirically derived constant, Equation 2.7
C_T	realizable time scale coefficient
D	coefficient of porous viscous resistance
D_f	diffusion flux ($kg \cdot m^{-2} \cdot s^{-2}$)
E	entrainment rate ($kg \cdot s \cdot m^{-2}$); energy (W)
F	buoyancy flux ($N \cdot m^{-2}$)
g	gravitational constant ($m \cdot s^{-2}$)
G	turbulence production
Gr	Grashoff number
h	enthalpy ($kJ \cdot kg^{-1}$); heat transfer coefficient ($W \cdot m^{-2} \cdot K^{-1}$)
J	diffusion flux ($kg \cdot m^{-2} \cdot s^{-1}$)
k	turbulence kinetic energy ($m^2 \cdot s^{-2}$); thermal conductivity ($kJ \cdot m^{-1} \cdot K^{-1}$)
L	distance (m)

m	mass (kg)
$\dot{m}$	mass flow rate ($kg \cdot s^{-1}$)
Nu	Nusselt number
p	pressure (Pa)
P	power (W)
Pr	Prandlt number
q	heat flux ($W \cdot m^{-2}$)
Q	volume flux ($m \cdot s^{-1}$); heat transfer (W)
Q_b	beam capacity (W)
r	radius (m)
Re	Reynolds number
S	source term; strain rate tensor (s^{-1})
t	time (s)
T	temperature (°C); turbulent time scale (s)
u	x-component of velocity ($m \cdot s^{-1}$)
u^+	dimensionless velocity
v	y-component of velocity ($m \cdot s^{-1}$)
V	mean velocity ($m \cdot s^{-1}$); volume (m^3); volume flux ($m \cdot s^{-1}$)
w	z-component of velocity ($m \cdot s^{-1}$)
x	coordinate of distance (m)
X	body force (N)
y	coordinate of distance (m)
y^+	dimensionless wall distance
Y_M	dilatation dissipation

Y_y	Yap correction
z	coordinate of distance (m)

Greek Symbols

α	entrainment coefficient; half angle (rad)
β	coefficient of thermal expansion ($°C^{-1}$)
δ_{ij}	Kronecker delta
Δt	change in time (s)
ΔT_{RM}	reference temperature minus the mean water temperature (°C)
ε	dissipation rate of turbulence energy ($m^2 \cdot s^{-3}$)
η	efficiency
φ	general scalar
γ	porosity
Γ	ratio of buoyancy force to momentum force of a plume; diffusivity ($kg \cdot s^{-1}$)
Γ_f	diffusion coefficient
κ	von Karman constant
Λ	plume heating characteristic
$\nabla\phi$	gradient of general scalar
$\nabla\rho$	gradient of density ($kg \cdot m^{-3}$)
∇T	gradient of temperature (°C)
ρ	density ($kg \cdot m^{-3}$)
σ	Schmidt number
σ_t	turbulent Prandtl number
τ	shear stress ($N \cdot m^{-2}$)

τ_{ij}	Reynolds stress ($kg \cdot m^{-1} \cdot s^{-2}$)
μ	viscosity ($kg \cdot m^{-1} \cdot s^{-1}$)
v	kinematic viscosity ($m^2 \cdot s^{-1}$)
ω	specific turbulence dissipation (s^{-1})
ω_μ	under-relaxation factor

Subscripts

0	bulk fluid
1	reference fluid
∞	ambient or free stream value
a	air
al	aluminum
ave	average
b	buoyancy; beam
beam	passive chilled beam
cu	copper
eff	effective
ε	turbulence energy dissipation rate
D	reference
f	fluid; cell face
fin	passive chilled beam fin
ϕ	general scalar
h	horizontal
i	inlet; general index
j	general index

k	turbulence kinetic energy; general index
L	length
max	maximum
mid	middle
min	minimum
nl	non-linear
o	outlet
r	reconstruction
ref	reference
RG	resolved grid
s	solid; surface
t	turbulent
T	realizable time scale
TC	thermocouple
TG	test grid
τ	friction
v	vertical
w	water

Superscripts

‴	volumetric flux
*	reference value
h	enthalpy
n	time step
new	newly calculated value

Abbreviations

BP	beam position
CFD	computational fluid dynamics
DAQ	data acquisition
DDC	direct digital control
DES	detached-eddy simulation
DIA	diameter
DR	draft rating
HVAC	heating, ventilating, and air conditioning
LES	large-eddy simulation
MWT	mean water temperature
MTT	Morton, Taylor, and Turner
PMV	predicted mean vote
PPD	predicted percentage dissatisfied
RANS	Reynolds-averaged Navier-Stokes
RNG	renormalization group
RSM	Reynolds-stress model
RTD	resistance temperature detector
SCR	silicon-controlled rectifier

TABLE OF CONTENTS

Page

Page

Page

LIST OF FIGURES

Figure Page

Figure Page

Figure Page

Figure Page

Figure Page

Figure Page

Figure Page

Figure Page

LIST OF TABLES

Table Page

Table Page

CHAPTER I

INTRODUCTION AND BACKGROUND

The description of room airflow characteristics in buildings is necessary to evaluate the thermal comfort of occupants and optimize the energy use of the climate control system [1]. Radiation, conduction and forced and natural convection heat transfer between surfaces, occupants and room air define the flow of energy in indoor spaces. Natural convection heat transfer produces a buoyant force of the locally heated or cooled air that interacts with other sources of fluid momentum [2]. The primary airflow characteristics that can be used to predict thermal comfort in a space are the air temperature, air speed, radiant temperature and humidity [3]. Buoyant flows may impact thermal comfort based on the temperature and velocity of plumes and the differences in radiant sources. In spaces with non-uniform thermal environments, single point analysis for the zone will reduce the accuracy of the predictions. A careful prediction of the indoor thermal comfort includes analysis of the non-uniform environment and the direct effect on the airflow characteristics that impact occupant thermal comfort. Experimental methods of characterizing buoyant room airflow necessitate many hours [4] for the conditions to stabilize at each operating point and must be conducted with sophisticated measurement equipment and techniques [5] that are restricted to laboratory environments.

Modeling is another approach to understand the room airflow dynamics. Buoyancy driven indoor airflows require highly detailed modeling of the natural

convection and radiation heat transfer between room surfaces and the air to correctly characterize time-dependent energy and mass flows [6]. Indoor airflow modeling characterizes room conditions by solving the fundamental principles of energy, momentum and mass flow [7] to predict the interactions of inlet and outlet mass flows with the heat sources and sinks. The nature of air movement and heat transfer throughout the space yields many interdependent relationships [2] that must be resolved at very small scales throughout regions many orders of magnitude larger [8]. Several simplification methodologies have been developed that enable solutions of complex airflows that reduce the modeling effort and the overall time and expense [9]. Computational fluid dynamics (CFD) has emerged as the dominate simulation technique for modeling indoor airflows because of the ability to accurately model extremely complex flows with computational power that has dramatically increased in the last twenty years [10].

Alternative designs for comfort control in buildings separate the functions of equipment used to meet the ventilation requirement, and latent and sensible loads in the space, as shown in Figure 1. With designs that include a central primary system to provide dehumidified fresh air to the zones and a local secondary system for sensible loads, the equipment sizing and operating conditions impact the occupant comfort differently than mixed air systems. Multiple sources of momentum and buoyancy interact to provide a non-uniform thermal environment and the resultant airflow characteristics.

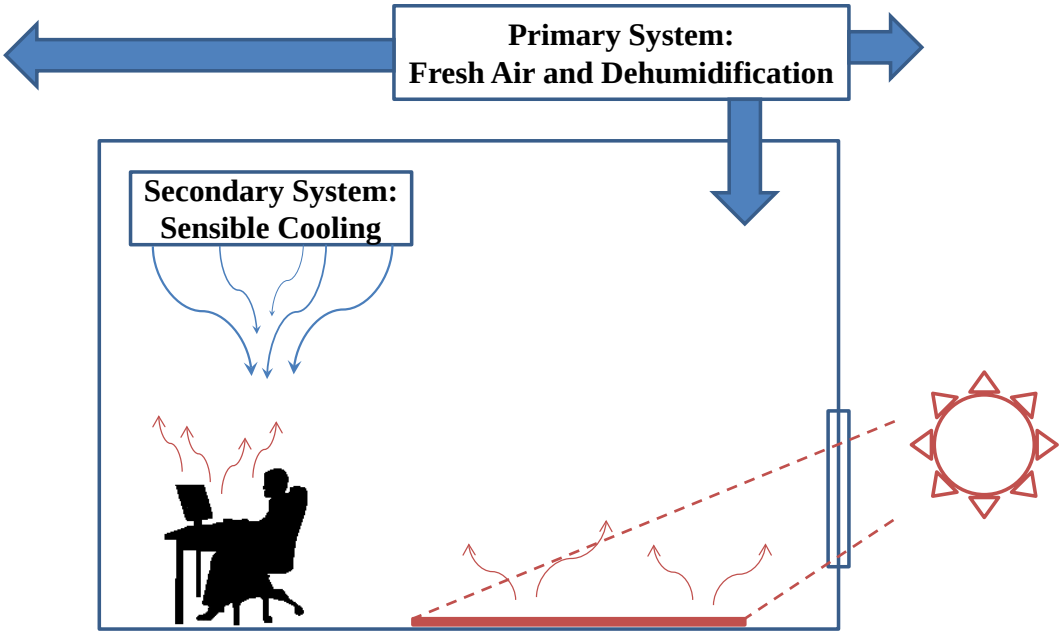

Figure 1. Indoor air schematic with primary and secondary system configuration showing sources of momentum and buoyancy.

Buoyancy is the driving force of the airflow in rooms supplied by stratification-based heating, ventilation and air conditioning (HVAC) designs and in traditional mixed air systems incorporating passive cooling or heating [2]. Passive cooling technologies provide controlled heat rejection in a space utilizing chilled surfaces that generate buoyant flows [11]. Chilled beams directly cool room air with exposed water coils supplied with chilled water and can be classified into two types: passive and active. Passive beams deliver cooling to the room by induction only. The room air rejects heat to the coil through natural convection. The air-side and water-side operation of the passive chilled beam is shown in Figure 2. As the room air is cooled by the coil, the increased density creates a buoyancy force that causes the mass of air to sink directly beneath the beam [12]. The volumetric flow rate from a passive beam depends on the

heat exchange at the coil that results from a difference in temperature between the room air and the coil surface. On the coil side, the chilled water supply flow rate and temperature are control set points for the beam operation. Whereas, the room air temperature is the result of the heat gain in the space. Time-dependent internal loads result in time-dependent beam characteristics, such as cooling capacity and plume velocity. The airflow generated by passive beams has been described using simplified models and experimental flow visualization in few publications.

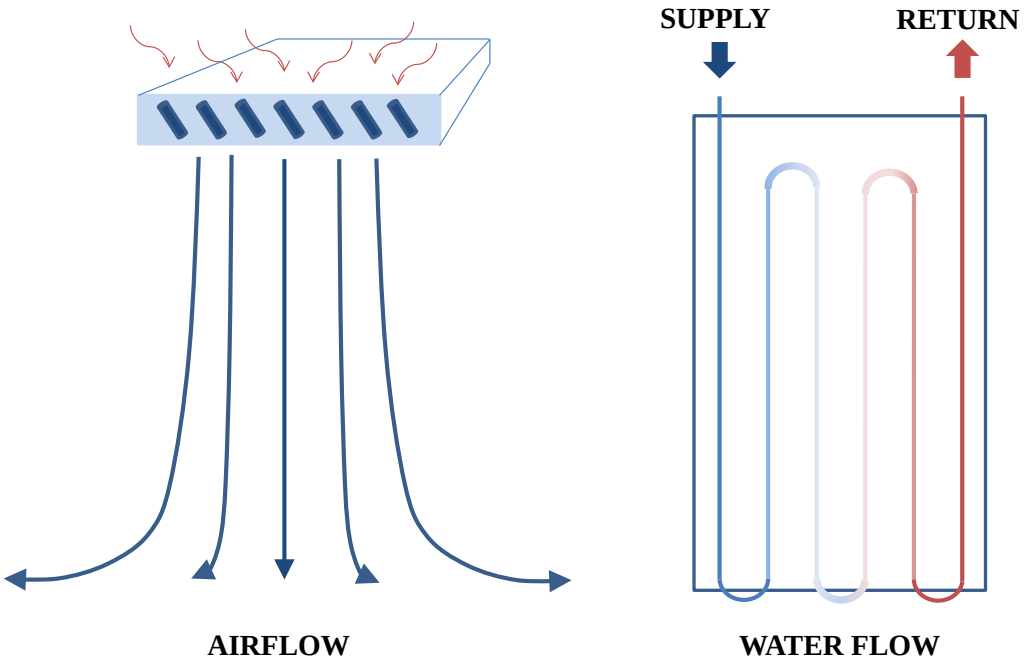

Figure 2. Passive chilled beam schematic showing air and water flow.

For designs that incorporate air buoyancy, the airflow characteristics should fall within thermal comfort requirements. The analytical models reviewed in the literature

predict characteristics of individual buoyancy sources. Integrating these for application to multiple sources of air buoyancy to predict the resultant airflow becomes overly complex and very difficult to generalize [2]. CFD has been applied to room airflow prediction for mixed and stratified environments and used to study the heat transfer by forced, free and mixed convection airflow[13]. Buoyant flow modeling with CFD presents many challenges including the use of a turbulence model to account for the anisotropic nature of the low-Reynolds flow [14] and long simulation times (5,000 s to 27,400 s) for the solution to reach steady state [15]. Additionally, the geometrical characteristics of passive beams preclude a full scale meshing in an indoor environment because of the fine grid necessary to model the densely packed fins.

The purpose of this study was to analyze passive chilled beam operation as effected by heat loads in the space and to create a reliable method of modeling a passive chilled beam using CFD for studies of beam efficiency and thermal comfort predictions. Multiple sources of momentum and buoyancy in the space result in airflow characteristics through the room that require sophisticated models to incorporate the competing forces. The first of three objectives of the CFD model development was to create a generalized methodology for a passive chilled beam that can be applied in CFD commercial packages. The second objective was that the model be validated with experimental data to predict the passive chilled beam performance and resultant plume airflow characteristics. The third objective for the CFD model development was documented input values and specifications based on experimental data or engineering analysis. Additional objectives of the project included quantifying the effect of the heat

load configuration on the passive chilled beam capacity and airflow characteristics of the plume and establishing an explanation for the effect of the heat load configuration on the passive chilled beam.

The project methodology for accomplishing the objectives of the study was to collect experimental data of a passive chilled beam, use the model predictions for the test conditions to validate the model and use the model to calculate the airflow characteristics for additional scenarios outside of the scope of the testing. Experiments were conducted with a passive chilled beam and heat loads in a climatic chamber. Different spatial arrangements and types of heat loads were tested and the effect on the passive chilled beam capacity measured. A CFD model was developed based in part on the observations during testing. The results of the simulations for the climatic chamber experiments were compared to the data for assessing the validity of the model construction. Additional simulations of the passive chilled beam and heat loads were conducted to study scenarios not tested experimentally and to analyze changes in the airflow characteristics that resulted in changed performance of the passive chilled beam. The techniques used to model the passive beam, validated by the experimental data, can be used by designers or building energy engineers within commercial CFD packages or other numerical simulations that solve the flow equations for indoor air cooled by systems that include passive beams.

This dissertation is organized into nine chapters. Published literature on the effect of thermal loads on airflow characteristics in buildings, CFD modeling techniques for indoor airflow, and experimental techniques and results for buoyancy-driven indoor

airflows are reviewed in Chapter II. The experimental setup and method of testing is described in Chapter III. Chapter IV documents the construction of the CFD model and in Chapter V an analytical model for the fin-to-air heat transfer of the passive beam is developed. Chapter VI presents the results of the experimental data, model predictions and the comparisons used to validate the CFD model. The effects of heat loads in the space on the performance of passive beams and airflow characteristics of room air are provided in Chapter VII. Chapter VIII presents the results of the CFD model used to predict the passive beam cooling capacity and the airflow characteristics in the occupied zone for different spatial arrangements of the simulated volume and locations of the heat sources and passive beam. Chapter IX presents the conclusions of the study and includes remarks on using the passive beam model and opportunities for additional research.

CHAPTER II

LITERATURE REVIEW

2.1 Introduction

This literature review is divided into three sections that supported the hypothesis that heat load characteristics affect the resultant airflow of a passive chilled beam and helped guide the formation of the passive chilled beam modeling. Section 2.2 covers thermal plume experimental results and the effect of thermal loads on room air characteristics and the impact on equipment performance in indoor environments. Section 2.3 includes plume modeling techniques and results from numerical simulations of plume equations. Section 2.4 covers the techniques used for CFD simulations of room airflow including turbulence modeling and simplifications of complex geometries.

2.2 Thermal Plume Experiments in Indoor Environments

For passive chilled beam installations that service stratified indoor environments where buoyancy determines the airflow patterns in the room, the buoyant flow indoor environments are characterized by low velocity airflow and non-uniform surface temperatures [2]. The thermal comfort of occupants exposed to buoyant flow conditions is an active area of research and the results from studies [16-19] show that the surface temperatures and locations of buoyancy sources in indoor spaces govern the airflow characteristics. Some studies of displacement ventilation systems using chilled ceilings isolate the variations in buoyancy sources responsible for airflow characteristic changes

[16, 20]. In one study [20], experiments were conducted to assess thermal comfort in offices with chilled ceilings and displacement ventilation. An office with an average cooling load of 60 W/m^2 was constructed with control of the supply airflow rate, air temperature, relative humidity, mean radiant temperature and the surface temperature of the chilled ceiling. The conducted tests showed that occupants experienced thermal comfort based on calculations of the Predicted Mean Vote (PMV) and Predicted Percentage Dissatisfied (PPD) according to the BS EN ISO 7730 Standard method. However, it was observed that at low ceiling temperatures (14 °C – 16 °C) the combined system did not function with a stratified air distribution because of the disruptive convective currents caused by the natural convection at the ceiling. The data also showed that despite the higher local velocities due to the lower ceiling temperatures, the comfort levels were not affected due to draft. In spaces with more than one buoyancy source, the combined airflows were found to disrupt thermal comfort. Additional experiments were conducted to study the indoor air quality of a cooled ceiling ventilated by displacement compared to mixed air distribution [16]. The surface temperature of the cooled ceiling affected the room airflow by disrupting the displacement ventilation stratification and developed airflow patterns similar to the mixed air distribution in the occupancy zone. Three buoyant airflow movements were observed that contributed to the mixed air conditions with the displacement ventilation system: 1) buoyant airflow moving from the ceiling to the floor from the warm air rejecting heat to the cooled ceiling, 2) buoyant airflow moving towards the floor from the walls caused by radiative

heat transfer from the cooled ceiling and 3) buoyant airflow created from heat sources near the floor moving towards the ceiling.

The interaction of convective currents in the room and the relationship to thermal load intensity was studied experimentally [21]. A scaled test room was used to visualize the air distribution and measure the air velocity in a room over a range of heat loads generating thermal plumes from multiple sources along the floor. The tests showed that at heat loads of 50 W/m^2 and above, the airflow pattern in the room became more turbulent than at lower heat load densities and was best characterized as a floor to ceiling vortex. It was found that the maximum velocities recorded in the room increased proportionally with the recorded power input to the heat load. In a study of the thermal comfort of occupants in a room with active chilled beams, Melikov, Yordanova, Bozhov, Zboril and Kosonen used a test room to measure the air temperature and velocity over a range of internal heat loads [22]. The test subjects in the experiments responded to different conditions by filling in surveys to describe their comfort levels. The authors noted that convection from windows, the solar load on the floor, the people, and the computer were strong enough to affect the room airflow patterns created by the chilled beams. As heat loads increased, the non-uniformity of the thermal environment increased, which resulted in decreased thermal comfort.

The effect of variations on the interior heat loads in a room cooled with active chilled beams was studied [17]. The supply air discharged from active chilled beams remains attached to the ceiling until it is re-directed towards the floor by the walls. Solar loads from windows increase the local surface temperature on the floor creating

convective airflow that in the experiments was observed to increase the air velocity of active chilled beam supply at the floor. By increasing the solar load in the room, the draft rating increased due to the increased convective flow from the floor. Additionally, the position of the chilled beams in the ceiling was shown to significantly impact thermal comfort as the characteristics of the combined momentum and buoyancy sources of supply air jet and surface temperature convection were highly dependent on source location.

The convective airflow patterns created by heat loads interacting with active chilled beam airflow was studied by Kosonen and Melikov [18]. The heat loads used in the space were computers (100 W), thermal manikins (60 W), lighting (144 W) and one window (350 W, 142 W/m^2) with a heated mat on the floor to simulate solar load (300 W). The experimental results showed the maximum air velocity recorded in the room was proportional to the value of the total heat load in the space and also dependent on the heat load distribution through the room. In a similar study, the effect of internal loads on the airflow produced by chilled beams was studied with a simulated office test room [23]. Active chilled beams were installed 2.5 m from the floor with a water flow rate between 0.03-0.1 kg/s at an inlet temperature of 14 °C and an airflow rate of 2.0 $l/s/m^2$ at a supply temperature of 18 °C. Internal loads were simulated with computers, thermal manikins, lights, heated floor panels and one window. Smoke visualizations and temperature and velocity measurements showed that with heat loads above 56 W/m^2, the air distribution from the chilled beam was affected. The maximum velocities recorded in the space were shown to increase with the higher internal loads while the supply

airflow rate was held constant. In this scenario, the draft ratings were not significantly affected since the maximum velocities did not surpass 0.26 m/s. Additionally, the distribution of heat loads in the space was studied and found to affect the location of the maximum velocity but did not affect the magnitude of the maximum velocity.

The study of the effect on occupant comfort in a room cooled with active chilled beams was continued by experimentally observing the air distribution in a test room with varying heat loads and air supply flow rates [19]. At average heat loads of 80 W/m^2 50 % of the measured area recorded a draft rating (DR) higher than 15 %. Also, at supply flow rates of 3 $l/s/m^2$, over 80 % of the area measured a DR above 15 %.

The few studies that have published the results of tested passive chilled beams have measured the thermal plume characteristics. Fredriksson, Sandberg and Moshfegh [24] studied the thermal plume created by an exposed passive chilled beam in an enclosed test room. Using flow visualization techniques the thermal plume development was recorded using laser-illuminated smoke injected above the beam. The captured pictures show the transition from the laminar to turbulent flow as the cooler air descends from the beam. Anemometers and thermocouples were used to characterize the velocity and temperature of the cooled air and the authors used thermal plume models to compare with the data captured from the experiments. The application of the models to the experimental work showed an over-prediction of the thermal plume strength, defined by lower temperatures and higher velocities. Fluctuations in the plume location were attributed to the motion of thermals descending from the cooling coil. Using instability criterion theory and the calculated Rayleigh number of the air at the fins, the frequency

of descending thermals was estimated to be 4 s. It was noted that the beam sensitivity to heat sources was a necessary continuation of the research. Additionally, it was suggested that the oscillations of the thermal plume reported in this article may cause occupant discomfort and contribute to a sensation of draft.

The thermal plume from heat loads directly underneath a passive beam was studied [25]. Using a simulated person at a workspace with a computer, positioned directly below or 0.5 m from the center of the beam, the results showed that the thermal plume from the beam was much stronger than the heat load plumes. The variation in beam thermal plume characteristics were attributed to the geometric shape of the simulated heat loads as the results were similar with and without power.

The return openings in false ceilings were studied to access the impact on the cooling effectiveness of passive chilled beams [26]. The study found that the cooling effectiveness of the beam, the ratio of cooling delivered to heat generated in the space, was dependent on the area of return grating and the location. The highest cooling effectiveness (81 %) was found with grating area twice as large as the chilled beam and located near the walls.

2.3 Analytical Models of Thermal Plumes

The cold airflow generated by passive chilled beams is driven by the density difference between the cold air and the ambient room air resulting in a buoyancy force that directs the cold air toward the floor [11]. The buoyant airflow from the chilled beam can be described as a plume, which is generally used to describe constant

buoyancy source flows. The increase in diameter as a function of the distance from the source is caused by large turbulent eddies across the well-defined boundary separating the turbulent plume air from the quiescent room air [27]. Studies of buoyant flow [28] were first conducted based on an interest in environmental fluid flows. The time-averaged values of the temperature and velocity values of a plume from both a point source and a line source were predicted by using a Gaussian distribution.

The theoretical model development of plumes by Morton, Taylor and Turner (MTT) [29], using the conservation equations of volume flux, momentum flux and buoyancy flux for a steady point source in stably stratified or uniformly stratified environments, remains the most effective modeling of plumes [30]. The main assumptions of this modeling for both environments include a constant value for the entrainment rate and that the local variations of density are small compared to the reference density of the ambient fluid at the level of the source. For the case of a stably stratified environment, velocity and buoyancy force profiles are assumed uniform, independent of height above the point source. With these assumptions, the solution for a point source in a stably stratified environment was represented by three equations [29]. The first, the conservation of mass, was derived as:

$$\frac{\mathrm{d}}{\mathrm{d}x}(b^2u) = 2b\alpha u \tag{2.1}$$

where b is a characteristic length scale, u is the axial vertical velocity and α is the entrainment coefficient. The conservation of momentum was derived as:

$$\frac{\mathrm{d}}{\mathrm{d}x}(b^2u^2) = 2b^2g\frac{\rho_0 - \rho}{\rho_1} \tag{2.2}$$

where g is the gravitational constant, ρ_0 is the density outside the plume, ρ is the density inside the plume and ρ_1 is the reference density for the system. The third equation, the conservation of density deficiency was derived as:

$$\frac{\mathrm{d}}{\mathrm{d}x}\left(b^2 u g \frac{\rho_0 - \rho}{\rho_1}\right) = 2b^2 u \frac{g}{\rho_1}\frac{\mathrm{d}\rho_0}{\mathrm{d}x}. \qquad 2.3$$

A schematic of the plume equation parameters is presented in Figure 3.

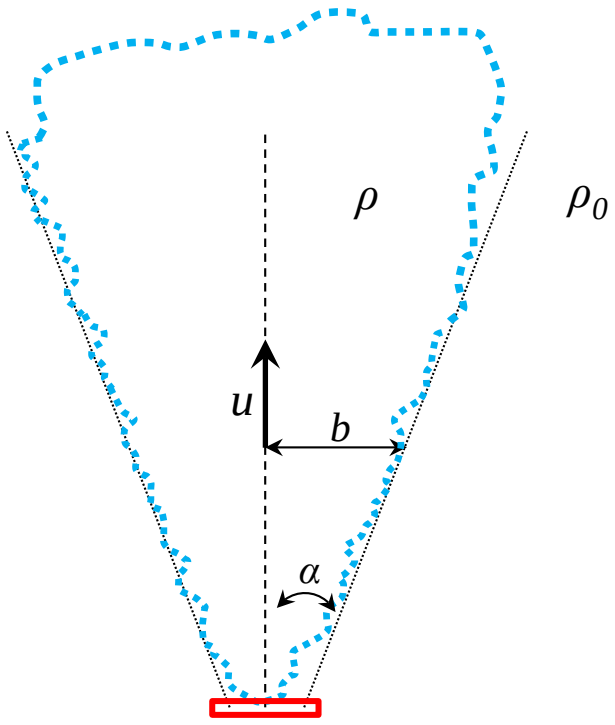

Figure 3. Schematic of plume parameters for MTT equation derivations.

Turner [31] studied turbulent plume development of atmospheric thermals using laboratory experiments scaled by similarity and found that the entrainment rate of the thermal can be described by:

$$E = \frac{3 \propto}{r} \qquad 2.4$$

where E is the entrainment rate, α is the half angle of radial spread of the plume and r is the radius of the thermal. The experiments were setup to simulate constant temperature, constant velocity, or constant density plumes and the results of all three tests showed that the radius increased linearly with distance from the source [32]. It was observed that the mechanism for entrainment was by large eddy motion. Baines [33] found that the entrainment rate was a function of only the Froude number and was dependent only on the plume characteristics and boundary density difference. The parameter Γ was defined to be the ratio of the buoyancy force and momentum force of a plume. The plume was defined as forced if $\Gamma < 1$, lazy if $\Gamma > 1$, or pure if $\Gamma = 1$ [34].

Corrections to the model source conditions for plumes with different values of Γ have been studied since the MTT equations were developed for idealized plume sources. Empirical measurements [32], application of a conical shape to the plume boundary [29], jet-length scaling [35], and a method based on the source conditions [35], have been developed to assign a correction to the source location of forced, lazy, and pure plumes. Additionally, a new plume parameter ($C_c = 1 - 1/\Gamma$) was developed and the equations for Q_0 (volume flux), F_0 (buoyancy flux) and C_c were solved numerically [36] to find the volume flux based on the distance from the source. The virtual origin of lazy plumes [37] was the main objective of a study that presented a one-step method similar to the

MTT method of virtual source location. Hunt and Kaye [38] introduced a dimensionless parameter, Λ, a heating characteristic of the plume and solved the MTT equations for lazy plumes. The steady state solutions showed a reduced entrainment rate for lazy plumes when compared to pure plumes. The work verified that the MTT equations (and the entrainment rate assumption) applied for near source analysis if the correct source conditions are used in the modeling.

Dynamic source conditions of buoyant plumes have been studied to examine the effect on plume behavior of increasing or decreasing source strength. Scase, Caulfied and Dalziel numerically solved the MTT equations and defined a region of narrowing in the plume development for decreased source strength [39]. Within a stratified environment, two regions in the plume can be described with a transition from the near source area to greater heights. With decreased source strength, the stall time of the plume ascent was predicted based on the buoyancy frequency. The work was continued for uniform environments [30] and showed that three regions existed for a decreased source strength: an upper region unaffected by the changing source conditions, a lower region characterized by the reduced buoyancy and a transition region with a narrowing of the plume. The authors note that in the near-source region, the constant entrainment assumption may not be valid and lead to a pinch-off of the plume.

The transition from laminar to turbulent plume flow was studied using laboratory experiments with cigarette smoke [40]. The observations from the project characterized the transition as a sinusoidal function with a wavelength that scaled with the plume diameter. This characterization of plume transition was derived to include asymmetric

plume response [41]. Through the equation derivation, the observed unstable sinusoidal behavior of the plume was shown theoretically.

2.4 Indoor Airflow Numerical Modeling

CFD is a numerical simulation technique that is able to predict fluid flow by iteratively solving the Navier-Stokes equations [42]. The application of these techniques to room airflow has greatly increased the ability to study implications of air distribution design and simulate real-life scenarios [43]. Within CFD, the choice of models used to approximately solve the Navier-Stokes equations is flow-type dependent. Turbulence models, boundary conditions for surfaces, mesh sizing and radiation modeling include the main areas of continued research in room airflow [2]. Additionally, simplifications to complex geometries have been studied to reduce the mesh size and computational resources necessary to model full scale rooms and buildings [8].

Many different turbulence models have been applied to room airflow in order to correctly characterize the laminar turbulent flow. Reynolds-averaged Navier-Stokes (RANS) and large-eddy simulation (LES) methods have been the predominate approaches used in indoor air simulations. Of the RANS models, two main categories exist: eddy viscosity models and Reynolds-stress models (RSM) [44]. Eddy viscosity models, also termed eddy diffusivity, rely on estimating the turbulence by considering the velocity fluctuations effect on the fluid characteristics: specifically, the variation of the viscosity of the fluid. The effective viscosity, μ_{eff}, of the fluid can be defined as:

$$\mu_{eff} = \mu_t + \mu \tag{2.5}$$

where μ_t is the turbulent viscosity and μ is the physical viscosity. Variations within the eddy viscosity models center on the calculation of the turbulent viscosity term [45]. There are many different models that include zero-equation, one-equation, two-equation and multiple-equation methodologies to calculate the turbulent viscosity. Chen and Xu [4] developed a zero-equation model that uses an algebraic relationship to model the turbulent viscosity that is dependent on the density, local mean velocity and characteristic length scale of the flow. The turbulent viscosity is calculated as:

$$\mu_t = 0.03874\ \rho V L \tag{2.6}$$

where ρ is the density, V is the local mean velocity, L is the distance to the nearest wall and the constant is determined empirically. One-equation models, such as the model developed by Spalart and Allmaras [46], use an equation to calculate the turbulent viscosity that consists of another parameter, the turbulent kinetic energy, determined by solving the transport equation. The standard *k*-*ε* model developed by Launder and Spalding [47] has been used extensively for indoor flows [45]. The turbulence kinetic energy, *k*, with the dissipation rate of turbulence energy, *ε*, is used in to calculate the turbulent viscosity:

$$\mu_t = C_\mu \rho \frac{k^2}{\varepsilon} \tag{2.7}$$

where ρ is the fluid density and C_μ is an empirically derived constant [47]. Many variations of the standard *k*-*ε* model were developed that attempt to better predict the turbulence for low Reynolds flow [48-51]. Different approaches to using the *k*-*ε* model

in scenarios with both fully turbulent flow and low velocity, laminar flow incorporate damping functions to the model development to account for the airflow near boundaries and for areas with destruction of the turbulent kinetic energy due to buoyancy [45]. The renormalization group (RNG) k-ε model [52] is another two-equation model that uses additional techniques to predict the fully turbulent regions and the near-wall regions in room airflow. Gan [53] compared the RNG k-ε model to the standard k-ε model and found the former to be a more accurate predictor of turbulent buoyant flow. Similarly, in their study of low velocity diffusers, Cehlin and Moshfegh [54] found that the RNG k-ε model predictions were the most stable and comparable to temperature distributions and velocity profiles of the measured data. The RNG k-ε model was used successfully for predictions of natural displacement ventilation in an enclosure connected to an atrium [55], simplifications of low velocity displacement ventilation diffusers [56], the thermal plume from a time-dependent thermal model of a human body [57] and other studies of indoor airflow [5, 58-63].

Simplification of complex geometries is an important method to reduce computing time for room air simulations [13]. The detailed geometry of the supply diffuser significantly influences the room air characteristics [8]. Simplification methodologies have been developed to model the supply diffuser without distorting the airflow characteristics [64-67]. Zhao, Li and Yan combined a diffuser simplification methodology with a zero-equation turbulence model and an error calculation methodology. The system predicted the room air characteristics with a calculation rate eighty five percent faster than the calculation rate of a similar solution using the standard

k-ε model with basic solver methods [68]. The box and momentum methods were developed to simplify the CFD mesh around complicated diffuser geometries [7]. The box method applies the velocity inlet boundary condition to a much larger volume surrounding the diffuser until the airflow is approximately uniform [66]. A method of testing for experimental data was shown to obtain the input parameters used in the methods [8].

The implications on the predicted throw profile were studied with five supply diffuser modeling techniques along with a comparison between the standard *k*-ε and RNG *k*-ε turbulence models [69]. It was shown that the momentum method should be applied to displacement and combined jet mixing diffusers and that the box method should be used for nozzle, slot and valve diffusers that discharge separate jets [7]. Zhang, Lee and Chen [56] used a cell-blocking method to simplify inlet diffuser simulation. Individual cells in the calculation grid were blocked from mass flow in order to account for the effective area ratio of the diffuser.

CFD has been employed to study the minute details of flow development for buoyant plumes. Soteriou, Dong and Cetegen [70] were able to simulate the pulsation frequency of the plume generation and showed that the symmetry of the plume development grew with increased buoyancy dominance. It was shown that the pulsation frequency was dependent on nozzle width and density ratio but almost entirely independent of external flow parameters.

The *k*-ε model was used to simulate airflow distribution of a task conditioning system in a typical office space with the assumptions that the air is incompressible, the

Boussinesq approximation is applicable, and the airflow is steadily turbulent with a high Reynolds number and isotropic turbulence viscosity [71]. The interior walls, ceiling and floor were set to adiabatic boundaries with an exterior wall subject to convective heat transfer with a heat transfer coefficient of 1.5 W/m^2K. The airflow distributed by an active chilled beam was simulated without simplifying the complex diffuser geometry [72]. The non-validated simulation results show room air temperatures and velocities for a typical office during both the cooling and heating season.

The diameter and curvature of convective rolls from a cooled ceiling were studied for a wide range of Rayleigh numbers [73]. The numerical simulations showed that the change in the average roll diameters was effected by the transition into an oscillatory flow regime. Using the freeze-flow method of unsteady simulation, Cook, Zitzmann and Pfrommer [74] modeled a dynamic thermal indoor environment and calculated the temperature distributions for two temperature-controlled walls and also for the cooling of a solid wall. The k-ω model for calculating the eddy viscosity was used in conjunction with the discrete transfer model for radiative heat transfer.

CFD was used to study the thermal plume from a thermal manikin in a room with displacement ventilation [75]. Comparisons between different turbulence models with and without radiation showed that the detached-eddy simulation (DES) including radiative heat transfer best matched the experimental data. Another study using the k-ε model for turbulence modeling varied the location of a convective heat source in a two dimensional displacement ventilation setup [76]. The results showed the temperature stratification and the air recirculation patterns of the room disrupted by the heat source.

A comparison study between a radiative cooling panel system to an all-air system showed the CFD predictions validated by experimental data [77]. The calculated air velocities and room air temperature measurements were shown to match closely to the test room data by using the k-ε turbulence model and the coupled flow solver. The walls were setup with estimated heat transfer coefficients and reference temperatures dependent on material and location.

CHAPTER III

EXPERIMENTS AND METHODOLOGY

3.1 Experimental Facility

3.1.1 Test Room

Experimental data was collected at the Price Research Center in Winnipeg, Canada using a hydronic test chamber shown in Figure 4. The chamber was developed for the testing of chilled beams and radiant panels and featured temperature control and monitoring on each interior surface. The room was constructed with a 4 in (10.16 cm) layer of R-20 insulation, a 6 in (15.24 cm) air gap, radiant panels and a second 4 in (10.16 cm) layer of R-20 insulation, as listed from the exterior wall to the interior wall, as shown in Figure 4. Temperature-controlled water was circulated through the radiant panel coils to provide a uniform and consistent surface temperature on the interior surfaces of the room. Each wall was designated as the North wall, East wall, South wall, or West wall. The opening shown in Figure 4 was on the South wall.

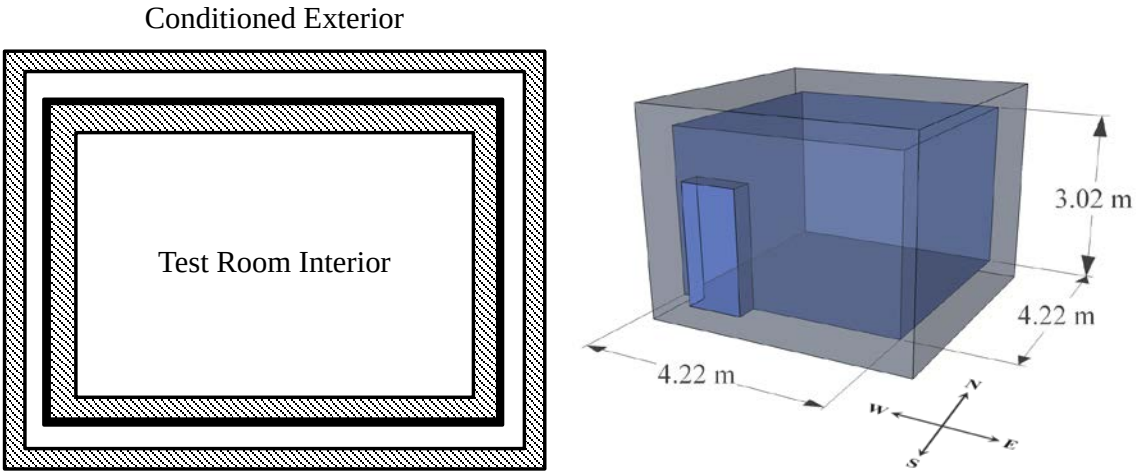

Figure 4. Temperature-controlled test chamber cross section shown at left and inside dimensions at right.

The supply water was controlled with a direct digital control (DDC) valve adjusting the flow rate to the beam. A secondary loop of chilled water, connected thermally to the primary loop by a series of heat exchangers, provided heat rejection with either a dry or wet chiller located outside the testing facility. To reduce water temperature variations in the secondary supply, a buffer tank (approximately 380 l capacity) was connected in series and included an internal gas-fired burner.

A passive chilled beam (Figure 5), 61 cm in width and 244 cm in length was attached to a bracket 0.25 meters from the ceiling of the room, centered from the walls. The beam was constructed of 12.7 mm diameter copper tubing with aluminum extruded fins measuring 15 cm in height and 61 cm in length and 2.4 mm thick. The beam was a two-row, twelve-pass coil with an aluminum shroud extending down around the outside

of the fins and an additional 46 cm from the bottom of the fins. The total number of fins was 384 at a spacing of 1.6 fins/cm (4 fins/in).

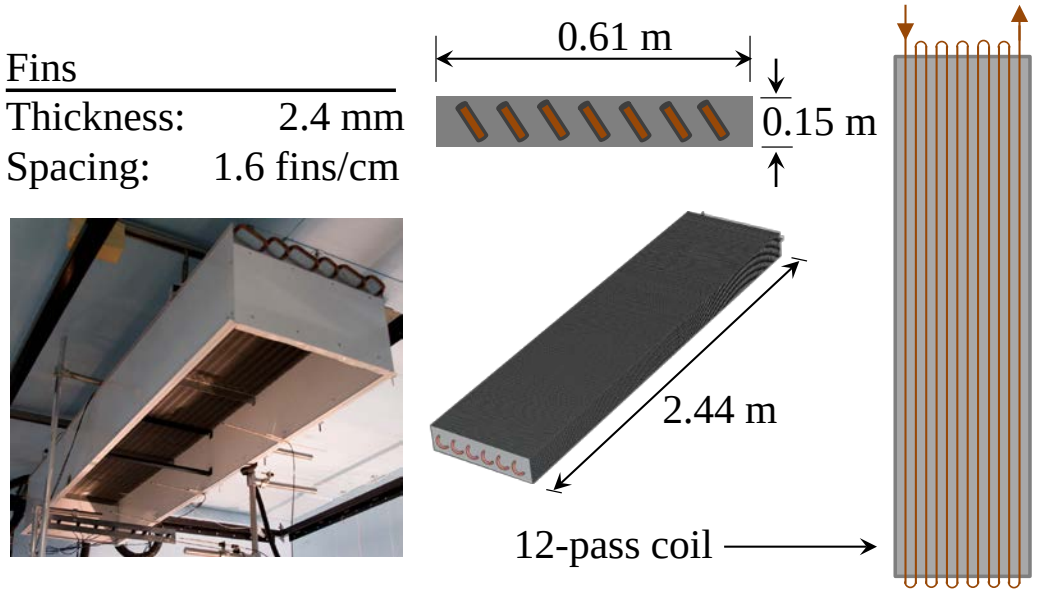

Figure 5. Passive Chilled Beam (PCB) geometry and dimensions.

Thermal manikins were used as one type of heat source in the space, shown in Figure 6. Each manikin was constructed to conform to standard EN 14240 and could be controlled with a digital silicon-controlled rectifier (SCR) up to 194 W of power. The metal cylinders, coated with high emissivity paint, contain three light bulbs and openings at the top and bottom to simulate the radiation and convection heat transfer of a person. Twelve manikins, connected in series, were used in the testing with a possible total heat input of 2300 W.

Figure 6. Thermal manikins used in testing.

A second type of heat source, radiant panels, was also tested. Each panel measured 61 cm by 122 cm and 5 cm thick. A layer of insulation was placed beneath each panel and the floor to reduce the transfer of heat generated by the radiant panels to floor. The panels were connected to the same power outlets as the thermal manikins.

3.1.2 Sensors

Temperature sensor calibrations were conducted using a metrology well calibrator. The reference Resistance Temperature Detector (RTD) was calibrated by a calibration service laboratory to an accuracy of ± 0.03 °C. The metrology well calibrator was used to maintain a uniform internal temperature and the temperature probe under test was compared to the reference RTD through a range of temperature points. Each

temperature sensor was calibrated with the data acquisition boards and power supplies used in the experiments.

The primary measurements in the testing included the supply and return water temperatures to the beam, the supply water mass flow, the power input to the thermal manikins, and air temperature and velocity measurements of the plume generated by the beam. Four-wire RTDs were used on the supply and return of the beam water. The temperature sensors were calibrated as a pair before conducting the experiments and the estimated accuracy was ± 2.2 % for the eight comparison points over the temperature range 40 °F – 126 °F. A coriolis flow meter measured the flow rate on the supply-side to the beam. The manufacturer specifications of the meter list an accuracy of ± 0.1 % of the measured mass flow rate and laboratory calibration of the meter resulted in an accuracy of ± 0.3 %. The input power to the heat sources was measured with a watt meter with an accuracy of ± 0.5 % of the measured power. Six omni-directional velocity transducers were supported by a vertical stand and positioned symmetrically below the beam along a central path of the descending plume air. The velocity sensors were calibrated prior to running the experiments and were found to have an accuracy of ± 3.3 % over the velocity range of 25–500 feet per minute. Four-wire RTDs were attached to the stand in the same location as the velocity probes to measure the temperature, as shown in Figure 7. Three omni-directional velocity sensors measured the discharge velocity from the beam twelve inches from the coil, spaced equally along the centerline of the beam. Three four-wire RTDs were positioned above the beam to measure the room air reference temperature and were calibrated before conducting the experiments

with an estimated accuracy of ± 0.12 % for the fourteen comparison points over the temperature range 50 °F – 120 °F. Additionally, a globe temperature sensor was positioned 1.1 m from the floor outside of the path of the beam plume. Table 1 presents a summary of the sensor specifications. The locations of the sensors are shown in Figure 8.

Figure 7. RTD probe and TSI omni-directional velocity probe pictured left to right, respectively.

Table 1. Sensor specifications for test room experiments.

Sensor	*Type*	*Accuracy*	*Range*
Inlet and outlet beam water temperatures	RTD	± 2.2 % of reading	40–126 °F
Supply water mass flow rate	Coriolis	± 0.3 % of reading	0-95 kg/h
Thermal manikin input power	Watt meter	± 0.5 % of reading	0-150 VAC, 0-30 AAC
Plume air velocity	Omni-directional	± 3.3 % of reading	25-500 fpm
Reference air temperature	RTD	± 0.12 % of reading	50–120 °F

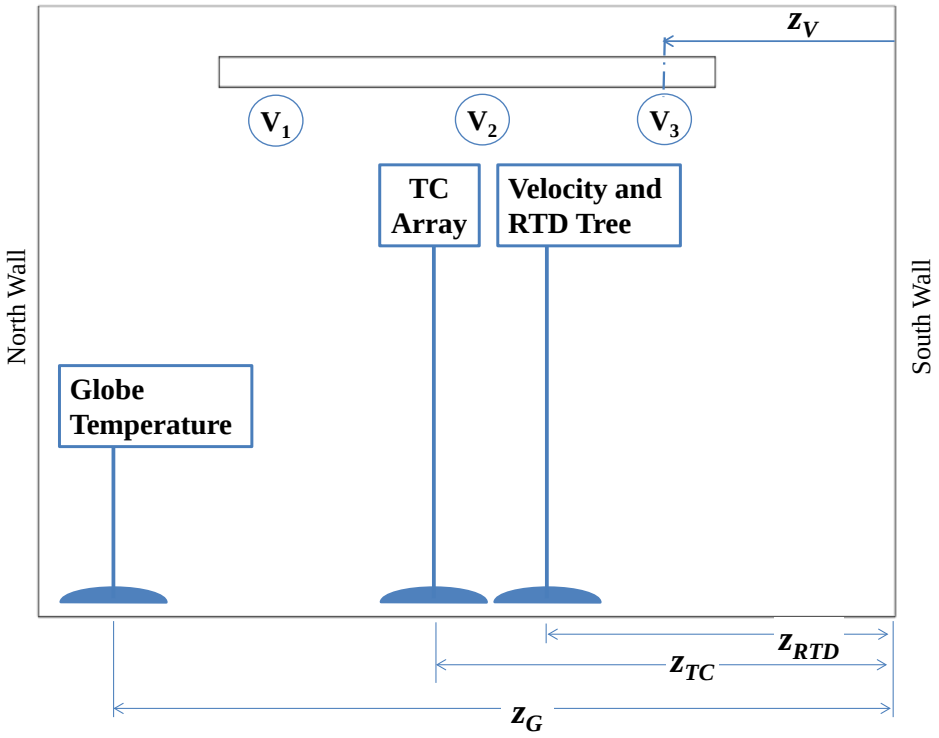

Figure 8. Sensor locations of the plume temperature thermocouple array (Z_{TC} = 2.3 m), the plume velocity and RTD tree (Z_{RTD} = 2.1 m), the outlet velocities from the beam (Z_{v3} = 1.9 m, Z_{v2} = 2.2 m, Z_{v1} = 2.7 m) and the globe temperature sensor (Z_G = 3.5 m).

Air temperatures were recorded with T-type thermocouples constructed with soldered junctions no more than 1 mm in diameter as shown in Figure 9. The thermocouples were connected to a Keithly 2700 data logger. Calibration was conducted on each thermocouple used in the experiments. The Fluke 9171 Metrology Well was used in a two point comparison with the reference RTD at 70 °F and 135 °F, resulting in an error of ± 2 % (± 1.4 °F at 70 °F).

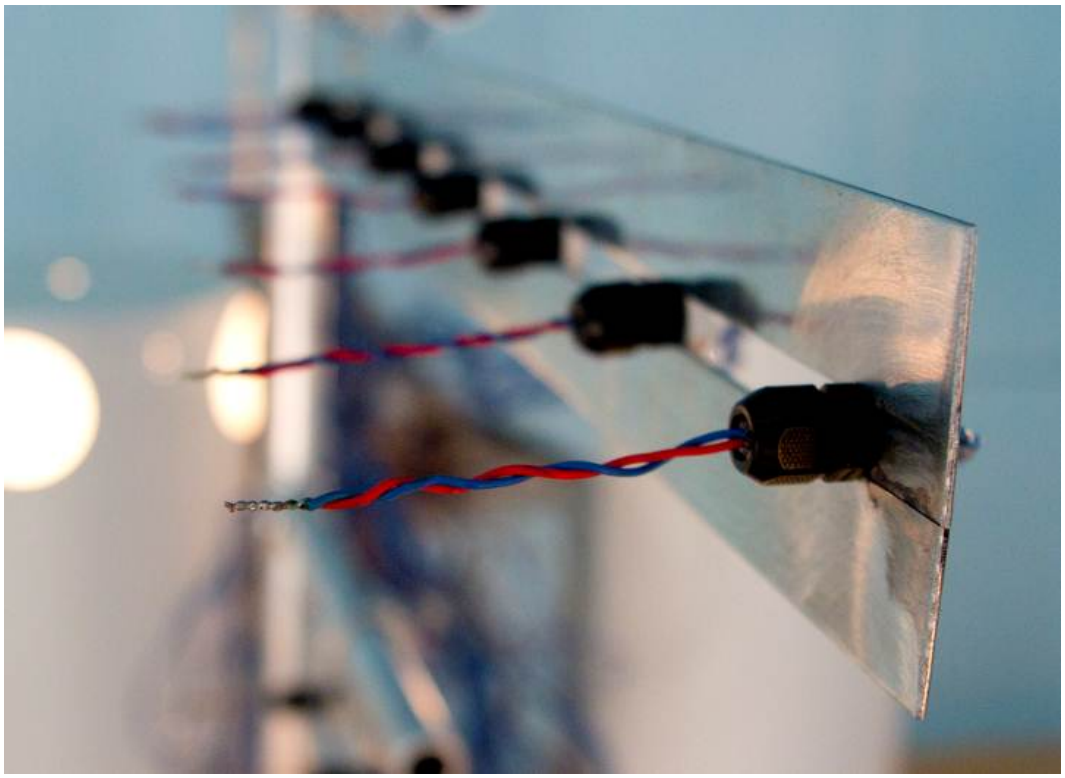

Figure 9. T-type thermocouples measured the beam plume air temperatures.

Two thermocouple arrays were constructed to measure the air temperatures below the beam as shown in Figure 10. The first, a seven-by-five grid positioned directly below the beam, consisted of a vertical stand with slotted arms supporting each row of seven T-type thermocouples spaced eight inches apart laterally. The second array construction featured two rows with 13 cm between each sensor and 13 cm between each row. The stand was positioned to capture the plume air directly beneath the beam and continue to the space above the heat sources.

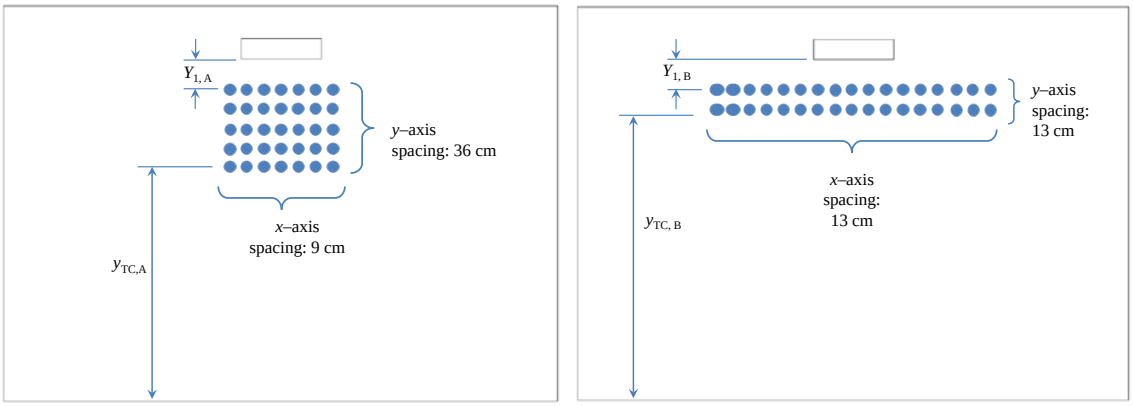

Figure 10. Thermocouple array configurations for measuring the Passive Chilled Beam (PCB) plume air temperatures ($y_{1,A}$ = 22 cm, $y_{TC,A}$ = 1.0 m, $y_{1,B}$ = 52 cm, $y_{TC,B}$ = 1.9 m).

Each wall radiant panel, sized 61 cm x 427 cm, contained twelve thermocouples connected by an averaging joint, and measured the inside and outside surface temperatures throughout the room as shown in Figure 11.

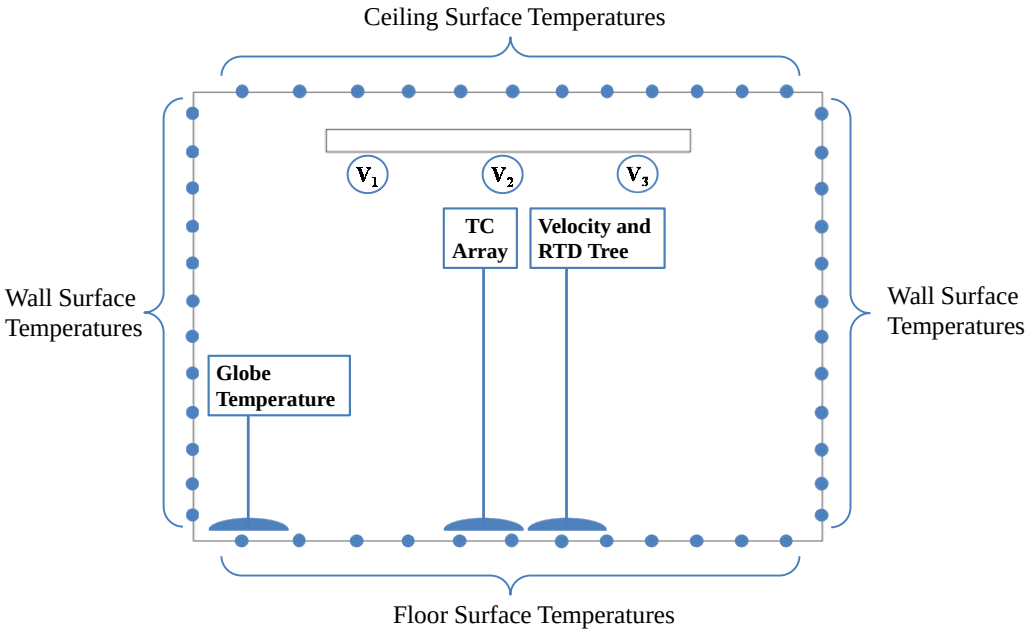

Figure 11. Wall, ceiling and floor surface temperature measurements.

The beam capacity was calculated as the product of the mass flow rate of water through the beam, specific heat of water at the average temperature measured between the inlet and outlet, and the difference in temperature between the inlet and outlet. The equation for the measured beam capacity is the following:

$$Q_b = \dot{m}_w c_{pw}\left(T_{w,o} - T_{w,i}\right) \tag{3.1}$$

where Q_b is the passive beam capacity, $\dot{m}_w$ is the mass flow rate of the supply water as measured from the Siemens mass flow meter, c_{pw} is the specific heat capacity of the water evaluated at the average of the inlet and supply water temperatures, $T_{w,o}$ is the outlet water temperature from the beam, and $T_{w,i}$ is the inlet water temperature to the beam, both measured with the RTD sensors.

The estimated error of the measured beam capacity was calculated by incorporating the cumulative accuracies of the sensors measuring the water temperatures and mass flow. The water temperature sensors were calibrated as a pair and their accuracy was estimated to be ± 2.2 % of the reading. The mass flow meter was calibrated by Siemens with an estimated accuracy of ± 0.3 % of the reading. The total error of the measured beam capacity was then estimated at an accuracy of ± 3 % of the reading.

3.1.3 Data Collection

The data was networked on the local Ethernet connections in the lab from the National Instruments data acquisition (DAQ) boards to a supervisory data logging server located in the control room. An overview of the data logging system is shown in Figure 12.

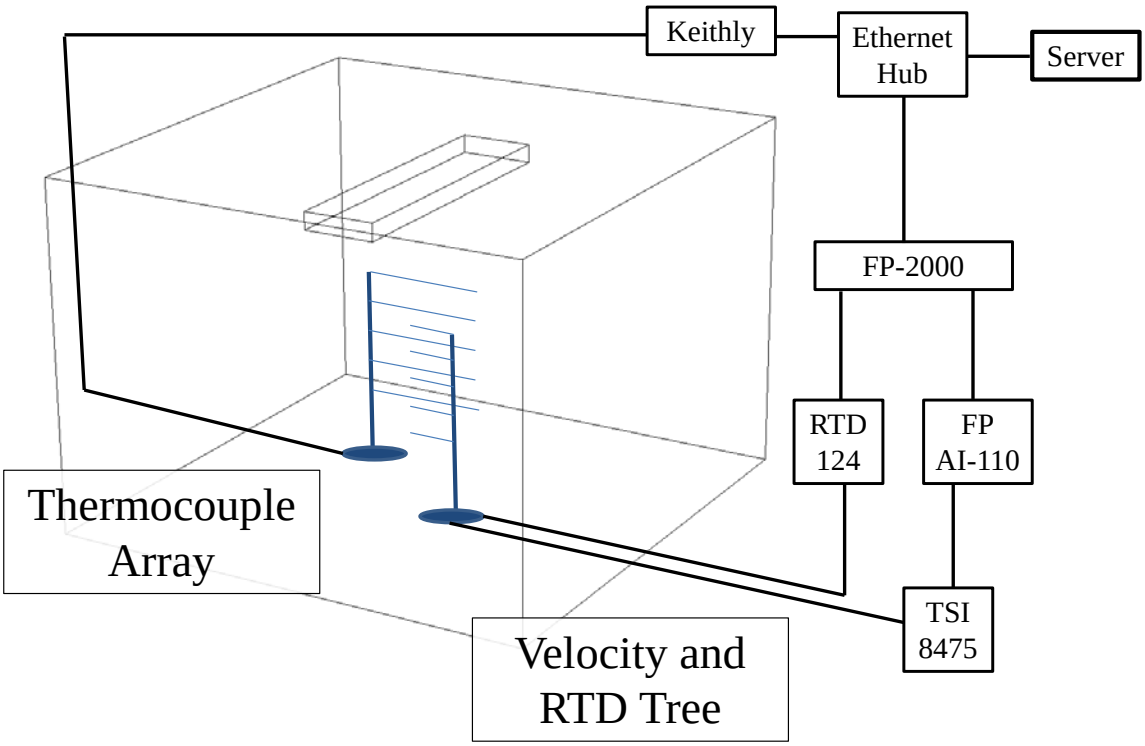

Figure 12. Data collection in test room of thermocouple, RTD and velocity measurements.

The thermocouples connected to the Keithly 2700 were installed in a thermocouple control module and the system capability was a maximum of 3500 readings/s at a maximum scanning rate of 500 channels/s. The data logger converted the voltage signals from the thermocouples to °F that were then broadcast through the Ethernet connection to the data logging server at 22-bit resolution. The averaged readings from the thermocouples in °F were recorded in 20 s increments in the database test file.

The measurements from the velocity and RTD sensors were conducted with a 0-10V analog voltage loop between the sensor transducers and the field point modules in

16-bit resolution. The temperature readings were linearized and scaled in the RTD 124 module, with a 1.08 s update period, a 2 mA excitation current, a 60 Hz rejection filter, and were configured for temperature readings in °C. The velocity readings in the National Instruments AI-110 analogue input module were filtered at 60 Hz with a channel update rate of 1.47 s. The National Instruments FP-2000 network module sent the input module data from the RTDs and velocity sensors through the Ethernet connection to the supervisory data logging computer at a 10 Mb/s communication rate.

3.2 Test Methodology

3.2.1 Validation

The approach to validating the numerical model was to test a passive chilled beam in a thermally controlled environment with symmetrically positioned heat loads and run a series of simulations to predict air characteristics of the modeled test room for the same test operating set points. By thermally isolating the test conditions from the external environment (and measuring any heat transfer into or out of the experiment), the passive chilled beam operation was measured without any additional unaccounted for effects. The experimental set points were designed to test over a range of thermal loads and passive chilled beam capacities. The passive chilled beam water conditions (mass flow rate, inlet and outlet temperatures), temperature profiles of the room air above and below the beam, velocity profiles in the beam plume, the power input to the thermal loads, and surface temperatures of the inside walls of the test chamber were measured so as to compare with the CFD model predictions. The CFD model was then used to

predict the steady state thermal conditions of each test set point based on the initial and operating conditions of the tests. Table 2 lists the experimental set points for each test that were used in the CFD model to calculate the airflow characteristics.

Table 2. Measured test data used for CFD model inputs.

Test	*Thermal Manikin Power (W)*	*Beam Capacity (W)*	*Floor Surface Temperature (°C)*	*Ceiling Surface Temperature (°C)*	*Wall Surface Temperature (°C)*
1	474	578	26.4	25.6	25.7
2	514	599	26.6	25.6	25.7
3	533	555	26.8	25.5	25.6
4	622	790	26.3	25.4	25.5
5	691	765	26.4	25.4	25.4
6	735	767	26.6	25.3	25.3
7	841	1035	26.1	25.3	25.2
8	912	973	26.3	25.2	25.2
9	979	1017	26.7	25.2	25.2
10	1101	1280	26.1	25.2	25.2

3.2.2 Test Setup and Initial Conditions

The primary objective for data collection was to record temperature and velocity measurements in the test space that would be used to compare with predicted values using the CFD model. The experimental procedure followed similar specifications listed in EN 14518 [78] for the testing of passive chilled beams. The beam supply water temperature and flow rate were specified for each set point of the test and the input power to the thermal manikins was controlled to meet a specified value for the reference temperature above the beam. Once the set point values were reached and the standard deviations of water flow rate, supply temperature, and the reference temperatures were

below 0.1 for 60 min, the data was recorded and the testing procedure moved onto the next set point value. Figure 13 shows the sensors for the testing procedure that were used as either test set point targets or feedback for the control system and Table 3 lists the parameters used for each set point in each test.

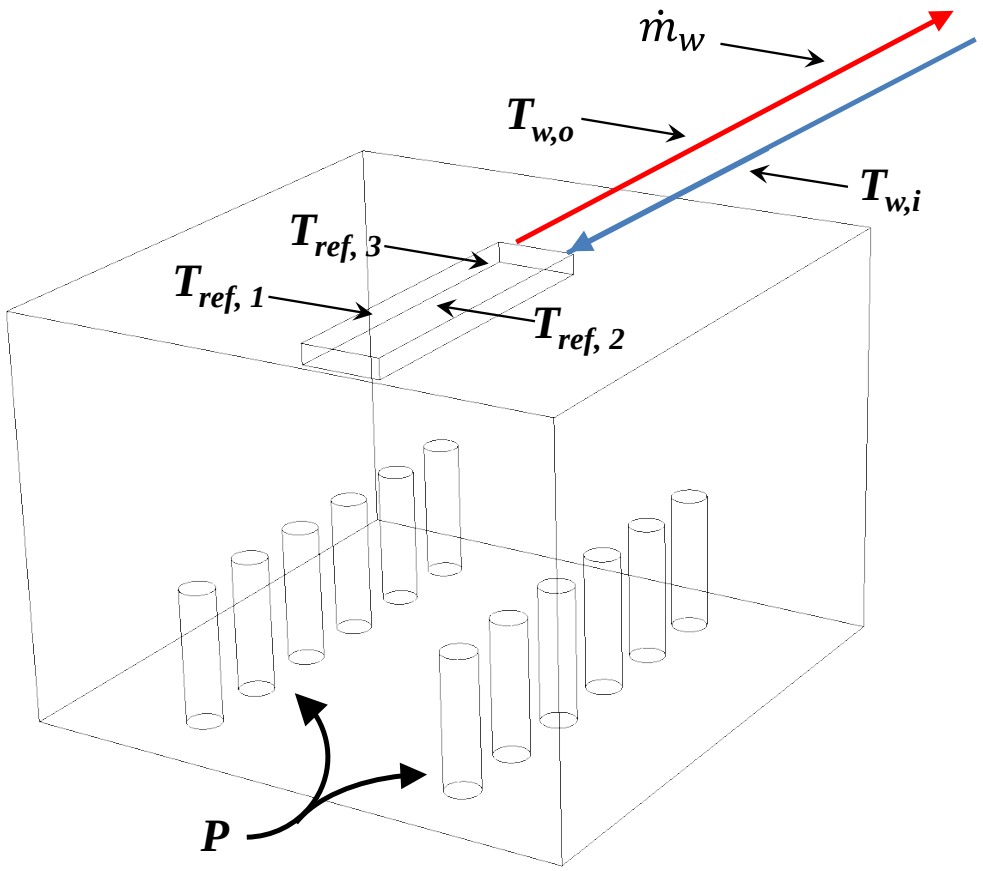

Figure 13. Sensors used for the testing procedure set points: power input to the thermal manikins (P), supply water mass flow and inlet and outlet temperatures ($\dot{m}_w$, $T_{w,i}$, $T_{w,o}$), reference air temperatures above the beam ($T_{ref,1}$, $T_{ref,2}$, $T_{ref,3}$).

Table 3. Inlet water temperature and supply flow rate for each test set point.

Set Point	*Inlet Water Temperature (°C)*	*Supply Water Flow Rate (l/hr)*
1	18	453.5
2	18	340.2
3	18	226.8
4	16	453.5
5	16	340.2
6	16	226.8
7	14	453.5
8	14	340.2
9	14	226.8
10	11	453.5

Each test required between 15 hr and 20 hr to complete. During each test, the measured values from the thermocouples, velocity probes, RTDs, watt meter, and mass flow meter were recorded at 20 s increments.

Symmetric and asymmetric heat load configurations were tested. The thermal manikins were arranged 104 cm from the outer wall to the center of the thermal manikin, spaced equally apart parallel to the length of the beam. Two rows of six thermal manikins each were placed on both sides of the beam in the symmetric configuration, shown in Figure 14 and both rows on one side in the asymmetric configuration as shown in Figure 15.

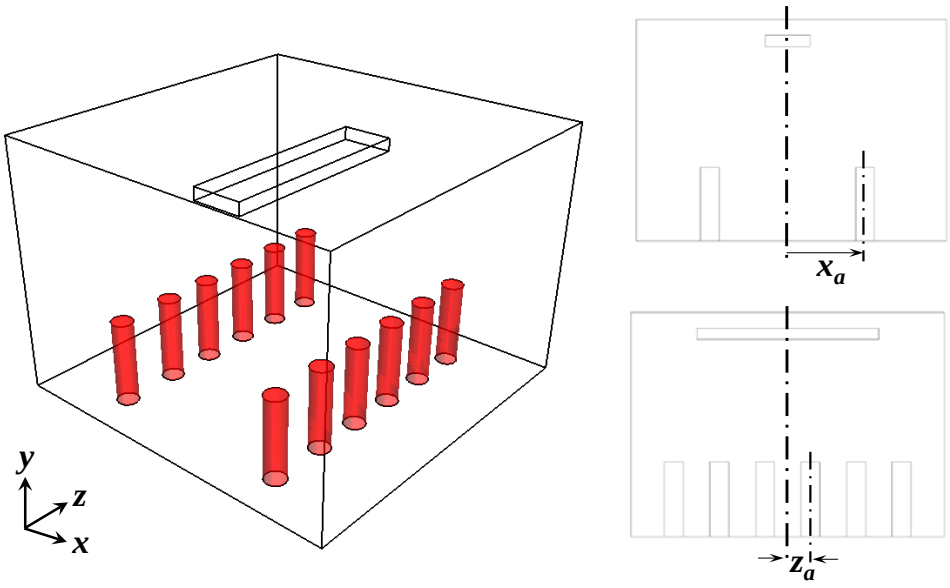

Figure 14. Test setup A with symmetric placement of thermal manikins, where x_a = 1.1 m and z_a = 30 cm.

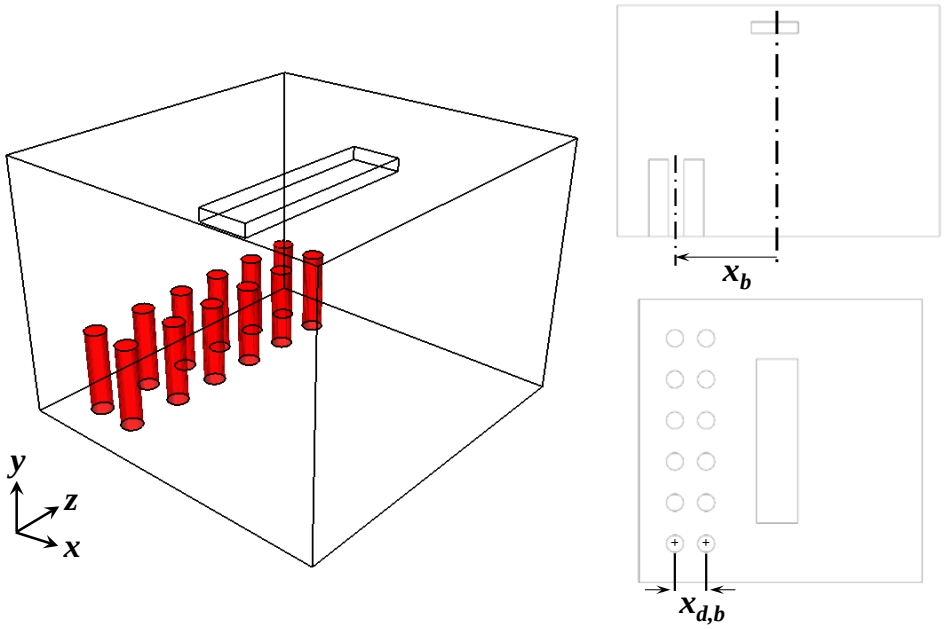

Figure 15. Test setup B with asymmetric thermal dummy placement, where x_b = 1.1 m and $z_{d,b}$ = 30 cm.

Radiant panels were also used as heat sources in a third configuration, shown in Figure 16 to test for the beam operation and plume characteristic differences based on the type of heat source. The radiant panels measured 61 cm by 122 cm. Two panels were placed on either side of the beam with the panel centers 104 cm from the wall. A layer of insulation was placed beneath each panel.

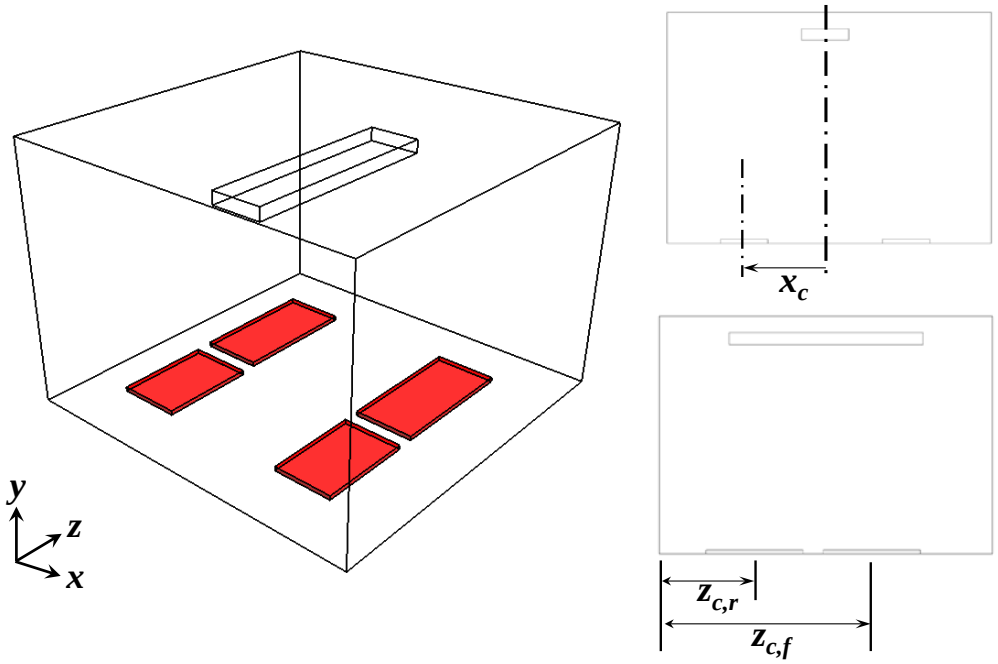

Figure 16. Test setup C with symmetrically placed radiant panels, where x_c = 1.1 m, $z_{c,f}$ = 1.3 m, and $z_{c,r}$ = 2.7 m.

CHAPTER IV

NUMERICAL MODEL

4.1 Introduction

The numerical simulation was constructed using Star CCM+ v6.06. The following section, first, documents the methodology for simplifying the passive beam geometry using a porous medium. Second, the applied boundary conditions, turbulence model and solver techniques are reported. Third, the mesh construction is explained and the results of a grid convergence study are documented. The methodology and techniques used to develop the passive chilled beam simulations are available in other commercial CFD packages and should produce equivalent model results. A derivation and explanation of the fundamental equations in CFD can be found in Appendix A.

4.2 Porous Region

The passive chilled beam geometry and heat transfer characteristics were simplified by using the porous region function for the volume encompassing the passive chilled beam in the room simulation. The porous medium model simulates a specified region within the simulation volume as a solid with channels that allow fluid flow. The geometric characteristics of the solid and the channels are not specified. Instead, the movement of the flow through the region is governed by a set of user inputs that determine the heat transfer and momentum exchange within the volume. The primary calculations applied to the porous medium are a momentum source term added to the

momentum equation and an energy source term added to the energy equation. The momentum source term, S_{ij}, is calculated as a function of viscous and inertial resistance:

$$S_{ij} = -\left(\sum_{j=1}^{3} D_{ij}\mu u_j + \sum_{j=1}^{3} C_{ij}\frac{1}{2}\rho|u|u_j\right) \quad 4.1$$

where D_{ij} is the coefficient of porous viscous resistance and C_{ij} is the coefficient of porous inertial resistance. The first term on the right hand side of Equation 4.1 is the viscous resistance and the second term on the right hand side of Equation 4.1 is the inertial resistance. The energy source term is added to the energy equation for all cells in the designated volume to model heat transfer through the porous region:

$$\frac{\partial}{\partial t}\left(\gamma\rho_f E_f + (1-\gamma)\rho_s E_s\right) + \nabla\cdot\left(\vec{u}\left(\rho_f E_f + p\right)\right) = \nabla\cdot\left[k_{\text{eff}}\nabla T - \left(\sum_i h_i J_i\right) + (\bar{\bar{\tau}}\cdot\vec{u})\right] + S_f^h \quad 4.2$$

where γ is the porosity, E_f is the total fluid energy, E_s is the total solid medium energy, p is the pressure, k_{eff} is the effective thermal conductivity of the medium, ∇T is the temperature gradient, h is the enthalpy, J is the diffusion flux, τ is the shear stress, and S^h_f is the fluid enthalpy source term. The following sections detail the functions and user inputs that were specified for the porous medium region of the passive chilled beam simulations.

4.2.1 Energy

A positive or negative value for the energy source term designates the porous region as either a source or sink of heat, respectively. To model the passive chilled beam, the energy source option was selected to specify the region as a heat sink and to

provide cooling to the room air. For the validation simulations, the beam capacity at each test point from the experiments was used to define the value of the volumetric energy source of the porous region, E_f'''. Additionally, the value for the energy source term was calculated at each iteration as a function of the temperature difference between the room air above the beam and the mean water temperature assumed for the beam for simulations with a varying beam capacity. The equation used in the simulations included a coefficient, C_{bc}, that was determined based on the experimental data:

$$E_f''' = C_{bc} \frac{T_{ref} - T_{w,ave}}{V} \quad 4.3$$

where T_{ref} is the average reference temperature measured across a horizontal plane in the simulation 0.14 m above the porous medium, $T_{w,ave}$ is an assumed mean water temperature for a typical passive chilled beam, and V is the volume of porous medium region. $T_{w,ave}$ was 18 °C and V was 0.223 m^3. The value of C_{bc} was calculated at each iteration based on a relationship to $T_{ref} - T_{w,ave}$ that was derived from experimental data. The calculation method and the equation development for C_{bc} is reported in Chapter VII.

4.2.2 Porosity

The porosity of the volume was set based on the geometry of the passive beam. The total volume of a one fin section of the passive beam was 517 cm^3, as shown in Figure 17. Within the total volume that accounts for both the passive beam and the air, the beam volume (one fin plus twelve sections of the coil) was 229 cm^3. The remaining air volume was 287 cm^3. The volume porosity was calculated as the ratio of the volume of the air in a one-fin section of the coil to the total volume of a one-fin section of the

coil. The porosity of the passive beam was calculated to be 0.56 based on this approximation method.

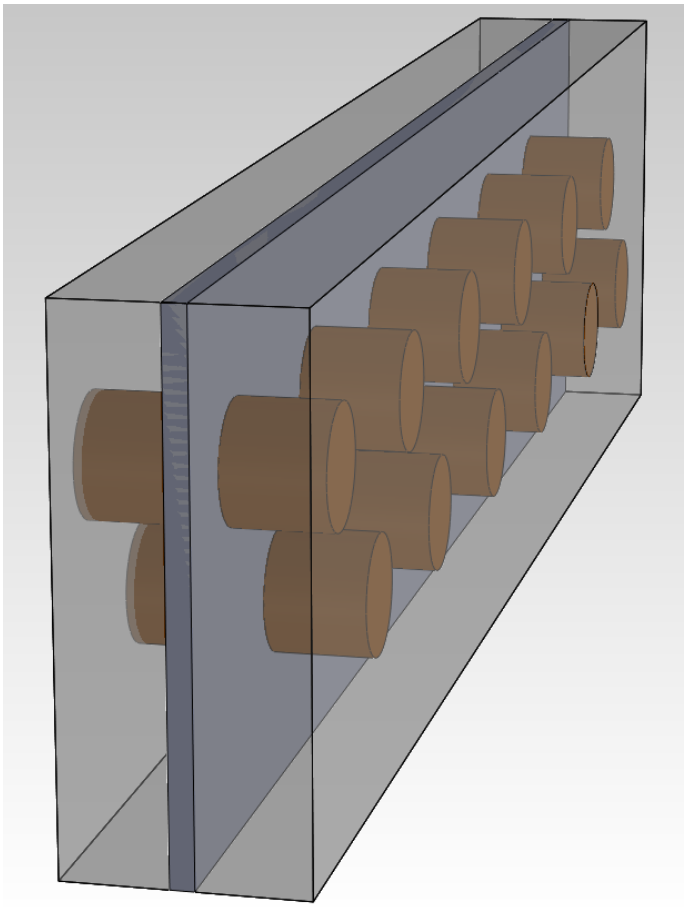

Figure 17. One fin section of passive chilled beam volume of air used in porosity approximation.

4.2.3 Porous Inertial Resistance

The porous inertial resistance coefficient, C_{ij}, is used to calculate the inertial resistance contribution to the overall momentum source term for the porous region as shown in Equation 4.1. A positive value of C_{ij} would have the effect of slowing down the velocity of the fluid flowing through the region and is similar to the effect of constricted flow through a pipe with a decrease in pipe diameter. A uniform inertial resistance can be specified or a directional inertial resistance based on the three components. With the geometry of the passive chilled beam fin bank, a three component inertial resistance was applied for the passive chilled beam simulations. The *x*-component of inertial resistance was set many orders of magnitude higher than the *y*-component and the *z*-component to restrict the room airflow in the direction perpendicular to the fin surfaces.

4.2.4 Porous Viscous Resistance

The porous viscous resistance coefficient, D_{ij}, is used to calculate the viscous resistance contribution to the overall momentum source term for the porous region as shown in Equation 4.1. A positive value of D_{ij} would have the effect of slowing down the velocity of the fluid flowing through the region and is similar to the effect of constricted flow through a pipe with an increase in roughness along the surface of the pipe. A uniform viscous resistance can be specified or a directional viscous resistance based on the three components. With the geometry of the passive chilled beam fin bank, a three component viscous resistance was applied for the passive chilled beam simulations. The *x*-component of viscous resistance was set many orders of magnitude

higher than the *y*-component and the *z*-component to restrict the room airflow in the direction perpendicular to the fin surfaces.

4.2.5 Solid Thermal Conductivity

The solid thermal conductivity is used to calculate the effective thermal conductivity of the volume consisting of the fluid and solid. The equation for the effective thermal conductivity, which is used in the energy equation, is based on the porosity of the region:

$$k_{\text{eff}} = \gamma k_f + (1-\gamma)k_s \tag{4.4}$$

where k_f is the fluid thermal conductivity, and k_s is the solid medium thermal conductivity. The thermal conductivity of the solid region was estimated based on the thermal conductivity of extruded aluminum and copper along with the mass ratio of aluminum to copper in the passive beam. The following equation was used:

$$k_{\text{s}} = \frac{m_{al}}{m_{cu}} k_{\text{al}} + \left(1 - \frac{m_{al}}{m_{cu}}\right) k_{cu} \tag{4.5}$$

where k_s is the effective solid thermal conductivity, m_{al} is the mass of aluminum, m_{cu} is the mass of copper, k_{al} is the thermal conductivity of aluminum, and k_{cu} is the thermal conductivity of copper. k_s was calculated to be 200 W/mK.

4.2.6 Interfaces

The boundaries of the porous medium region were setup as two different types of interfaces: an in-place interface that did not restrict fluid flow or heat transfer, and an in-place interface that was defined as an adiabatic baffle that both restricted fluid flow and heat transfer. The passive chilled beam is surrounded by sheet metal that restricts airflow in the direction parallel to the length of the fin. The inlet and the outlet to the

beam are open to the room air without any flow restriction. In order to replicate the airflow characteristics through the passive chilled beam boundaries, the inlet and outlet were defined as in-place interfaces with no restriction to fluid flow or heat transfer and the four sides of the beam were defined as adiabatic baffles.

4.3 Boundary Conditions

Wall boundary conditions were used for solid-to-fluid interfaces in the simulation volume. The velocities were defined based on the no-slip condition where the wall velocity was set to zero ($u_i = 0$). The heat transfer at the wall boundaries was defined by either a surface temperature (taken from experimental data) or a constant heat flux for the heat sources. The interface between the passive chilled beam region and the room air region were defined as either an adiabatic baffle or an in-place interface without heat transfer or fluid flow restrictions. A summary of the boundary condition applications is shown in Figure 18.

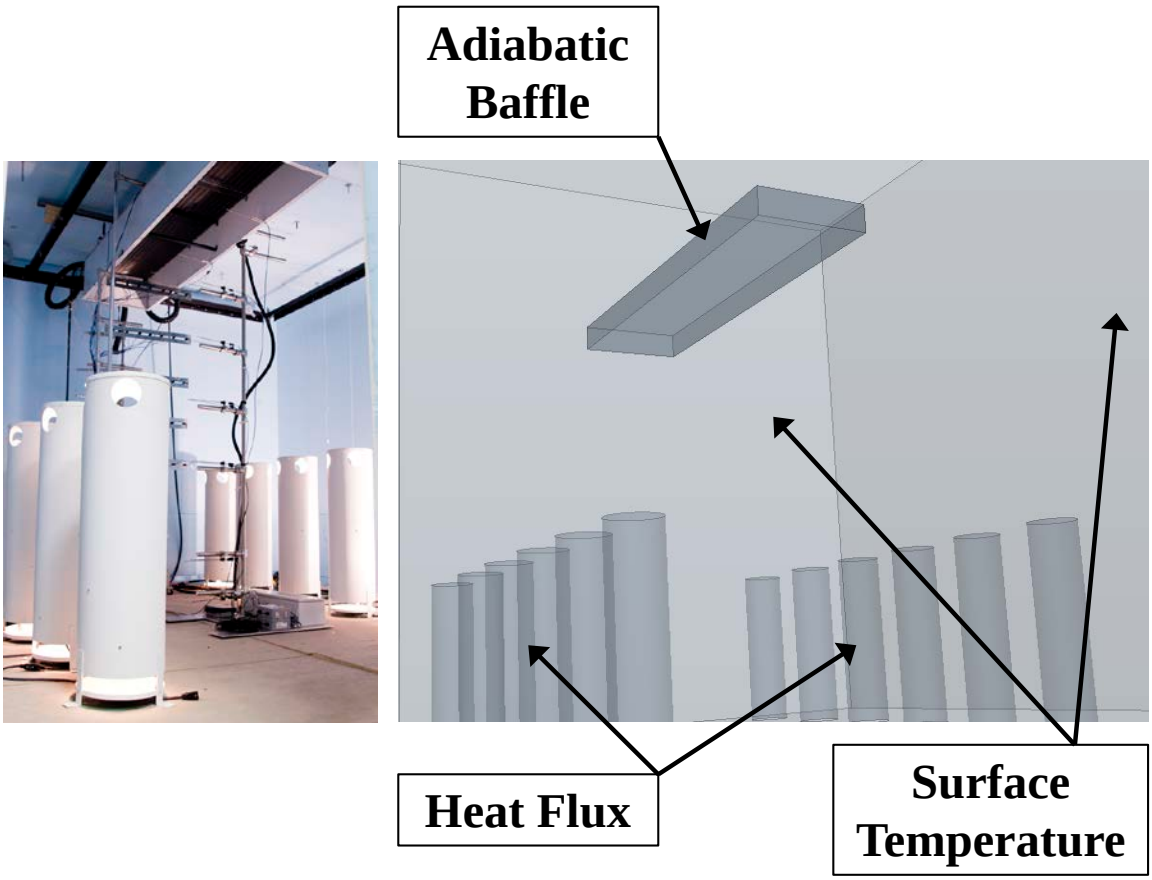

Figure 18. Boundary conditions for passive chilled beam model.

4.4 Turbulence Model

The standard k-ε turbulence model was used for the CFD simulations. This turbulence model is based on a RANS two-equation eddy viscosity method for approximating the turbulent flow. Star CCM+ uses a finite volume discretization of the flow equations and the governing equations for the flow represented in differential form as derived in Appendix A are:

$$\left(\frac{\partial \rho}{\partial t} + u_j \frac{\partial \rho}{\partial x_j}\right) + \rho \frac{\partial u_j}{\partial x_j} = 0 \quad 4.6$$

$$\rho\left(\frac{\partial u_i}{\partial t} + u_j \frac{\partial u_i}{\partial x_j}\right) = -\frac{\partial p}{\partial x_i} + \frac{\partial T_{ij}}{\partial x_j} \quad 4.7$$

The velocity (u) and pressure (p) can be decomposed into a mean ($\bar{u}, \bar{p}$) and fluctuating (u', p') component to represent the instantaneous values of Equations 4.1 and 4.2 and are defined as:

$$u = \bar{u} + u' \quad 4.8$$

$$p = \bar{p} + p' \quad 4.9$$

Using Equations 4.8 and 4.9 and reinserting into Equations 4.6 and 4.7, the rearranged equations become:

$$\frac{\partial u_j}{\partial x_j} \quad 4.10$$

$$\rho\left(\frac{\partial \bar{u}_i}{\partial t} + \bar{u}_j \frac{\partial \bar{u}_i}{\partial x_j}\right) = -\frac{\partial \bar{p}}{\partial x_i} + \frac{\partial}{\partial x_j}\left[\overline{T_{ij}} - \rho\left(u_i' u_j'\right)\right] \quad 4.11$$

The last term on the right-hand-side, $\rho\left(u_i' u_j'\right)$, is defined as the Reynolds Stress and is an approximation of the flow behavior that does not directly represent a characteristic of the fluid or the flow. As a result, the Reynolds Stress must be modeled based on fluid and flow properties. The Boussinesq eddy viscosity assumption relates the Reynolds Stress, τ_{ij} to the turbulent kinetic energy, the mean strain rate, and a term defined as the turbulent viscosity:

$$\tau_{ij} = 2\mu_t S_{ij} - \frac{2}{3}\rho k \delta_{ij} \quad 4.12$$

where μ_t is the turbulent viscosity, δ_{ij} is the Kronecker delta, and S_{ij} is the strain rate tensor defined as:

$$S_{ij} = \frac{1}{2}\left(\frac{\partial u_i}{\partial x_j} + \frac{\partial u_j}{\partial x_i}\right) \tag{4.13}$$

The turbulent viscosity is modeled, as defined by Launder and Spalding, as:

$$\mu_T = \rho C_\mu \frac{k^2}{\varepsilon} \tag{4.14}$$

where C_μ is a constant, k, is the turbulent kinetic energy, and ε is the turbulent dissipation. The turbulent kinetic energy and the turbulent dissipation are defined as:

$$k \equiv \frac{1}{2}\overline{u_\iota u_\iota} \tag{4.15}$$

$$\varepsilon \equiv \nu \overline{\frac{\partial u_\iota \partial u_\iota}{\partial x_k \partial x_k}} \tag{4.16}$$

where ν is the kinematic viscosity.

The method of solution of the transport equations used to calculate k and ε is reviewed below and can be found documented in the Star CCM+ user guide. The transport equations used to calculate the turbulent kinetic energy and the turbulent dissipation written in differential form are the following:

$$\frac{\partial}{\partial t}(\rho k) + \frac{\partial}{\partial x_i}(\rho k u_i) = \frac{\partial}{\partial x_j}\left[\left(\mu + \frac{\mu_t}{\sigma_k}\right)\frac{\partial k}{\partial x_j}\right] + G_k + G_{nl} - \rho\varepsilon - Y_M + S_k \tag{4.17}$$

$$\frac{\partial}{\partial t}(\rho\varepsilon) + \frac{\partial}{\partial x_i}(\rho\varepsilon u_i) = \frac{\partial}{\partial x_j}\left[\left(\mu + \frac{\mu_t}{\sigma_\varepsilon}\right)\frac{\partial \varepsilon}{\partial x_j}\right] + C_{1\varepsilon}\frac{\varepsilon}{k}(G_k + C_{3\varepsilon}G_b) - C_{2\varepsilon}\rho\frac{\varepsilon^2}{k} + S_\varepsilon \quad (4.18)$$

where S_k and S_ε are optional user-specified source terms, σ_k and σ_ε are the turbulent Schmidt numbers for the respective transport equations, G_k, G_{nl}, G_b are turbulence production terms, Y_M is the dilatation dissipation, and $C_{1\varepsilon}$, $C_{2\varepsilon}$ and $C_{3\varepsilon}$ are specified coefficients.

The turbulent production, G_k, was calculated by:

$$G_k = \mu_t\left(\frac{\partial u_i}{\partial x_j} + \frac{\partial u_j}{\partial x_i}\right)\frac{\partial u_i}{\partial x_j} - \frac{2}{3}\frac{\partial u_k}{\partial x_k}\left(3\mu_t\frac{\partial u_k}{\partial x_k} + \rho k\right) \quad (4.19)$$

The non-linear model was not included in this research project and, therefore, G_{nl} was set to zero. The turbulent production due to buoyancy, G_b, was calculated based on the Boussinesq buoyancy model by:

$$G_b = \beta\frac{\mu_t}{\sigma_t}g_i\frac{\partial T}{\partial x_i} \quad (4.20)$$

where β is the coefficient of thermal expansion, g is the gravitational vector, and σ_t is the turbulent Prandtl number. The ideal gas relation was used in this research project and, using the Boussinesq approximation, the coefficient of thermal expansion was calculated as:

$$\beta = -\frac{1}{\rho}\frac{\partial \rho}{\partial T} \quad (4.21)$$

The coefficient $C_{3\varepsilon}$ was calculated by:

$$C_{3\varepsilon} = \tanh|v_v/u_h| \quad 4.22$$

where v_v is the vertical velocity component (parallel to g) and u_h is the horizontal velocity component (perpendicular to g). Outside the natural convection boundary layers, $C_{3\varepsilon}$ is set to zero. The dilatation dissipation, Y_M was calculated as:

$$Y_M = \frac{C_M k\varepsilon}{c^2} \quad 4.23$$

where c is the speed of sound and C_M is a coefficient set to 2. The Yap correction, Y_y, was set to zero as a two-layer model was not included. Table 4 lists the model coefficients used.

Table 4. Standard k-ε coefficient values.

Model Coefficient	*User-specified Value*
$C_{1\varepsilon}$	1.44
$C_{2\varepsilon}$	1.92
C_μ	0.09
σ_k	1.0
σ_ε	1.3
C_t	1

Finally, the turbulent viscosity, μ_t is calculated as:

$$\mu_t = \rho C_\mu k T \quad 4.24$$

where T, the turbulent time scale is calculated as the maximum of the k to ε ratio and the product of the realizable time scale coefficient, C_T, and the square root of the ratio of the kinematic viscosity to the turbulence dissipation:

$$T = max\left(\frac{k}{\varepsilon}, C_T\sqrt{\frac{\nu}{\varepsilon}}\right) \quad 4.25$$

The wall treatment for the standard k-ε turbulence model in the Star CCM+ environment used the high-y^+ formulation and calculated the reference velocity, u^*, as:

$$u^* = \sqrt{C_\mu^{1/2} k} \quad 4.26$$

The turbulent production at the wall, Gk, is calculated as:

$$G_k = \frac{1}{\mu}\left(\rho u^* \frac{u}{u^+}\right)^2 \frac{\partial u^+}{\partial y^+} \quad 4.27$$

where u^+ is a dimensionless velocity and y^+ is the dimensionless wall distance. The wall-cell dissipation was calculated as:

$$\varepsilon = \frac{u^{*3}}{\kappa y} \quad 4.28$$

where κ is the von Karman constant.

4.5 Solver Specifications

The Star CCM+ solver uses a finite volume discretization to solve the flow equations. Integral forms of the transport equations are discretized and applied at each cell of the computational grid. This process results in a set of linear equations with the number of unknowns equal to the number of cells in the grid. The Star CCM+ algebraic

multigrid solver then calculates the solution of the system of equations. This section follows the documentation of the solver specification in the Star CCM+ user guide.

For the first step, finite volume discretization, the transport equation in differential form of an example scalar or vector, ϕ, can be written as:

$$\frac{\partial \rho \phi}{\partial t} + \nabla \cdot (\rho \vec{u} \phi) = \nabla \cdot (\Gamma \nabla \phi) + S_{\phi} \tag{4.29}$$

where Γ is the diffusion coefficient or diffusivity. The first term on the left hand side of Equation 4.29 represents the transient term or the amount of ϕ that enters the control volume, while the second term represents the convection term or the transport of ϕ due to the velocity field. The first term on the right hand side of Equation 4.29 represents the transport of ϕ due to gradients and is defined as the diffusion term, while the second term is the source term that calculates sources or sinks of the variable ϕ.

The Star CCM+ solver uses either a first or second order temporal scheme to solve the transient term. For this research project, a second-order temporal scheme was used to solve for the transient term:

$$\frac{\partial \rho \phi}{\partial t} = \frac{3(\rho_0 \phi_0)^{n+1} - 4(\rho_0 \phi_0)^{n} + (\rho_0 \phi_0)^{n-1}}{2\Delta t} \tag{4.30}$$

where n+1 is the solution at the current time level, n is equal to the previous time level, n-1 is equal to the solution from two previous time levels before the current time level, and Δt is the change in time.

Many options within the Star CCM+ environment exist for solving the convection term, including first-order upwind, second-order upwind and central-differencing. A second-order upwind differencing scheme was applied for the

discretization of the convection term in this research project and was calculated as follows:

$$\nabla \cdot (\rho \vec{u} \phi) = (\dot{m}\phi)_f = \dot{m}_f \phi_f \tag{4.31}$$

and

$$(\dot{m}\phi)_f = \begin{cases} \dot{m}_f \phi_{f,0} & for\ \dot{m}_f \geq 0 \\ \dot{m}_f \phi_{f,1} & for\ \dot{m}_f < 0 \end{cases} \tag{4.32}$$

where the subscript *f* signifies the value at the cell face, and $\phi_{f,0}$ and $\phi_{f,1}$ are linearly interpolated face values of the faces on either side of the cell:

$$\phi_{f,0} = \phi_0 + \mathrm{s}_0 \cdot (\nabla \phi)_{r,0} \tag{4.33}$$

$$\phi_{f,1} = \phi_1 + \mathrm{s}_1 \cdot (\nabla \phi)_{r,1} \tag{4.34}$$

where $(\nabla \phi)_{r,0}$ and $(\nabla \phi)_{r,1}$ are the respective reconstruction gradients for cells 0 and 1, and:

$$s_0 = x_f - x_0 \tag{4.35}$$

$$s_1 = x_f - x_1 \tag{4.36}$$

Finally, the diffusion term is solved implicitly for the cell values ϕ_0 and ϕ_1 based on a decomposition of the face value:

$$\nabla \phi_f = (\phi_0 - \phi_1)\vec{\alpha} + \overline{\nabla \phi} - (\overline{\nabla \phi} \cdot \mathrm{ds})\vec{\alpha} \tag{4.37}$$

where:

$$\vec{\alpha} = \frac{\mathbf{a}}{\mathbf{a} \cdot \mathrm{ds}} \tag{4.38}$$

$$\mathrm{ds} = \mathrm{x}_1 - \mathrm{x}_0 \tag{4.39}$$

$$\overline{\nabla\phi} = \frac{(\nabla\phi_0 + \nabla\phi_1)}{2} \tag{4.40}$$

and **a** is the area vector. The diffusion flux can then be written as:

$$D_f = \Gamma_f \nabla\phi_f \cdot \mathbf{a} = \Gamma_f \begin{bmatrix} (\phi_0 - \phi_1)\vec{\alpha} \cdot \mathbf{a} + \overline{\nabla\phi} \cdot \mathbf{a} \\ -(\overline{\nabla\phi} \cdot \mathrm{ds})\vec{\alpha} \cdot \mathbf{a} \end{bmatrix} \tag{4.41}$$

4.5.1 K-Epsilon Solver

The Star CCM+ k-ε turbulence solver calculates the values for each transport variable, k and ε, by first updating the boundary conditions, computing the reconstruction and cell gradients, constructing the linear system for the face values using Gauss' divergence theorem, computing the residual sum, solving the linear system, and updating the transport variable values. The turbulent viscosity, μ_t, for each iteration is calculated using the Laudner and Spalding equation based on the transport variables as described in Section 4.4. However, the assigned value, μ_t^{n+1}, for the iteration is calculated using the new calculated value, μ_t^{new}, combined with the assigned value of the previous iteration, μ_t^n, based on the following equation:

$$\mu_t^{n+1} = \omega_\mu \mu_t^{\mathrm{new}} + (1 - \omega_\mu)\mu_t^n \tag{4.42}$$

where ω_μ is the under-relaxation factor. The under-relaxation factor was assigned a value of 1.0 for this research project.

4.6 Meshing

The meshing was completed in the Star CCM+ v6.06 environment. An unstructured polyhedral meshing scheme was used with a single prism layer as the first cell along the walls, ceiling and floor. The distance between the wall surface and the

first cell in the volume mesh was specified by iteratively solving for the dimensionless wall distance, y^+, defined as:

$$y^+ \equiv \frac{u_\tau y}{\nu} \tag{4.43}$$

where u_τ is the friction velocity at the wall, y is the distance to the wall, and ν is the kinematic viscosity. Since the calculation depends on the fluid and flow properties, a value for the first layer cell distance from the wall was estimated and used in a solution. At the completion of the solution, the y^+ value was calculated and the average for all the wall surfaces was used to determine if the estimated first layer cell distance needed to be adjusted. The target value for y^+ when using the standard k-ε turbulence model was approximately 30.

Within the Star CCM+ mesher, input values to control the mesh construction were adjusted to vary the overall number of cells generated within the volume mesh and the density of cells in specific locations within the volume mesh. For each construction, the base cell size, number of prism layers, prism layer thickness, surface growth rate, and the minimum and target sizes for the surface were adjusted to obtain a volume mesh that would sufficiently resolve the flow conditions with the fewest number of cells. In Figure 19, an example is shown of a highly dense volume mesh of room air with symmetrically positioned thermal manikins and a passive chilled beam. The characteristics of this volume mesh are listed in Table 5.

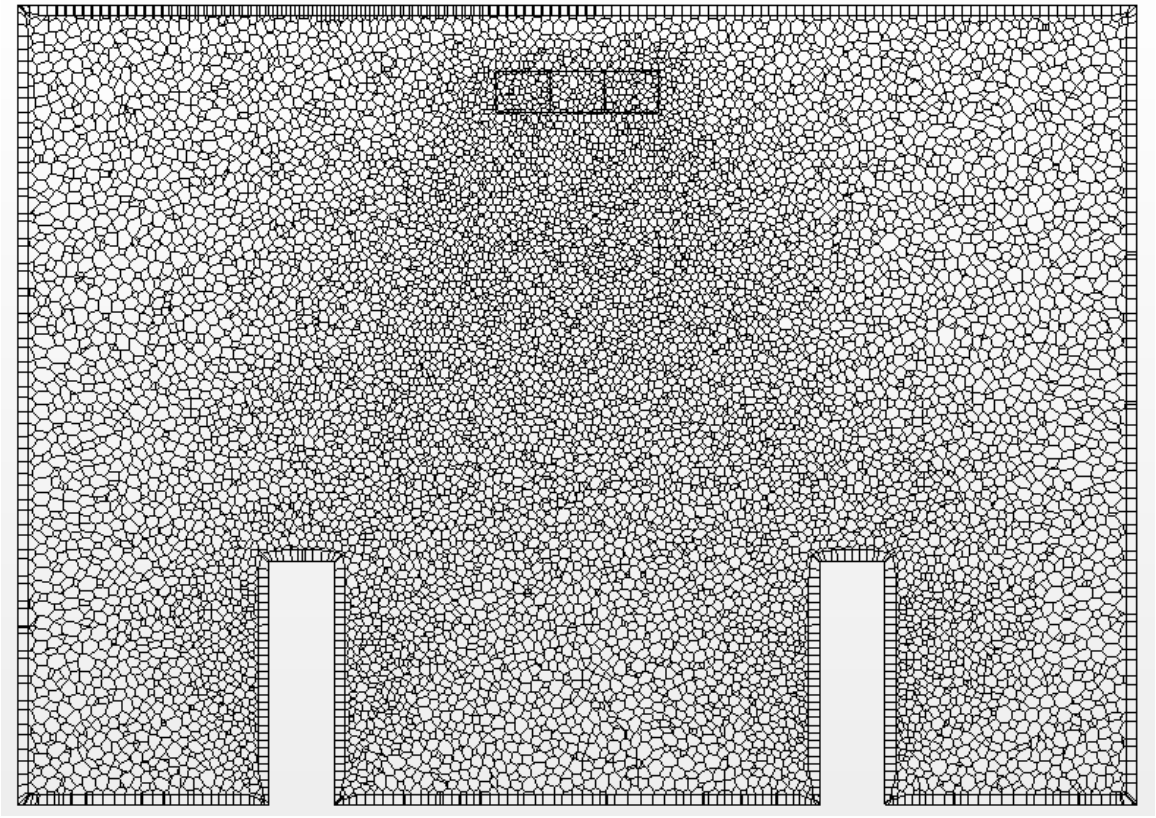

Figure 19. Cross-sectional view of volume mesh of 1.2 million cells.

Table 5. Mesh parameters for 1.2 million cell volume mesh.

Number of Cells	1,195,994
Base Cell Size	4 cm
Number of Prism Layers	1
Prism Layer Thickness	4 cm
Surface Growth Rate	1.3
Minimum Surface Size	1cm
Target Surface Size	4 cm
Beam surface mesh size	2 cm

In Figure 20, an example is shown of a moderately dense volume mesh of room air with symmetrically positioned thermal manikins and a passive chilled beam. The characteristics of the volume mesh are listed in Table 6.

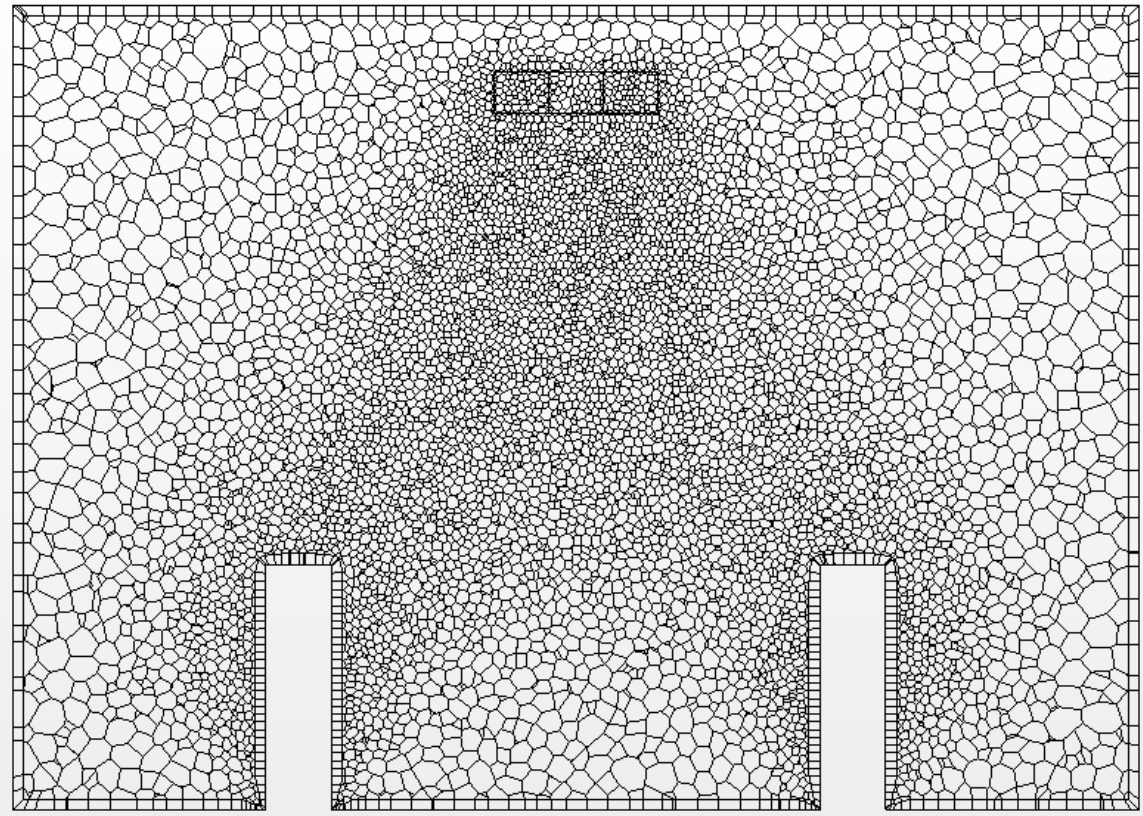

Figure 20. Cross-sectional view of volume mesh of 560,000 cells.

Table 6. Mesh parameters for 560,000 cell volume mesh.

Number of Cells	563,181
Base Cell Size	8 cm
Number of Prism Layers	1
Prism Layer Thickness	4 cm
Surface Growth Rate	1.3
Minimum Surface Size	2 cm
Target Surface Size	8 cm
Beam surface mesh size	2 cm

In Figure 21, an example is shown of a low density volume mesh of room air with symmetrically positioned thermal manikins and a passive chilled beam. The characteristics of the volume mesh are listed in Table 7.

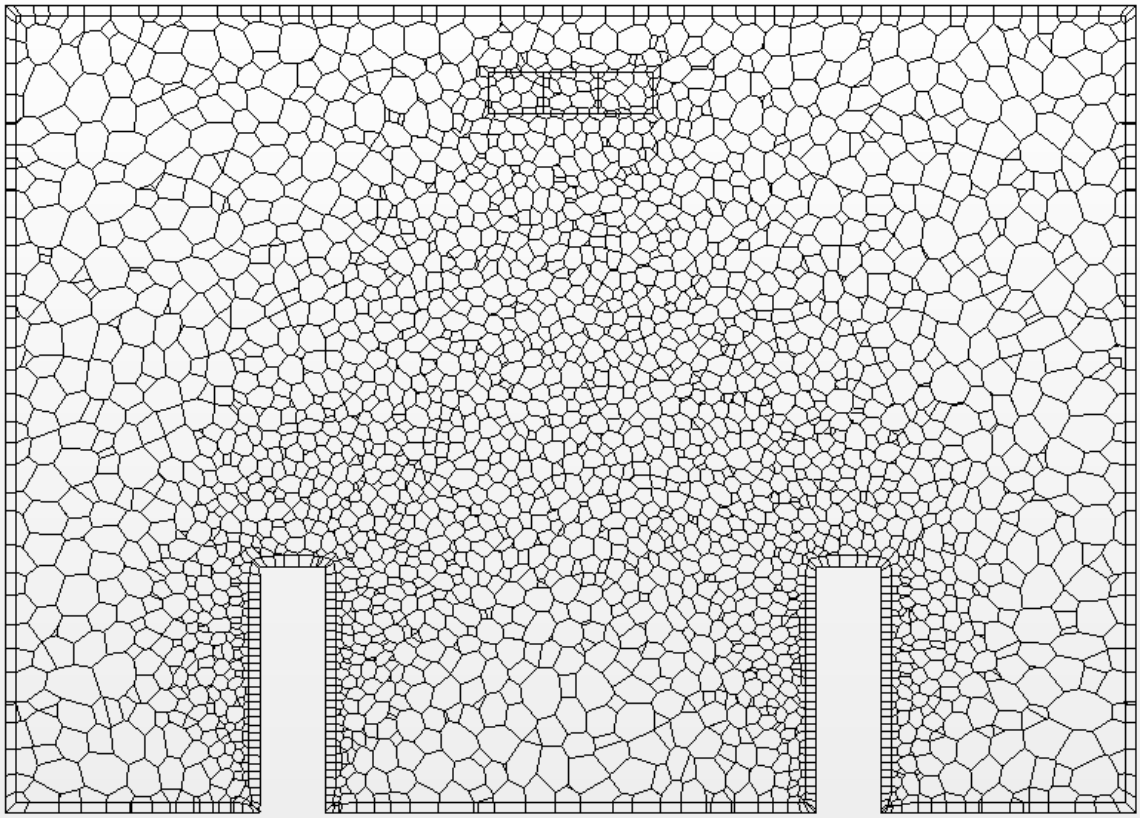

Figure 21. Cross-sectional view of volume mesh of 138,000 cells.

Table 7. Mesh parameters for 138,000 cell volume mesh.

Number of Cells	137,831
Base Cell Size	12 cm
Number of Prism Layers	1
Prism Layer Thickness	4 cm
Surface Growth Rate	1.3
Minimum Surface Size	3 cm
Target Surface Size	12 cm
Beam surface mesh size	6 cm

4.7 Grid Convergence Study

In order to establish the solution results of the CFD model as unaffected by the size of the mesh, a grid dependency study was conducted. For a CFD model, as the grid resolution is refined, the solution results will remain similar if the cell sizes are sufficiently small to capture the motion of the fluid flow. The degree of similarity between simulation results is a subjective comparison and depending on the area of application, the acceptance of the solution as grid independent depends on the value of change between simulation parameters. Since the cooling of the passive chilled beam was the primary focus of this research study, the mass flow through the beam was used to compare simulation results as the grid was resolved.

Three characteristics of the mesh were found to influence the grid dependency of the solution: the surface size of the mesh on the porous region, the distance between the wall and the first cell in the volume mesh, and the size of the cells in the volume mesh between the ceiling and the porous region. Through initial testing, the cell surface size on the porous region was found to impact the grid dependence results. The mesh was constructed by modifying the base cell size in the mesher to obtain solutions for a range of total cells in the volume mesh. The range of total cells tested was between 30,000 cells and 1,000,000 cells.

The grid dependency can be assessed by calculating the difference between the finest resolved grid and the compared grid. The result of this comparison is defined as the simulation grid error and is calculated as:

$$Error_{TG} = \frac{\dot{m}_{TG} - \dot{m}_{RG}}{\dot{m}_{RG}} \quad 4.44$$

where $\dot{m}_{TG}$ is the outlet mass flow through the beam calculated by the grid under test and $\dot{m}_{RG}$ is the outlet mass flow through the beam calculated by the most resolved grid (highest number of total cells). The results of plotting the error of the resolved grids, for a log plot, should appear as a straight line with a slope of -2 for second-order discretization. The results from the initial grid dependence test are shown in Figure 22.

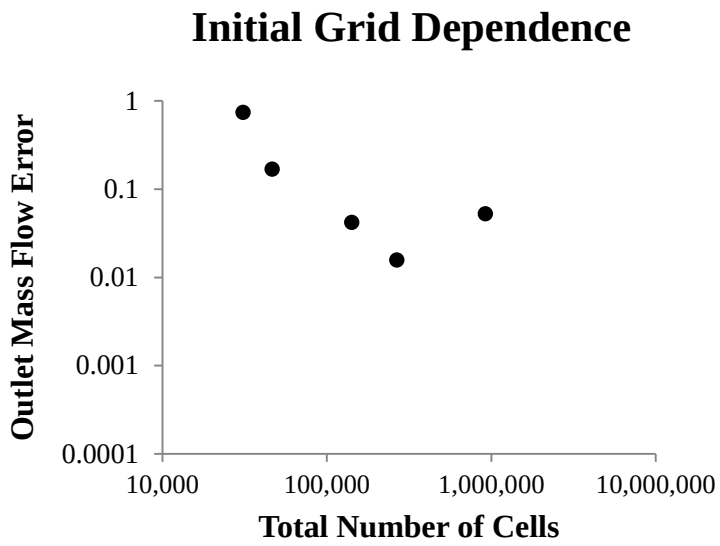

Figure 22. Initial grid dependence test.

The construction of the mesh needed further refinement as the initial grid dependence test showed that the flow was not fully resolved. The difference between

the calculated outlet mass flow rates was inconsistent as the grid was resolved into higher total cell counts and required additional steps in defining the mesh.

The next step was to define the surface size of the mesh along the boundaries of the porous region to remain constant as the total number of cells was increased as the grid was resolved. A grid spacing of 2 cm was used uniformly on the surface of the porous region boundaries. Additionally the volume mesh characteristics along the wall surfaces were considered.

The distance between the wall and the first cell was selected based on the turbulence model. Some turbulence models approximate the viscous boundary layer with built-in calculations while some models do not and additional functions are used to calculate the thermal and fluidic properties of the flow near walls. The calculated value y^+, is a dimensionless parameter that accounts for the friction velocity, kinematic viscosity and distance to the nearest wall and can be used to define the viscous boundary layer of a fluid flow bounded by a wall. The standard k-ε turbulence model accounts for the boundary layer and a larger distance between the wall and the first cell can be used than for different turbulence models that require more calculation points through the boundary layer. The y^+ value acceptable for a certain turbulence model is application specific and depends on the agreed values within research areas. Large ($y^+ > 50$), medium ($25 < y^+ < 50$) and small ($y^+ < 25$) values of y^+ were tested in the grid dependence study to determine an appropriate value for the passive beam modeling. Cross-sectional views of the simulations displaying the mesh for the three y^+ values, each with a total cell count of approximately one million, are shown in Figure 23.

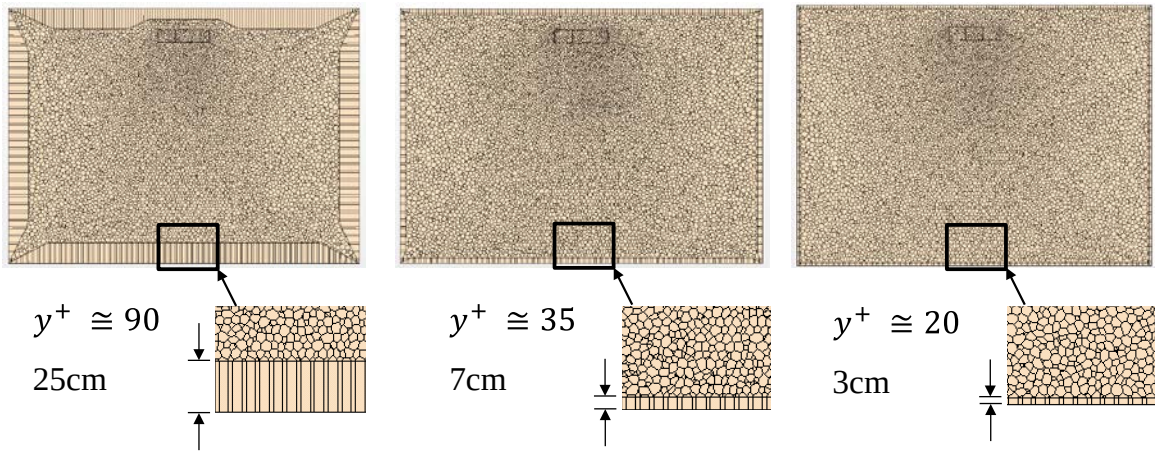

Figure 23. One million cell meshes with large, medium and small y^+ values.

The grid dependency test was applied over the range of 125,000 cells to 1,500,000 cells for the large, medium and small values of y^+. Each mesh was constructed with a single prism layer that defined the distance between the wall and the first cell in the volume mesh. The value of y^+ was held approximately constant by specifying the same value for the single prism layer for each mesh of a different number of total cells. A course grid steady state solution (7,000 iterations) was used as initial conditions for the y^+ grid dependency tests. The outlet mass flow to the beam was calculated after 2.0 s at a 0.1 s time step and the values compared. The results are listed in Tables 8-10. The results are plotted in Figures 24-26 for each y^+ characterization.

Table 8. Grid dependency test for large values of y^+.

Total Number of Cells	y^+	*Outlet Mass Flow (kg/s)*
110,701	98	-0.200
217,474	96	-0.196
294,543	95	-0.195
819,353	94	-0.204
1,293,587	94	-0.204

Table 9. Grid dependency test for medium values of y^+.

Total Number of Cells	y^+	*Outlet Mass Flow (kg/s)*
133,610	35	-0.191
268,570	35	-0.194
373,902	35	-0.194
1,037,246	34	-0.194
1,640,054	33	-0.194

Table 10. Grid dependency test for small values of y^+.

Total Number of Cells	y^+	*Outlet Mass Flow (kg/s)*
139,125	19	-0.200
281,721	19	-0.196
390,253	19	-0.195
1,089,006	20	-0.204
1,735,129	19	-0.204

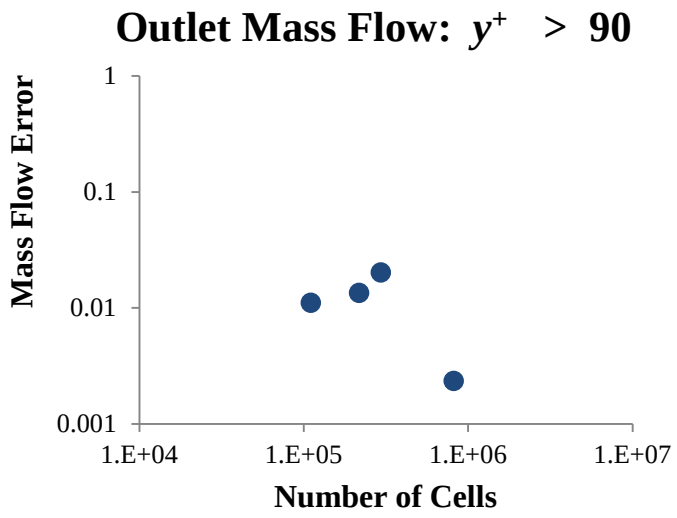

Figure 24. Grid dependency results for simulations characterized by large y^+ values.

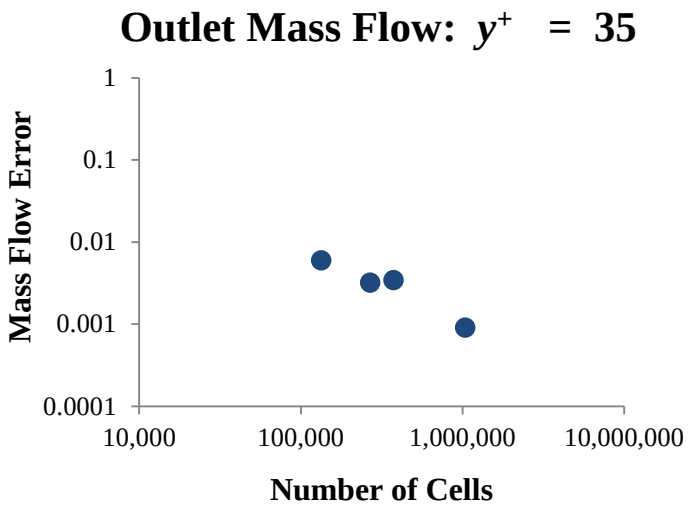

Figure 25. Grid dependency results for simulations characterized by medium y^+ values.

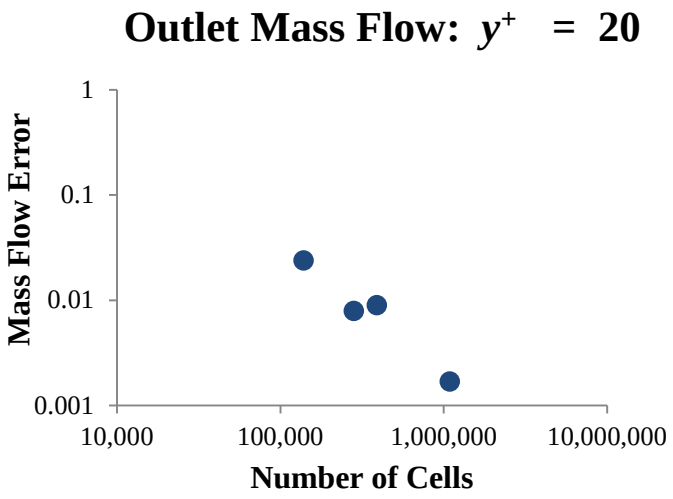

Figure 26. Grid dependency results for simulations characterized by small y^+ values.

The large, medium and small y^+ value error plots did not resolve linearly with a slope of -2, but the small y^+ values were most similar. The mesh was further refined with small y^+ values (less than 25).

Together with the defined surface size of 2 cm along the boundary of the porous region and the y^+ values less than 25, the construction of the grid in the region of the volume mesh between the porous region and the ceiling was specified for an average cell size of 2 cm and the grid dependent test was run over the range of total cell counts between 300,000 and 2,800,000. The simulation results were calculated by starting the converged steady state course grid solution from an initial condition of uniform temperature throughout the room (25 °C), surface temperature boundary conditions of 25 °C along the walls and ceiling, uniform heat flux from the floor equal to 25 W/m^2 and a constant heat source condition of the porous region as -1000 W. The solution was then

run for a period of 0.1 s at a time step of 0.001 s. The results of the simulation runs are listed in Table 11 and the error values as a function of the total cell count plotted in Figure 27.

Table 11. Simulation results from grid dependency test.

Total Number of Cells	*Outlet Mass Flow Rate (kg/s)*	*Outlet Mass Flow Rate Error*
293,217	0.2645	0.0192
580,794	0.2617	0.0085
1,441,719	0.2600	0.0019
2,756,772	0.2595	

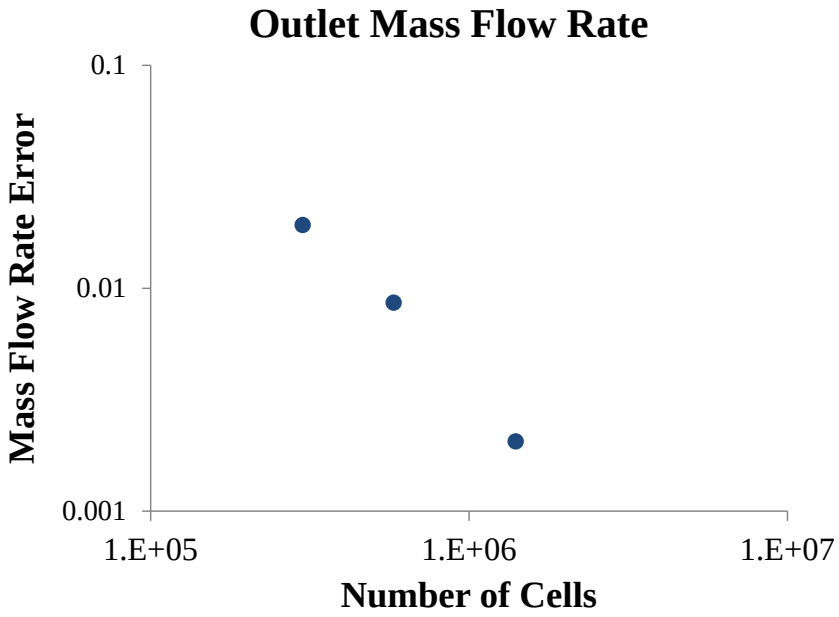

Figure 27. Results of grid dependency tests for the outlet mass flow rates.

It was observed from Figure 27 that the solution converged as the grid resolved. The difference between the compared grid calculation for the outlet mass flow rate of the porous region and the 2,400,000 cell grid decreased consistently as the grid was resolved into higher total cell counts.

CHAPTER V

ANALYTICAL MODEL

5.1 Objective

An analytical model was developed for a passive chilled beam in order to compare with the results obtained in the experiments. The objective of the analytical model was to predict the overall heat transfer from room air at the experimentally measured conditions to the passive chilled beam. Fundamental heat transfer relationships were applied to simulate the free convection at the surface of the fins in order to predict the total cooling capacity of the beam from the fin surface temperature and the quiescent air temperature.

5.2 Simplifications and Assumptions

The fin surface temperature distribution was assumed to be uniform in both the horizontal and vertical directions. The average water temperature of the supply and return of the passive chilled beam measured during the experiment was used as the fin surface temperature. Additionally, the variations in the density of air were assumed negligible. The passive chilled beam was simplified to be a series of two dimensional vertical flat plates, the number of plates equaling two times the number of fins. The remaining simplifications, assumptions and approximations are explained in the following section of the equation derivations.

5.3 Boundary Layer Heat Transfer

The heat transfer relationships in the boundary layer on the fin surface were derived beginning with the conservation of mass, momentum and energy equations. Beginning with the momentum equation in the *x*-direction:

$$\rho\left(u\frac{\partial u}{\partial x}+v\frac{\partial u}{\partial y}\right)=-\frac{\partial p}{\partial x}+\mu\left(\frac{\partial^2 u}{\partial x^2}+\frac{\partial^2 u}{\partial y^2}\right)+X \tag{5.1}$$

where u is the *x*-component of velocity, v is the *y*-component of velocity, ρ is the density, p is the pressure, μ is the viscosity, and X is the *x*-component of the body force. Since the solution is for the boundary layer, several approximations and simplifications can be applied. The velocity in the *x*-direction (u) is much larger than in the *y*-direction (v) and v can then be ignored. Similarly, the gradient of u with respect to $y\left(\frac{\partial u}{\partial y}\right)$ is much larger than the gradient of u with respect to x, the gradient of v with respect to y, and the gradient of v with respect to x. For this solution, it is assumed steady, two-dimensional, incompressible (with one exception to be explained below), viscous and constant properties. With these assumptions and simplifications applied:

$$u\frac{\partial u}{\partial x}+v\frac{\partial u}{\partial y}=-\frac{1}{\rho}\frac{\partial p}{\partial x}+\nu\frac{\partial^2 u}{\partial y^2}+X \tag{5.2}$$

where ν is the kinematic viscosity. For free convection, the body force can be described as the product of the density and the gravitational constant:

$$u\frac{\partial u}{\partial x}+v\frac{\partial u}{\partial y}=-\frac{1}{\rho}\frac{\partial p}{\partial x}-g+\nu\frac{\partial^2 u}{\partial y^2} \tag{5.3}$$

where g is the gravitational constant. The *y*-component of the momentum equation is:

$$\rho\left(u\frac{\partial v}{\partial x}+v\frac{\partial v}{\partial y}\right)=-\frac{\partial p}{\partial y}+\mu\left(\frac{\partial^2 v}{\partial x^2}+\frac{\partial^2 v}{\partial y^2}\right)+X \tag{5.4}$$

The same approximations and assumptions can be applied with the addition of the following: the *y*-component of the body force is equal to the pressure gradient with respect to *y*. However, the *y*-component of the body force is equal to zero, which leads to:

$$\frac{\partial p}{\partial y}=0 \tag{5.5}$$

It follows that if the pressure gradient with respect to *y* is zero, then the pressure gradient with respect to *x* inside the boundary layer must equal the pressure gradient outside the boundary layer. Since *u* is equal to zero outside the boundary layer, the *x*-component of the momentum equation (outside the boundary layer) reduces to:

$$\frac{\partial p}{\partial x}=-\rho_\infty g \tag{5.6}$$

where ρ_∞ is the free stream density. Using this result for the solution inside the boundary layer and since the pressure gradient with respect to *x* is equal inside and outside the boundary layer, is the following:

$$u\frac{\partial u}{\partial x}+v\frac{\partial u}{\partial y}=g\left(\Delta\rho/\rho\right)+\nu\frac{\partial^2 u}{\partial y^2} \tag{5.7}$$

where $\Delta\rho=\rho_\infty-\rho$. If the temperature variation in the fluid is the only factor creating a density variation, the first term on the right hand side of Equation 1.7 can be related to β, the coefficient of thermal expansion defined by:

$$\beta = -\frac{1}{\rho}\left(\frac{\partial \rho}{\partial T}\right)_p \tag{5.8}$$

The following approximations can then be applied:

$$\beta \approx -\frac{1}{\rho}\frac{\Delta \rho}{\Delta T} = -\frac{1}{\rho}\frac{\rho_\infty - \rho}{T_\infty - T} \tag{5.9}$$

$$\rho_\infty - \rho \approx \rho\beta(T - T_\infty) \tag{5.10}$$

where T is the temperature and T_∞ is the free stream temperature. This result is termed the Boussinesq approximation. Substituting Equation 5.10 into Equation 5.7:

$$u\frac{\partial u}{\partial x} + v\frac{\partial u}{\partial y} = g\beta(T - T_\infty) + \nu\frac{\partial^2 u}{\partial y^2} \tag{5.11}$$

Equation 5.11, the momentum equation in the *x*-direction, is used to solve the vertical flat plate boundary layer along with the conversation of mass and energy equations:

$$\frac{\partial u}{\partial x} + \frac{\partial v}{\partial y} = 0 \tag{5.12}$$

$$u\frac{\partial T}{\partial x} + v\frac{\partial T}{\partial y} = \alpha\frac{\partial^2 T}{\partial y^2} \tag{5.13}$$

where α is the thermal diffusivity. Non-dimensional parameters can be defined for these three equations that contribute to a simplified solution. These parameters are as follows:

$$x^* \equiv \frac{x}{L} \tag{5.14}$$

$$y^* \equiv \frac{y}{L} \tag{5.15}$$

$$u^* \equiv \frac{u}{u_D} \tag{5.16}$$

$$v^* \equiv \frac{v}{u_D} \tag{5.17}$$

$$T^* \equiv \frac{T - T_s}{T_s - T_\infty} \tag{5.18}$$

where L is a characteristic length, u_D is an arbitrary reference velocity (since the quiescent fluid velocity is zero), and T_s is the surface temperature. When inserted into Equations 5.11 and 5.13, the momentum and energy equations become:

$$u^* \frac{\partial u^*}{\partial x^*} + v^* \frac{\partial u^*}{\partial y^*} = \frac{g\beta(T_s - T_\infty)L}{{u_D}^2} T^* + \frac{1}{\mathrm{Re}_L} \frac{\partial^2 u^*}{\partial {y^*}^2} \tag{5.19}$$

$$u^* \frac{\partial T^*}{\partial x^*} + v^* \frac{\partial T^*}{\partial y^*} = \frac{1}{\mathrm{Re}_L \mathrm{Pr}} \frac{\partial^2 T^*}{\partial {y^*}^2} \tag{5.20}$$

where Re_L is the Reynolds number and Pr is the Prandtl number. The momentum equation can be further simplified by multiplying by the square of the Reynolds number resulting in the first term on the right hand side becoming Gr_L, the Grashoff number:

$$u^* \frac{\partial u^*}{\partial x^*} + v^* \frac{\partial u^*}{\partial y^*} = \frac{\mathrm{Gr}_L}{{\mathrm{Re}_L}^2} T^* + \frac{1}{\mathrm{Re}_L} \frac{\partial^2 u^*}{\partial {y^*}^2} \tag{5.21}$$

where,

$$\mathrm{Gr}_L = \frac{g\beta(T_s - T_\infty)L^3}{\nu^2} \tag{5.22}$$

The Grashoff number of the fluid is significant as it is the ratio of the buoyancy force to the viscous force and can be used to characterize the flow. LeFevre [79] found that the Nusselt number, Nu_L of the fluid could be described by:

$$\overline{\mathrm{Nu}_L} = \frac{\bar{h}L}{k} = \frac{4}{3}\left(\frac{\mathrm{Gr}_L}{4}\right)^{1/4} g(\mathrm{Pr}) \tag{5.23}$$

where h is the heat transfer coefficient, k is the thermal conductivity and,

$$g(\mathrm{Pr}) = \frac{0.75\mathrm{Pr}^{1/2}}{\left(0.609 + 1.221\mathrm{Pr}^{1/2} + 1.238\mathrm{Pr}\right)^{1/4}} \quad 5.24$$

Using the calculated Nusselt number to solve for the heat transfer coefficient, the total heat transfer from a vertical flat plate, Q_{plate}, is calculated as:

$$Q_{plate} = \bar{h}A(T_s - T_\infty) \quad 5.25$$

where A is the area of the plate. To simplify the analysis of the fin heat transfer, the total heat transfer from the vertical flat plate was used to estimate the total heat transfer from the fin, Q_{fin}, yielding:

$$Q_{fin} \approx 2Q_{plate} \quad 5.26$$

The total heat transfer between the room air and the passive chilled beam can be calculated as the product of Q_{fin} and the total number of fins. Additionally, the maximum velocity of the air in the boundary layer can be estimated by equating the gain in kinetic energy to the work done by the buoyant fluid resulting in:

$$\frac{1}{2}\rho v^2 \cong g\Delta\rho L \quad 5.27$$

After rearranging, the velocity at the outlet of the beam can be calculated as:

$$v \cong \sqrt{\left(\frac{\Delta\rho}{\rho} gL\right)} \quad 5.28$$

CHAPTER VI

VALIDATION OF THE NUMERICAL MODEL

6.1 Introduction

This chapter presents the results of the passive chilled beam experiments conducted in the thermal climate chamber used to validate the CFD model. Section 6.2 contains the recorded values of the beam capacity and the temperature profile at the outlet of the beam for the tests conducted with the thermal manikins configured symmetrically. In Section 6.3, the adjustments to the CFD model to account for momentum loss of the air passing through the passive chilled beam region is documented. Sections 6.4-6.7 contain the comparisons of the test results to the CFD model calculations for the reference temperatures above the beam, the temperature profiles at the outlet of the beam, the temperatures along the vertical centerline, and the beam outlet air velocities. As reported in Chapter III, the experiments were named with a letter according to the thermal manikin configuration followed by a number to designate the test set point conditions. The symmetric thermal manikin tests presented in this chapter were Test A. Test set points 1, 5, 7, and 10 are presented for low, medium-low, medium-high, and high load conditions, respectively.

6.2 Thermal Manikins Symmetrical Configuration Experiments

The thermocouple array readings from below the beam were used to determine the center of the plume location. The measurements shown in Figures 28-31 were recorded at the first thermocouple row beneath the beam every 20 s. In the left of each figure, the points plotted are the measured points, termed the test measurement points, taken once the criteria for stability had been achieved, as described in Chapter III. The right side of each figure shows the 20 s data over a period of 300 s leading up to the recording of the measured points. The results in Figure 28 show that the center of the plume (based on the minimum temperature measurement) was recorded 9 cm from the vertical centerline of the beam for Test A1 (symmetric, low load). At the location of the minimum temperature reading (9 cm from the centerline), the temperature varied between 21.2 °C and 21.9 °C for the 300 s period.

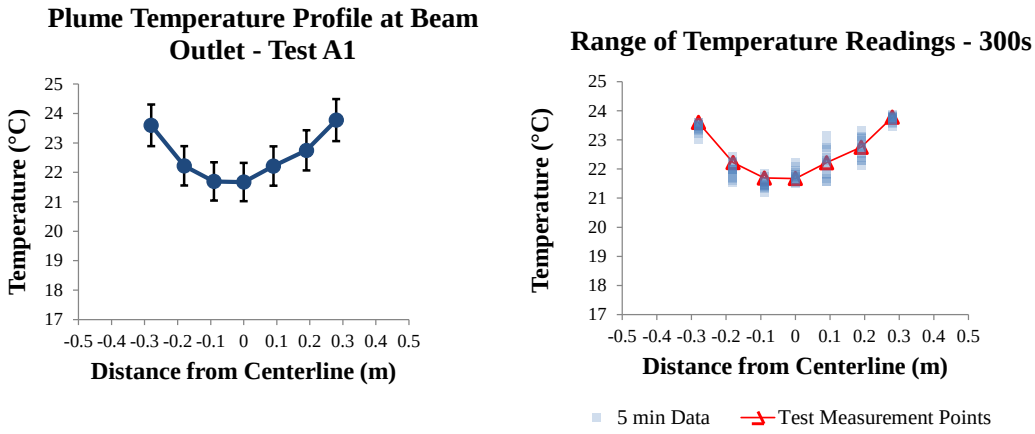

Figure 28. Test A1 measured temperatures at the beam outlet and the temperature measurements for the range of values over a 300 s period.

The Figure 29 results for Test A5 (symmetric, medium-low load) are similar to Test A1 in that the minimum temperature was recorded in the location 9 cm from the vertical centerline of the beam. The variation in temperature measurements was studied by recording the temperatures over a period of 300 s. At the location of the minimum temperature reading (9 cm from the centerline), the temperature varied between 20.3 °C and 20.9 °C for the 300 s period. The results of Test A7 (symmetric, medium-high load), in Figure 30, and Test A10 (symmetric, high load), in Figure 31, also show the minimum temperature 9 cm from the vertical centerline of the beam with variations in the temperature reading between 19.2 °C and 20.0 °C, and 17.8 °C and 18.9 °C, respectively.

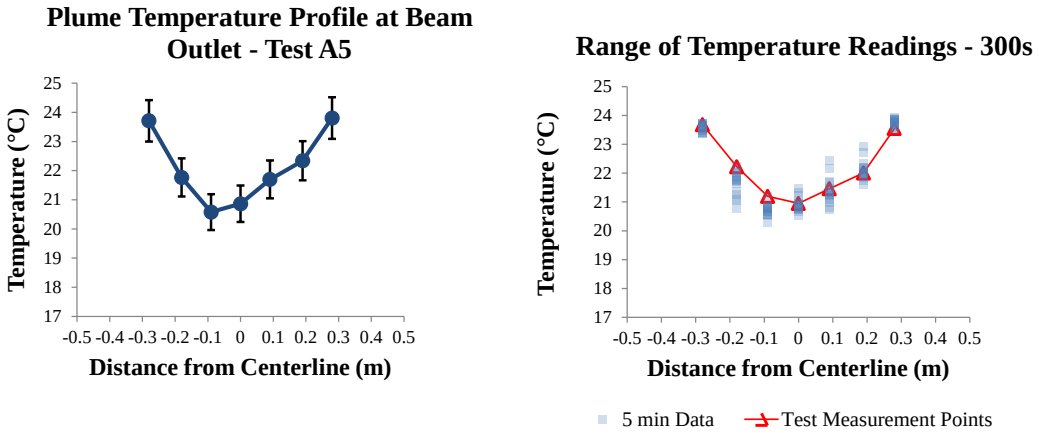

Figure 29. Test A5 measured temperatures at the beam outlet and the temperature measurements for the range of values over a 300 s period.

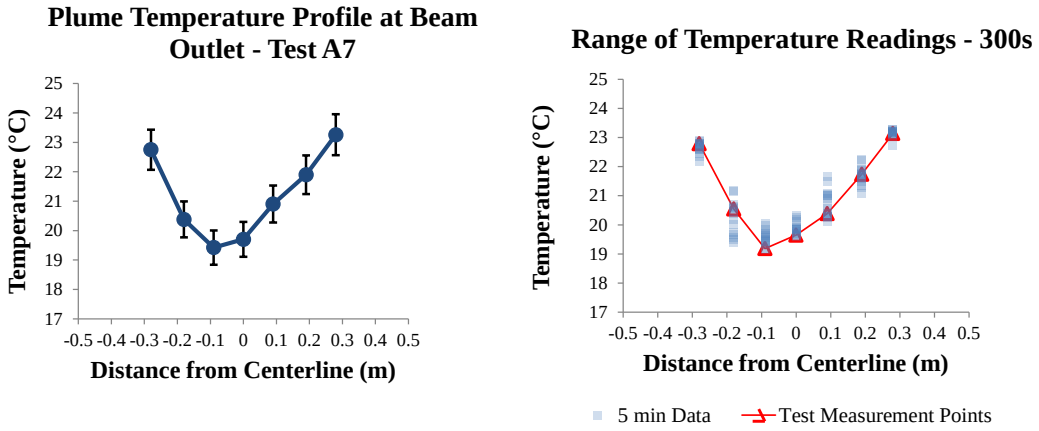

Figure 30. Test A7 measured temperatures at the beam outlet and the temperature measurements for the range of values over a 300 s period.

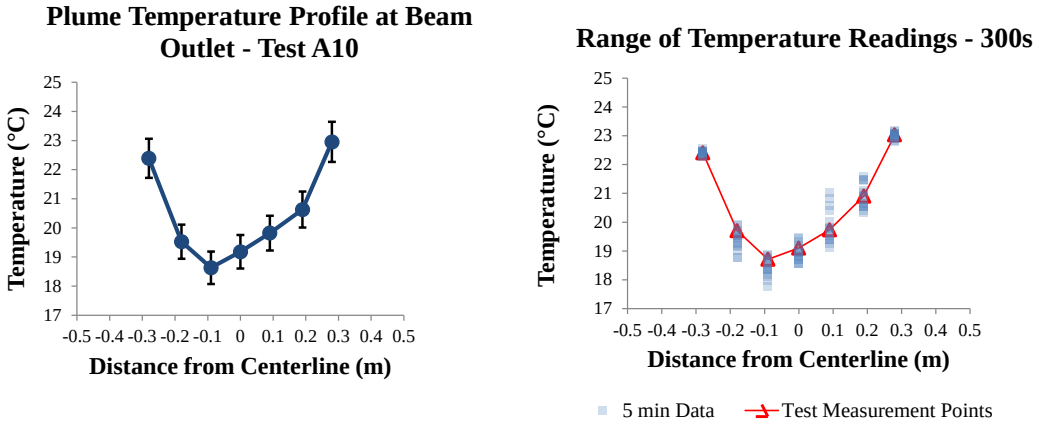

Figure 31. Test A10 measured temperatures at the beam outlet and the temperature measurements for the range of values over a 300 s period.

The results of the outlet temperatures from the beam in Tests A1, A5, A7 and A10 are summarized in Table 12.

Table 12. Summary of outlet temperature results from Test A1, A5, A7, and A10.

	A1	*A5*	*A7*	*A10*
Test Measurement Point Minimum Temperature (°C)	21.4	20.6	19.4	18.6
Minimum Temperature Location (Distance from Vertical Centerline)	9 cm	9 cm	9 cm	9 cm
Maximum Temperature in 300 s Period (°C)	21.9	20.9	20.0	18.9
Minimum Temperature in 300 s Period (°C)	21.2	20.3	19.2	17.8

6.3 CFD Model Predictions

The CFD model was compared to the results of the experiments with the reference temperature measurements. Additionally, the plume temperature and velocity measurements were compared. Initial comparisons of the model results found that the calculated outlet velocities of the CFD simulations were as much as two times higher than the measured values. The beam outlet velocity was estimated in order to compare with the calculated CFD results and the measured values. A simplified control volume was used to account for the mass of air entering and exiting the beam, using the measured inlet and outlet temperatures of the beam and comparing the estimated beam cooling capacity using both the measured and the CFD calculated velocities. The beam

cooling capacity was calculated as follows based on the air-side measurements and CFD calculations:

$$Q_b = \dot{m}_a c_{pa}\left(T_{a,i} - T_{a,o}\right) \quad 6.1$$

For the Test A10 conditions, the air temperature difference between the inlet and the outlet was approximately 2.7 °C in both the measured results and the CFD calculations. Using 1,000 $\frac{J}{kgK}$ as the specific heat of air at the average temperature between the inlet and the outlet, the beam cooling was estimated to be 1024 W from the measured values on the air-side. From the simulation results, the beam cooling capacity was calculated as 1365 W. The beam cooling capacity calculated according to Equation 3.1 with the water-side measured values was 1297 W and taken to be the reference value for the comparisons. When compared to the water-side measurement capacity calculation, the estimation of beam capacity based on the outlet air velocity was 21.0 % lower. The estimated beam capacity with the CFD-calculated outlet velocity was 5.2 % higher than the measured beam capacity. A summary of the results of this analysis are listed in Table 13.

Table 13. Estimated beam cooling capacities for inlet conditions of measured and CFD results compared to measured beam capacity.

	$T_{a,i}$	$T_{a,o}$	*Outlet Velocity (m/s)*	*Estimated Beam Cooling Capacity (W)*	*% Difference from Measured (1297 W)*
Air-side Measurements	23.1 °C	20.4 °C	0.21	1024	-21.0 %
CFD Calculations	23.4 °C	20.7 °C	0.28	1365	5.2 %

One of the two porous medium region specifications applies to the momentum increase or decrease through the volume. The two parameters of the momentum within the porous medium are the porous inertial resistance and the porous viscous resistance. The fin bank of the passive chilled beam consists of many fins and tube passes that create a resistance to airflow. In the initial CFD solutions, the added resistance of tubes and fins were not accounted for as either an inertial or viscous resistance. The resistance to airflow in the beam was increased by increasing the porous inertial resistance coefficient (Equation 4.1) in the porous medium region. Tests of different values of the porous inertial resistance coefficient in the *y*-component direction were studied to match the outlet velocities from the CFD calculations to the measured values, as shown in Figure 32.

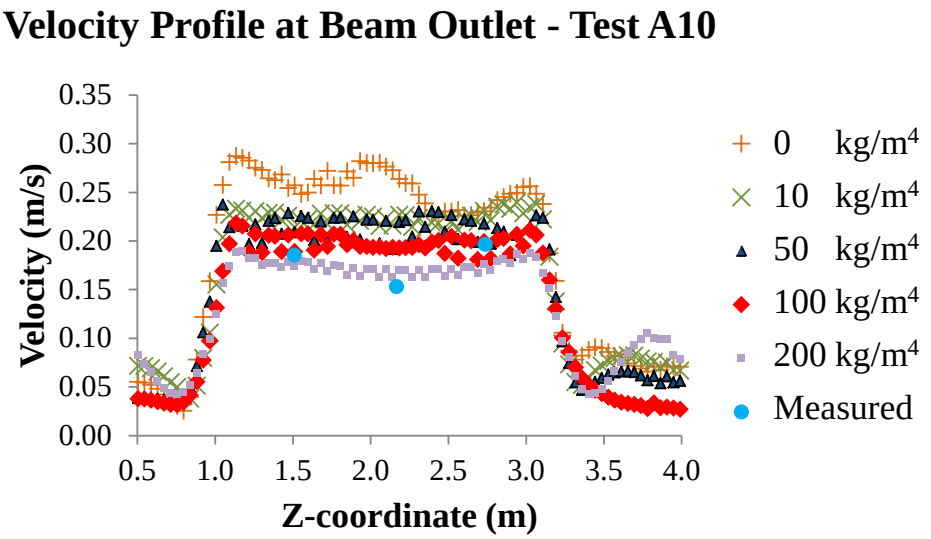

Figure 32. Outlet velocity calculations for different porous inertial resistance coefficient values as compared to measured values.

From the test results, the differences between the measured values and the calculated values were used to determine the porous inertial resistance coefficient that best matched the data. The results are shown in Table 14, and based on the analysis a value equal to 100 kg/m^4 was used for the porous inertial resistance coefficient.

Table 14. Average velocity and absolute difference compared to the measured values of the outlet velocity of the beam for different values of the porous inertial resistance coefficient.

Sensor Location	Measured (m/s)	10 kg/m^4		50 kg/m^4		100 kg/m^4		200 kg/m^4	
		Velocity (m/s)	Diff (m/s)	Velocity (m/s)	Diff (m/s)	Velocity (m/s)	Diff (m/s)	Velocity (m/s)	Diff (m/s)
V1	0.185	0.215	0.030	0.210	0.025	0.190	0.005	0.174	-0.011
V2	0.153	0.222	0.069	0.205	0.052	0.193	0.040	0.167	0.014
V3	0.196	0.242	0.046	0.214	0.018	0.196	0.000	0.174	-0.022

6.4 Reference Temperature Comparison

The three room air temperatures measured directly above the beam were compared to the calculated temperature profile from the CFD solution. The temperature profile from the CFD solution was configured 2.8 m from the floor and 6 cm from the centerline in the positive *x*-direction to correspond to the measurement locations. The two data sets for the Test A1 conditions (578 W beam capacity) are plotted in Figure 33. The calculated temperature values compare well to the measured values. The maximum difference between the three measured points and the corresponding CFD calculated values is 0.7 °C.

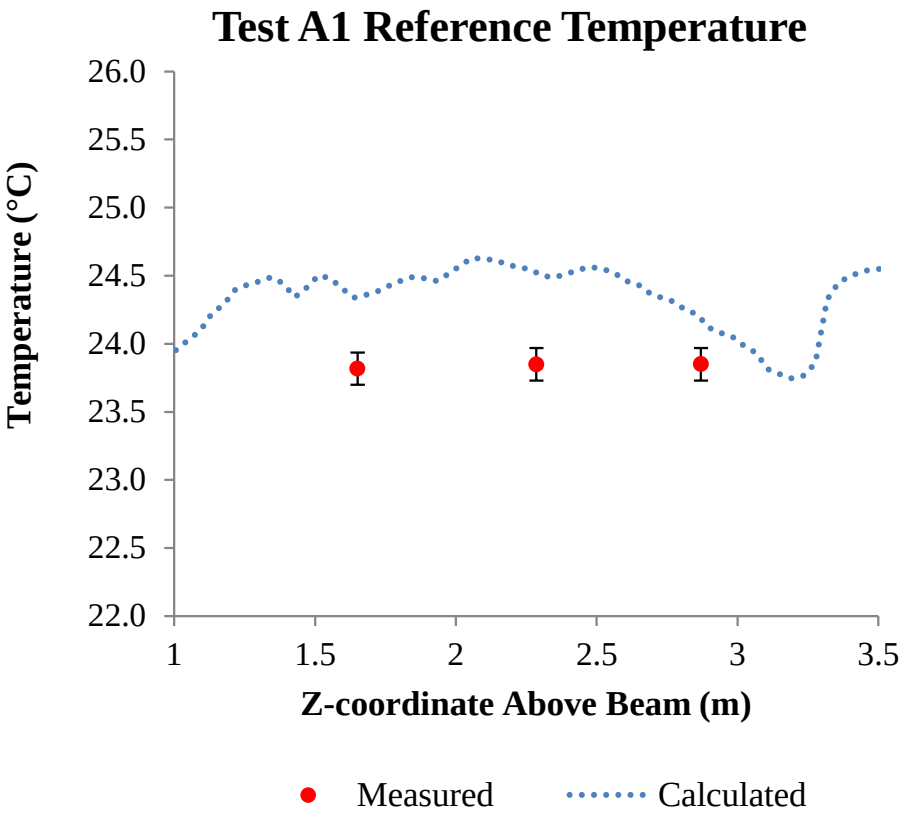

Figure 33. Measured and calculated temperatures 2.8 m above the floor at the Test A1 conditions.

The measured and calculated references temperatures were compared for the Test A5 conditions (765 W beam capacity) as above. The calculated temperature values compared to the measured values, shown in Figure 34, resulted in a maximum difference of 0.6 °C.

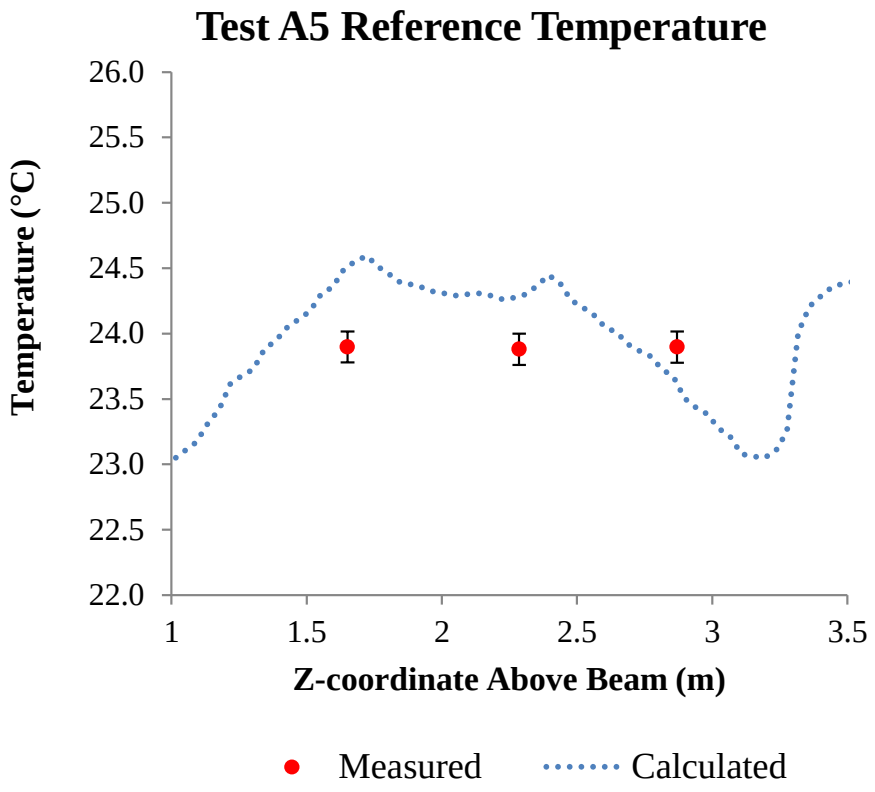

Figure 34. Measured and calculated temperatures 2.8 m above the floor at the Test A5 conditions.

The measured and calculated references temperatures were compared for the Test A7 conditions (1035 W beam capacity) as above. The calculated temperature values compared to the measured values, shown in Figure 35, resulted in a maximum difference of 1.2 °C.

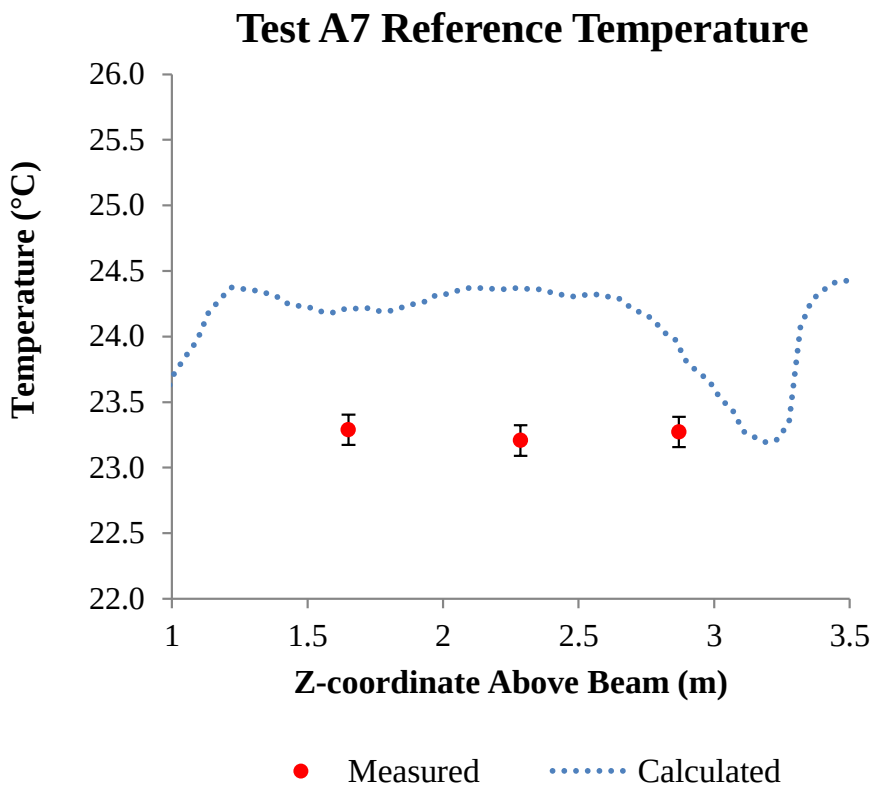

Figure 35. Measured and calculated temperatures 2.8 m above the floor at the Test A7 conditions.

The measured and calculated references temperatures were compared for the Test A10 conditions (1297 W beam capacity) as above. The calculated temperature values compared to the measured values, shown in Figure 36, resulted in maximum difference of 1.2 °C. A summary of the results from Tests A1, A5, A7, and A10 are listed in Table 15.

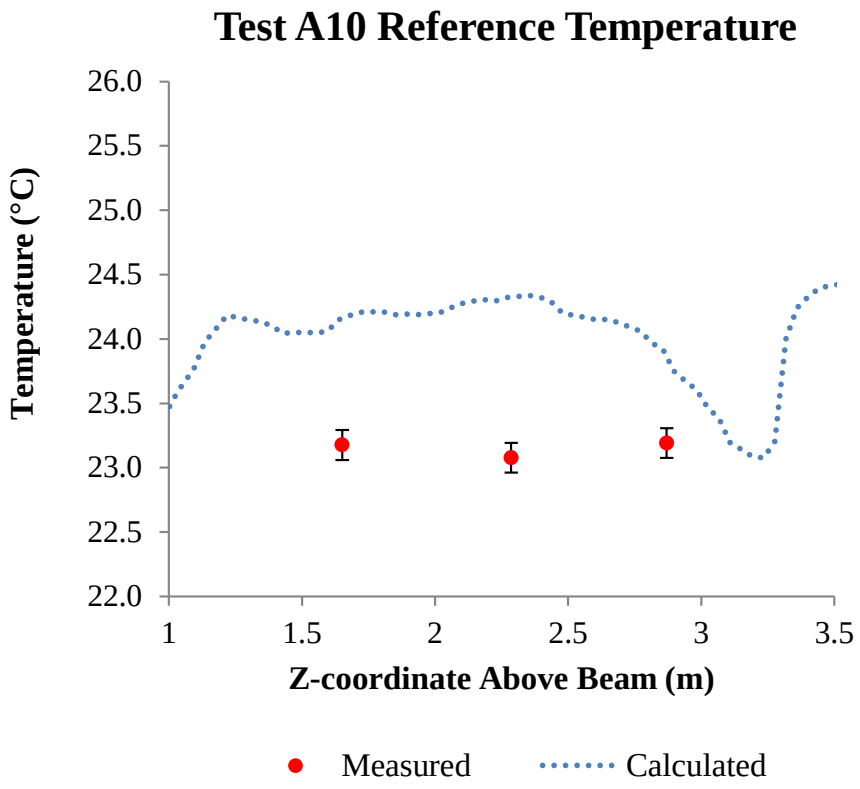

Figure 36. Measured and calculated temperatures 2.8 m above the floor at the Test A10 conditions.

Table 15. Measured and calculated reference temperatures 6 cm from the centerline in the positive *x*-direction.

	Z-coordinate (m)	*Measured (°C)*	*Calculated (°C)*	*Difference (°C)*
Test A1 (578 W beam capacity)	1.65	23.8	24.3	0.5
	2.29	23.8	24.5	0.7
	2.87	23.8	24.2	0.4
Test A5 (765 W beam capacity)	1.65	23.9	24.5	0.6
	2.29	23.9	24.3	0.4
	2.87	23.9	23.6	-0.3
Test A7 (1035 W beam capacity)	1.65	23.3	24.2	0.9
	2.29	23.2	24.4	1.2
	2.87	23.3	23.9	0.6
Test A10 (1279 W beam capacity)	1.65	23.2	24.2	1.0
	2.29	23.1	24.3	1.2
	2.87	23.2	23.9	0.7

6.5 Vertical Temperature Distribution Comparison

Additionally, the vertical temperature profiles below the beam along the centerline were compared between the measured and calculated values. The measured values were recorded with Thermocouple Array #1 (5x7 grid) and the CFD solution profile was calculated along the beam centerline (x = 2.1 m) from the floor to the ceiling, 2.3 m from the wall along the z-axis to correspond to the measured locations. Figure 37 and Table 16 show the comparisons for the Test A1, A5, A7 and A10 conditions.

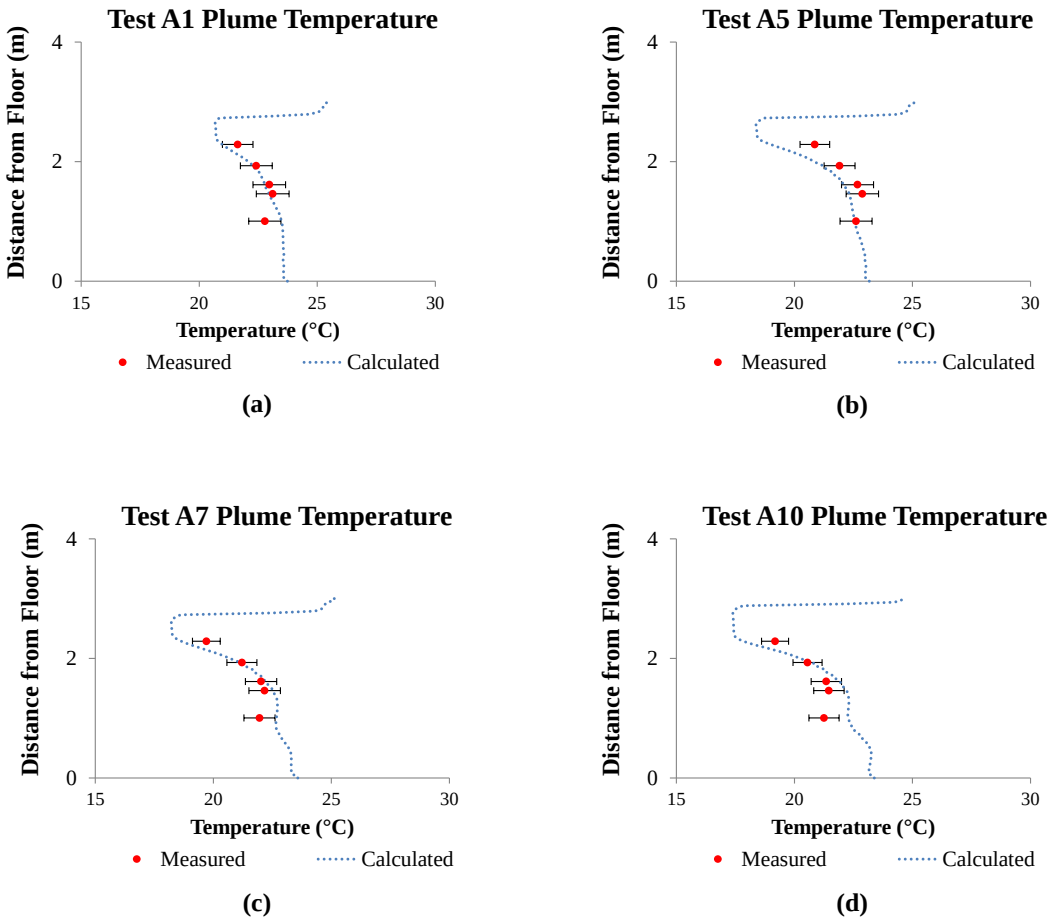

Figure 37. Plume temperature profile of measured and calculated values for (a) Test A1, (b) Test A5, (c) Test A7, and (d) Test A10.

Table 16. Measured and calculated plume temperatures along the centerline in the *y*-direction.

	y-coordinate (m)	*Measured (°C)*	*Calculated (°C)*	*Difference (°C)*
Test A1 (578 W beam capacity)	2.286	21.6	21.0	-0.6
	1.930	22.4	22.3	-0.1
	1.613	23.0	22.8	-0.2
	1.461	23.1	23.0	-0.1
	1.003	22.8	23.5	0.7
Test A5 (765 W beam capacity)	2.286	20.9	19.0	-1.9
	1.930	21.9	21.3	-0.6
	1.613	22.7	22.1	-0.6
	1.461	22.9	22.3	-0.6
	1.003	22.6	22.5	-0.1
Test A7 (1035 W beam capacity)	2.286	19.7	18.7	-1.0
	1.930	21.2	21.2	0.0
	1.613	22.0	22.2	0.2
	1.461	22.2	22.5	0.3
	1.003	22.0	22.7	0.7
Test A10 (1279 W beam capacity)	2.286	19.2	17.9	-1.3
	1.930	20.6	20.8	0.2
	1.613	21.4	21.9	0.5
	1.461	21.5	22.2	0.7
	1.003	21.3	22.3	1.0

6.6 Outlet Temperature Comparison

As was described in Section 6.2, the center of the plume can be defined by the minimum temperature observed through a horizontal temperature profile, parallel to the beam outlet. The location of the plume was compared between the measured and calculated values 2.29 m from the floor, 31 cm from the bottom of the beam coils. The results of comparison between the predicted plume temperatures and the measured plume temperatures are shown in Figure 38 and listed in Table 17.

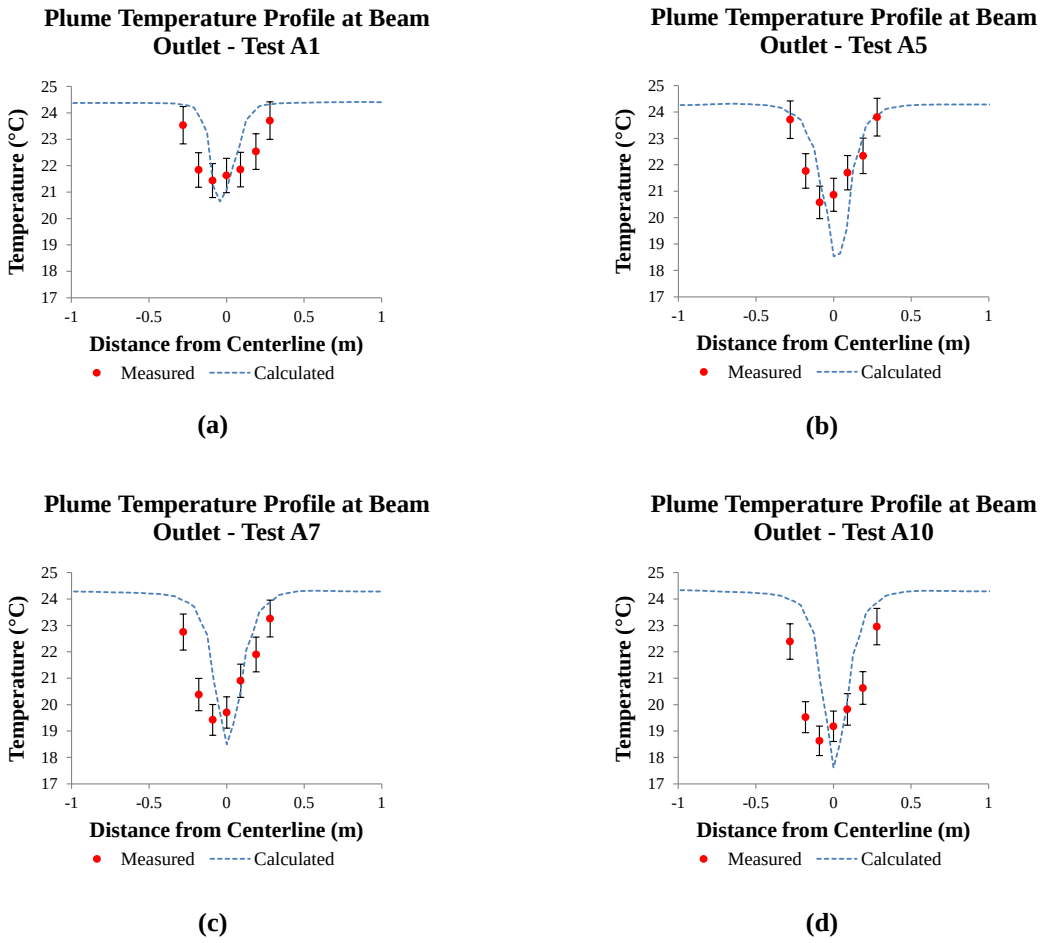

Figure 38. Plume temperature profile at the outlet of the beam for (a) Test A1, (b) Test A5, (c) Test A7 and (d) Test A10.

Table 17. Measured and calculated outlet temperatures 31 cm from bottom of the beam coils.

	Distance from Centerline (m)	*Measured (°C)*	*Calculated (°C)*	*Difference (°C)*
Test A1 (578 W beam capacity)	-0.28	23.5	24.3	0.8
	-0.18	21.8	23.9	2.1
	-0.09	21.4	21.5	0.1
	0.00	21.6	21.1	-0.5
	0.09	21.9	22.9	1.0
	0.19	22.5	24.1	1.6
	0.28	23.7	24.3	0.6
Test A5 (765 W beam capacity)	-0.28	23.7	24.0	0.3
	-0.18	21.8	23.2	1.4
	-0.09	20.6	21.4	0.8
	0.00	20.9	18.5	-2.4
	0.09	21.7	19.9	-1.8
	0.19	22.3	23.1	0.8
	0.28	23.8	23.9	0.1
Test A7 (1035 W beam capacity)	-0.28	22.8	23.9	1.1
	-0.18	20.4	23.3	2.9
	-0.09	19.4	21.2	1.8
	0.00	19.7	18.5	-1.2
	0.09	20.9	20.6	-0.3
	0.19	21.9	23.1	1.2
	0.28	23.3	23.9	0.6
Test A10 (1279 W beam capacity)	-0.28	22.4	24.0	1.6
	-0.18	19.5	23.4	3.9
	-0.09	18.6	21.1	2.5
	0.00	19.2	17.6	-1.6
	0.09	19.8	20.1	0.3
	0.19	20.6	23.1	2.5
	0.28	23.0	23.9	0.9

6.7 Outlet Velocity Comparison

The three plume velocities measured at the outlet of the beam were compared to the calculated velocity profile from the CFD solution for Tests A1, A5, A7, and A10 as shown in Figure 39. The velocity profile from the CFD solution was configured 2.4 m from the floor and 3 cm from the centerline in the negative *x*-direction to correspond to the measurement locations.

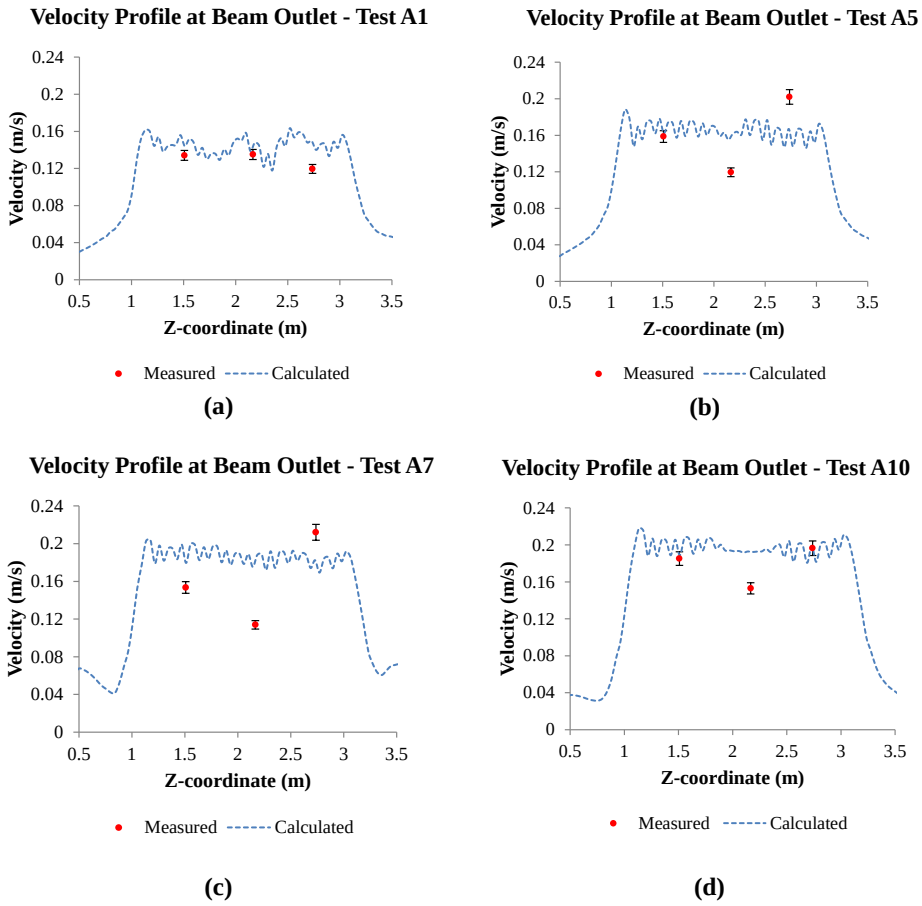

Figure 39. Measured and calculated air velocities at the beam outlet for (a) Test A1, (b) Test A5, (c) Test A7 and (d) Test A10.

On average, the CFD solution calculated higher velocities than the measured results in all the tests conducted. In Test A1 the calculated values were a maximum of 0.029 m/s higher than the measured velocities, 0.040 m/s higher in Test A5, 0.069 m/s higher in Test A7, and 0.040 m/s higher in Test A10.

Table 18. Measured and calculated outlet velocities 10 cm from the bottom of the beam coils.

	Z-coordinate (m)	*Measured (m/s)*	*Calculated (m/s)*	*Difference (m/s)*
Test A1 (578 W beam capacity)	1.51	0.134	0.145	0.011
	2.17	0.135	0.144	0.009
	2.74	0.119	0.148	0.029
Test A5 (765 W beam capacity)	1.51	0.159	0.163	0.004
	2.17	0.119	0.159	0.040
	2.74	0.202	0.163	-0.039
Test A7 (1035 W beam capacity)	1.51	0.153	0.181	0.028
	2.17	0.114	0.183	0.069
	2.74	0.212	0.180	-0.032
Test A10 (1279 W beam capacity)	1.51	0.185	0.190	0.005
	2.17	0.153	0.193	0.040
	2.74	0.196	0.196	0.000

However, the time variation of the velocity measurements was considered to investigate large differences between the calculated values and the experimental values. The 20 s recorded data points were plotted as a function of time for a 600 s period prior to the recording of the measured values reported. The results from the three velocity transducers beneath the beam are shown in Figure 40. The average percent variation

from the three sensors was calculated to be 36 % with a frequency between 40 s and 60 s. If the 36 % variation in recorded values over the 600 s period is taken into consideration when compared to the model predictions, the differences between the measured and calculated values are highly dependent on the time variation component of the measured values.

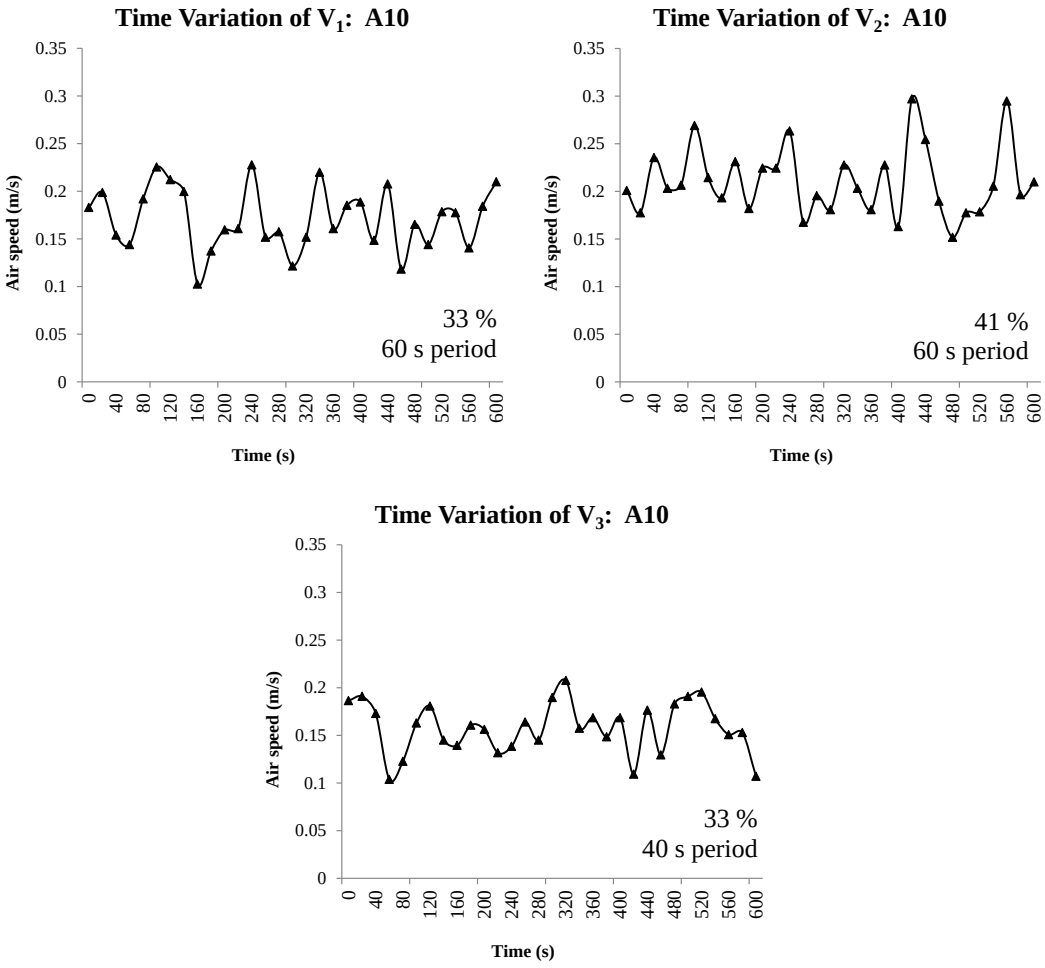

Figure 40. Time variation in velocity measurements below the beam for a 600 s period before the final measurement.

6.8 Summary

The CFD model initially compared well to the results of the experiment for the reference temperatures (less than 1.2 °C difference), the plume temperatures (less than 1.9 °C difference), and the outlet temperatures (less than 3.9 °C difference). However, the outlet velocities calculated with the CFD model were as much as two times higher than the measured values. The initial simulations did not account for momentum loss through the fin bank in the vertical direction. However, when the added inertial resistance of the fins and tubes of the passive chilled beam were included in the model calculations, the outlet velocities compared more closely to the measured results but still significantly deviated from the experiment values. Though, when the time variance of the plume characteristics was considered, the modeled results matched closely within the range of variance to the recorded values. The plume generated by the passive chilled beam can be described as dynamic as the temperature distributions and velocity profiles oscillate over time even with steady loads. For accurate measurement of the outlet conditions, quick response directional velocity sensors should be used in order to measure the changing velocity field well.

CHAPTER VII

EFFECT OF HEAT SOURCE CONFIGURATIONS

7.1 Introduction

The effect of heat source geometric configurations was studied using the results of experiments and simulations from the CFD model. The objective of the tests was to isolate the effect of the position and the type of heat sources on the beam cooling performance and plume characteristics. A symmetric arrangement and an asymmetric arrangement of thermal manikins were tested to study the effect of heat source location. To study the effect of heat source type, tests of symmetrically arranged thermal manikins and radiant panels were performed. The CFD model was used to calculate the airflow characteristics for the symmetric and asymmetric thermal manikin tests and was then compared to the experimental data. Additionally, the results of the CFD simulations were used to further investigate the observed change in performance of the beam cooling capacity based on the arrangement of the thermal manikins.

7.2 Results of the Symmetrically Configured Thermal Manikins Experiments

The heat transfer between the warmer room air and the colder passive chilled beam fin surfaces can be described as the beam cooling capacity, or the total cooling provided by the beam to the room. As described in Chapter III, the beam cooling capacity, Q_b, was calculated using Equation 3.1 based on the mass flow rate, supply temperature, and return temperature of chilled water through the beam. Figure 41 shows

the beam cooling capacity as a function of the difference of ΔT_{RM}, the reference air temperature (average of the three temperature measurements above the beam) and the mean water temperature (average of the inlet and outlet water temperature), for tests A1-A10. The data was fit with a linear regression as plotted. The regression is characterized by an R-squared value of 0.95. As expected, the beam cooling capacity is directly related to the driving temperature difference in the room: the warm room air surrounding the cooler fin surfaces on the passive chilled beam.

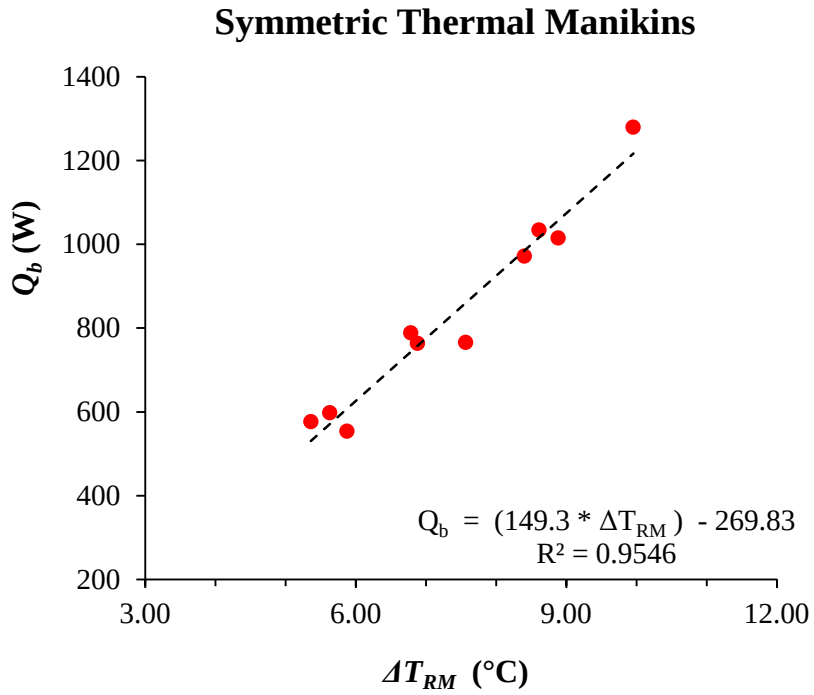

Figure 41. Measured beam capacity, Q_b, as a function of the reference temperature minus the mean water temperature, ΔT_{RM}, for the symmetric heat load configuration; $\Delta T_{RM} = T_{ref} - T_{w,ave}$.

Though the data fits closely to the linear regression, the difference in expected values of the regressed equation and measured points is not fully accounted for by the sensor error. The error associated with the sensors based on calibrations at steady state does not include the dynamic nature of the airflow in the test room. The beam capacity and ΔT_{RM} measurements were an average of data collected over a 20 s period recorded once the measured values of T_{ref} stabilized based on the qualifications listed in Chapter III. To fully account for the variation in expected values of beam capacity as a function of the ΔT_{RM}, the time-dependency of the measurements were considered. For the Test A10 measurement of beam capacity, the 20 s data was plotted as a function of time for a 2,000 s period (100 data points) prior to the final data point used in Figure 41. The results as shown in Figure 42 reveal a 9 % variation in the measured beam capacity with respect to time.

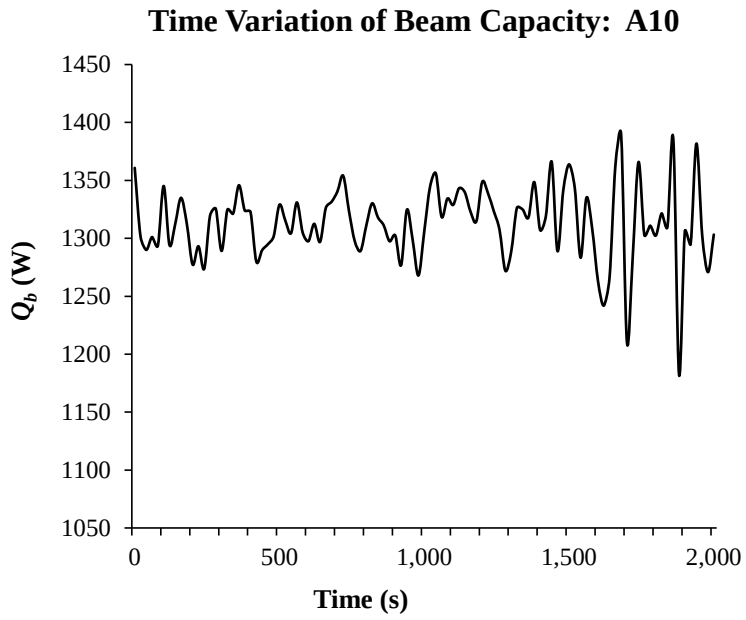

Figure 42. The beam cooling capacity as a function of time for a 2,000 s period prior to the measured data point for Test A10.

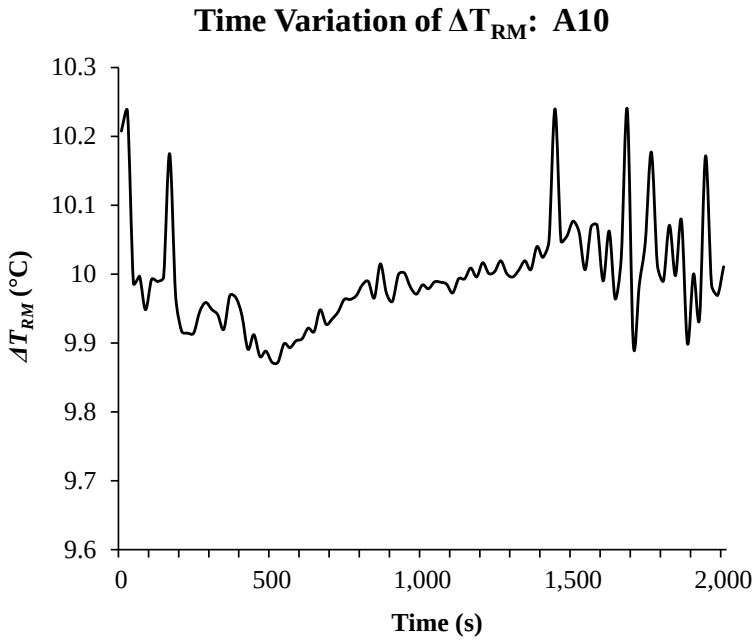

Figure 43. ΔT_{RM} as a function of time for a 2,000 s period prior to the measured data point for Test A10.

Similarly, the time variation of ΔT_{RM} over the same 2,000 s time period reveals a 3 % variation in values, as shown in Figure 43. The results of Figure 42 and Figure 43 confirm that while the control point variables in the room had stabilized based on the test criteria, the cooling rate delivered to the room by the passive chilled beam varied as a function of time at a frequency dependent on additional test room characteristics. As applied to the measured data points in Figure 41, the combined 9 % variation along the *y*-axis and the 3 % variation along the *x*-axis are represented as the blue shaded area for each point in Figure 44. The shaded area representing the time variance of the data point for all the plotted points from Tests A1-10 fall on the linear regression indicating a strong correlation between the beam cooling capacity and ΔT_{RM} once the dynamic nature of the test room experiments was accounted for. The variation with respect to time of the beam capacity and ΔT_{RM} may be attributed to elements of the experiment that were controlled with a tolerance for time-variance. The small fluctuations in the control variables were representative of additional fluctuations in heat transfer and fluid flow throughout the test room.

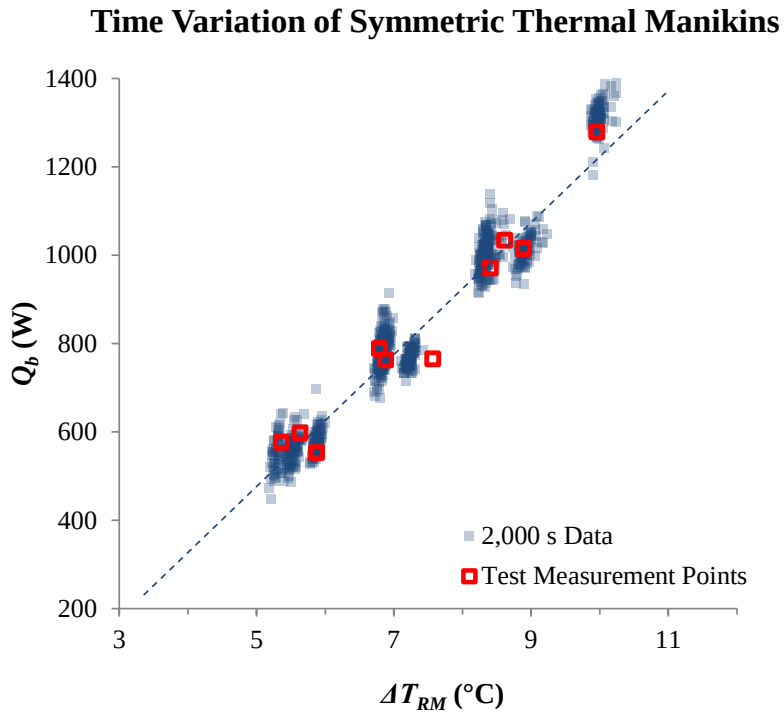

Figure 44. The beam cooling capacity, Q_b, as a function of ΔT_{RM}, showing the time-variance of the plotted data points; $\Delta T_{RM} = T_{ref} - T_{w,ave}$.

As discussed in Chapter II, Fredriksson *et al.* [24], observed that the airflow rate through the beam was characterized as time-dependent based on the buoyancy potential of the volume of cooled air reaching a threshold value at which point the density difference between the cooled volume and the surrounding room air is great enough to create flow and the volume of air exits the beam. Subsequently, a new volume of room air enters the beam and is cooled for a period of time until the threshold value is again reached and the air exited. Fredriksson *et al.* estimated the airflow oscillation to occur at a frequency of 4 s based on the critical Rayleigh number of the flow for the tested conditions.

Using the water temperature and mass flow rate measurements of the chilled water through the beam for the Test A10 data, the frequency of the beam cooling capacity estimated from Figure 42 was approximately 100 s, a much longer frequency than the exit airflow frequency predicted by Fredriksson *et al*.

The experiment was repeated to use a re-configured thermocouple array to measure the air temperature below the beam. The second test run of the data is plotted together with the first data set in Figure 45. The results show the degree of repeatability in the test procedure with measured values. When plotted together, both data sets resulted in a linear regression of the beam capacity as a function of the reference temperature minus the mean water temperature with an R-squared value of 0.98.

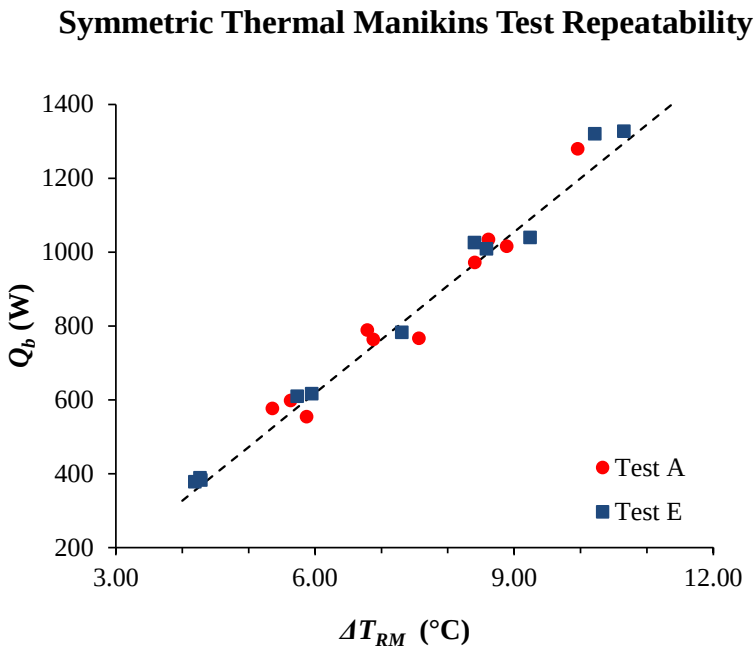

Figure 45. Measured beam capacity data from tests A1-A10 and E1-E10.

The results of both tests show that when the time-dependency of the beam capacity and ΔT_{RM} measurements are considered, the predictability of the beam cooling for a given ΔT_{RM} is high using a linear relationship. For the purpose of predicting the total beam cooling capacity using a simplified approach, the analytical model developed in Chapter V was based on the beam geometry, inlet water temperature and the properties of air at the bulk room air temperature. The total heat transfer from the passive chilled beam was calculated with information readily available to designers with knowledge of the passive chilled beam manufacturer catalogue information and the design conditions for the occupied zone in the space. The results of the analytical model predictions were compared to the experimental data obtained with thermal manikins arranged symmetrically for a passive chilled beam that featured 384 fins, each 15 cm tall, 61 cm long and 2.4 mm wide, with a vertical surface area of 915 cm^2 on each face. Table 19 lists the measured and predicted beam capacities.

Table 19. Comparison of measured beam capacity to predicted beam capacity for symmetric thermal manikins.

Test	*Temperature (°C)*			*Capacity (W)*		*Percent Difference (%)*
	Entering Water	Leaving Water	Reference Air	Measured	Predicted	
A1	17.9	19.0	23.8	577	568	-1.56
A2	17.9	19.5	24.3	598	605	1.17
A3	18.1	20.2	25.0	554	638	15.2
A4	16.0	17.5	23.6	789	767	-2.79
A5	16.0	18.0	23.9	763	780	2.23
A6	15.7	18.7	24.8	766	880	14.9
A7	13.7	15.6	23.6	1034	1039	0.48
A8	14.0	16.5	23.6	972	1007	3.60
A9	14.1	17.9	24.9	1015	1080	6.40
A10	12.0	14.4	23.2	1279	1250	-2.27

The results from Table 19 were plotted and shown in Figure 46. The prediction of the beam capacity as a function of ΔT_{RM} matches the measured data within a 15 % difference for the entire range of cooling capacities. If the time variation of the measured values of beam capacity and ΔT_{RM} are again applied, all the ranges of time-variance of the measured points overlap with the predicted values.

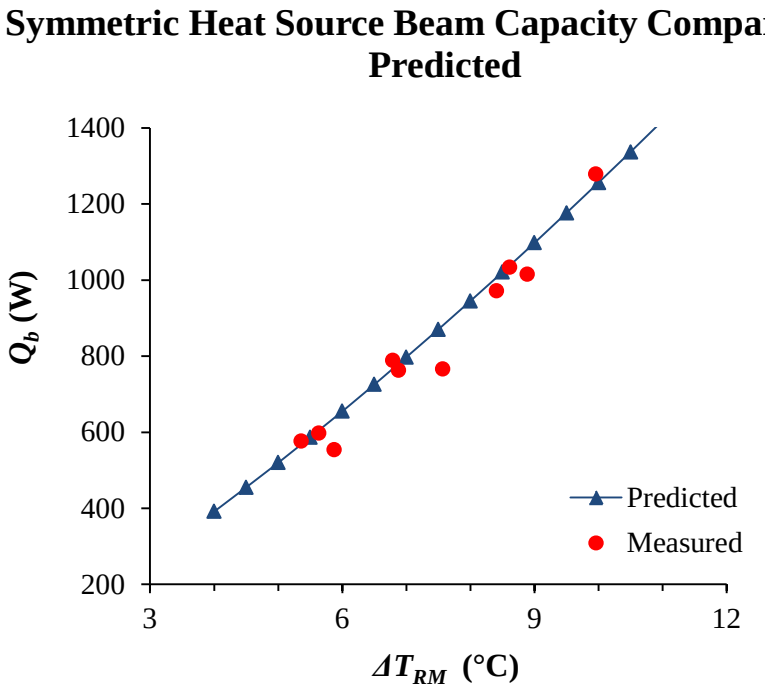

Figure 46. Measured and predicted beam capacity as a function of the difference between the reference temperature and the mean water temperature.

For field measurements of passive chilled beams, the water-side measurements are often difficult to conduct. Since a passive chilled beam produces a cold air plume, the temperature and mass flow rate of the plume exiting the beam are directly related to the cooling rate provided to the room through the passive chilled beam. To investigate a simplified approach to measuring the beam cooling capacity, the measured beam cooling capacity was plotted as a function of the minimum temperature recorded in the thermocouple array for tests A1-A10, as shown in Figure 47. As the beam capacity increased, the minimum temperature decreased as was expected for the plume since the cooling capacity of the beam is an indication of the strength of the buoyancy source,

which is directly related to the temperature difference between the bulk room air and the plume temperature. A linear regression was fit to the data and the R-squared value was found to be 0.88.

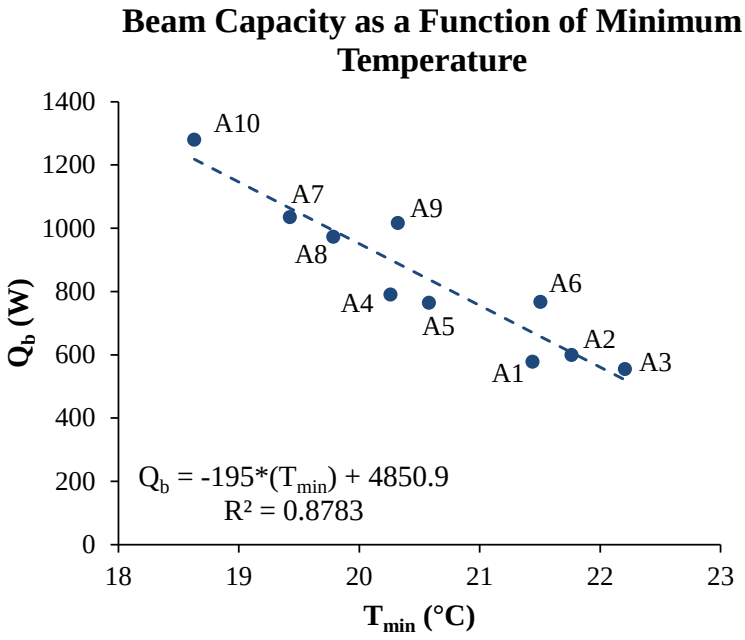

Figure 47. The beam cooling capacity, Q_b, as a function of the minimum temperature recorded in the thermocouple array, T_{min} for Tests A1-A10.

The significance of this result is that the beam cooling capacity can be predicted within 16 % using the minimum temperature measured at the outlet of the beam for a given reference temperature. However, the location of the minimum temperature is often not known without taking a grid of air temperature measurements near the beam

outlet. For single point measurement techniques, this process would be labor and time intensive and unjustifiable for field measurement applications. However, a single temperature measurement at a consistent location in relation to the beam outlet would be easily justifiable for field measurement. To investigate this possibility, the beam cooling capacity was plotted as a function of the temperature recorded at the middle position of the thermocouple array at the outlet of the beam, as shown in Figure 48. The data was linearly regressed with an R-squared value of 0.72.

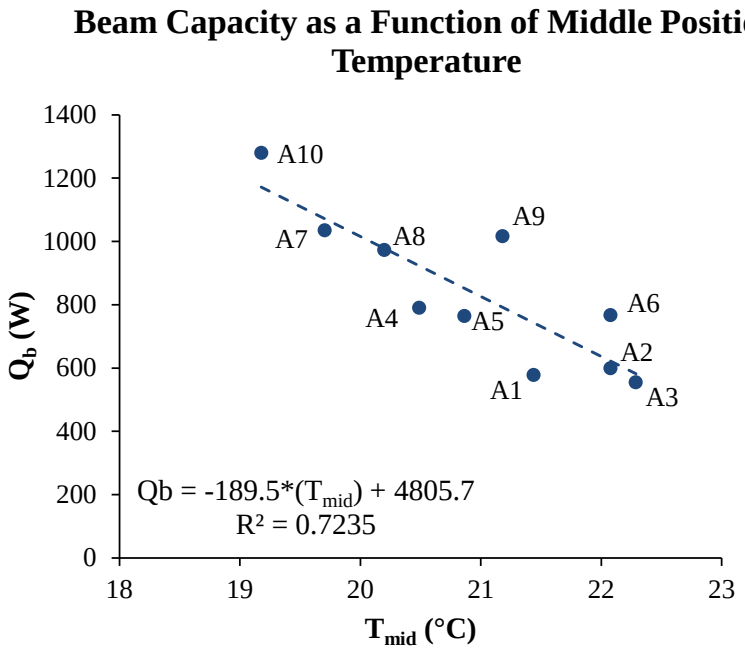

Figure 48. The beam cooling capacity, Q_b, as a function of the recorded temperature at the middle position of the thermocouple array, T_{mid}.

The data of Figure 48 is more scattered than Figure 47 and approximated the beam cooling capacity within a larger percent difference range of 30 %. This higher degree of uncertainty can be expected for a plume center that sways laterally upon exit of the beam. However, the beam capacity and the temperature measured at the middle position of the beam outlet were recorded over a 5 min period and averaged. The results, plotted in Figure 49, reveal a lower degree of scatter around the linear regression that results in predictions within 23 %.

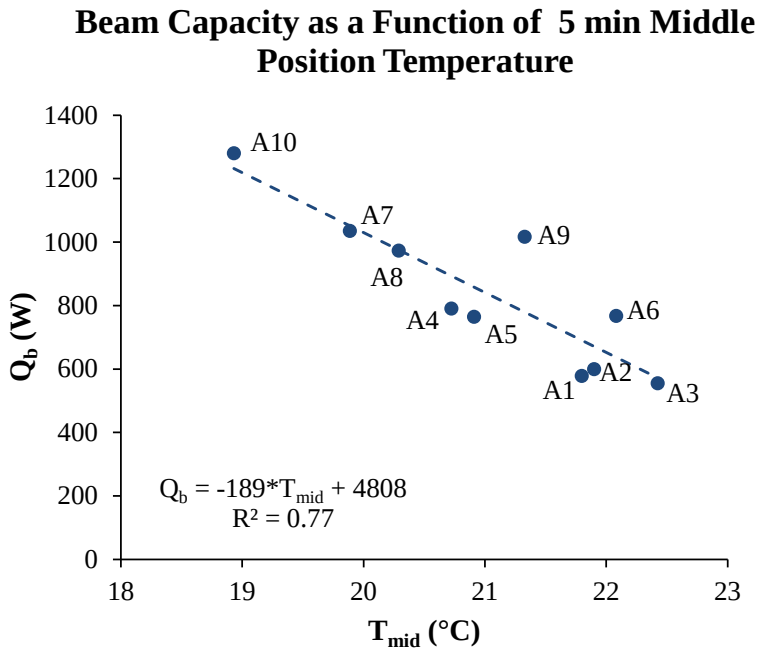

Figure 49. The beam cooling capacity, Q_b, as a function of the middle position temperature at the outlet of the beam, T_{mid}.

7.3 Results of the Asymmetrically Configured Thermal Manikins Experiments

Experimental data was collected using the asymmetric configuration of the thermal manikins and compared to the symmetric configuration. The beam cooling capacity as a function of the difference between the reference temperature and the mean water temperature was plotted in Figure 50 for the asymmetric configuration of thermal manikins. The data was fit to a linear regression with a characteristic R-squared value of 0.92.

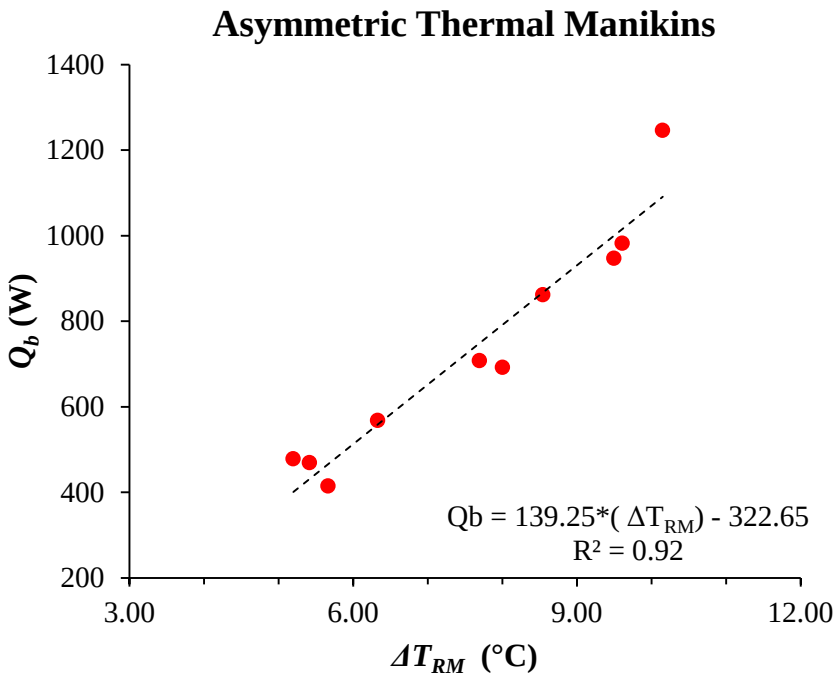

Figure 50. The beam capacity, Q_b, as a function of the difference between the reference temperature and the mean water temperature, ΔT_{RM}, for the thermal manikins in the asymmetric heat source configuration.

The asymmetric configuration was repeated in tests F1-F10 using a different thermocouple array to measure the plume air temperature, as in tests E1-E10 described in Section 7.2. The results in Figure 51 show repeatability of the experimental data and confirm the finding of a reduced beam capacity with an asymmetric heat source configuration. With a linear regression fit to the beam capacity as a function of the reference temperature minus the mean water temperature, the R-squared value was 0.95 for the combined data sets.

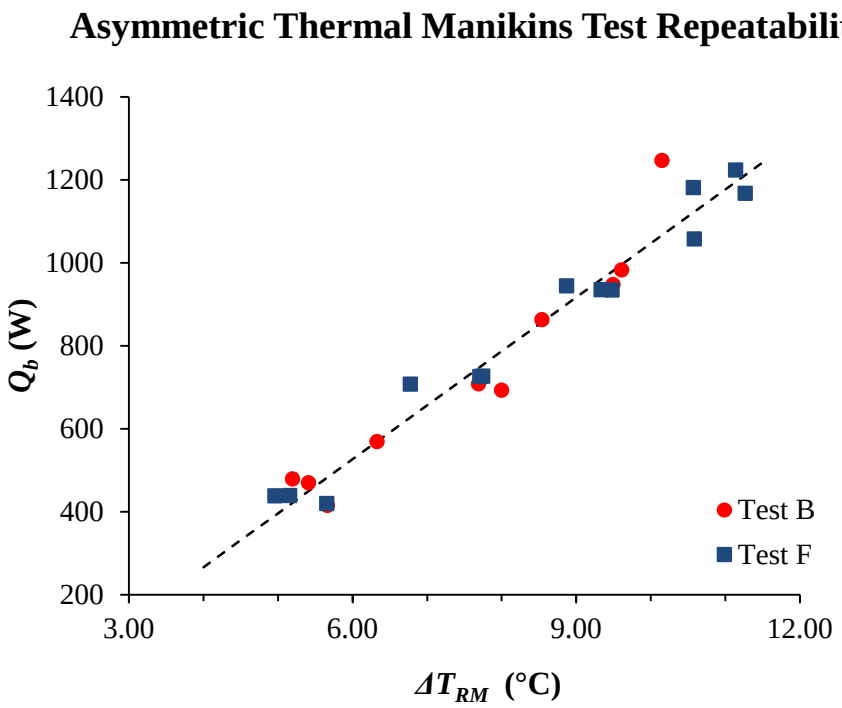

Figure 51. Repeatability of asymmetric thermal manikin configuration for Test B and Test F.

The results from the symmetric thermal manikin configuration of tests A1-A10 and the asymmetric thermal manikin configuration of tests B1-B10 show a reduced beam cooling capacity for the asymmetric configuration, as shown in Figure 52. The average reduction in the beam cooling capacity of 15 % was recorded for the asymmetric thermal manikin configuration as compared to the symmetric thermal manikin configuration.

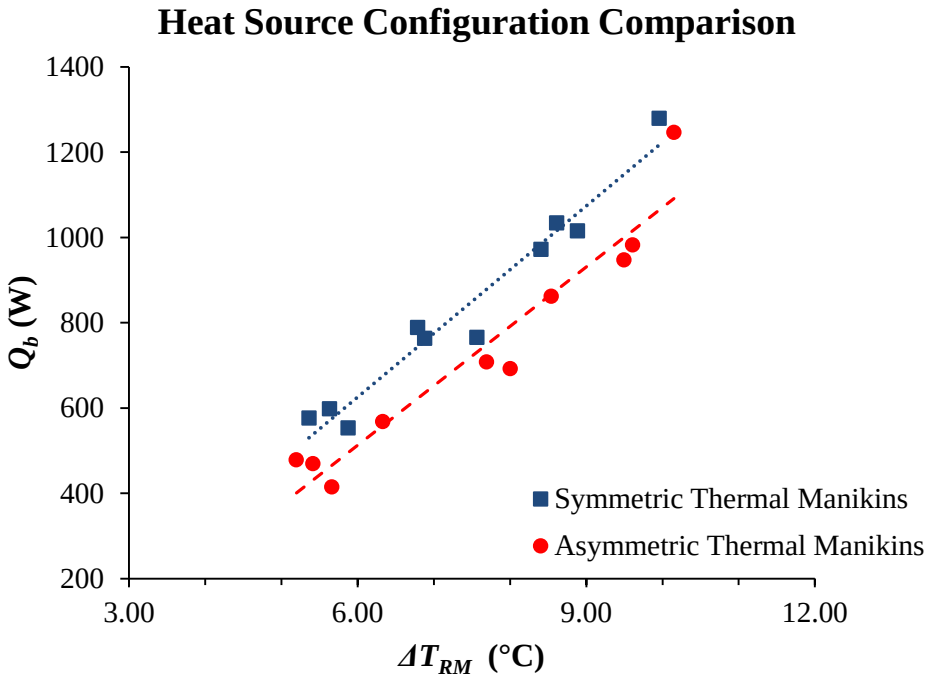

Figure 52. Beam cooling capacity for both the symmetric and asymmetric thermal manikin configurations.

Aggregating the results from tests A1-A10 and E1-E10 with tests B1-B10 and F1-F10, the reduced capacity of the beam cooling an asymmetric thermal manikin configuration is an average 16 % lower than the capacity of a beam cooling a symmetric heat load configuration. The R-squared value for the linear regression of the symmetric data set is 0.98 and the R-squared value of the linear regression of the asymmetric data is 0.95, as shown in Figure 53.

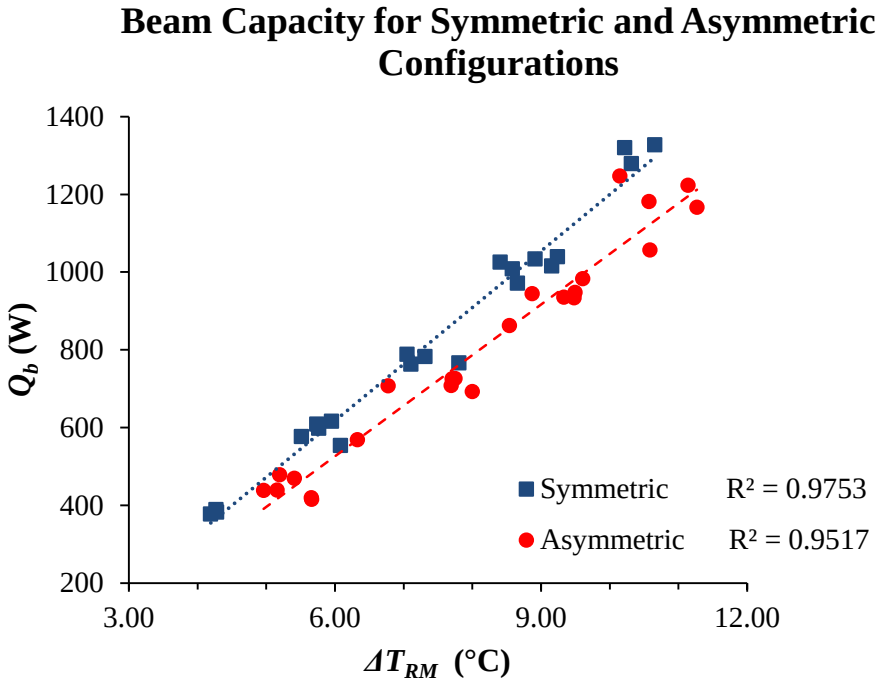

Figure 53. The beam cooling capacity as a function of the reference temperature and the mean water temperature for all test runs of the symmetric and asymmetric thermal manikin configurations.

The measured data obtained with the thermal manikins in tests B1-B10 was compared to the calculated beam capacity using the same method as described in Section 7.2. The analytical model does not include any provisions for differences in room heat load configurations and simplifies the beam surface temperatures as uniform and equal to the average of the inlet and outlet water temperatures. The results, shown in Figure 54, reveal that the analytical model over-predicts the capacity of the beam for the asymmetric thermal manikins by an average of 25 %.

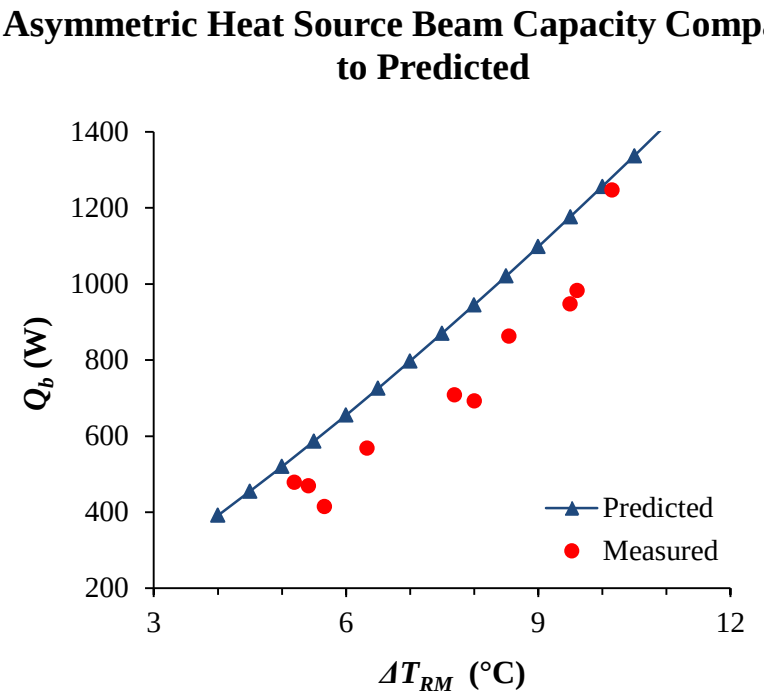

Figure 54. Measured and predicted beam capacity for thermal manikins in the asymmetric test configuration.

The results from Figure 46 combined with Figure 54 show that the analytical model failed to capture the change in beam capacity associated with the spatial arrangement of the thermal manikins, as shown in Figure 55.

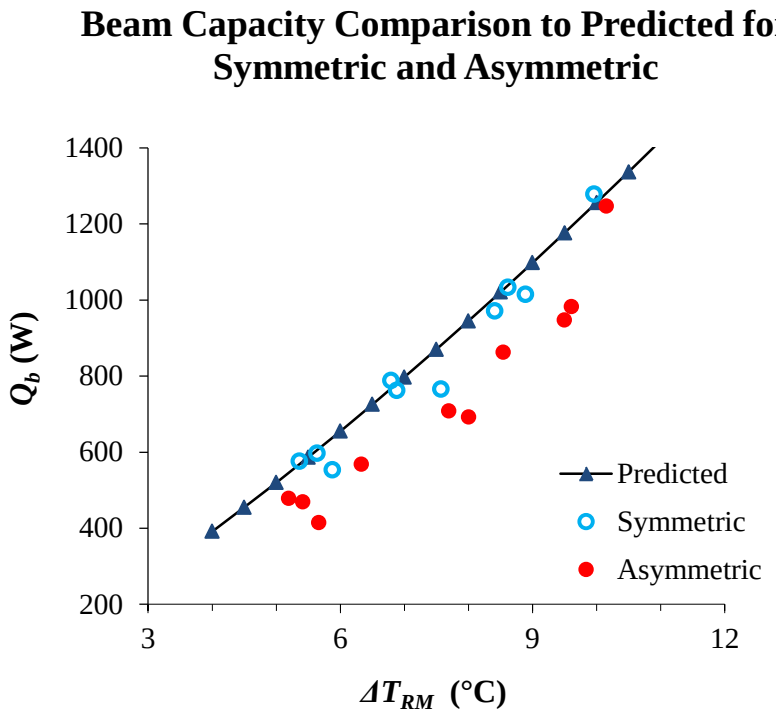

Figure 55. The beam cooling capacity prediction of symmetric and asymmetric thermal manikin configurations.

7.4 Experiment Results of Symmetrically Configured Radiant Panels

The beam capacity as a function of the difference between the reference temperature and the mean water temperature for the experiments using symmetrically

positioned radiant panels is shown in Figure 56. A linear regression was fit to the data with an R-squared value of 0.996.

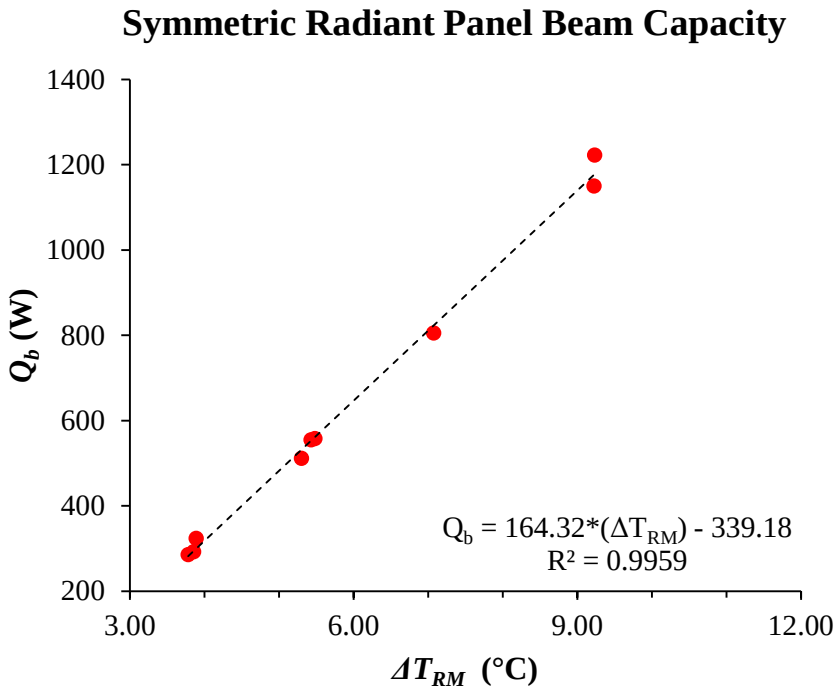

Figure 56. The passive beam cooling capacity as a function of the difference between the reference temperature and the mean water temperature for the symmetrically positioned radiant panels.

When compared to the thermal manikin symmetric tests, the radiant panel beam cooling capacity shows a negligible difference, as shown in Figure 57. The conclusion from these tests were that the beam cooling capacity is not dependent on the heat load type as compared between the thermal manikin heat sources and the radiant panel heat sources. The different heat plumes generated by both heat source types is either not

significant enough to effect the beam cooling capacity by changing the airflow characteristics above the beam, or the distance between the inlet to the beam and the source of the thermal plumes is large enough that the differences in source conditions are reduced to the point of being considered negligible.

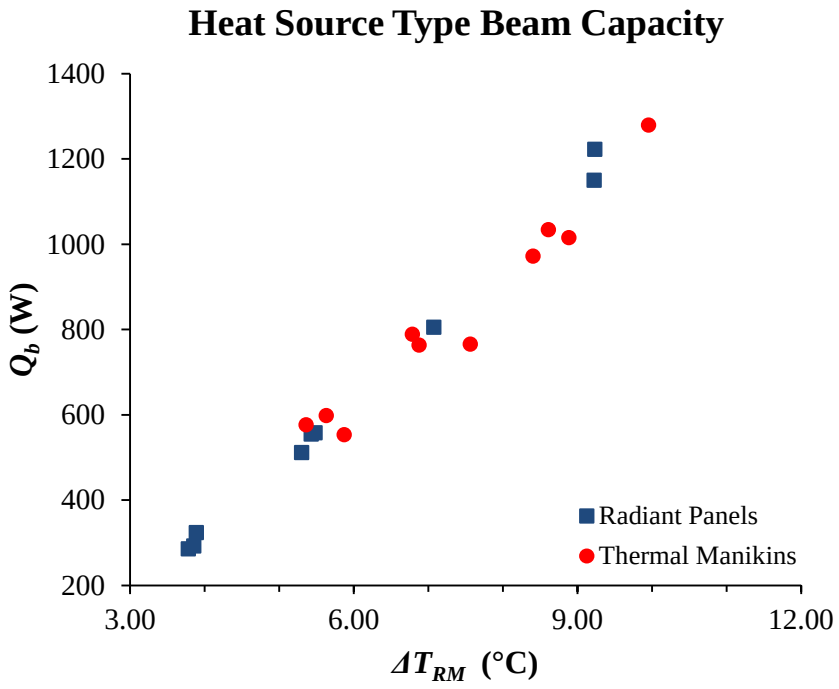

Figure 57. Comparison of the beam capacity for the thermal manikins and radiant panel heat sources.

7.5 CFD Simulation Results of Symmetric and Asymmetric Configurations

The difference in the beam performance between the symmetric and asymmetric heat source configurations was further explored with results from CFD simulations. As

detailed in Chapter VI for the simulations of the symmetrically arranged thermal manikins, the CFD model was setup and initialized based on the experiment test conditions for the asymmetrically arranged thermal manikins. In Figure 58 and Figure 59, the temperature distributions are shown for the cross-sectional views of both heat source arrangements. Figure 60 and Figure 61 show a cross-sectional view of the velocity fields for the symmetric and asymmetric arrangement of the thermal manikins, respectively. The temperature distributions reveal the beam and heat source plumes as well as areas throughout the room of varying temperature. In Figure 58, the temperature distribution throughout the space is symmetric with respect to the beam as the two halves of the room are similar. However, the temperature distribution plotted in Figure 59 shows areas of higher temperature near the thermal manikins in one half of the room.

These findings are confirmed with the velocity profiles for the symmetric and asymmetric thermal manikin simulations. The velocity profile for the symmetric thermal manikins in Figure 60 shows a balanced flow throughout the space. The cold air plume descends from the beam outlet, moves out to either wall and then recirculates back up to the inlet of the beam. The two halves of the room are equally mixed and the velocity profiles appear balanced. The contrast between the two thermal manikin configurations is more pronounced when the velocity profiles are compared. The asymmetric thermal manikin simulation shows a flow pattern that primarily mixes only one half of the room. The cold air plume descends from the beam to the floor, is directed towards the thermal manikins, and then circulated back up to the beam inlet. This motion is entirely contained within one half of the room with the thermal manikins.

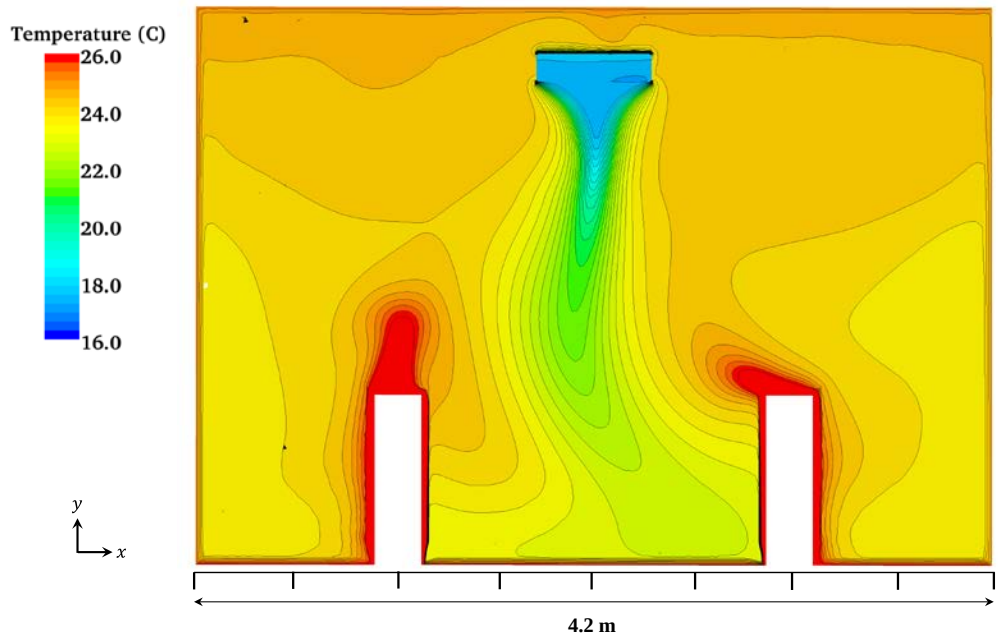

Figure 58. Cross-sectional view of the temperature distribution for the symmetrically arranged thermal manikins.

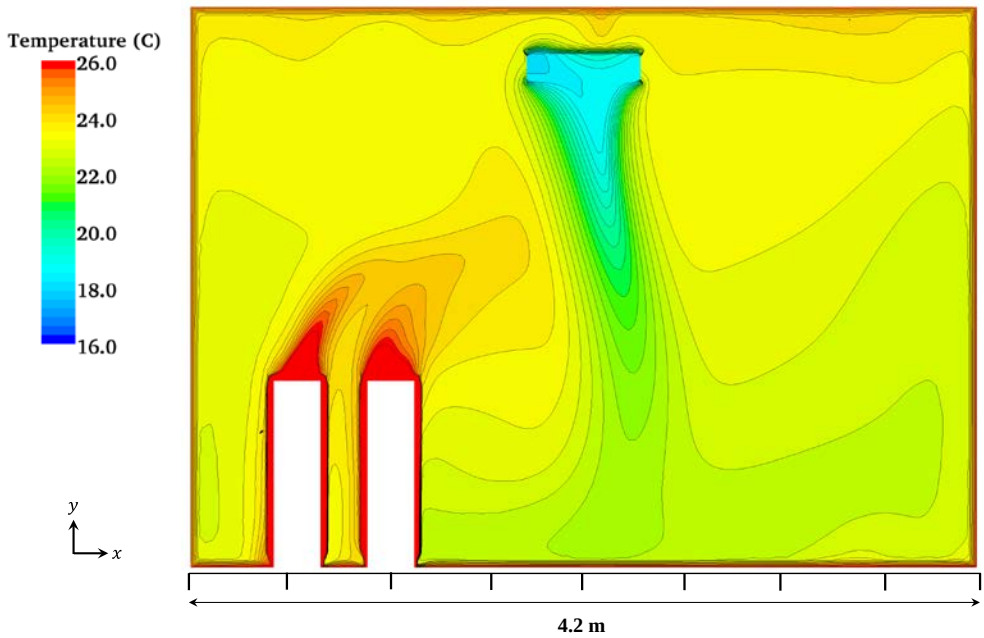

Figure 59. Cross-sectional view of the temperature distribution for the asymmetrically arranged thermal manikins.

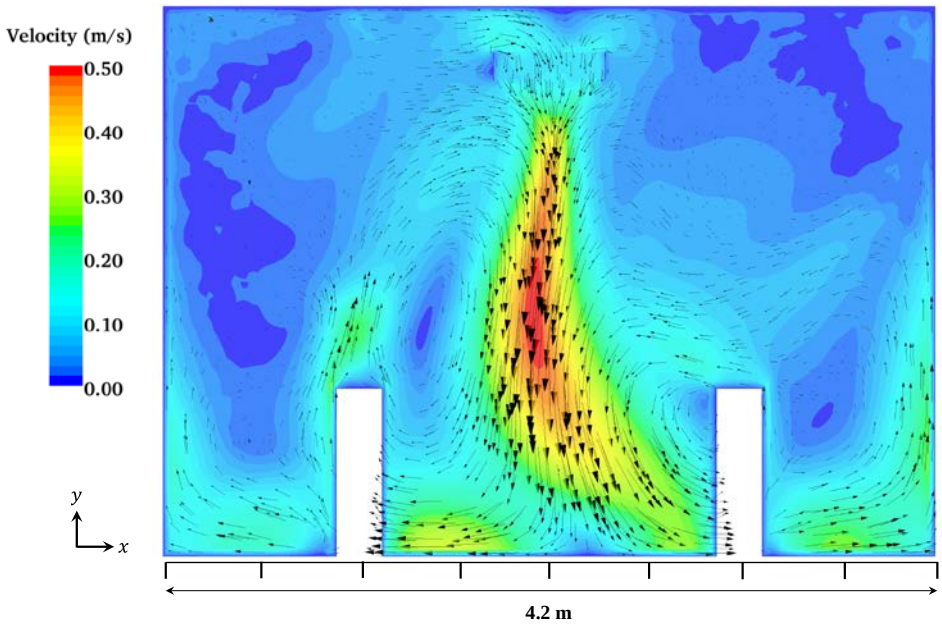

Figure 60. Cross-sectional view of the velocity field for the symmetrically arranged thermal manikins.

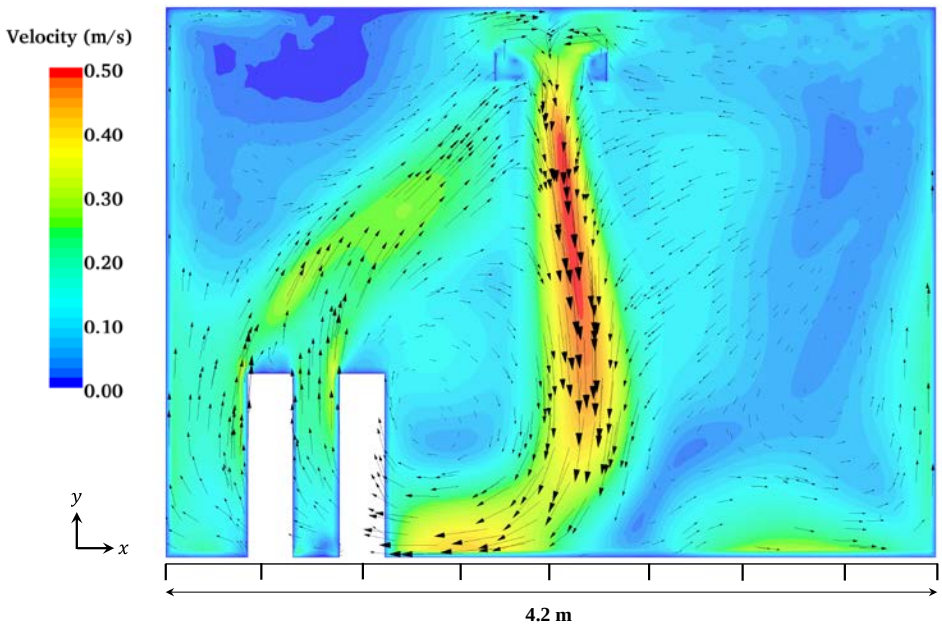

Figure 61. Cross-sectional view of the velocity field for the asymmetrically arranged thermal manikins.

For a three-dimensional representation of the beam plume, an isosurface was created from the results of the CFD simulations based on the defined temperature of 21.3 °C. In Figure 62, the thermal plume from the beam cooling the symmetric configuration of thermal manikins appears to descend directly below the beam without much contraction or significant variation from the vertical centerline along the entire length of the beam. The plume center (relative to the length of the beam) does not extend as far vertically as the front and rear sections. Time-dependent simulations were completed to investigate the shape of the plume as a function of time. A vertical oscillation in the middle section of the plume created a dumping motion from the beam outlet to the floor.

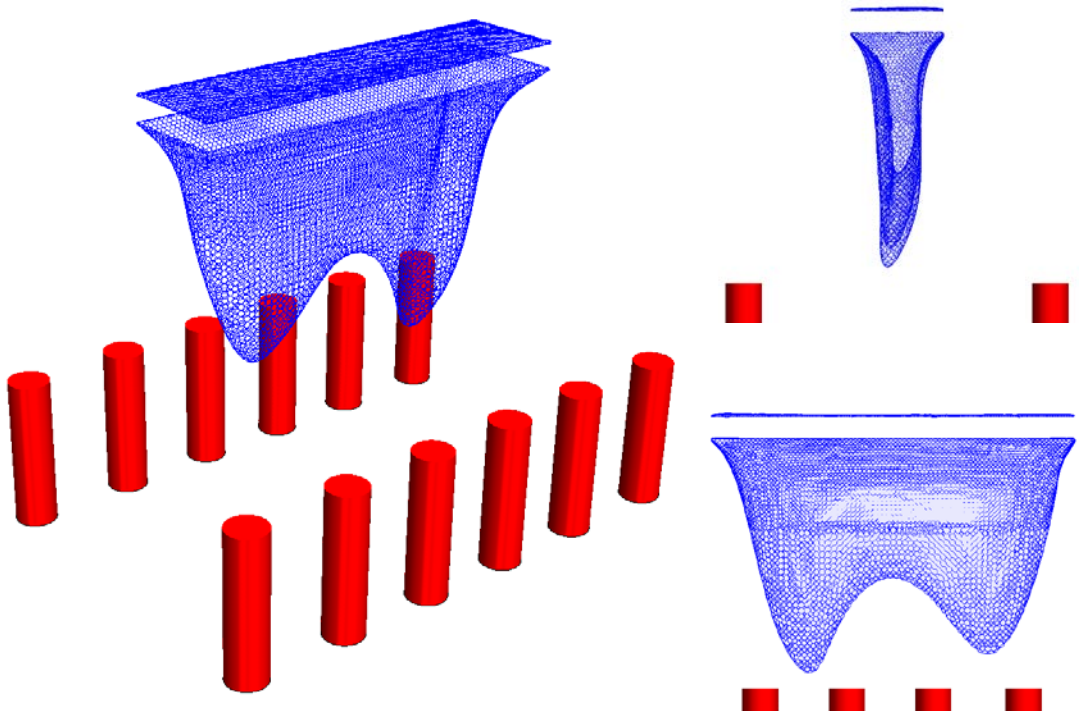

Figure 62. Three-dimensional isosurface of 21 °C for the symmetric thermal manikin configuration.

Throughout this time period equal to 90 s, the lateral movement of the beam followed a similar frequency of oscillation away from the vertical centerline of the beam. The center of the plume, as defined by the minimum temperature in each vertical row of a two-dimensional cross section, was recorded from the beam outlet to the floor for the symmetric heat source configuration. The minimum temperature location of each 1 s time step for the 90 s period was plotted along the vertical axis in Figure 63. The horizontal bars on each point signify the minimum and maximum distance from the vertical centerline where a minimum temperature was recorded at each time step. The circles in Figure 63 represent the averages of all the minimum temperature locations for the 90 s period.

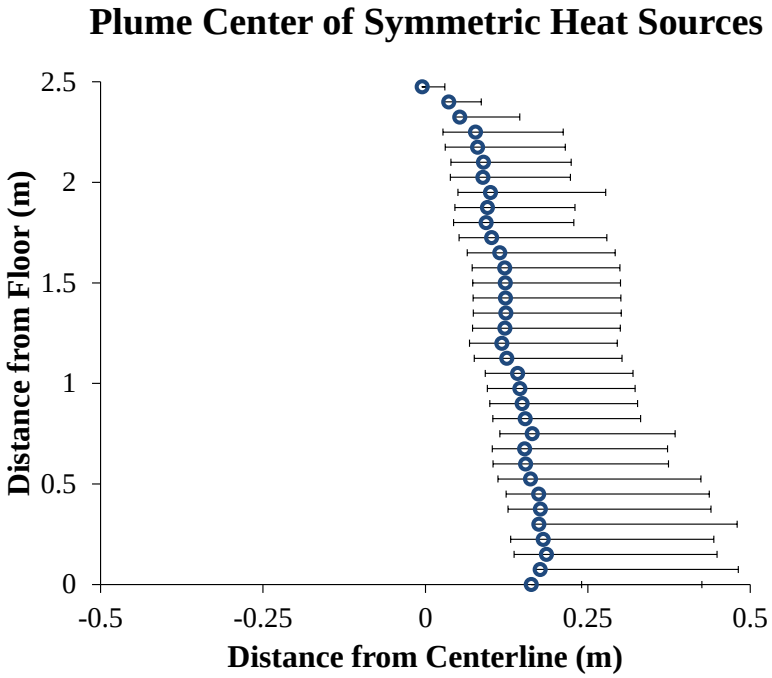

Figure 63. Minimum temperatures calculated for each vertical row over a 90 s period at 1 s increments for the symmetric heat source configuration.

Similarly, the simulation results of the asymmetric thermal manikin configuration were plotted as an isosurface equal to 21.3 °C. In Figure 64, the thermal plume created by the beam cooling the asymmetrically arranged thermal manikins appears with more variation than the symmetric thermal manikin results. Three distinct sections of the plume exist, each at different points along the beam centerline and each at different distances from the vertical centerline of the beam. A dumping motion with a frequency of oscillation that was similar to the symmetric configuration was observed. However, the movement of the beam with reference to the vertical centerline was more pronounced.

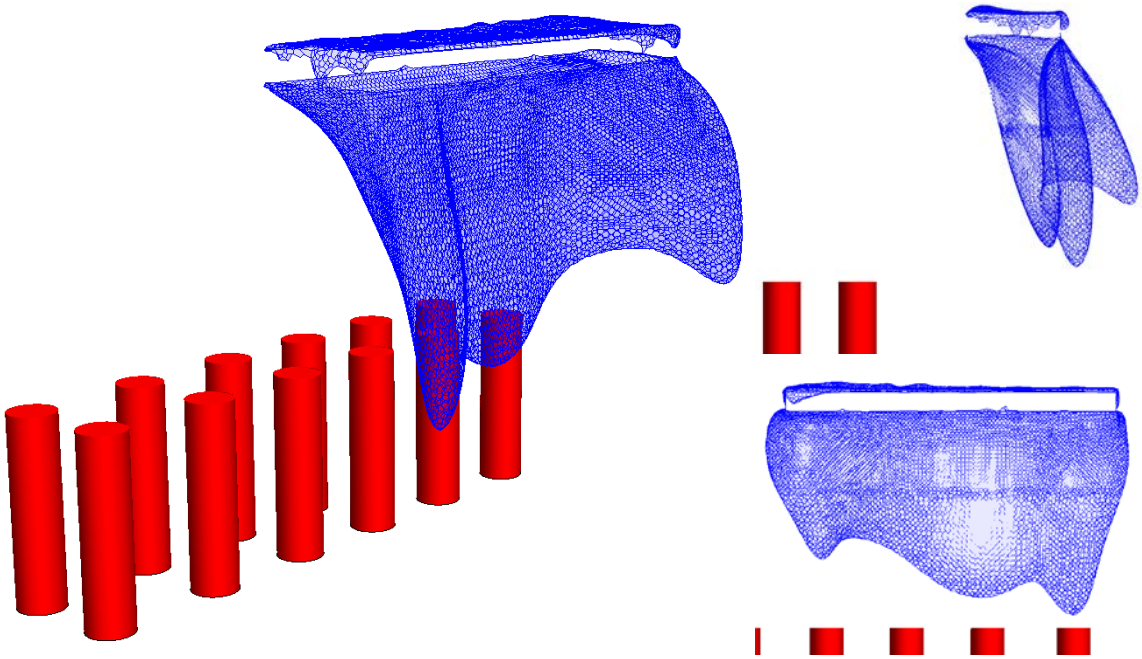

Figure 64. Three-dimensional isosurface of 21 °C for the asymmetric thermal manikin configuration.

As for the symmetric configuration, the center of the plume location, as defined by the minimum temperature along a two-dimensional row, was recorded for the asymmetric thermal manikin configuration. The results, in Figure 65, reveal a larger range of motion for the center of the plume. The median position of the oscillations is further from the vertical beam centerline and the magnitude of the range is larger than in the symmetric results. The unbalanced heat source locations in the room appear to contribute to instabilities in the room airflow and a beam plume with a higher range of motion.

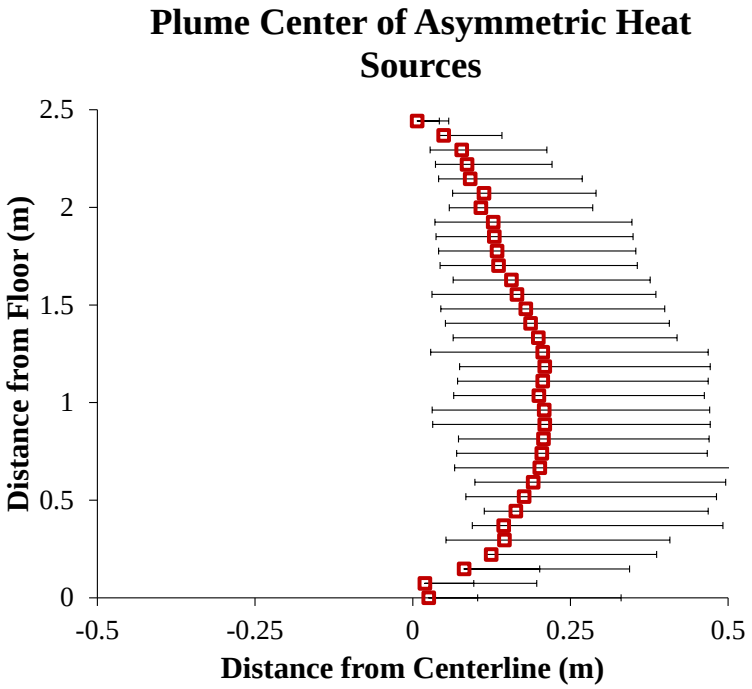

Figure 65. Minimum temperatures calculated for each vertical row over a 90 s period at 1 s increments for the asymmetric heat source configuration.

The impact on thermal comfort of occupants needs to be considered with the increased oscillatory behavior of the asymmetric thermal manikin configuration. A recent study [80] showed that fluctuations in the airflow surrounding occupants resulted in higher tolerances of the thermal conditions.

7.6 Beam Capacity Prediction

The simulation results from Section 7.5 were calculated with a constant value assigned for the heat rejection in the beam region. For additional simulations, the beam cooling rate was calculated for each iteration based on the value of the reference temperature sampled above the beam. The temperature difference between the average reference temperature and an assumed mean water temperature for typical operation was multiplied by the input parameter C_{bc} as defined in Chapter 4. The value of C_{bc} was calculated at each iteration based on the temperature difference between the reference temperature and the mean water temperature value. From the experiments, the relationship between C_{bc} and the reference temperature minus the mean water temperature was plotted in Figure 66.

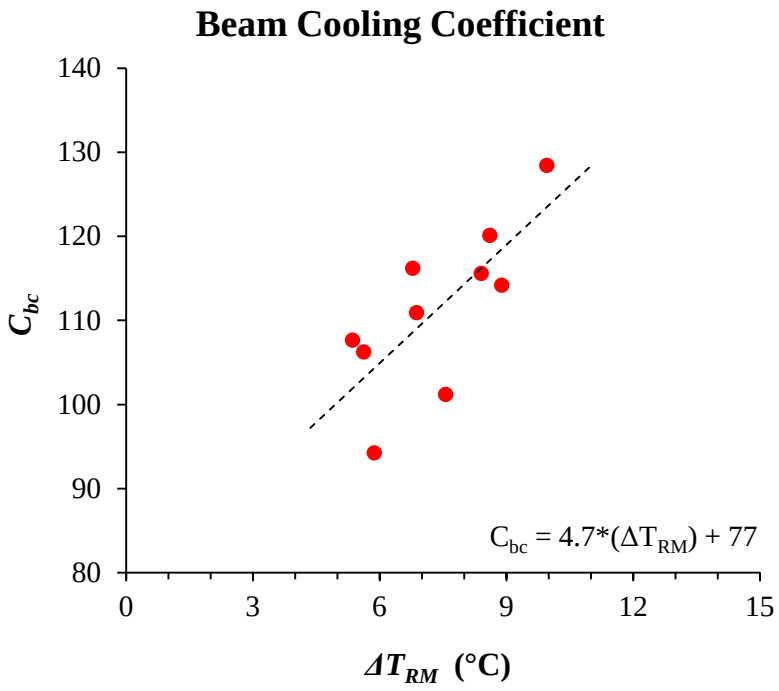

Figure 66. Linear regression for the beam cooling coefficient as a function of ΔT_{RM}.

From the data, a linear regression produced the following equation for calculating the beam cooling coefficient as a function of ΔT_{RM}:

$$C_{bc} = 4.7 * (\Delta T_{RM}) + 77 \quad (7.1)$$

The beam cooling capacity was then calculated as:

$$Q_b = C_{bc} * (\Delta T_{RM}) \quad (7.2)$$

The value Q_b was calculated at each iteration and used to assign the heat rejection for the porous region, which was updated for every simulation step. The wall surfaces were defined as adiabatic and the heat flux from the thermal manikins was set to 110 W/m^2 to coincide with the experiment conditions of Test A10. The simulations

were completed based on monitoring the average room and reference temperatures, shown in Figure 67 and Figure 68. The simulation was considered at a steady state condition once the average room air temperature, and the average reference temperature reached a constant value. For both the symmetric configuration and asymmetric configuration, the simulations reached a steady state condition after 8,000 iterations, for a total simulation time of 30,000 s. The average room air temperature and reference temperature as a function of simulation iteration are plotted in Figure 67 for the symmetric test, and in Figure 68, for the asymmetric test.

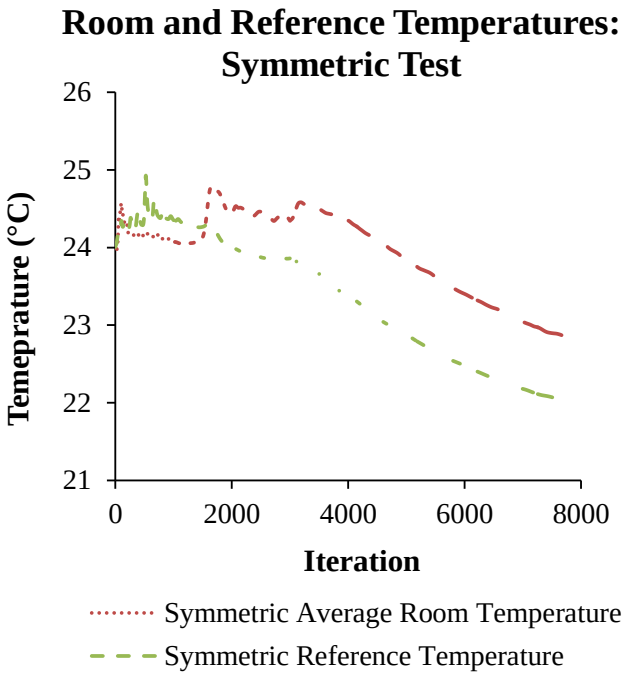

Figure 67. Average room temperature and T_{ref} for each iteration in the asymmetric simulation.

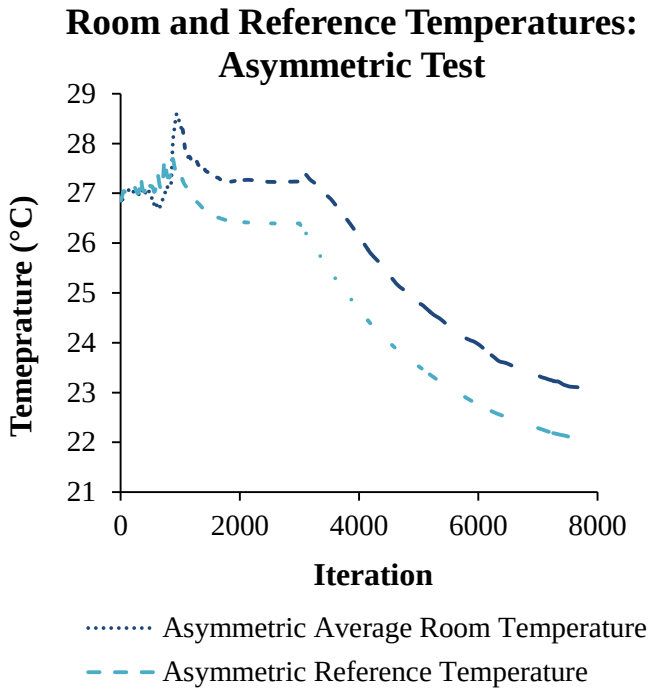

Figure 68. Average room temperature and T_{ref} for each iteration in the asymmetric simulation.

From the simulation results, the actual cooling delivered by the beam was calculated with the mass flow rate of air through the beam and the inlet and outlet temperatures according to the following equation:

$$Q_b = \dot{m}_{a,o} c_{pa} (T_{ref} - T_{a,o}) \quad 7.3$$

where $\dot{m}_{a,o}$ is the mass flow of air through the beam outlet, c_{pa} is the specific heat capacity of air, T_{ref} is the reference temperature, and $T_{a,o}$ is the temperature of air at the beam outlet. The results of the testing are listed in Table 20. The calculation of beam cooling capacity resulted in a similar result than the experimental testing. A 16.5 % reduction in beam cooling capacity was calculated for the asymmetric thermal manikins.

Additionally, the mass flow rate of air through the beam was almost 18 % lower in the asymmetric thermal manikin beam. The drop in cooling capacity of the beam was a result of the lower flow rate of air.

Table 20. Calculated beam cooling rate based on the capacity calculation.

	Symmetric Manikins	*Asymmetric Manikins*	*Percent Difference*
T_{ref} (°C)	22.9	23.1	0.87 %
ΔT_{RM} (°C)	9.87	10.11	2.43 %
Room Temperature (°C)	22.0	22.1	0.45 %
C_{bc}	123	124	0.81 %
$\dot{m}_{a,o}$ (kg/s)	0.158	0.130	-17.7 %
$T_{a,o}$ (°C)	16.1	16.2	0.62 %
Q_b (W)	1074	897	-16.5 %

7.7 Inlet Velocity Field

The reduced capacity of the asymmetric configuration was found in the experiments to be an average of 15 % when compared to the symmetric configuration. The velocity field above the beam was studied using the CFD simulation results with the capacity calculations that also showed a reduced capacity for the asymmetric configuration. Streamtubes were calculated and plotted for the inlet conditions above the beam region. For the simulations with the symmetrically arranged thermal manikins, the orientation of the streamtubes on both sides of the beam as the room air enters are similar, as shown in Figure 69.

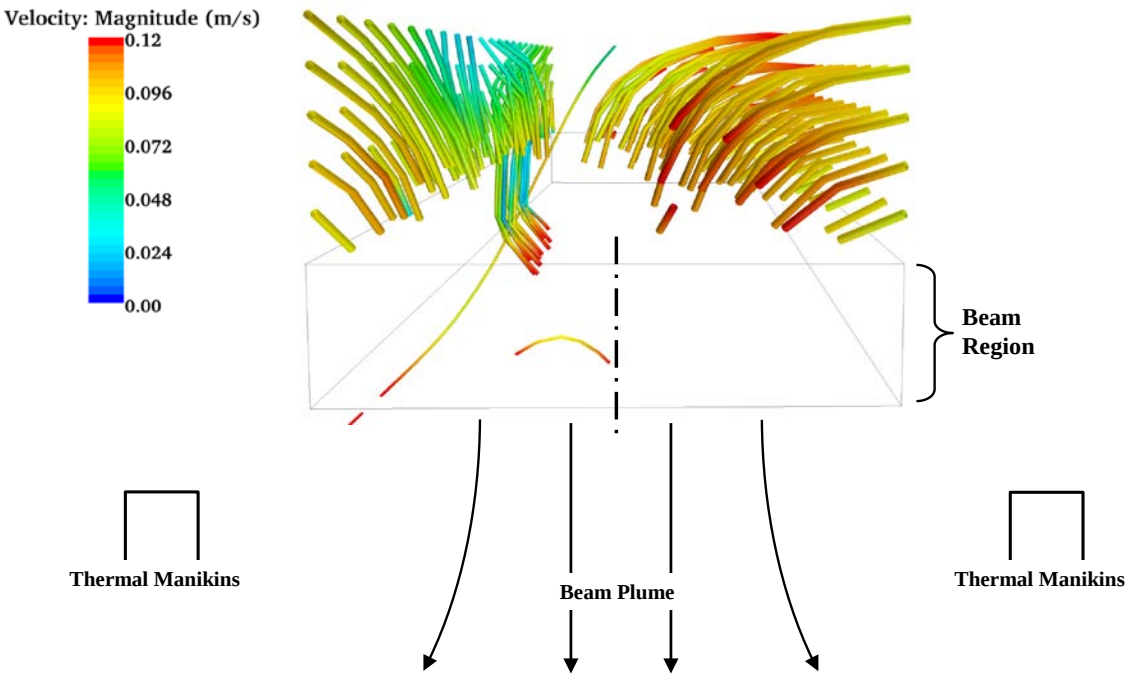

Figure 69. Streamtubes above the beam region for the simulations of symmetrically arranged thermal manikins.

The streamtubes for the simulations of the asymmetrically arranged thermal manikins were calculated and plotted in Figure 70. The difference in velocity fields above the beam between the two simulations is apparent as the streamtubes above the beam for asymmetrically arranged heat sources enter from the side of the beam closest to the thermal manikins and continue past the inlet to the beam. The magnitude of the entering air velocity is higher than the symmetric configuration and the direction of the flow is parallel to the beam inlet.

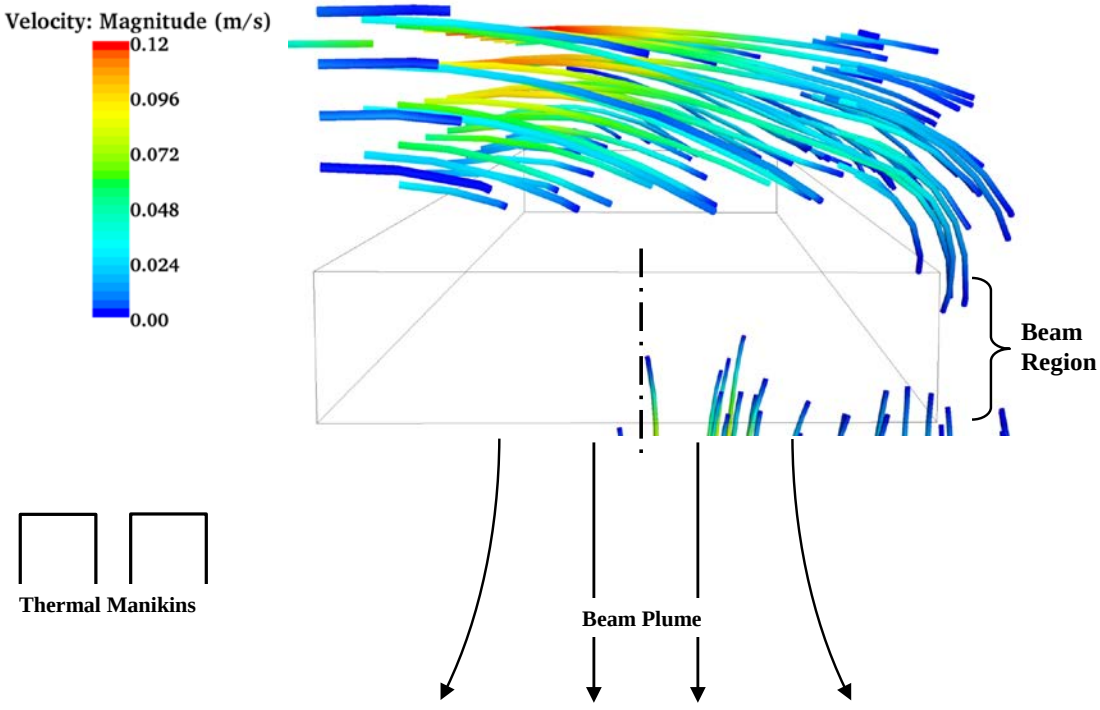

Figure 70. Streamtubes above the beam region for the asymmetrically arranged thermal manikins.

Likewise, Figure 71 is the velocity field above the beam region and shows the direction and magnitude of the air velocity vectors on the thermal manikin side of the beam as parallel to the beam inlet. On the opposite side of the beam region, according to the plotted velocity field vectors, the air is traveling from the thermal manikin side of the beam and past the inlet.

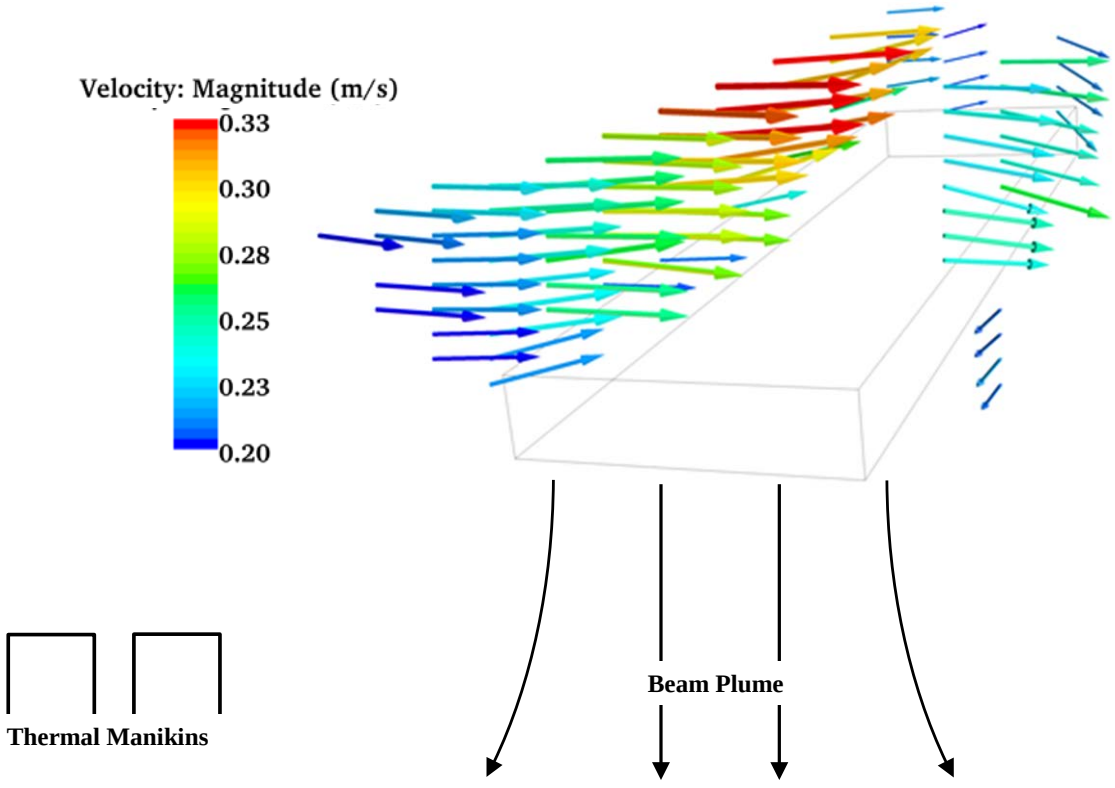

Figure 71. Vector field above the beam region for the asymmetrically arranged thermal manikins.

Additionally, the streamlines were calculated and plotted originating from the outlet of the beam for both configurations. The flow pattern shown in Figure 72 appears symmetric from the outlet of the beam as the air circulates back up towards the beam inlet with uniform mixing throughout the space. The streamlines plotted in Figure 72 match the temperature distribution and velocity profile of Figure 58 and Figure 60, respectively. The beam plume in Figure 72, identified by the region of higher velocity directly beneath the beam, exhibited the same oscillation as reported in Section 7.5 where the center of the beam plume was recorded by mapping the location of the minimum temperatures.

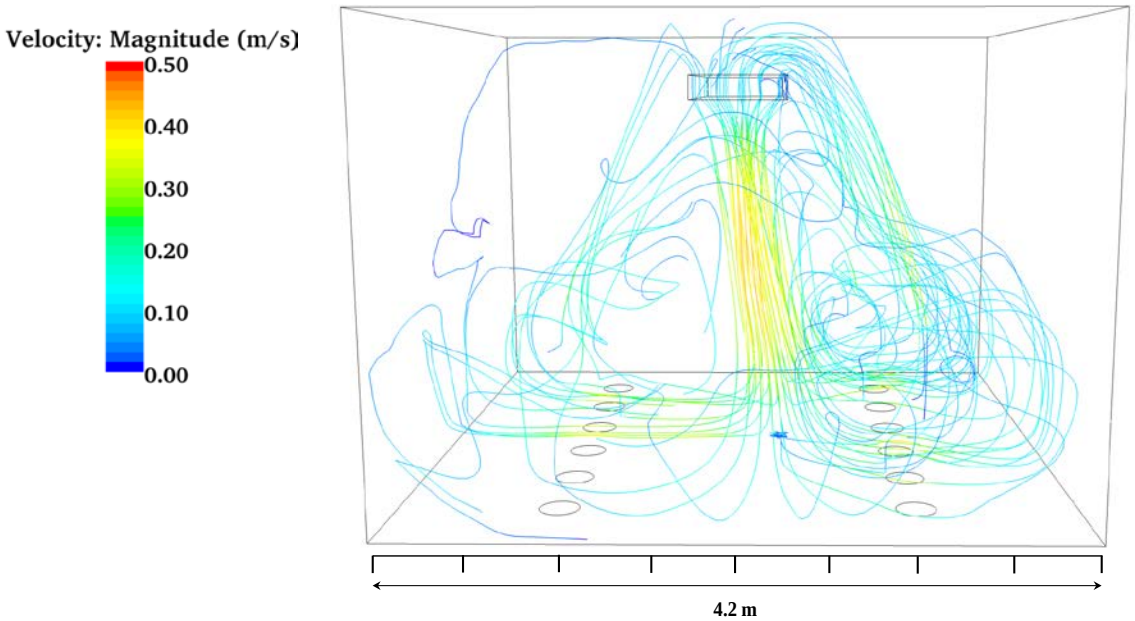

Figure 72. Streamlines from the outlet of the beam for the symmetrically arranged heat sources.

For the asymmetric thermal manikins, the streamlines plotted in Figure 73 reveal a flow pattern biased towards the side of the room with the heat sources. As the air leaves the beam, it travels towards the heat source locations and then back up to the beam inlet. The room appears to be less mixed than the room with the symmetrically arranged heat sources. The apparent difference in flow patterns throughout the rooms for both heat source arrangements contributes to a reduced mass flow of air through the beam cooling the asymmetrically arranged heat sources. The higher magnitude of the entering air velocity above the beam combined with the unbalanced flow, results in a lower rate of total cooling provided to the room from the passive chilled beam. As for the symmetric thermal manikin streamline results, the same oscillation reported in Section 7.5 for the asymmetric thermal manikins based on the minimum temperatures, was observed for the beam plume streamlines in Figure 73.

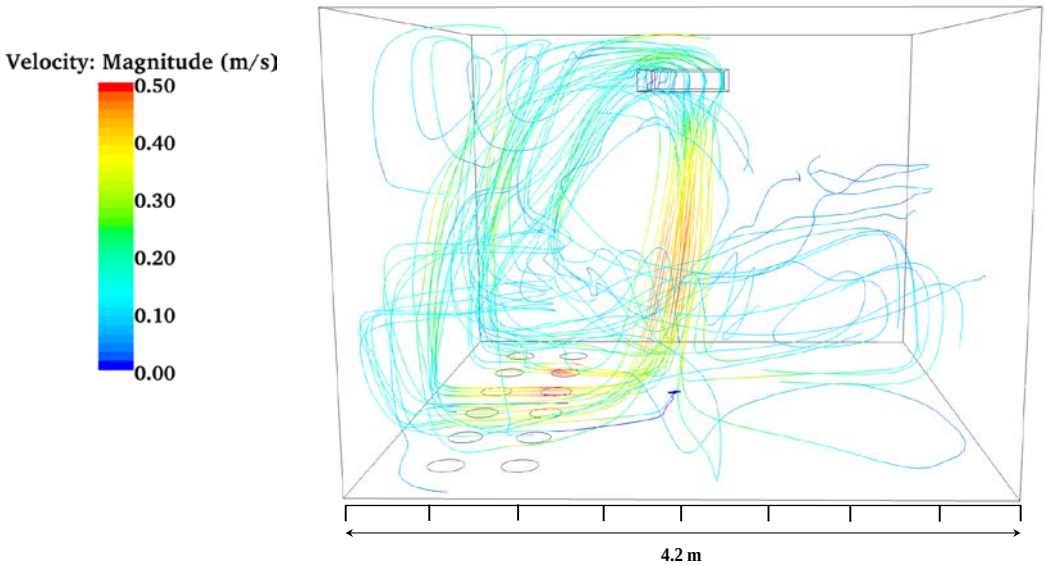

Figure 73. Streamlines from the beam outlet for the asymmetric arrangement of heat sources.

7.8 Summary

The measured beam cooling capacity for the tests with thermal manikins placed asymmetrically in the test chamber was 15 % lower than the beam cooling capacity of the symmetrically placed thermal manikins. CFD simulations of the two test arrangements revealed similar results, and with the beam capacity calculated at each simulation iteration, the calculated beam cooling capacity in the simulations with asymmetric thermal manikins was 17 % lower than the symmetric thermal manikins. The inlet velocity fields above the passive chilled beam for both heat load configurations were compared by calculating the streamlines of the entering air. This revealed that with the asymmetrically configured thermal manikins, the entering air velocity at the beam inlet was higher than for the symmetric thermal manikins. The bulk of the flow came from the side of the beam closest to the heat sources and circumvented the beam because of the magnitude and direction of the air velocity. Additionally, experimental test results showed a negligible difference in beam cooling capacity, Q_b, as a function of ΔT_{RM} between the symmetric thermal manikins and the symmetric radiant panels. The conclusion from the results of experimentation and simulation analysis is that the heat source location affects the performance of the passive chilled beam because of the difference in the inlet velocity fields, whereas the heat source type had negligible effect.

CHAPTER VIII

HEAT SOURCE CONFIGURATION PREDICTIONS

8.1 Introduction

The objective of this study was to determine the beam efficiencies for different spatial arrangements and the resultant thermal conditions inside the space. The CFD modeling method described in Chapter IV was applied to additional configurations than were experimentally tested to include variations of the inside room dimensions, the beam position, and heat source locations. Two sets of simulation runs were completed that included comparisons of 1) the calculated beam cooling capacities under equivalent heat fluxes from the thermal manikins and 2) the thermal plume and room air conditions at equivalent beam cooling capacities. For the first set of simulations, the method for calculation of the beam capacity was described in Chapter IV and Chapter VII. The predictions of the beam cooling capacity were used to determine the effect of the varied spatial parameters in the room on the efficiency of the beam to remove the generated heat. The equivalent beam cooling capacity tests were analyzed to compare the center of the plume position for each configuration and the temperature and velocity characteristics in the simulated room space.

8.2 Beam Capacity Predictions

The procedure developed in Chapter VII for calculating the beam cooling capacity was implemented to test various configurations of the simulation volume.

According to the steady state criteria listed in Chapter VII, the simulations finished once the average room air temperature and reference air temperature values remained constant. First, variations in the beam position with respect to room orientation and the height from the floor were simulated to isolate the observed reduction in cooling capacity for asymmetric heat sources. Additionally, various thermal manikin arrangements were simulated to generally represent typical heat source diversities expected in room design in order to develop some general observations and recommendations for positioning a passive beam to achieve the most cooling. The following section reports the results of the calculated beam cooling capacities for beam orientation, beam height, and thermal manikin arrangement.

8.2.1 Beam Orientation

Four beam orientations in relation to the room were simulated and were referred to by a designated position number: Beam Position (BP) 1 centered along the North-South axis, Beam Position 2 offset 1.1 m from the North-South axis, Beam Position 3 centered along the East-West axis, and Beam Position 4 offset 1.1 m from the East-West axis, as depicted in Figure 74.

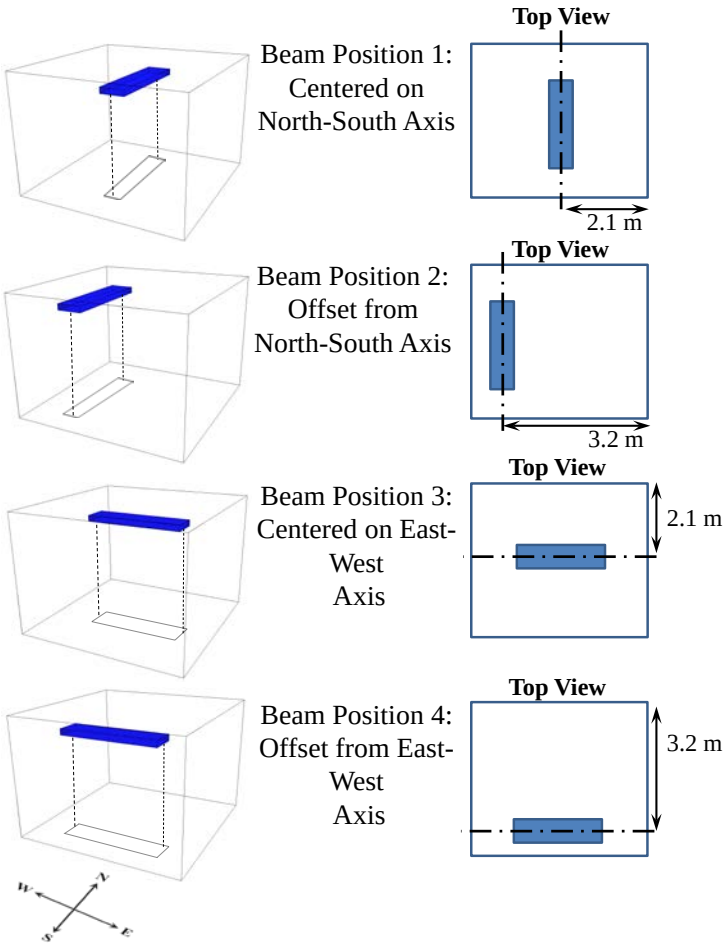

Figure 74. Beam orientation for the four test cases.

The simulations were conducted with adiabatic wall boundary conditions and thermal manikins positioned in the symmetric configuration with a heat flux of 110.1 W/m^2 for a total of 1101 W for the floor surface area of 17.6 m^2. The calculated beam cooling capacity was greatest for the beam oriented in the position centered on the East-West-axis (Beam Position 3). The offset positions of the beam in both directions (East-West and North-South) had negligible effect on the beam performance when compared

to the position centered on the North-South axis. The results of the testing are listed in Table 21 and include the values of the beam air mass flow rate ($\dot{m}_a$), the reference temperature (T_{ref}), the average air temperature throughout the entire room ($T_{room,ave}$), the beam cooling coefficient (C_{bc}), the average air temperature at the beam outlet ($T_{o,ave}$), and the calculated beam cooling capacity (Q_b).

Table 21. Results from the beam cooling capacity predictions for the four beam orientations.

	Beam Position 1	*Beam Position 2*	*Beam Position 3*	*Beam Position 4*
$\dot{m}_a$ (kg/s)	0.158	0.252	0.294	0.253
T_{ref} (°C)	22.9	23.0	23.2	22.9
$T_{room,ave}$ (°C)	22.0	22.4	22.5	22.3
C_{bc}	123	124	125	124
$T_{o,\,ave}$ (°C)	16.1	18.6	19.0	18.8
Calculated Q_b (W)	1074.4	1111.8	1215.4	1040.9

A method to calculate the efficiency of the beam was used for comparing the configuration changes effect on beam performance. The efficiency of the beam, η_b, for each configuration was calculated as the ratio of the beam cooling capacity, Q_b, to the thermodynamic limit of the beam cooling:

$$\eta_b = \frac{Q_b}{Q_{max}} \tag{8.1}$$

where Q_{max} is the theoretical maximum cooling capacity of the beam and Q_b was determined using the CFD simulations with the beam cooling capacity calculation, as defined in Chapter VII. The theoretical maximum cooling was defined as the

thermodynamic limit of heat transfer between the air and the water. To calculate the mass flow of air, $\dot{m}_a$, through the beam cooling a room at the theoretical maximum, Equation 5.28 was used to find the outlet velocity of the air together with:

$$\dot{m}_a = \rho_o \sqrt{\left(\frac{\Delta\rho}{\rho_o} gL\right)} A_o \tag{8.2}$$

where ρ_o is the density of air at the outlet temperature and pressure, $\Delta\rho$ is the difference in air density between the inlet and the outlet, and A_o is the area of the passive chilled beam outlet. Q_{max} was then calculated as the product of the mass flow of air, specific heat of air, and the temperature difference between the reference air and the supply water:

$$Q_{max} = \dot{m}_a c_{pa}\left(T_{ref} - T_{w,i}\right) \tag{8.3}$$

where c_{pa} is the specific heat capacity of air, T_{ref} is the reference air temperature above the beam, and $T_{w,i}$ is the supply water temperature. The result for an above beam temperature of 24 °C and an inlet water temperature of 14 °C was 3,437 W. The efficiency defined by the thermodynamic limit for the passive chilled beam was calculated to be 31.3 % for the beam position centered along the North-South axis. The efficiencies for the four configurations are listed in Table 22 and show that the beam in Beam Position 3 had the highest efficiency.

Table 22. Efficiencies for the passive chilled beam for four beam orientations with symmetrically configured thermal manikins.

	Calculated Q_b (W)	*η_b (%)*
Beam Position 1	1074	31
Beam Position 2	1112	32
Beam Position 3	1215	34
Beam Position 4	1041	30

8.2.2 Wall Lengths, Ceiling and Beam Height

Three geometric parameters of the simulation volume were changed to quantify the effect on the beam cooling capacity. The wall length was increased 1 m in each direction, the ceiling raised 1 m, and the beam height increased to 1 m, as shown in Figure 75. The thermal manikin positions remained in the symmetric configuration, each row spaced 1 m from the closest wall. Since changing any three of these parameters would require building a new test room to collect measured data, the validated method for modeling the passive chilled beam in CFD was used to calculate the beam cooling capacity for the additional configurations.

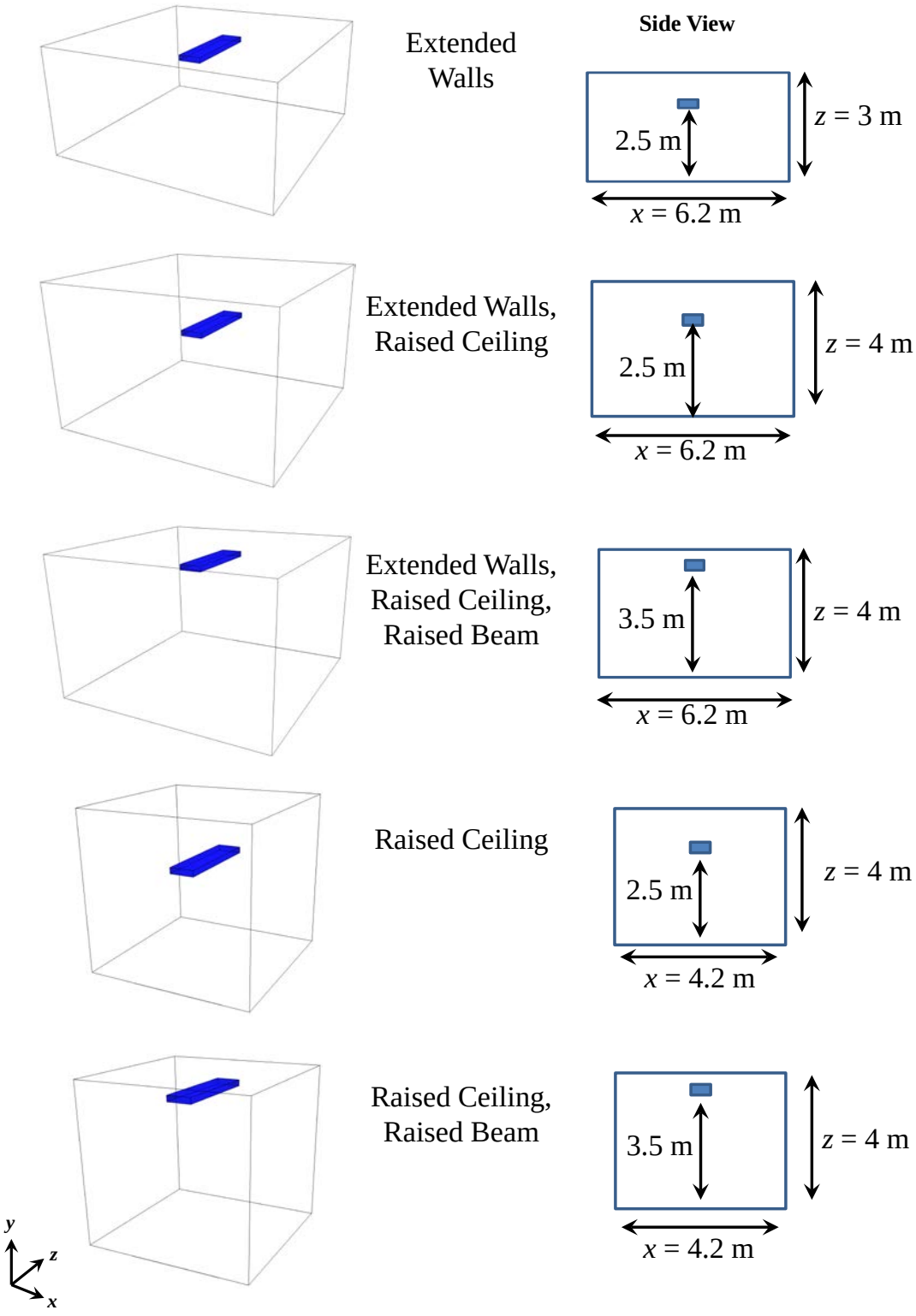

Figure 75. Configurations with extended walls, raised ceiling, and raised beam.

Table 23. Results from the beam cooling capacity predictions for the extended walls, raised ceiling, and raised beam tests.

	Extended Walls	*Extended Walls, Raised Ceiling*	*Extended Walls, Raised Ceiling, Raised Beam*	*Raised Ceiling*	*Raised Ceiling, Raised Beam*
$\dot{m}_a$ (kg/s)	0.240	0.320	0.270	0.296	0.297
T_{ref} (°C)	23.8	24.0	24.0	23.3	23.5
$T_{room,ave}$ (°C)	23.4	23.7	23.6	23.0	23.0
C_{bc}	128	129	129	125	126.3
$T_{o,\,ave}$ (°C)	18.8	19.9	19.4	19.2	19.5
Calculated Q_b (W)	1197.0	1309.1	1256.0	1198.3	1198.2
η_b (%)	30	32	31	33	32

8.2.3 Thermal Manikin Locations

In addition to the symmetrical and asymmetric thermal manikin configurations, six different configurations were tested, as shown in Figure 76 and Figure 77. In Configuration C, three manikins each were placed in the Northeast and Southwest corners of the room to simulate an off-balanced load. In Configuration D, the thermal manikins were removed from one side of the room in the symmetric configuration to test the beam performance with heat generated symmetrically in relation to the beam orientation but in just half of the room. In Configuration E, six thermal manikins were located in the Northeast corner of the room to calculate the effects of a concentrated heat source away from the beam. Twelve thermal manikins were used in Configuration F located directly beneath the beam in two symmetric rows to simulate a passive beam cooling a room where the thermal plume falls directly onto the heat sources. In Configuration G, six thermal manikins positioned in the center of the room in two rows were used to study the effect on the beam performance of a concentrated heat source directly beneath the beam. In the last configuration of the testing, Configuration H, the thermal manikin positions from Configuration G were moved from the center of the room to the North wall and remained directly under the beam.

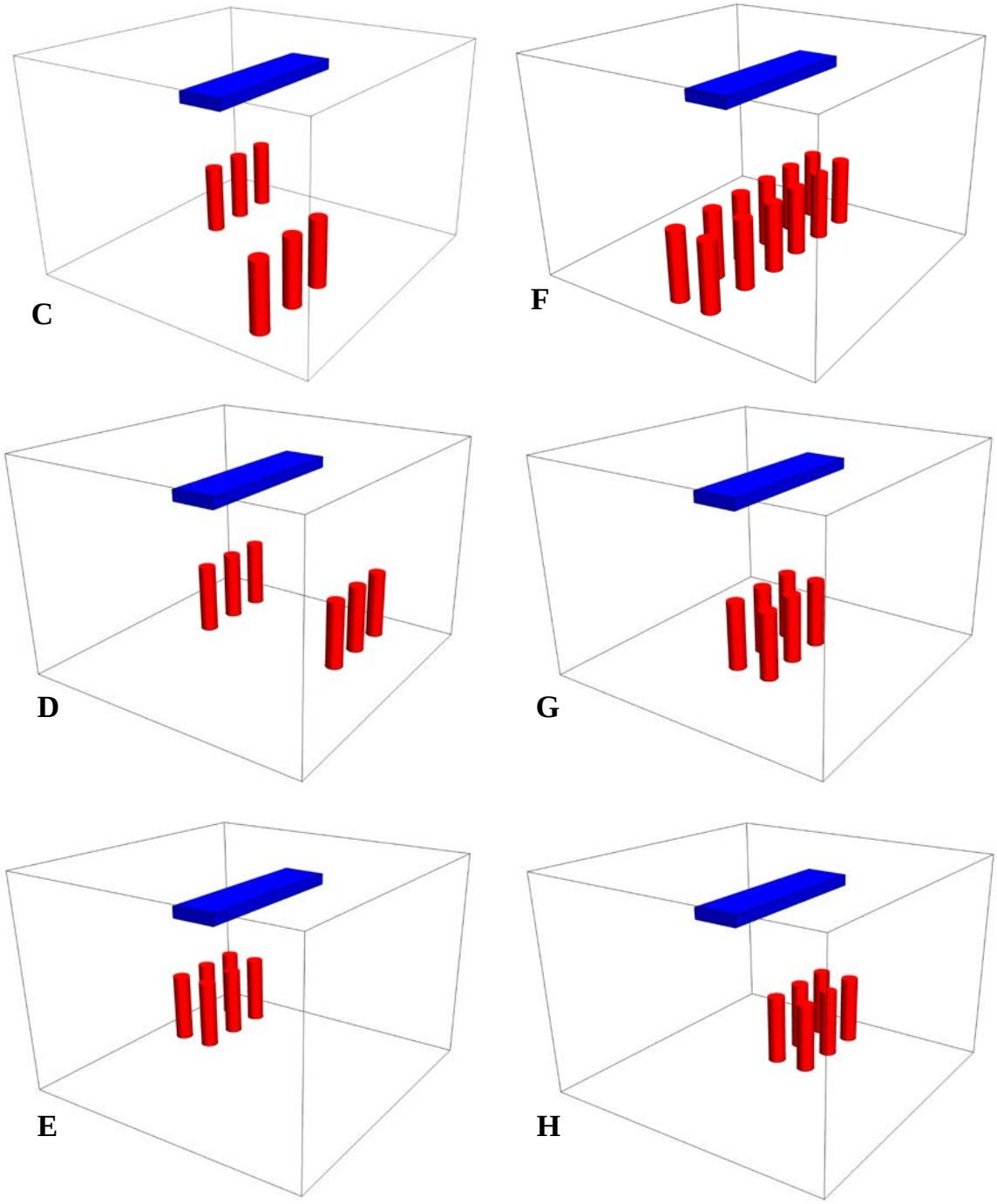

Figure 76. Thermal manikin locations for the C, D, E, F, G, and H configurations.

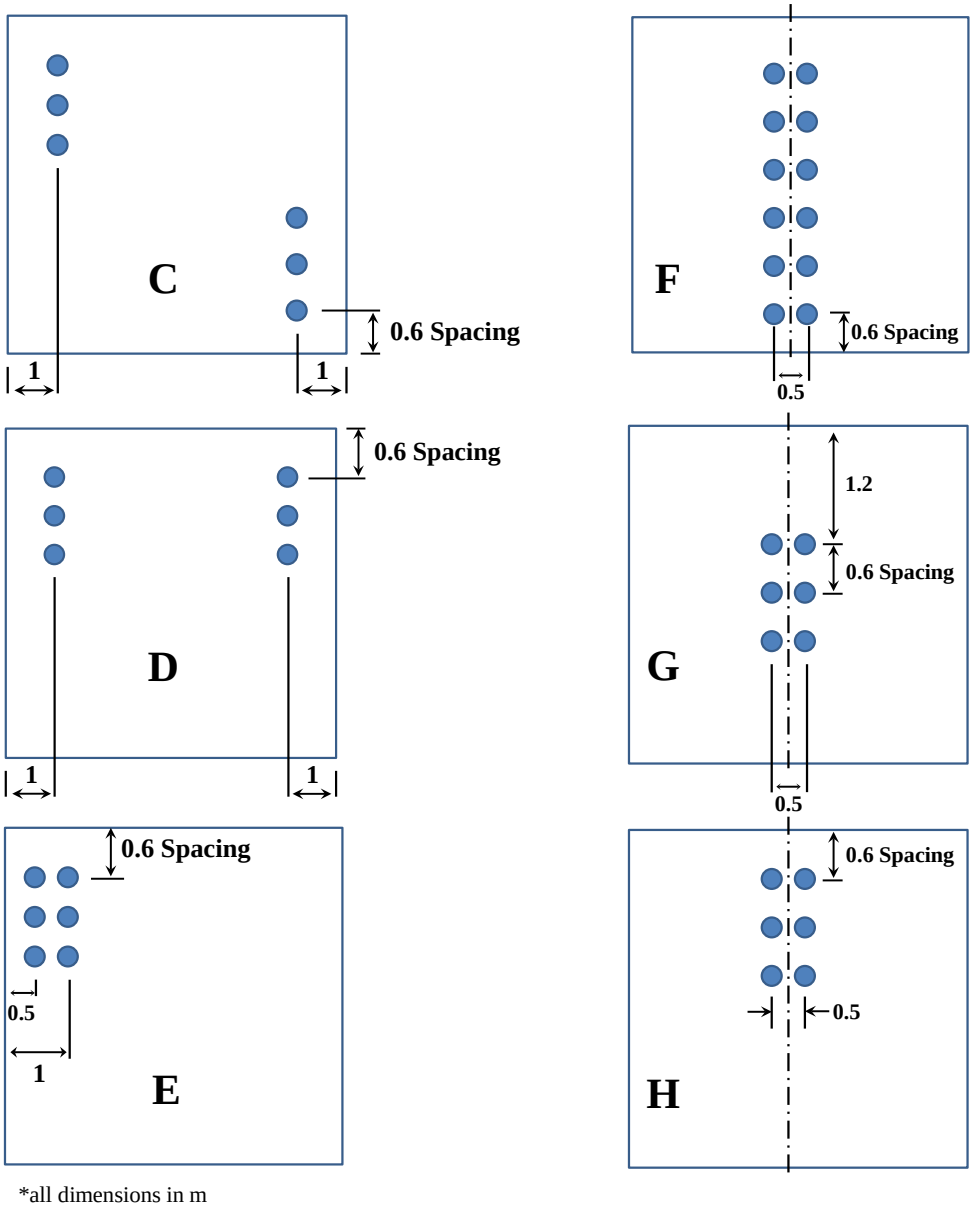

Figure 77. Dimensions of thermal manikin locations for the six configurations.

The simulation results are listed in Tables 24-29. For every configuration except Configuration D, the beam in Beam Position 3 had the highest efficiency. When the beam was oriented perpendicular to a row or grouping of heat sources, it resulted in

higher cooling rates. For Configuration D, the thermal manikins were placed in two rows and with Beam Position 3, were perpendicular to the beam. Based on the results of all other configurations, it was expected that the D3 simulation would produce the highest efficiency beam cooling. However, since the placement of the thermal manikins was essentially a 2 x 3 grid, two rows were perpendicular to the beam while three rows were parallel. Any advantage of the beam oriented perpendicular to the two rows of manikins, was counteracted by the three rows of manikins that created a similar airflow pattern as was observed in the Test B experiments and simulations. The beam efficiencies for each configuration grouped by beam position were plotted in Figure 78.

Table 24. Results from the beam cooling capacity predictions for the beam with thermal manikins in the C-configuration.

	C1	*C2*	*C3*	*C4*
$\dot{m}_a$ (kg/s)	0.156	0.240	0.285	0.238
T_{ref} (°C)	19.8	22.3	22.4	22.4
$T_{room,ave}$ (°C)	19.1	21.7	21.7	21.7
C_{bc}	109	121	121	121
$T_{o,\,ave}$ (°C)	16.6	18.1	18.7	18.1
Calculated Q_b (W)	506.2	1019.5	1049.3	1028.6
η_b (%)	28	33	33	33

Table 25. Results from the beam cooling capacity predictions for the beam with thermal manikins in the D-configuration.

	D1	*D2*	*D3*	*D4*
$\dot{m}_a$ (kg/s)	0.263	0.265	0.262	0.224
T_{ref} (°C)	20.2	22.5	22.7	22.6
$T_{room,ave}$ (°C)	19.3	21.8	21.9	21.9
C_{bc}	111	122	123	122.3
$T_{o,\,ave}$ (°C)	17.0	18.6	18.5	18.0
Calculated Q_b (W)	832.6	1033.6	1107.7	1029.4
η_b (%)	42	32	33	32

Table 26. Results from the beam cooling capacity predictions for the beam with thermal manikins in the E-configuration.

	E1	*E2*	*E3*	*E4*
$\dot{m}_a$ (kg/s)	0.19	0.212	0.282	0.228
T_{ref} (°C)	24.2	22.5	22.5	21.7
$T_{room,ave}$ (°C)	23.1	21.7	21.6	21.9
C_{bc}	130	122	122	118
$T_{o,\,ave}$ (°C)	18.2	18.1	18.5	18.8
Calculated Q_b (W)	1148.2	946.3	1141.4	656.0
η_b (%)	27	30	36	24

Table 27. Results from the beam cooling capacity predictions for the beam with thermal manikins in the F-configuration.

	F1	*F2*	*F3*	*F4*
$\dot{m}_a$ (kg/s)	0.083	0.239	0.228	0.228
T_{ref} (°C)	22.5	22.9	22.8	22.8
$T_{room,ave}$ (°C)	22.4	22.3	22.6	22.6
C_{bc}	122	124	123	123
$T_{o,\,ave}$ (°C)	18.8	18.7	19.0	18.9
Calculated Q_b (W)	313.6	1005.0	1165.6	894
η_b (%)	10	29	32	27

Table 28. Results from the beam cooling capacity predictions for the beam with thermal manikins in the G-configuration.

	G1	*G2*	*G3*	*G4*
$\dot{m}_a$ (kg/s)	0.169	0.223	0.263	0.228
T_{ref} (°C)	20.2	22.3	22.4	22.8
$T_{room,ave}$ (°C)	20.0	21.7	21.7	22.6
C_{bc}	111	121	121	123
$T_{o,\,ave}$ (°C)	17.1	18.2	18.4	18.9
Calculated Q_b (W)	526.1	919.4	1044.0	894
η_b (%)	26	30	33	27

Table 29. Results from the beam cooling capacity predictions for the beam with thermal manikins in the H-configuration.

	H1	*H2*	*H3*	*H4*
$\dot{m}_a$ (kg/s)	0.156	0.223	0.263	0.228
T_{ref} (°C)	20.1	22.3	22.4	22.8
$T_{room,ave}$ (°C)	19.4	21.7	21.7	22.6
C_{bc}	111	121	121	123
$T_{o,\,ave}$ (°C)	17.0	18.2	18.4	18.9
Calculated Q_b (W)	486.8	919.4	1044.0	894
η_b (%)	25	30	33	27

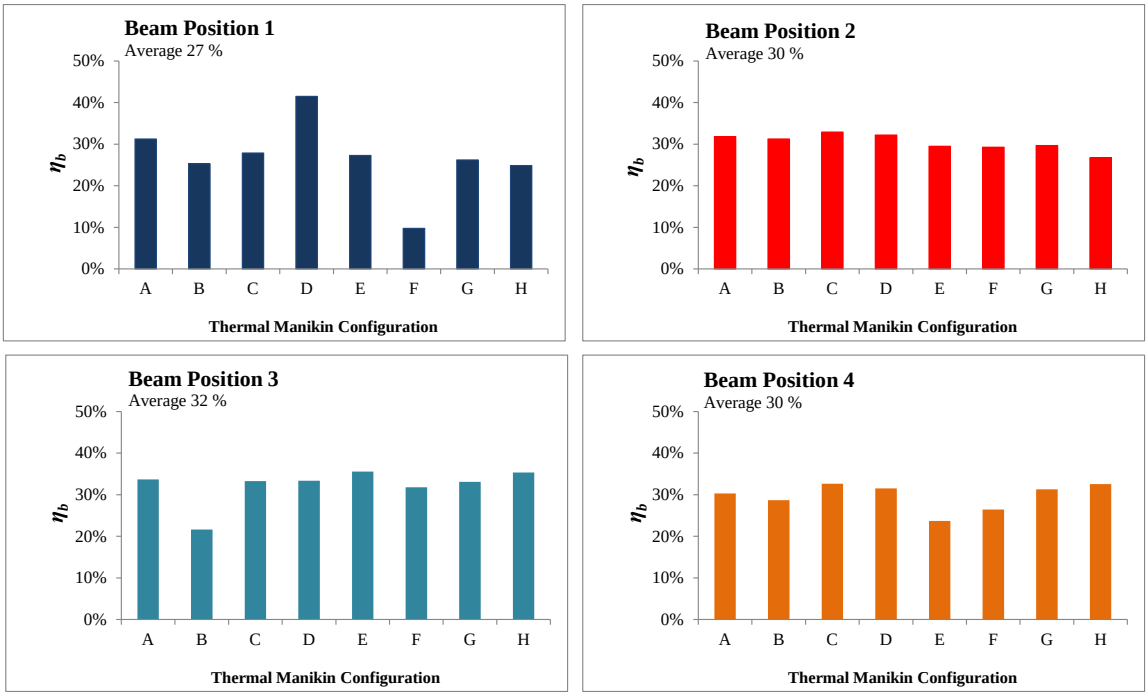

Figure 78. Beam efficiencies for the different configurations of thermal manikins grouped by the beam position.

8.3 Characteristics of Room Air and Thermal Plume

The effect of beam location, room dimensions, and heat source configurations on the beam efficiency was reported in Section 8.2. Additionally, the effect on the thermal characteristics in the occupied zone was studied to determine if the increase in beam efficiency resulting from a changed configuration would negatively affect the thermal characteristics impacting perceived thermal comfort. In order to compare the thermal plume and room air characteristics of the various configurations, the beam cooling

capacity was set to a constant value and the walls, ceiling, and floor were set as adiabatic. The simulations were each run at 30 s time steps for a total simulation time of 3,000 s. The center of the beam plume from the beam outlet to the floor was calculated based on the minimum temperature and used to compare the location of the plume in relation to the beam vertical centerline and heat sources. The occupied zone of the room was defined as all points within 1.8 m from the floor, and 0.3 m from the walls to follow the ASHRAE Standard 55 definition [3]. Within the occupied zone, the maximum and minimum temperatures as well as the maximum velocity were documented and used in the comparison between the configurations.

8.3.1 Beam Orientation

The results of the beam orientation tests for equivalent cooling capacities of Beam Positions 1-4 for thermal manikins positioned symmetrically and asymmetrically revealed that the beam position impacted the temperature and velocity distributions. The temperature distributions of both configurations of heat sources with Beam Positions 1 and 2 are shown in Figure 79 and with Beam Positions 3 and 4 in Figure 80. Likewise, the velocity profiles for cross-sectional planes through the simulation volumes are shown for Beam Positions 1 and 2 in Figure 81 and Beam Positions 3 and 4 in Figure 82. The three-dimensional representations of the thermal plumes generated from the passive chilled beams are shown in Figure 83 and Figure 84, and were calculated with isosurfaces of 21 °C. Generally, the center of the plume fell directly beneath the beam and did not depend on the location of the beam in relation to the heat sources. However,

the balanced flow conditions observed in the symmetric configuration with Beam Position 1 were replicated in the asymmetric configuration by rotating the beam 90°.

The unbalanced flow condition of the asymmetric configuration with Beam Position 1 was characterized by room air circulation created by the beam and the heat sources in the half of the room that contained the thermal manikins. A similar flow condition was observed for the symmetrically configured thermal manikins with Beam Position 2, directly above one row of the thermal manikins. The room air circulation was not limited to one half of the room as in the asymmetric configuration with Beam Position 1, but the flow mixed the entire space with one large rotation from the beam to the floor to the far wall and back to the beam. Additionally, the thermal plume of the asymmetric configuration with Beam Positions 3 and 4 was angled away from the location of the heat sources and cannot be considered uniform along the centerline of the beam.

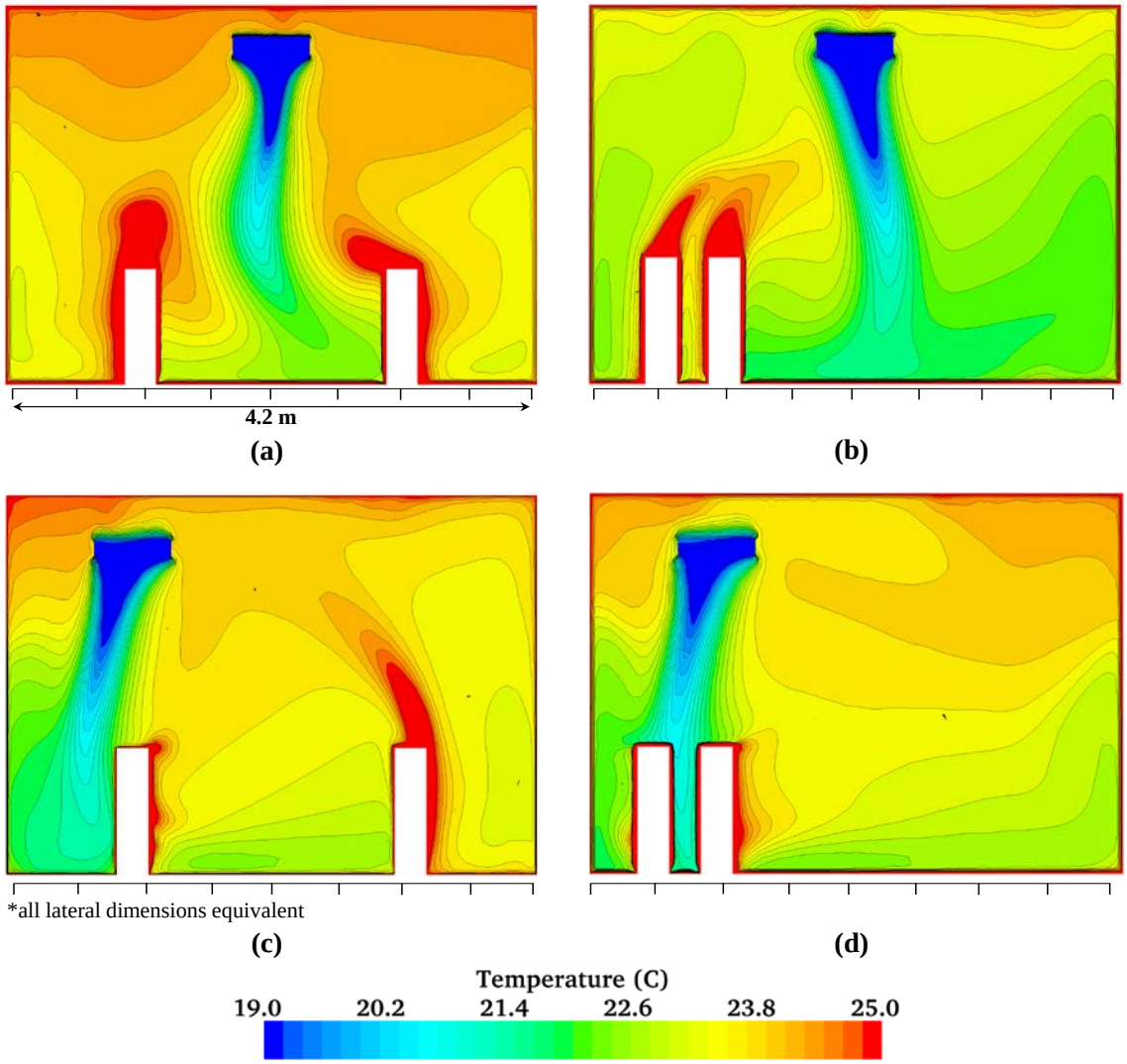

Figure 79. Cross-sectional temperature distribution for the thermal manikins placed (a) symmetrically with BP 1, (b) asymmetrically with BP 1, (c) symmetrically with BP 2, and (d) asymmetrically with BP 2.

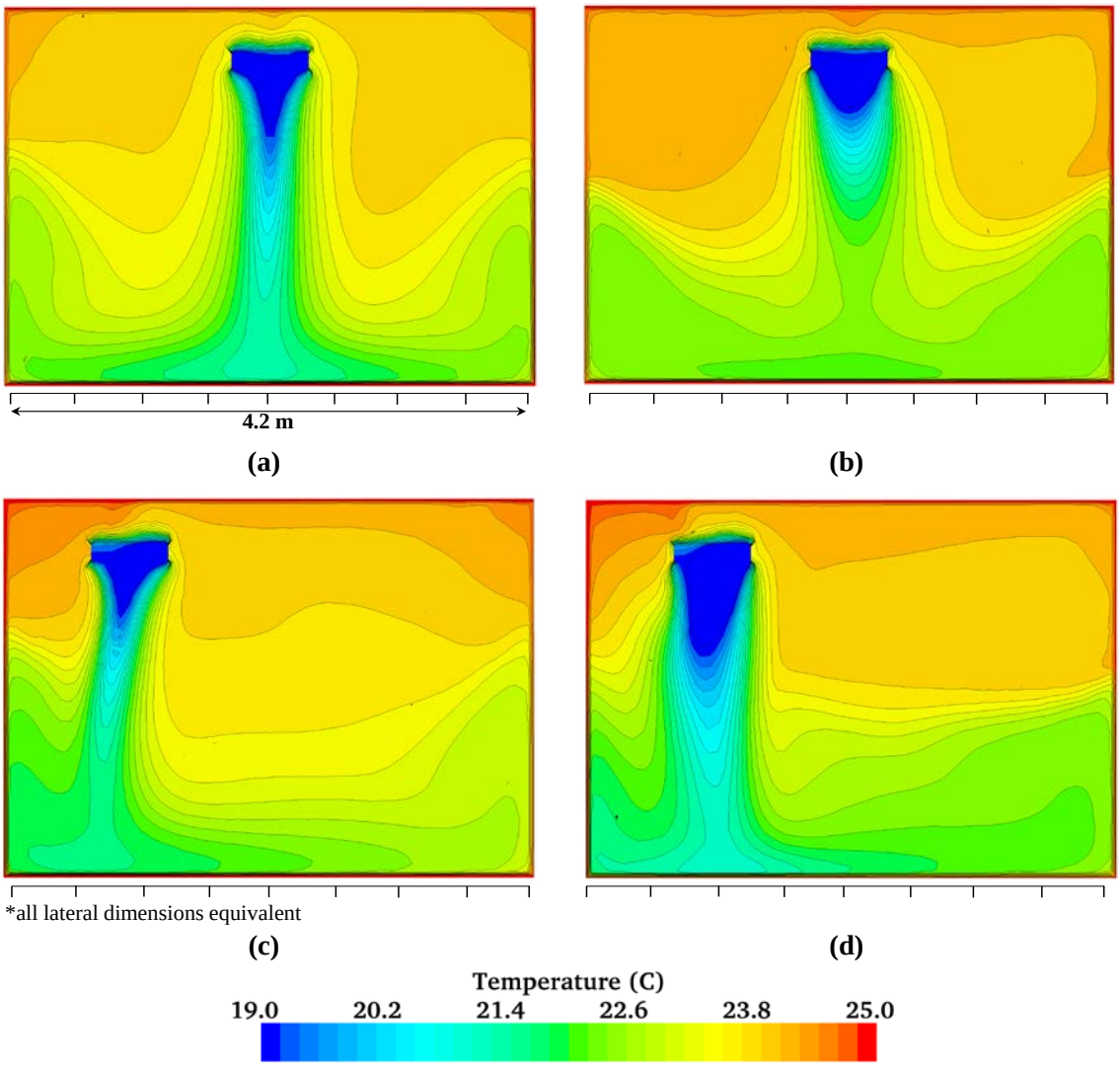

Figure 80. Cross-sectional temperature distribution for the thermal manikins placed (a) symmetrically with BP 3, (b) asymmetrically with BP 3, (c) symmetrically with BP 4, and (d) asymmetrically with BP 4.

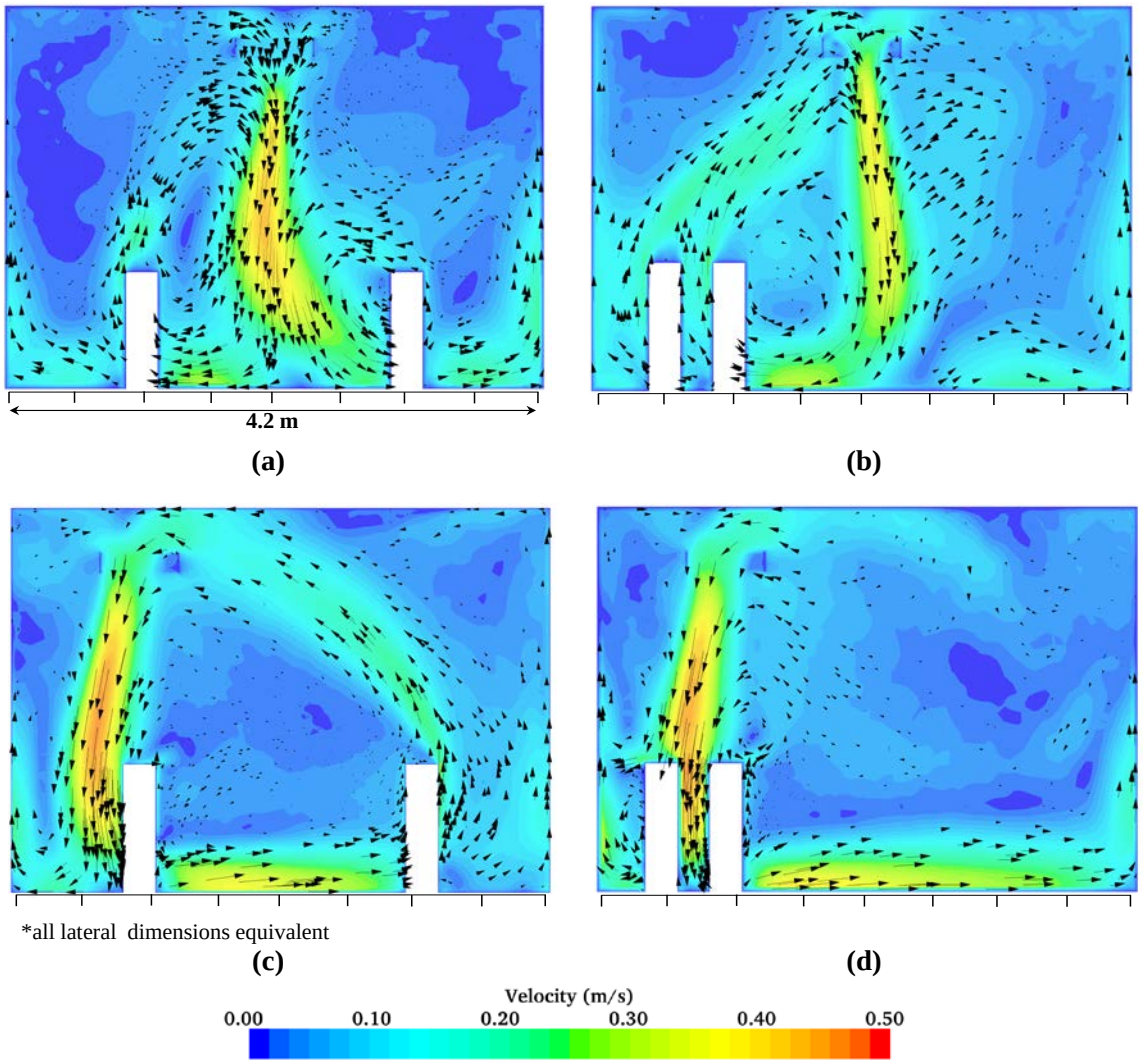

Figure 81. Cross-sectional velocity profiles for the thermal manikins placed (a) symmetrically with BP 1, (b) asymmetrically with BP 1, (c) symmetrically with BP 2, (d) asymmetrically with BP 2.

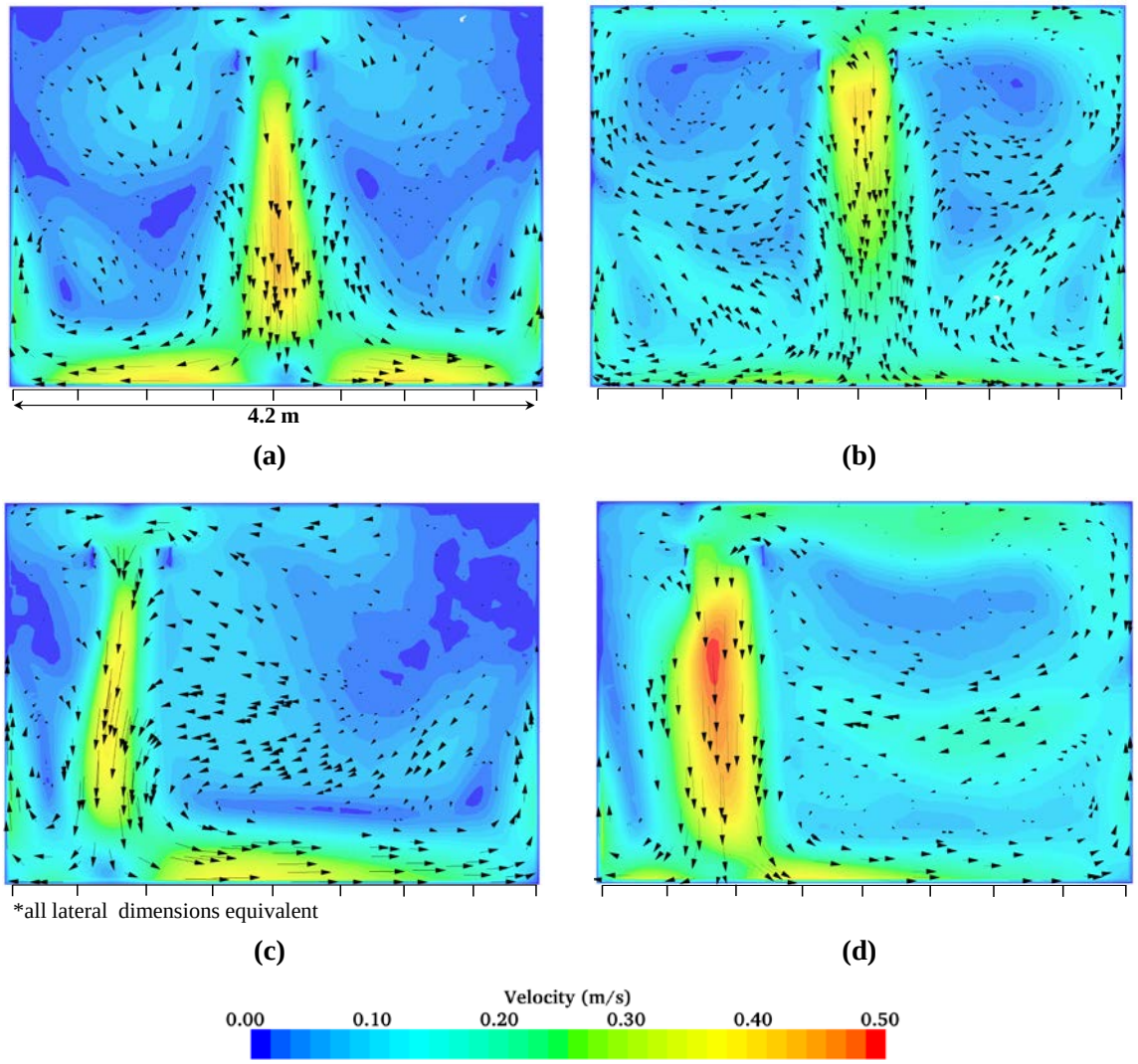

Figure 82. Cross-sectional velocity profiles for the thermal manikins placed (a) symmetrically with BP 3, (b) asymmetrically with BP 3, (c) symmetrically with BP 4, (d) asymmetrically with BP 4.

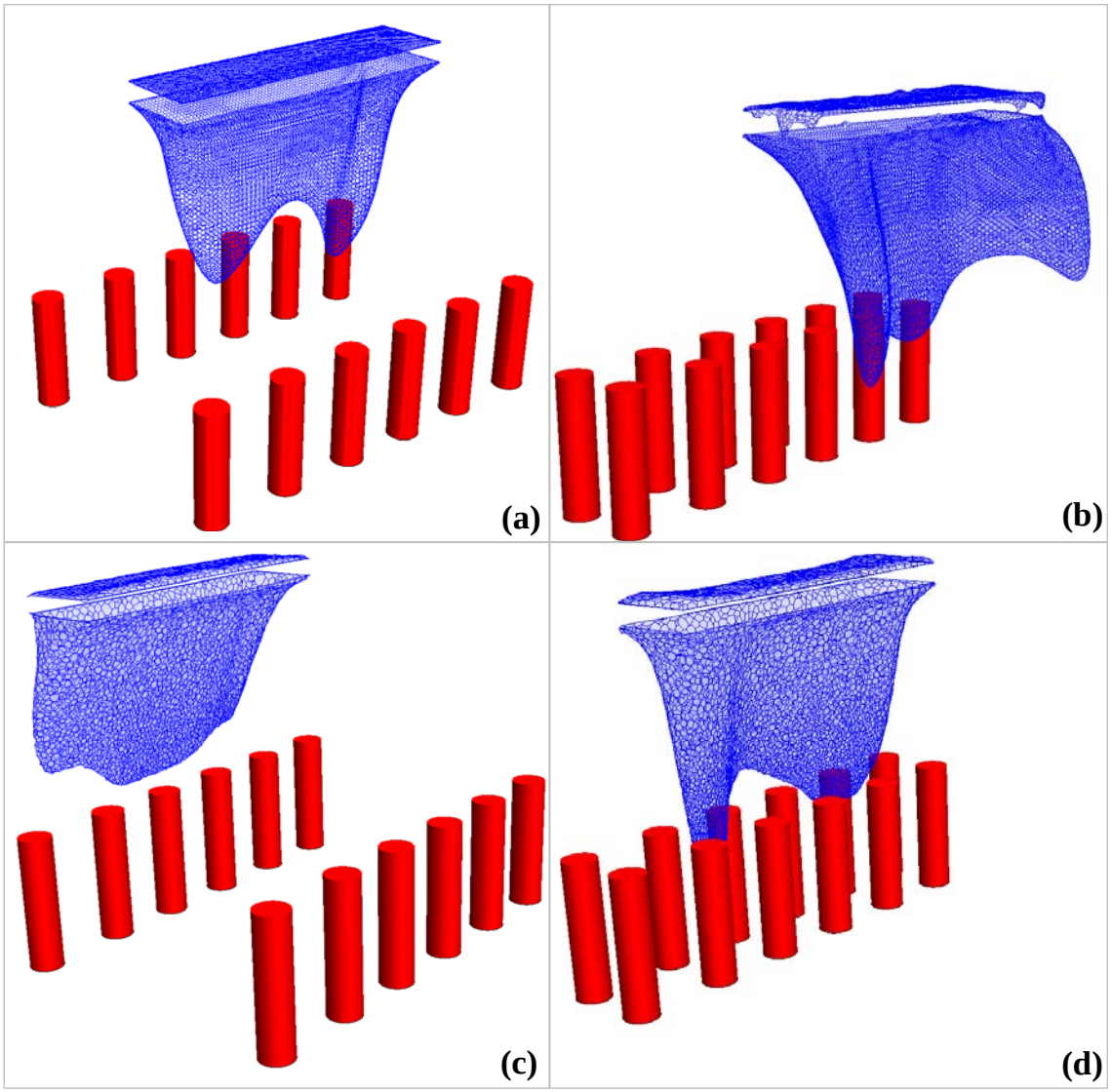

Figure 83. Three-dimensional plumes from the beam (21 °C) for the thermal manikins placed (a) symmetrically with BP 1, (b) asymmetrically with BP 1, (c) symmetrically with BP 2, (d) asymmetrically with BP 2.

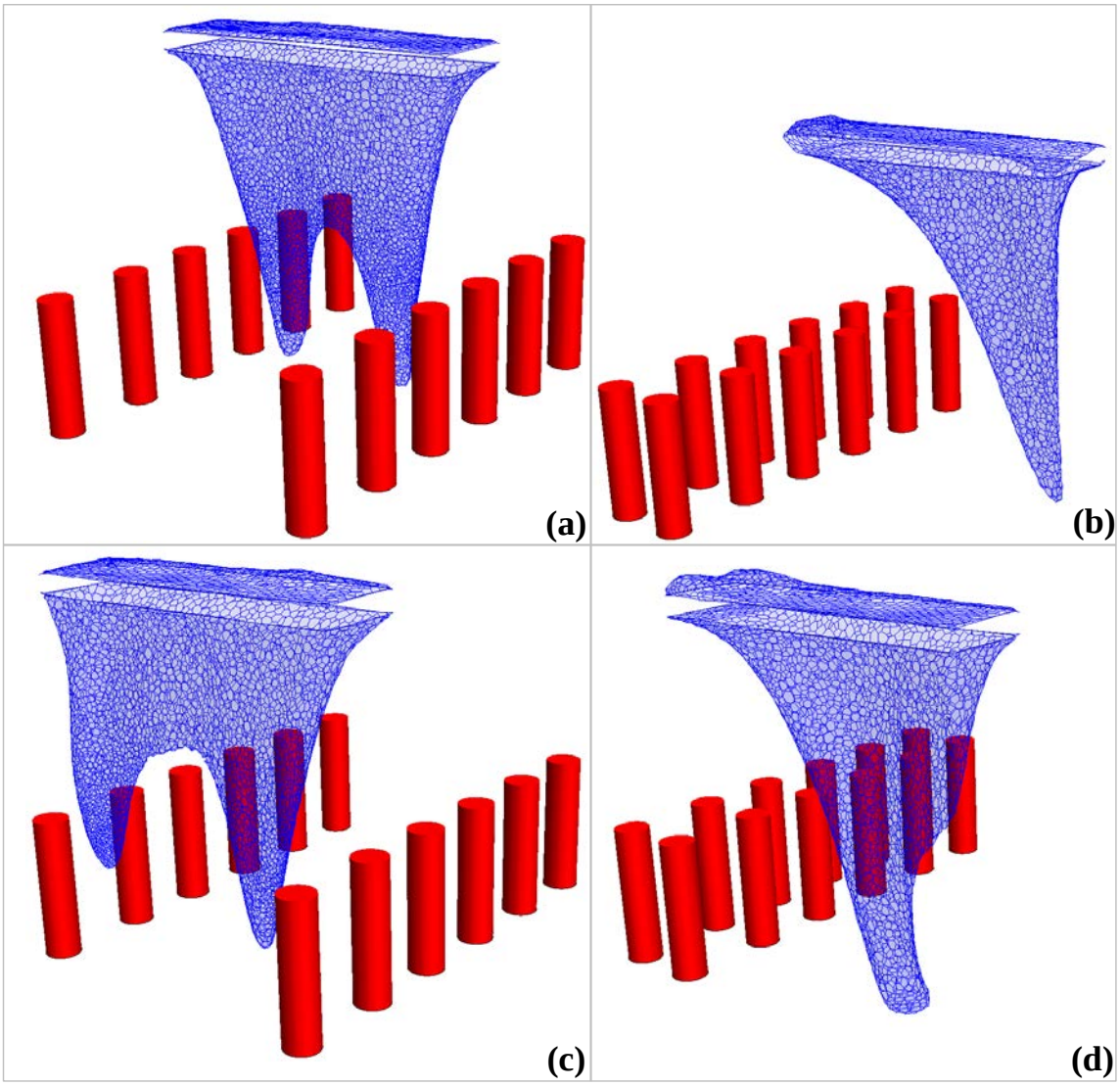

Figure 84. Three-dimensional plumes from the beam (21 °C) for the thermal manikins placed (a) symmetrically with BP 3, (b) asymmetrically with BP 3, (c) symmetrically with BP 4, (d) asymmetrically with BP 4.

The thermal characteristics of the occupied zone for the four beam positions are listed in Table 30. The maximum temperature difference in the occupied zone was highest for Beam Positions 2 and 4, which corresponded to both of the simulations with

asymmetric airflow. The plume centers plotted as a function of the lateral distance from the vertical beam centerline are shown in Figure 85. The configuration changes did not appear to affect the plume locations as the plume center for each configuration did not deviate highly from the vertical centerline.

Table 30. Minimum temperature and maximum temperature and velocity for the symmetric thermal manikin configuration for beam position tests.

	Beam Position 1	*Beam Position 2*	*Beam Position 3*	*Beam Position 4*
Minimum Temperature (°C)	20.9	20.9	20.6	21.6
Maximum Temperature (°C)	26.9	30.5	27.3	31.4
Maximum Velocity (m/s)	0.466	0.460	0.517	0.377
Maximum Temperature Difference (°C)	6.0	9.6	6.7	9.8

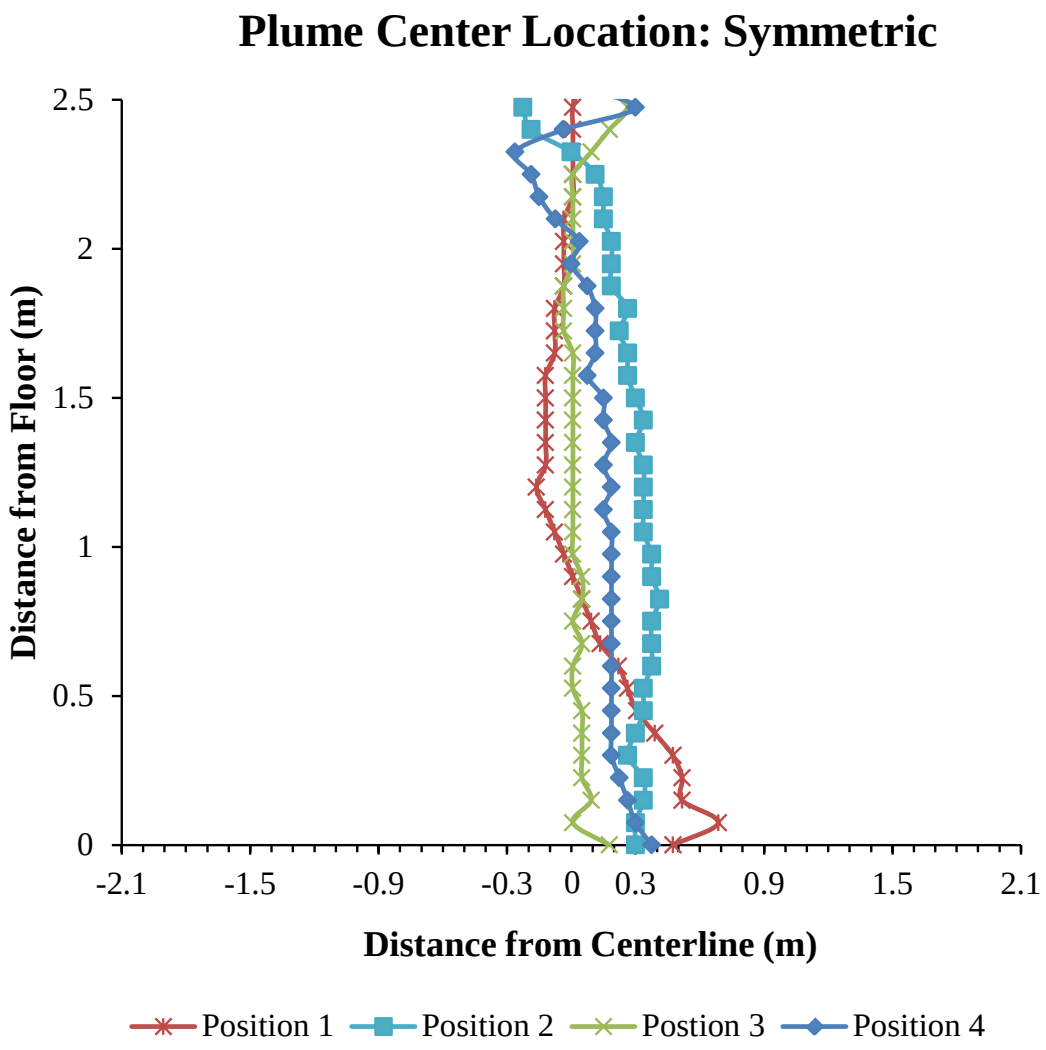

Figure 85. Plume center location as defined by the minimum temperature for the symmetric configuration of thermal manikins for the beam position tests.

From the asymmetric configuration simulations, Beam Position 3 created a maximum velocity 36 % higher than the next highest maximum velocity (Beam Position 4). While the resultant airflow in the space was symmetric once the beam was rotated

90°, the higher velocity created could negatively impact the thermal comfort of occupants.

Table 31. Minimum temperature and maximum temperature and velocity for the asymmetric thermal manikin configuration for beam position tests.

	Beam Position 1	*Beam Position 2*	*Beam Position 3*	*Beam Position 4*
Minimum Temperature (°C)	21.3	21.2	20.3	21.3
Maximum Temperature (°C)	27.4	26.2	26.6	27.0
Maximum Velocity (m/s)	0.387	0.441	0.632	0.466
Maximum Temperature Difference (°C)	6.1	5.0	6.3	5.7

The plume centers for the asymmetric configurations, plotted in Figure 86, show that the deviation from the vertical centerline present in Beam Positions 1 and 3 was reduced when the beam was rotated 90° to Beam Positions 3 and 4. The plume center that deviates most from the vertical centerline, Beam Position 2, is a result of the beam positioned directly above two rows of the thermal manikins. The strength of the heat source plumes was enough to push the beam plume away from its natural descent, directly beneath the beam outlet.

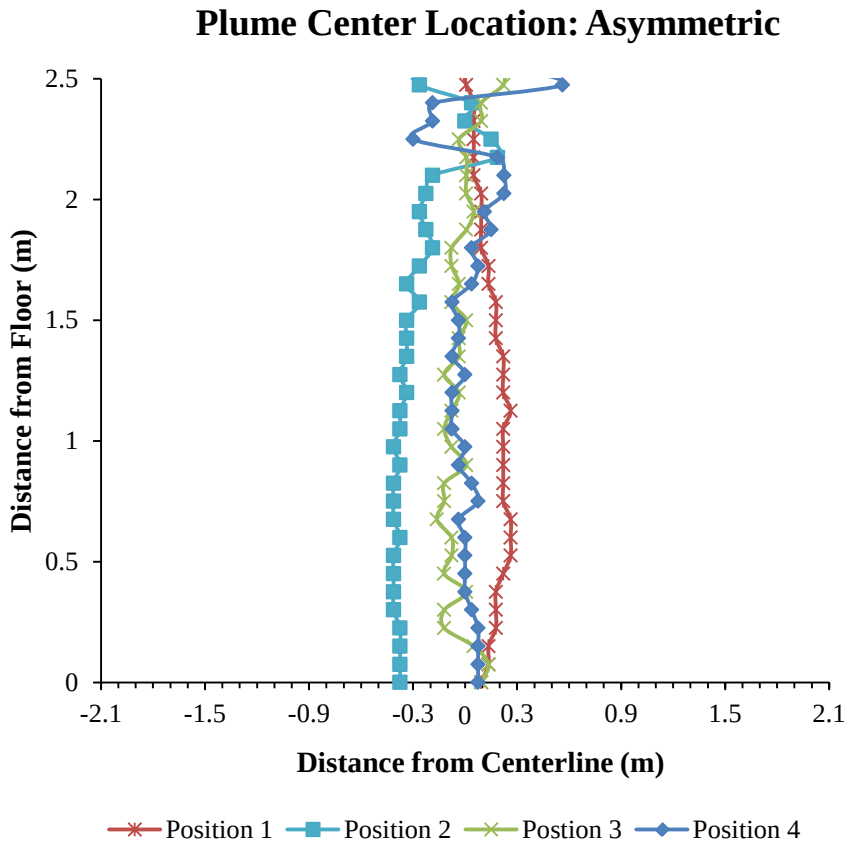

Figure 86. Plume center location as defined by the minimum temperature for the asymmetric configuration of thermal manikins for the beam position tests.

8.3.2 Wall Length, Ceiling and Beam Heights

The capacity of the beam for the extended walls, raised ceiling and raised beam tests was calculated to be approximately similar for all tests with the same thermal manikin configuration. The results of Figures 87-92 are similar as the temperature distributions, velocity profiles, and plume shapes did not vary significantly for the thermal manikins arranged equivalently for the different inside dimensions. For the asymmetric configuration with the beam in Beam Position 1, the reduced cooling capacity of the beam was found to be a result of the inlet air conditions that increased the amount of warmer air circulated around the beam and not through it. In Figures 87-90 the temperature profiles and velocity distributions of all the tests for the asymmetric configuration of thermal manikins revealed a similar result with room airflow that entered the above-the-beam region from the side closest to the thermal manikins, where room air circulation was limited to the half of the room with the thermal manikins.

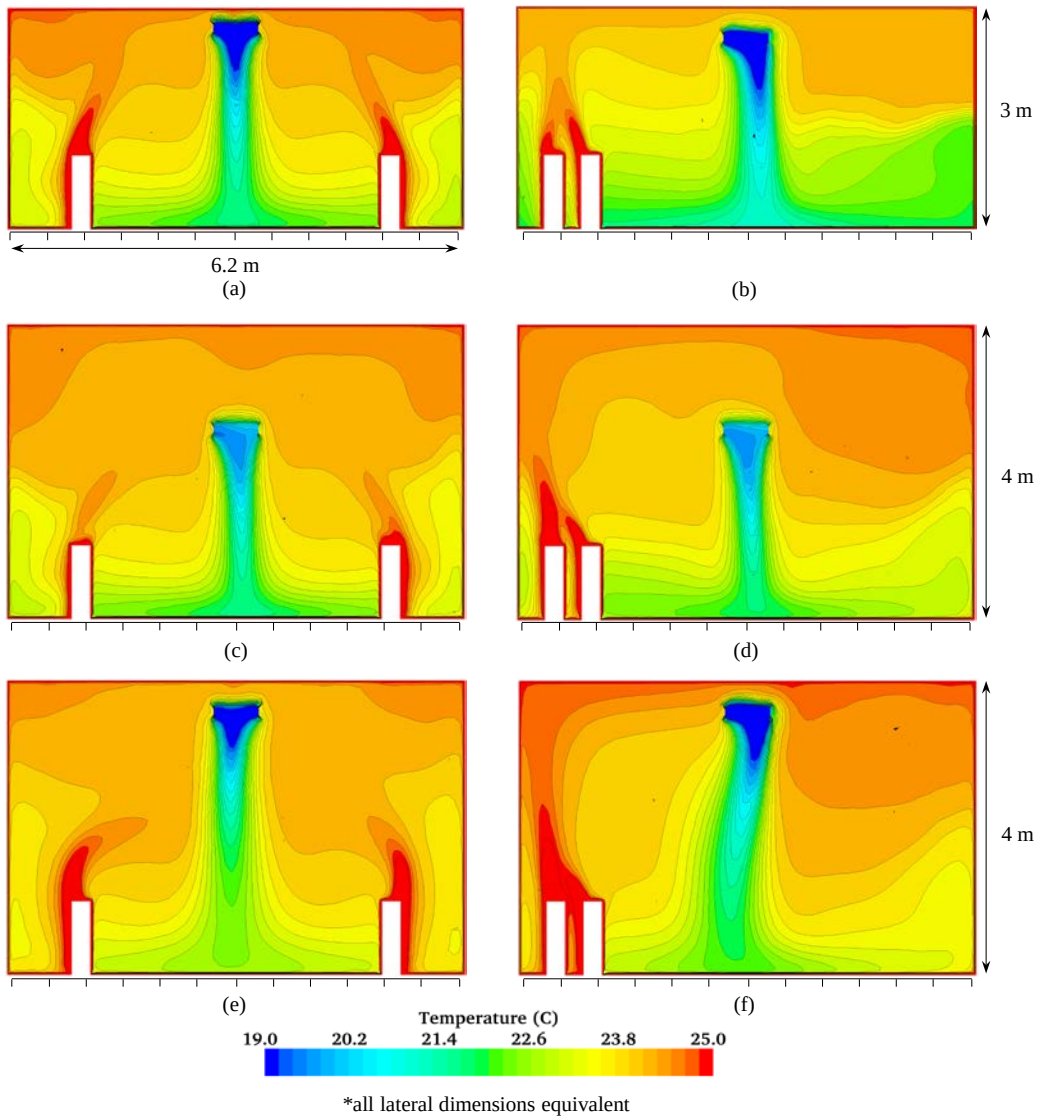

Figure 87. Cross-sectional temperature distribution for the thermal manikins placed (a) symmetrically with the walls extended, (b) asymmetrically with the walls extended, (c) symmetrically with the walls extended and ceiling raised, (d) asymmetrically with the walls extended and ceiling raised, (e) symmetrically with the walls extended and ceiling and beam raised, and (f) asymmetrically with the walls extended and ceiling and beam raised.

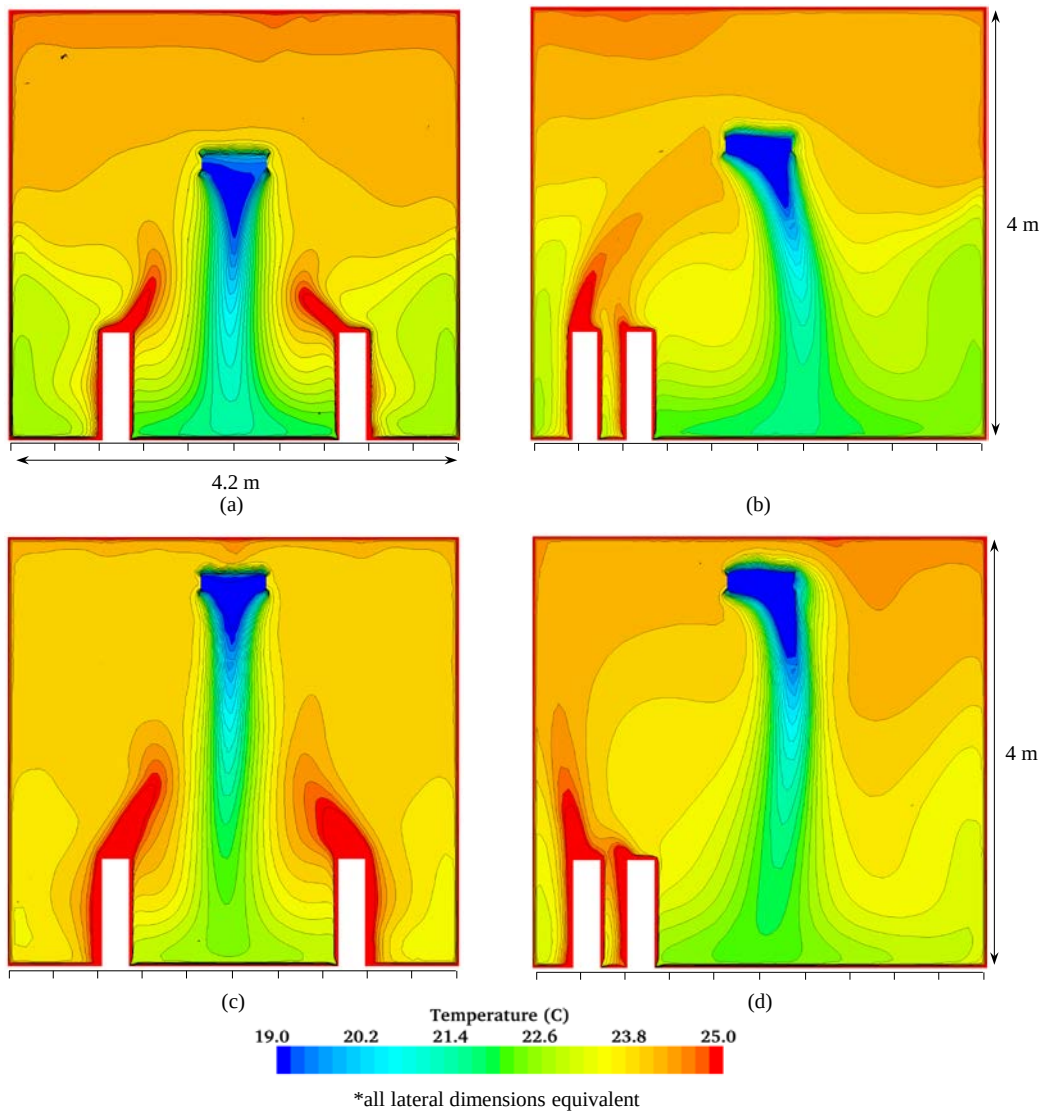

Figure 88. Cross-sectional temperature distribution for the thermal manikins placed, (a) symmetrically with the ceiling raised, (b) asymmetrically with the ceiling raised, (c) symmetrically with the ceiling and beam raised, and (d) asymmetrically with the ceiling and beam raised.

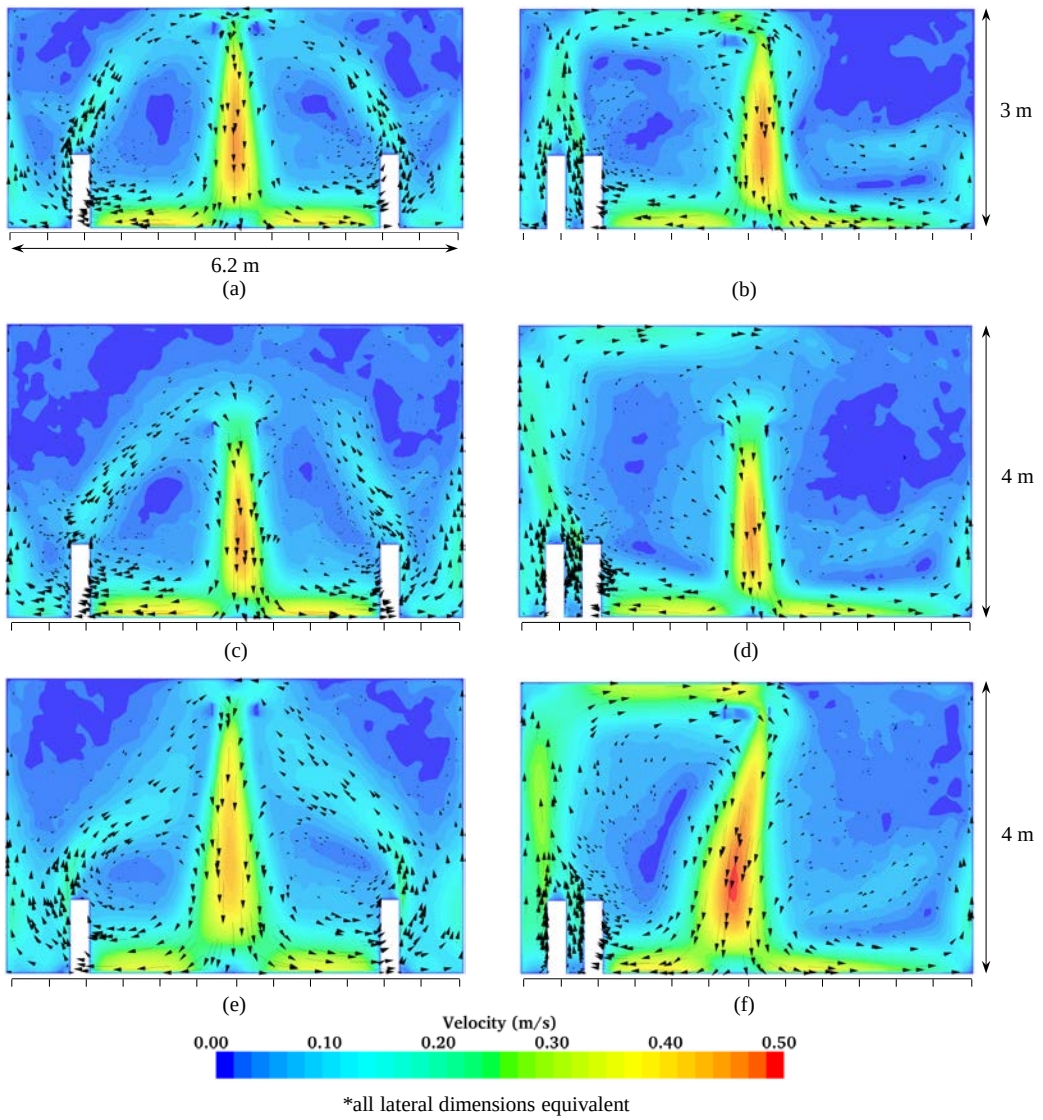

Figure 89. Cross-sectional velocity profiles for the thermal manikins placed (a) symmetrically with the walls extended, (b) asymmetrically with the walls extended, (c) symmetrically with the walls extended and ceiling raised, (d) asymmetrically with the walls extended and ceiling raised, (e) symmetrically with the walls extended and ceiling and beam raised, and (f) asymmetrically with the walls extended and ceiling and beam raised.

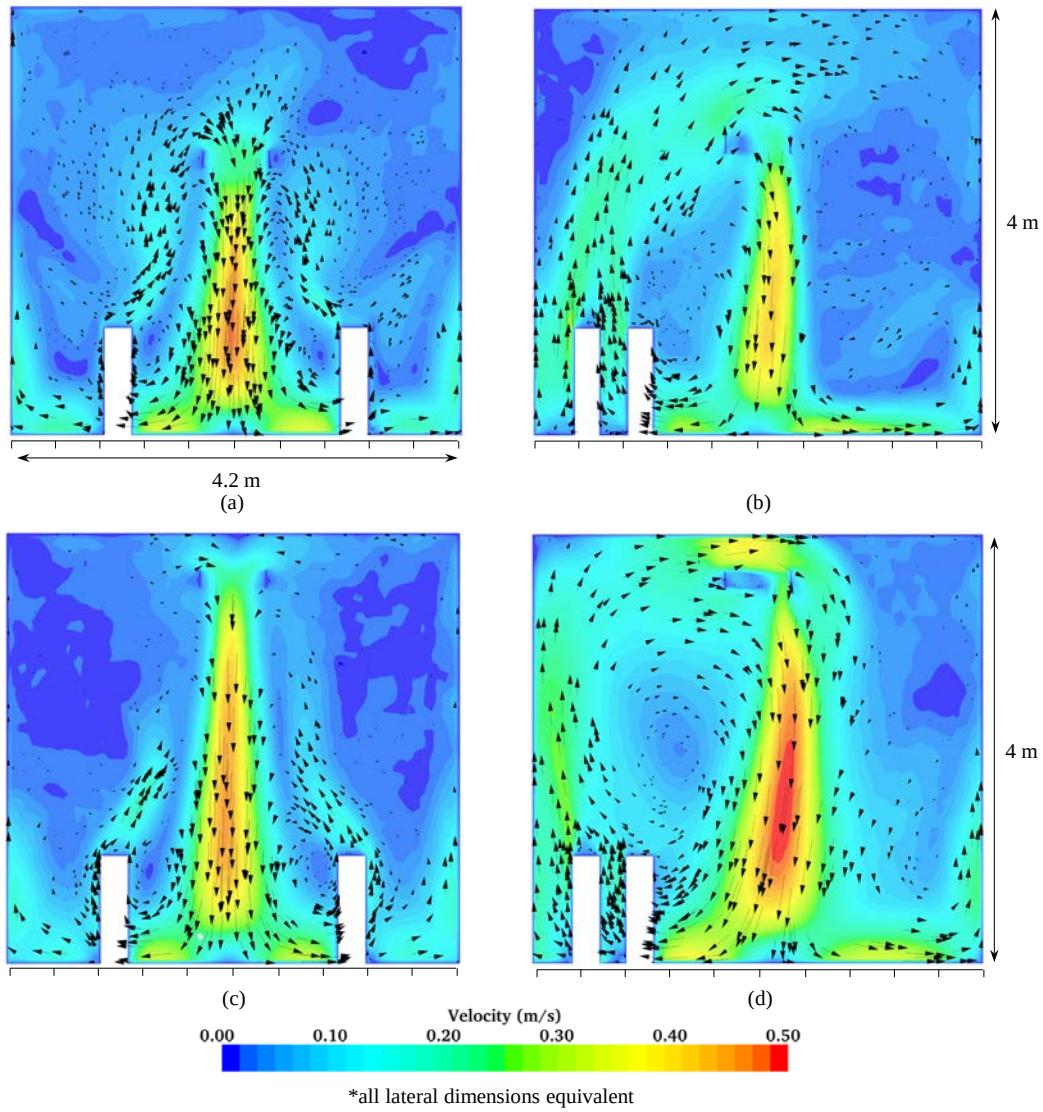

Figure 90. Cross-sectional-velocity profiles for the thermal manikins placed, (a) symmetrically with the ceiling raised, (b) asymmetrically with the ceiling raised, (c) symmetrically with the ceiling and beam raised, and (d) asymmetrically with the ceiling and beam raised.

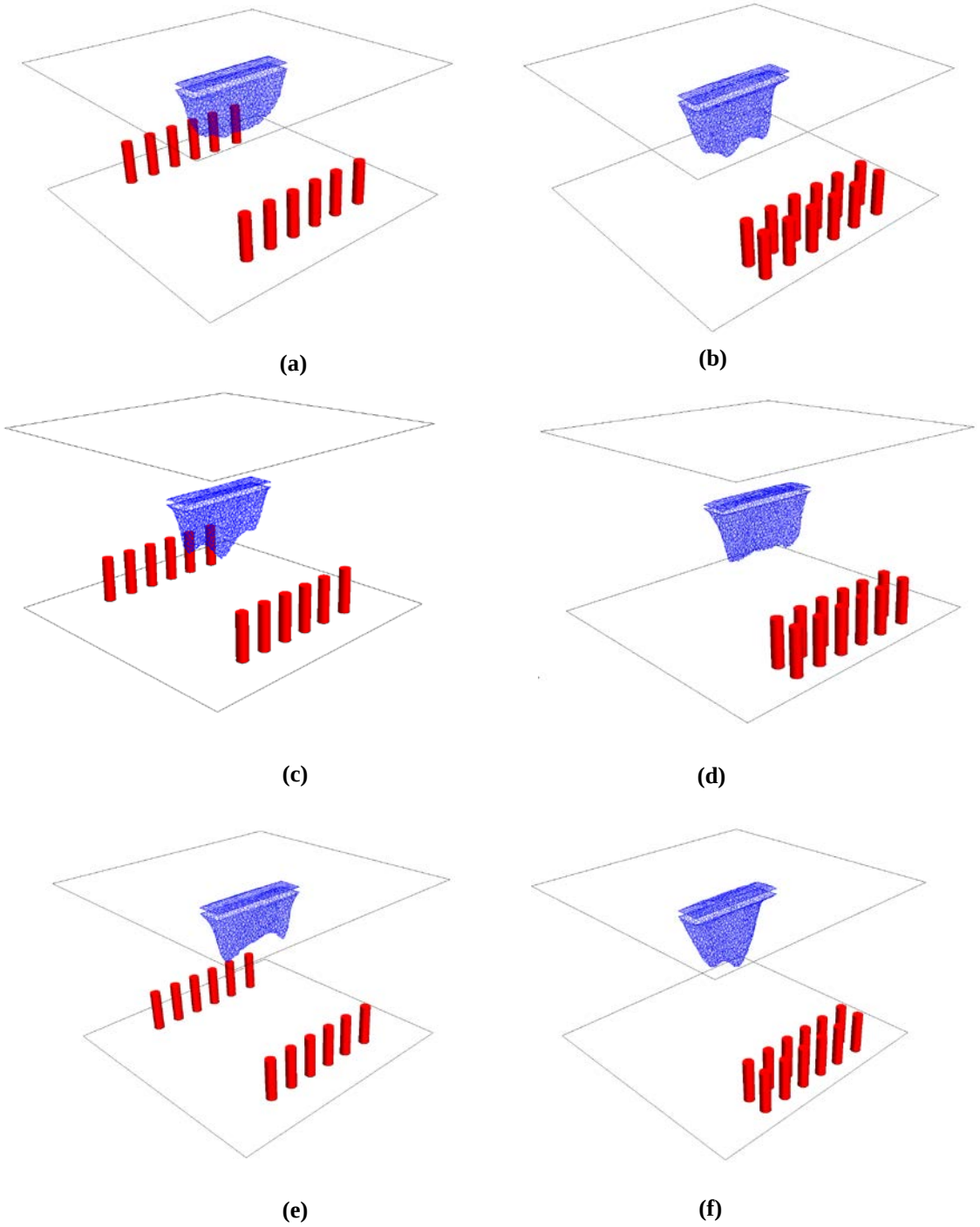

Figure 91. Three-dimensional plumes from the beam (21 °C) for the thermal manikins placed (a) symmetrically with the walls extended, (b) asymmetrically with the walls extended, (c) symmetrically with the walls extended and ceiling raised, (d) asymmetrically with the walls extended and ceiling raised, (e) symmetrically with the walls extended and ceiling and beam raised, (f) asymmetrically with the walls extended and ceiling and beam raised.

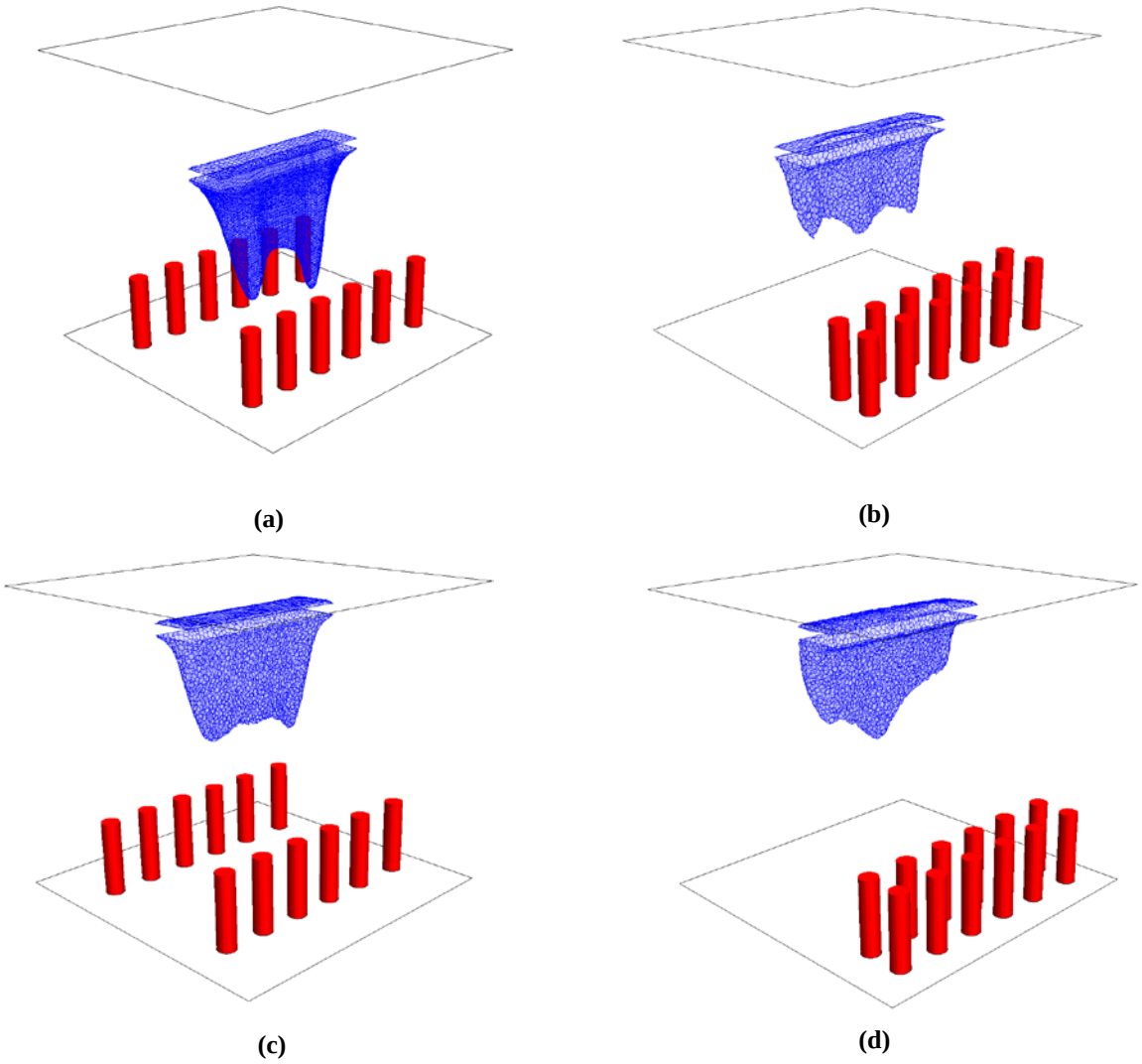

Figure 92. Three-dimensional plumes from the beam (21 °C) for the thermal manikins placed (a) symmetrically with the ceiling raised, (b) asymmetrically with the ceiling raised, (c) symmetrically with the ceiling and beam raised, and (d) asymmetrically with the ceiling and beam raised.

The room airflow characteristics listed in Table 32 for the symmetric configuration of thermal manikins show that for the simulations of higher ceilings with the beam positioned 2.5 m from the floor, the maximum temperature difference in the

occupied zone is larger than for other tests. Additionally, the maximum velocity in the occupied zone was relatively constant between each test within the range of 0.44 m/s to 0.51 m/s.

Table 32. Minimum temperature and maximum temperature and velocity for the symmetric thermal manikins configuration for the extended walls, raised ceiling, and raised beam tests.

	Base	*Extended Walls*	*Extended Walls, Raised Ceiling*	*Extended Walls, Raised Ceiling, Raised Beam*	*Raised Ceiling*	*Raised Ceiling, Raised Beam*
Minimum Temperature (°C)	20.9	21.3	20.9	22.4	20.6	22.0
Maximum Temperature (°C)	26.9	27.0	27.9	26.6	28.2	30.0
Maximum Velocity (m/s)	0.466	0.466	0.465	0.439	0.508	0.482
Maximum Temperature Difference (°C)	6.0	5.7	7.0	4.2	7.6	8.0

The minimum temperature location in relation to the beam centerline and vertical distance from the floor was plotted for each scenario of the symmetrically arranged thermal manikins in Figure 93. The plume center location shows little variance between the different simulations and deviated at most 20 cm from the beam centerline in the occupied zone.

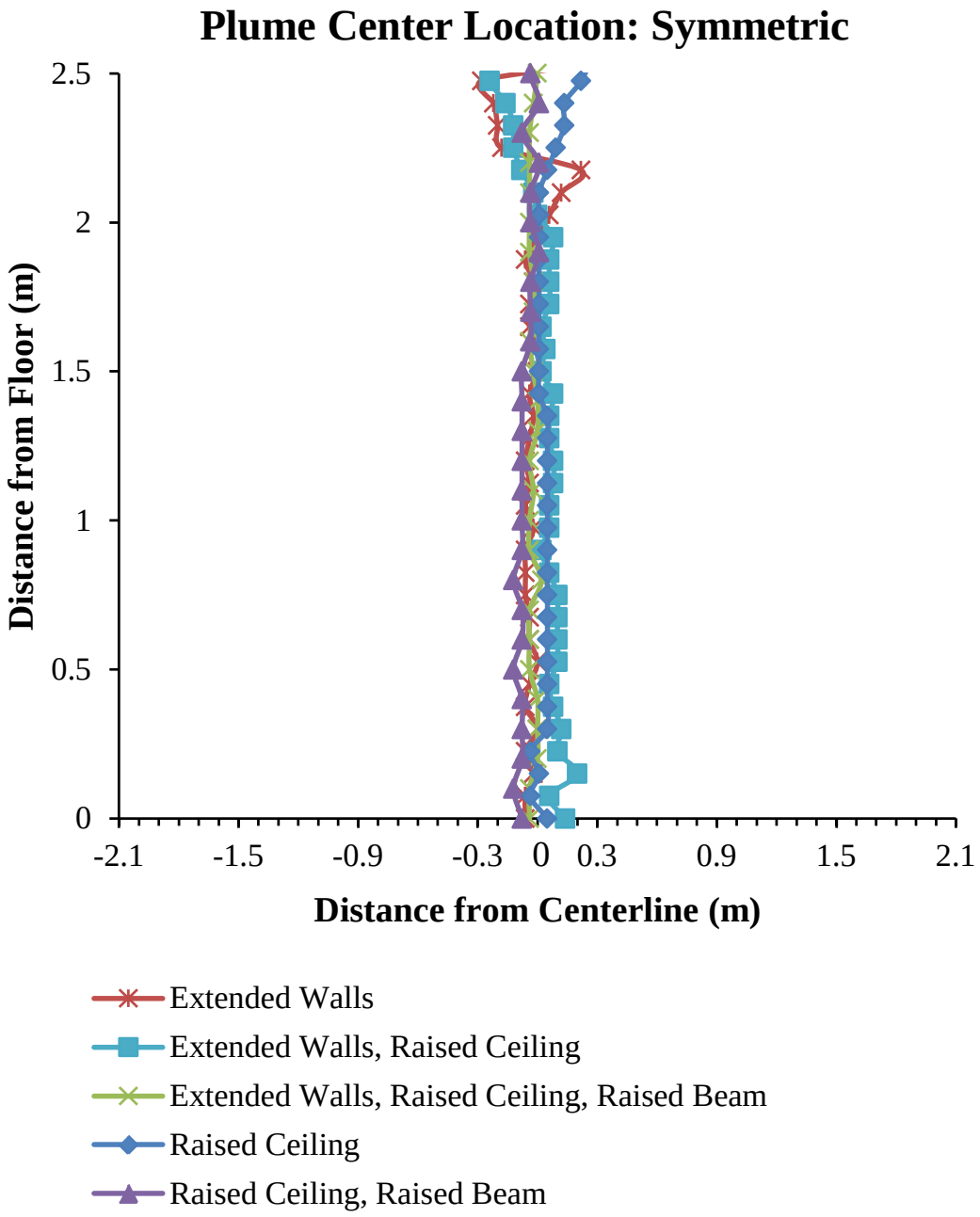

Figure 93. Plume center location as defined by the minimum temperature for the symmetric configuration of thermal manikins for the extended walls, raised ceiling, and raised beam tests.

For the asymmetric configuration, the airflow characteristics listed in Table 33 for the occupied zone show that the dimensions of the room and the beam height had little impact on the maximum temperature difference and maximum velocity in the occupied zone, the exception being the less than three degrees maximum temperature difference throughout the occupied zone for the extended walls and raised ceiling test.

The minimum temperature location in relation to the beam centerline and vertical distance from the floor was plotted for each scenario of the asymmetrically arranged thermal manikins in Figure 94. When compared to the results of the symmetric thermal manikin simulations, more variance between simulations existed in the plume location and a higher maximum deviation from the centerline (30 cm) in the occupied zone was calculated.

Table 33. Minimum temperature and maximum temperature and velocity for the asymmetric thermal manikins configuration for the extended walls, raised ceiling, and raised beam tests.

	Base	*Extended Walls*	*Extended Walls, Raised Ceiling*	*Extended Walls, Raised Ceiling, Raised Beam*	*Raised Ceiling*	*Raised Ceiling, Raised Beam*
Minimum Temperature (°C)	21.3	21.3	22.4	21.6	21.6	21.1
Maximum Temperature (°C)	27.4	27.6	25.2	28.8	28.1	28.3
Maximum Velocity (m/s)	0.387	0.411	0.441	0.536	0.433	0.479
Maximum Temperature Difference (°C)	6.1	6.3	2.8	7.2	6.5	7.2

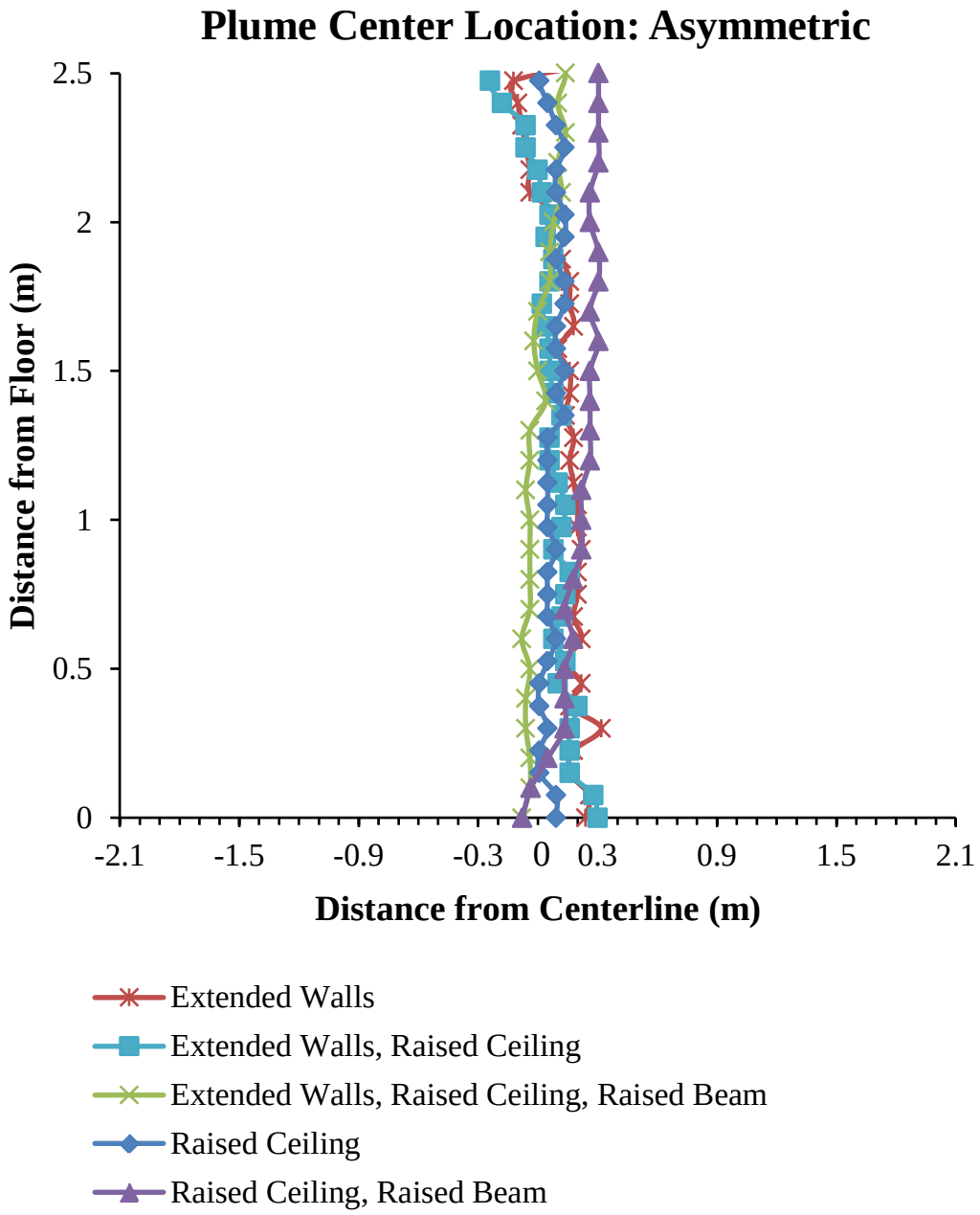

Figure 94. Plume center location as defined by the minimum temperature for the asymmetric configuration of thermal manikins for the extended walls, raised ceiling, and raised beam tests.

8.3.3 C-Configuration of Thermal Manikins

The temperature distributions, velocity profiles, and three-dimensional plumes for the thermal manikins in Configuration C are shown in Figures 95-97, respectively. The plumes from Beam Positions 1 and 3 displayed higher velocities than from the beam positions with a portion of the beam directly above the heat sources. The beam plumes descended directly beneath the beam outlet and the generated flow patterns were symmetric in the space. For Beam Positions 2 and 4, with part of the beam located directly above the heat sources, the center of the beam plume was located at an angle away from the vertical beam centerline displaced by the heated plume generated from the thermal manikins.

The test configurations with the highest velocity and largest temperature difference in the occupied zone were Beam Positions 3 and 4, with the beam oriented perpendicular to the rows of heat sources. The results are listed in Table 34. Beam Position 2 for the thermal manikins in the C-configuration can be considered the most well-mixed of the room spaces with the lowest maximum temperature difference. In contrast, the thermal characteristics of the room air were most varied with the beam in Beam Position 3, the test with the highest maximum velocity and largest temperature difference.

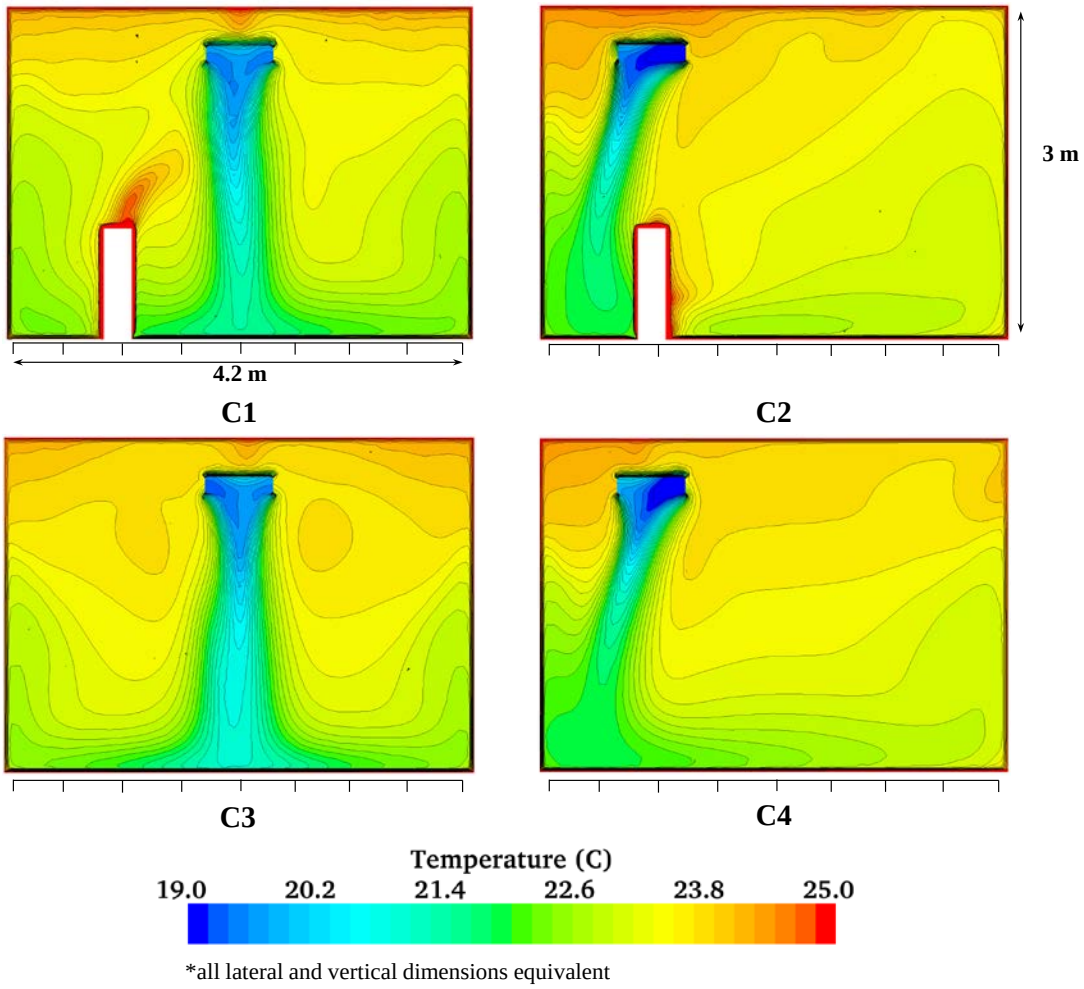

Figure 95. Temperature profiles for BPs 1-4 cooling the thermal manikins in the C-configuration.

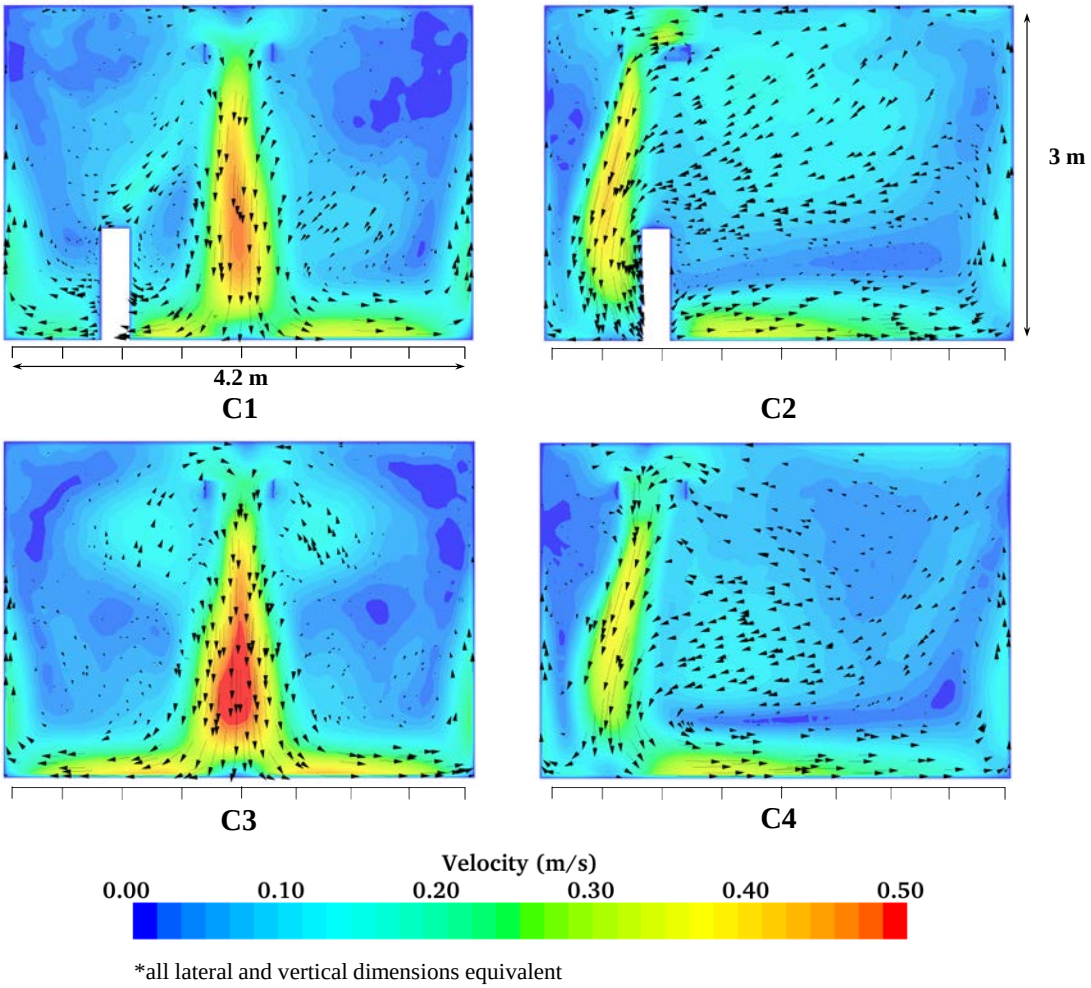

Figure 96. Velocity distributions for BPs 1-4 cooling the thermal manikins in the C-configuration.

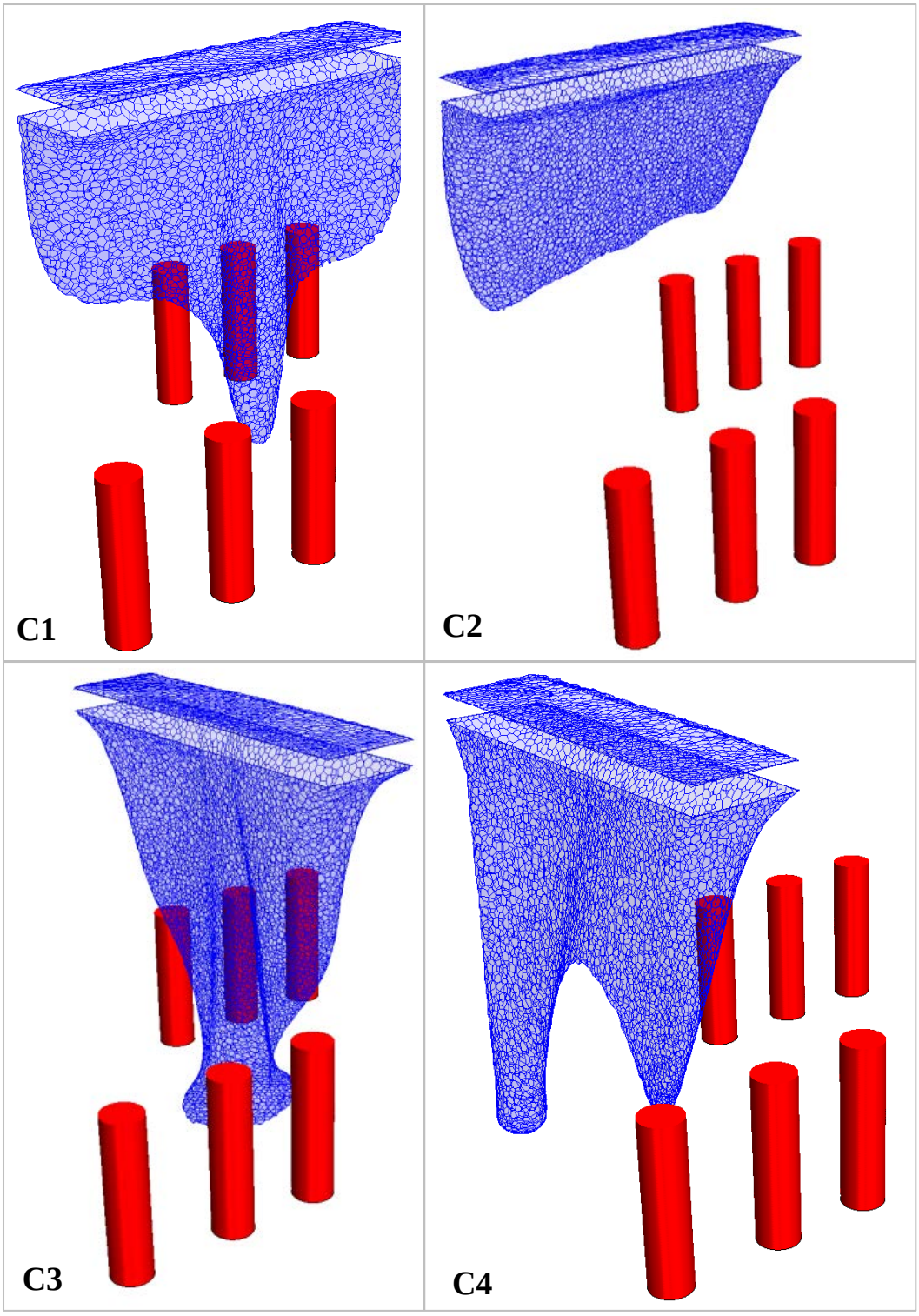

Figure 97. Three-dimensional plumes from the beam (21 °C) in BPs 1-4 cooling the thermal manikins in the C-configuration.

Table 34. Minimum temperature and maximum temperature and velocity for the Test C configuration.

	C1	*C2*	*C3*	*C4*
Minimum Temperature (°C)	20.7	20.8	20.1	21.2
Maximum Temperature (°C)	29.3	26.9	31.7	31.7
Maximum Velocity (m/s)	0.427	0.431	0.509	0.450
Maximum Temperature Difference (°C)	8.6	6.1	11.6	10.5

The minimum temperature location in relation to the beam centerline and vertical distance from the floor was plotted for each scenario of the C-configuration tests in Figure 98. The plume center closely follows the vertical centerline in all configurations except for Beam Position 2. In this position, the beam is directly above one row of the thermal manikins and the effect of the heat source plumes was to displace the beam plume, as observed by the center of the plume location as a function of distance from the floor.

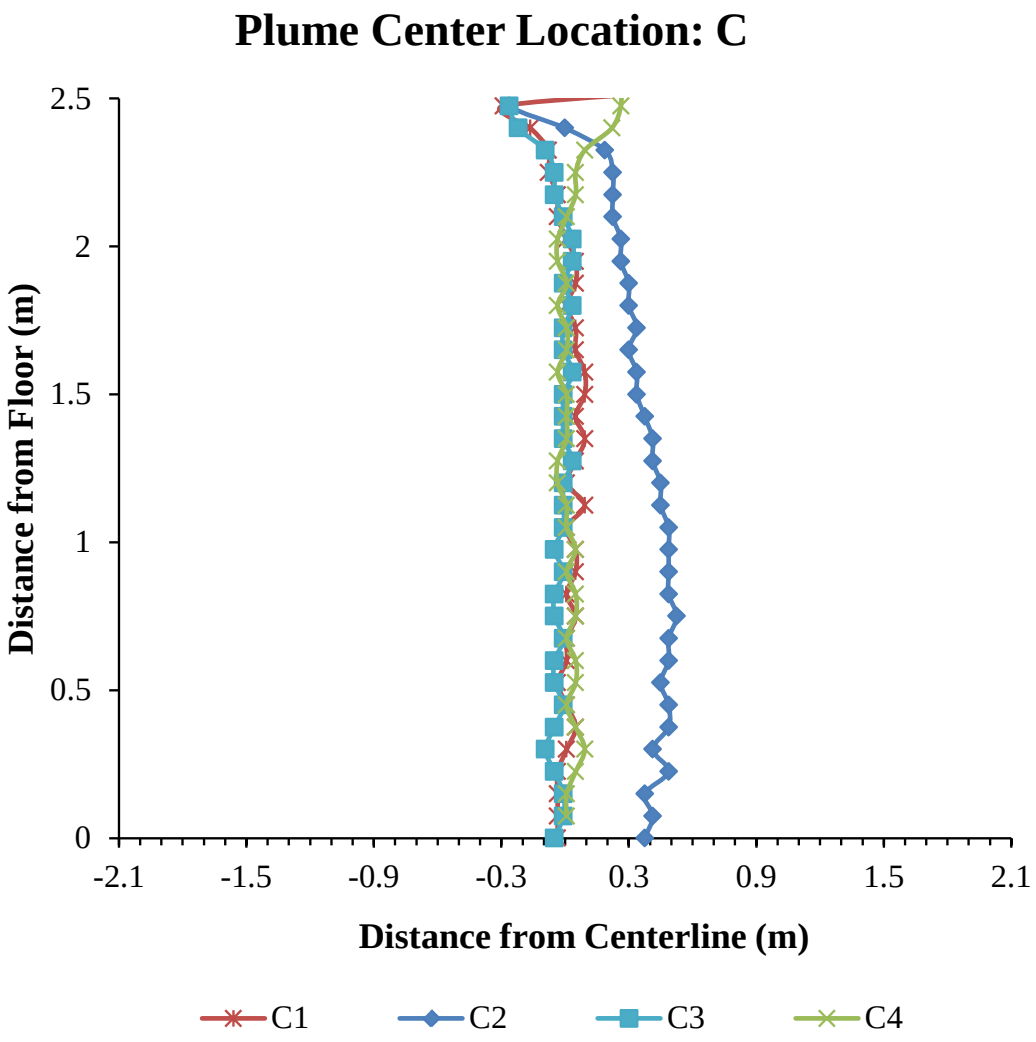

Figure 98. Plume center location for the C-configuration tests.

8.3.4 D-Configuration of Thermal Manikins

The temperature distributions, velocity profiles, and three-dimensional plumes for the thermal manikins in Configuration D are shown for the four beam positions in Figures 99-101, respectively. The results were similar to the C-configuration with symmetric airflow patterns for the beam positions centered in the room. Additionally,

beam Beam Positions 1 and 3 also resulted in higher plume velocities. The shape of the plume was noticeably dissimilar between the four beam positions. The beam in Beam Positions 3 and 4 was located perpendicular to the rows of thermal manikins and was closest to the thermal manikins in Beam Position 3. The plume from the beam in Beam Position 3 was drawn in towards the middle of the beam, whereas, the plume from the beam in Beam Position 4 branched out at the ends closest to the thermal manikin rows. The heat source thermal plumes affected the beam plume in both scenarios. For Beam Position 3, closest to the rows, the heat source plumes displaced the beam plume towards the middle of the room. For Beam Position 4, the heat source plumes were too far away to affect the shape of the beam plume in a similar way. The airflow at the beam inlet was greatest in the locations closest to the rows of thermal manikins. The higher mass flow rate of warmer air created localized areas of higher volumetric cooling within the beam region. The resulting beam plume shape reflected the areas within the beam of higher localized cooling capacity.

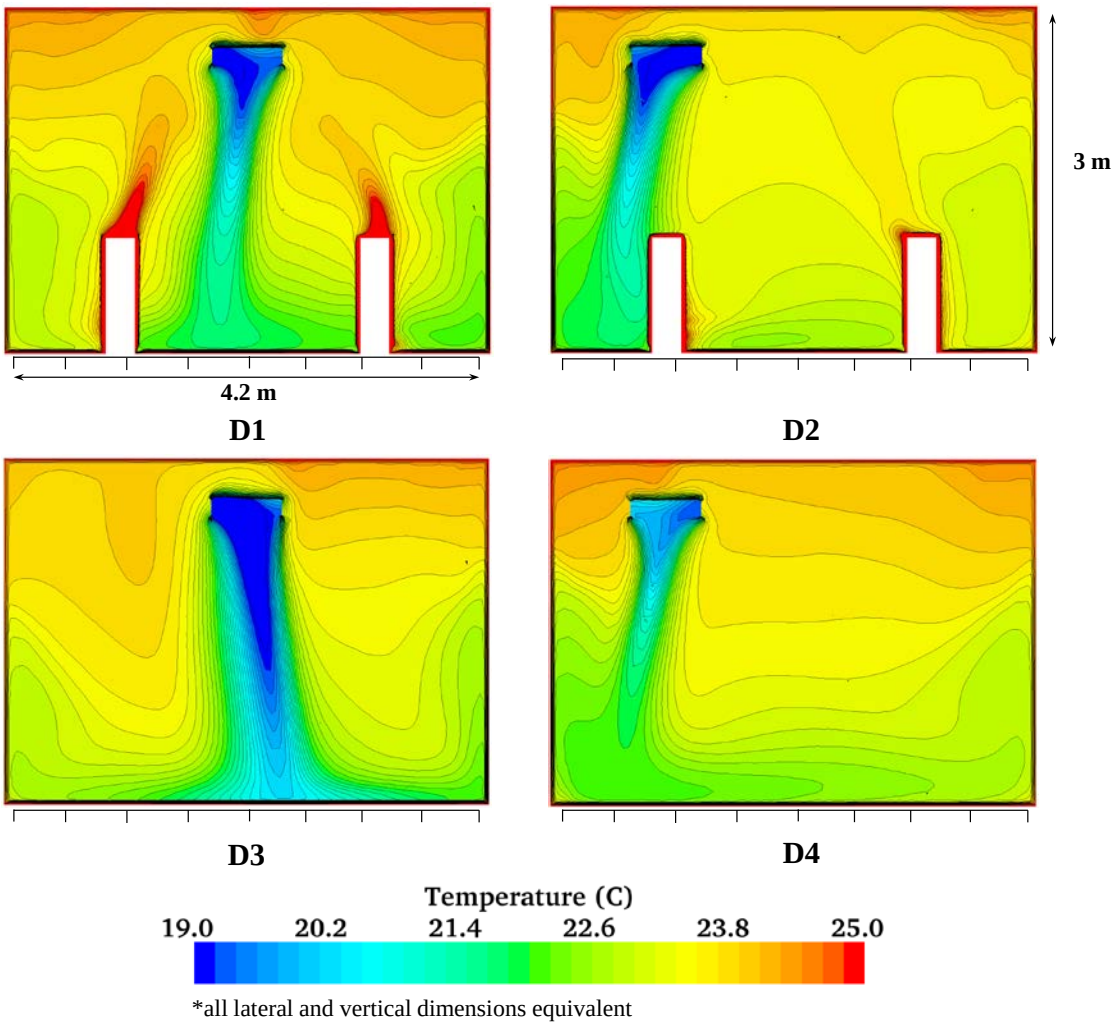

Figure 99. Temperature profiles for BPs 1-4 cooling the thermal manikins in the D-configuration.

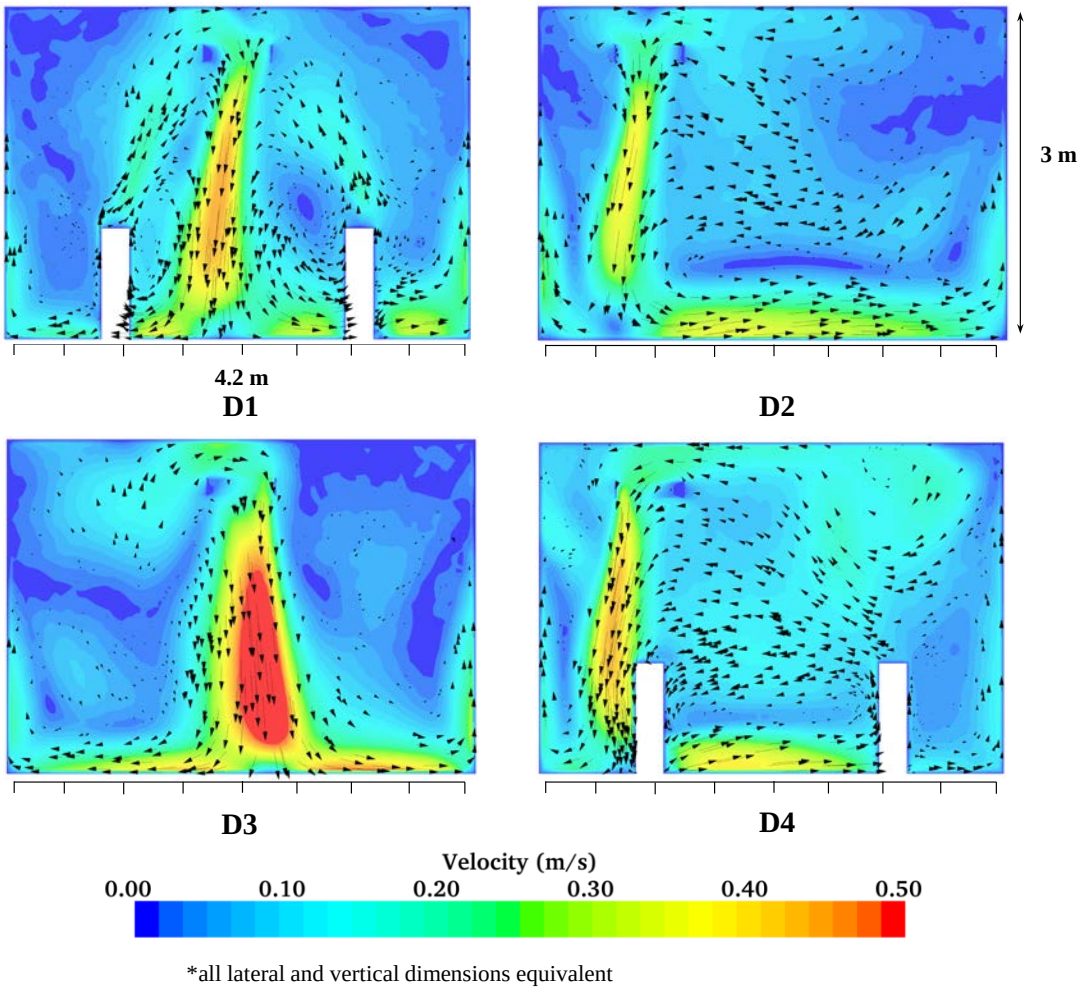

Figure 100. Velocity distributions for BPs 1-4 cooling the thermal manikins in the D-configuration.

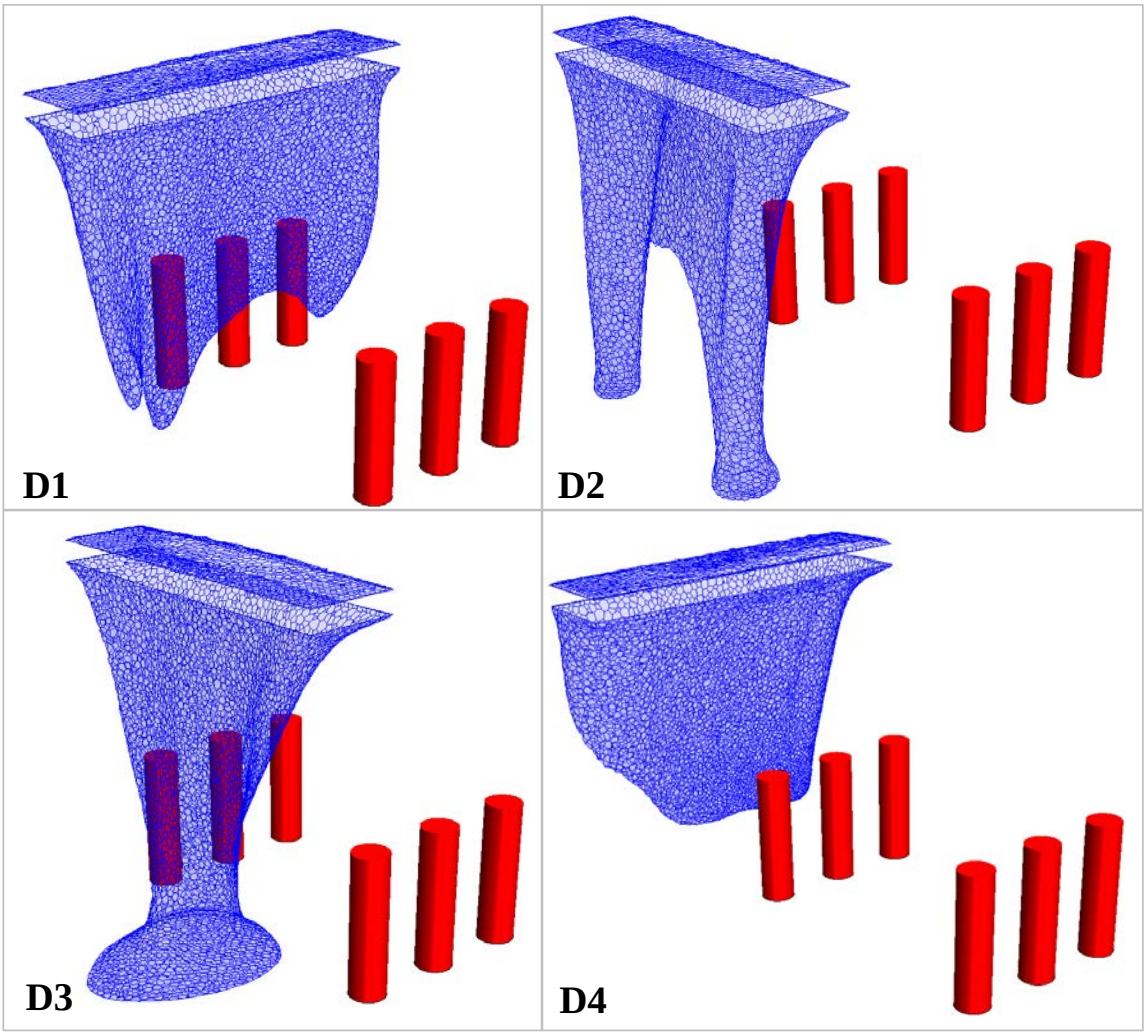

Figure 101. Three-dimensional plumes from the beam (21 °C) in BPs 1-4 cooling the thermal manikins in the D-configuration.

The airflow characteristics of the occupied zone, listed in Table 35, show that the beam orientations located at the center of the room produced the highest maximum temperature differences in the room air. The beam in Beam Position 2 created the most well-mixed occupied zone with the smallest maximum temperature difference. As in the

C-configuration tests, the beam in Beam Position 3 resulted in the highest maximum temperature difference and the highest maximum velocity in the occupied zone.

Table 35. Minimum temperature and maximum temperature and velocity for the Test D configuration.

	D1	*D2*	*D3*	*D4*
Minimum Temperature (°C)	20.6	20.5	19.5	21.4
Maximum Temperature (°C)	30.9	25.0	30.6	29.9
Maximum Velocity (m/s)	0.442	0.451	0.531	0.427
Maximum Temperature Difference (°C)	10.3	4.5	11.1	8.5

The minimum temperature location in relation to the beam centerline and vertical distance from the floor was plotted for each scenario of the D-configuration tests in Figure 102. All of the test configurations deviate from the beam vertical centerline. The beam in Beam Position 2 results in the largest deviation with the center of the plume over 40 cm from the vertical centerline.

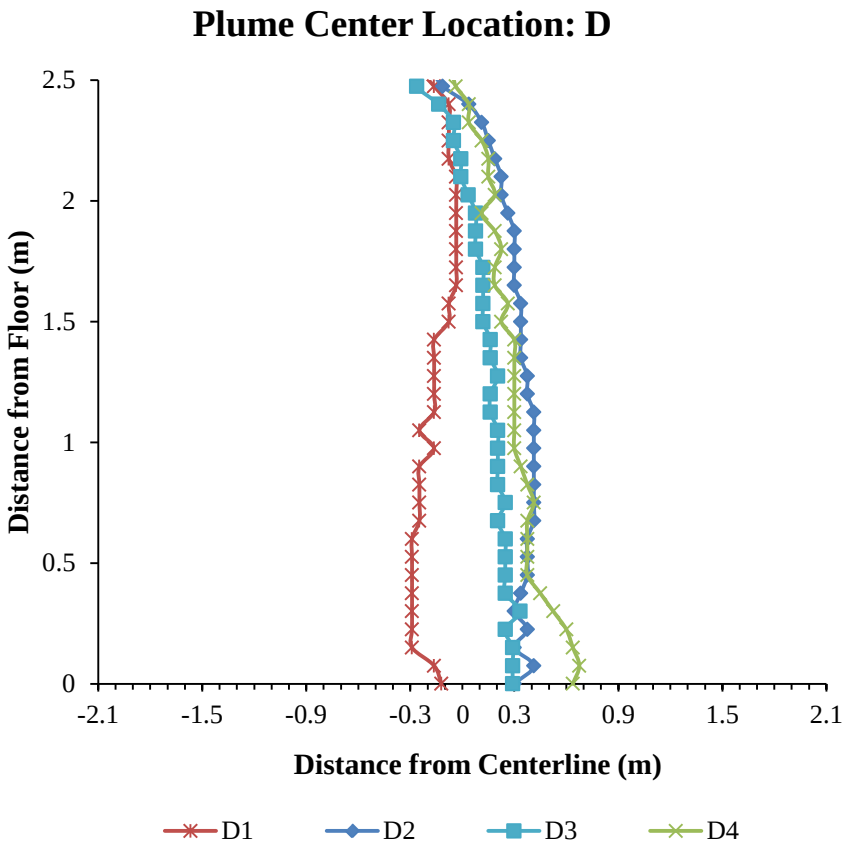

Figure 102. Plume center location for the D-configuration tests.

8.3.5 E-Configuration of Thermal Manikins

The temperature distributions, velocity profiles, and three-dimensional plumes for the thermal manikins in Configuration E are shown for the four beam positions in Figures 103-105, respectively. All four of the beam positions created airflows that were asymmetric. The shape of the plume for the beam in Beam Positions 3 and 4 was affected similarly to the D-configuration simulations. When the beam was located above the heat sources, the plumes generated by the thermal manikins displaced the beam

plume. However, when the beam was not positioned above the thermal manikins, the stronger airflow currents generated by the heat sources created a greater mass flow rate and subsequent rate of cooling through localized areas of the beam. The plume from the beam in Beam Position 4 demonstrates this as the plume is strongest underneath the section of the beam that is closest to the rows of thermal manikins.

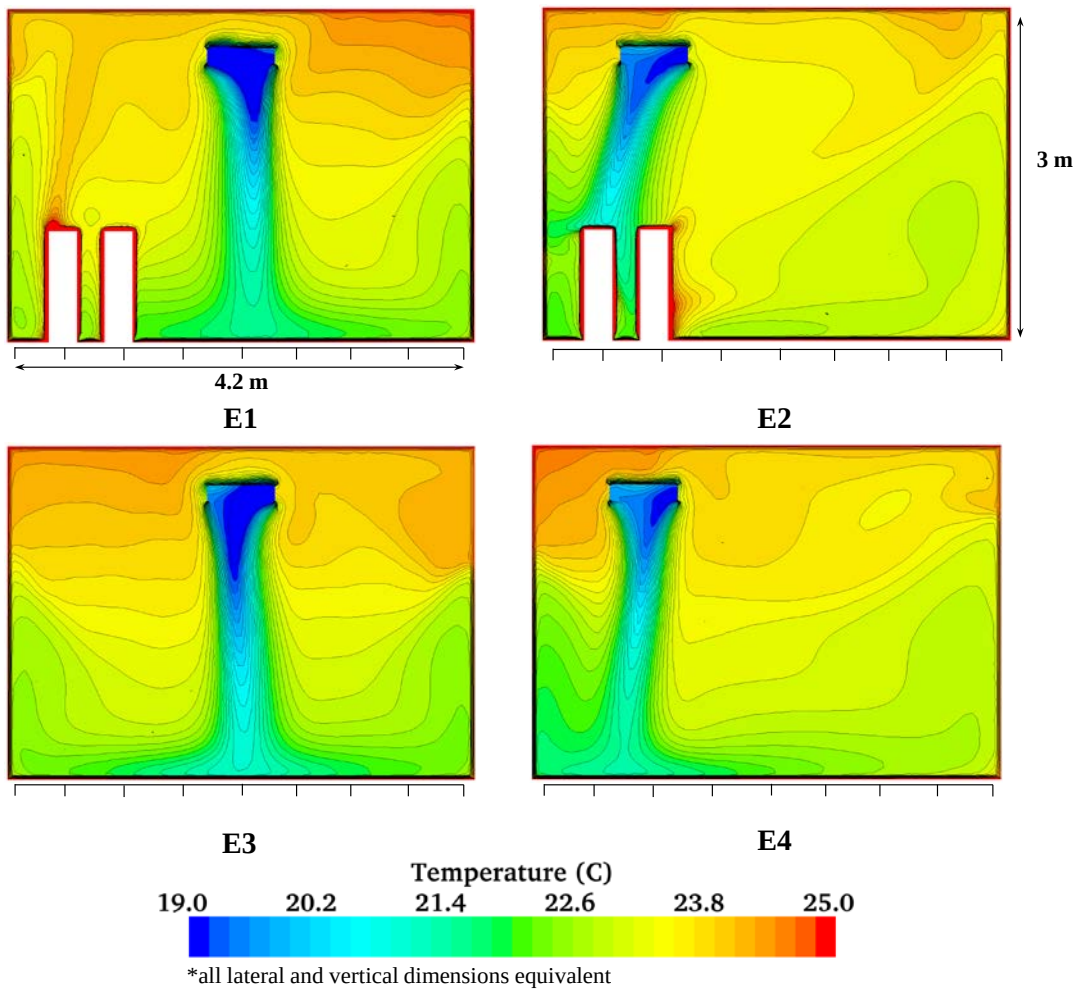

Figure 103. Temperature profiles for BPs 1-4 cooling the thermal manikins in the E-configuration.

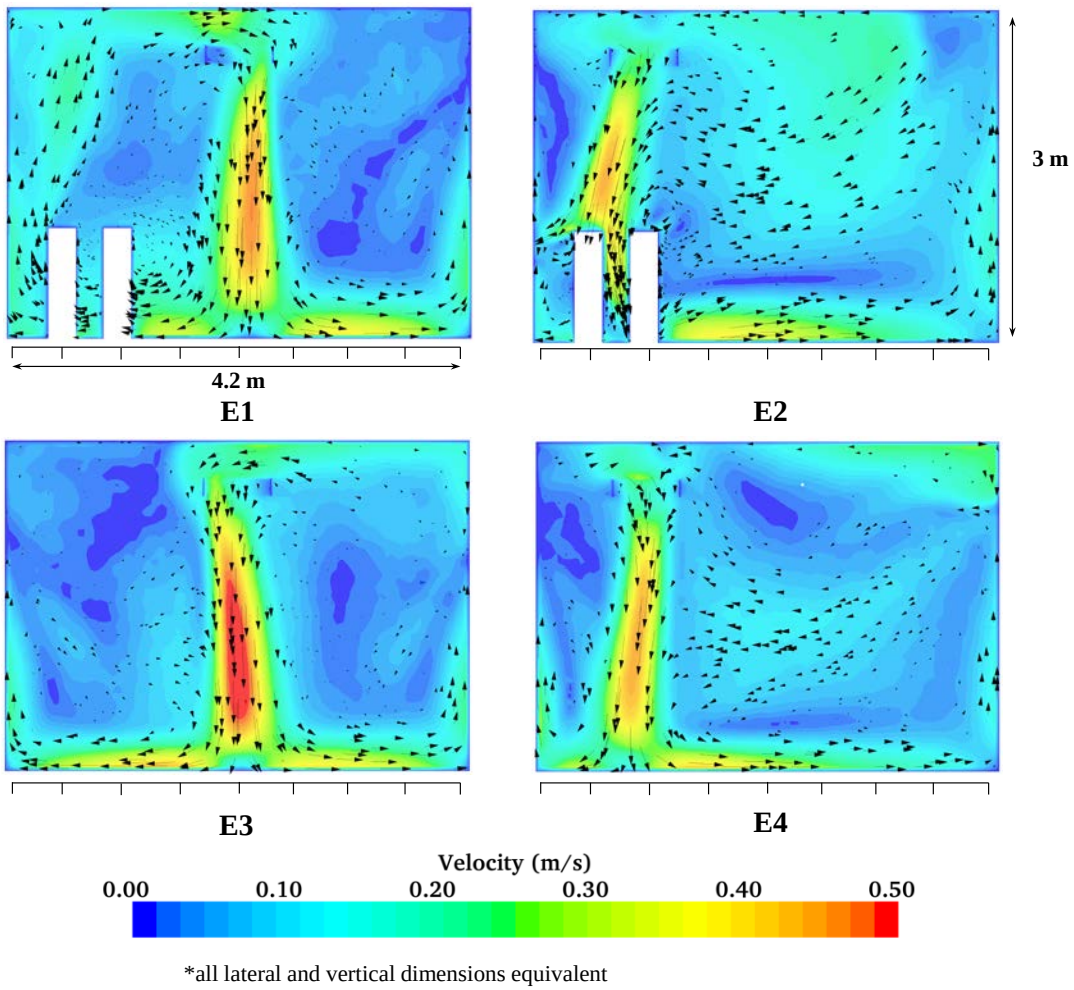

Figure 104. Velocity distributions for BPs 1-4 cooling the thermal manikins in the E-configuration.

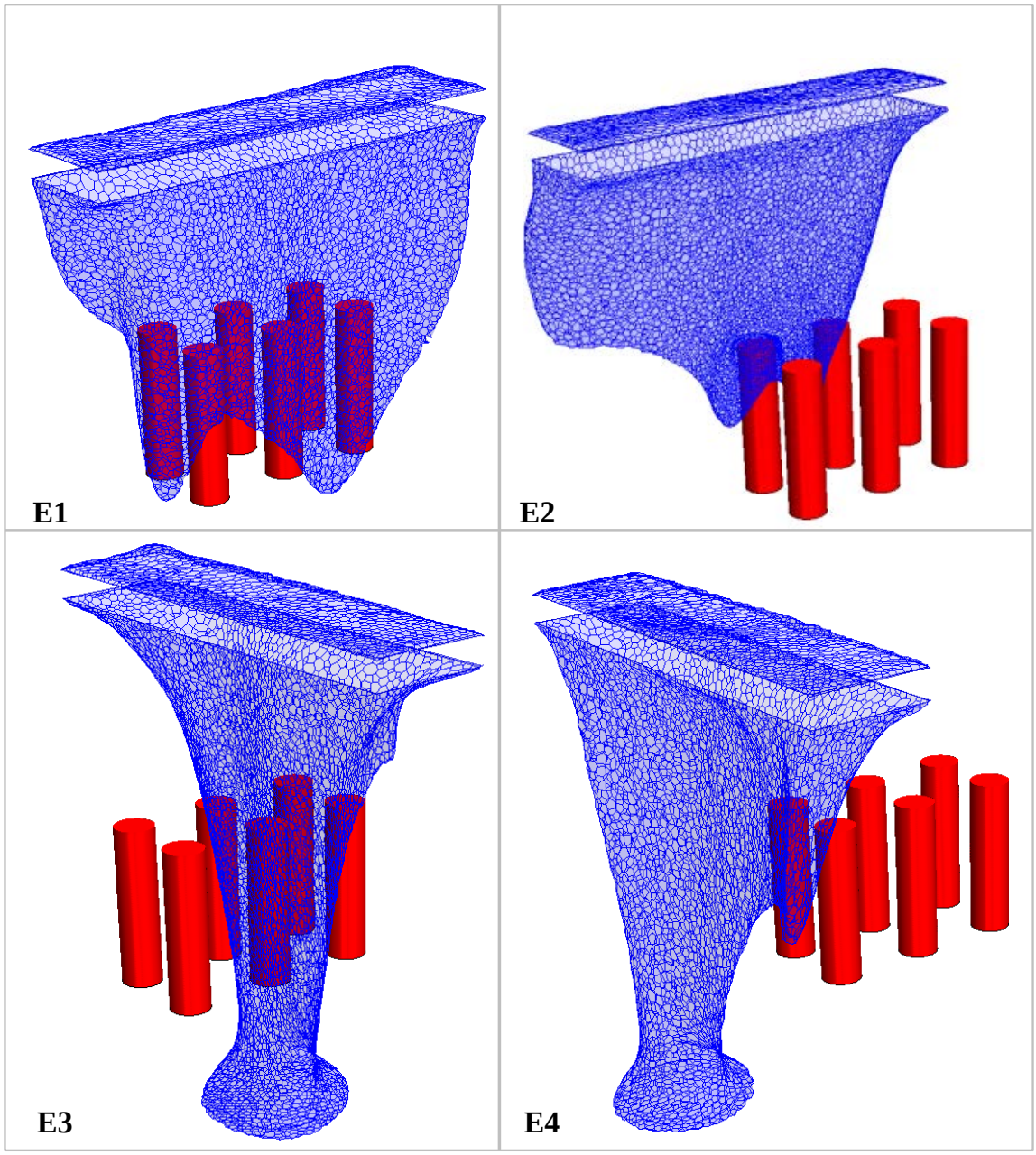

Figure 105. Three-dimensional plumes from the beam (21 °C) in BPs 1-4 cooling the thermal manikins in the E-configuration.

The airflow characteristics of the occupied zone, listed in Table 36, show that the beam orientation for the thermal manikins in the E-configuration had less effect on the room air characteristics than for the C or D thermal manikin configurations. The maximum velocity in the occupied zone for the E-configuration of thermal manikins was highest for Beam Position 3, perpendicular to the rows of thermal manikins.

Table 36. Minimum temperature and maximum temperature and velocity for the Test E-configuration.

	E1	*E2*	*E3*	*E4*
Minimum Temperature (°C)	21.3	20.4	19.7	21.0
Maximum Temperature (°C)	25.3	24.9	28.1	28.7
Maximum Velocity (m/s)	0.376	0.439	0.528	0.363
Maximum Temperature Difference (°C)	4.0	4.5	8.4	7.7

The center of the beam plumes generally followed the vertical centerline of the beam, as shown in Figure 106, except for Beam Position 2. As in the D-configuration of thermal manikins, the Beam Position 2 beam plume deviated from the vertical centerline by more than 40 cm, a result of the proximity of the thermal manikins located directly beneath the beam.

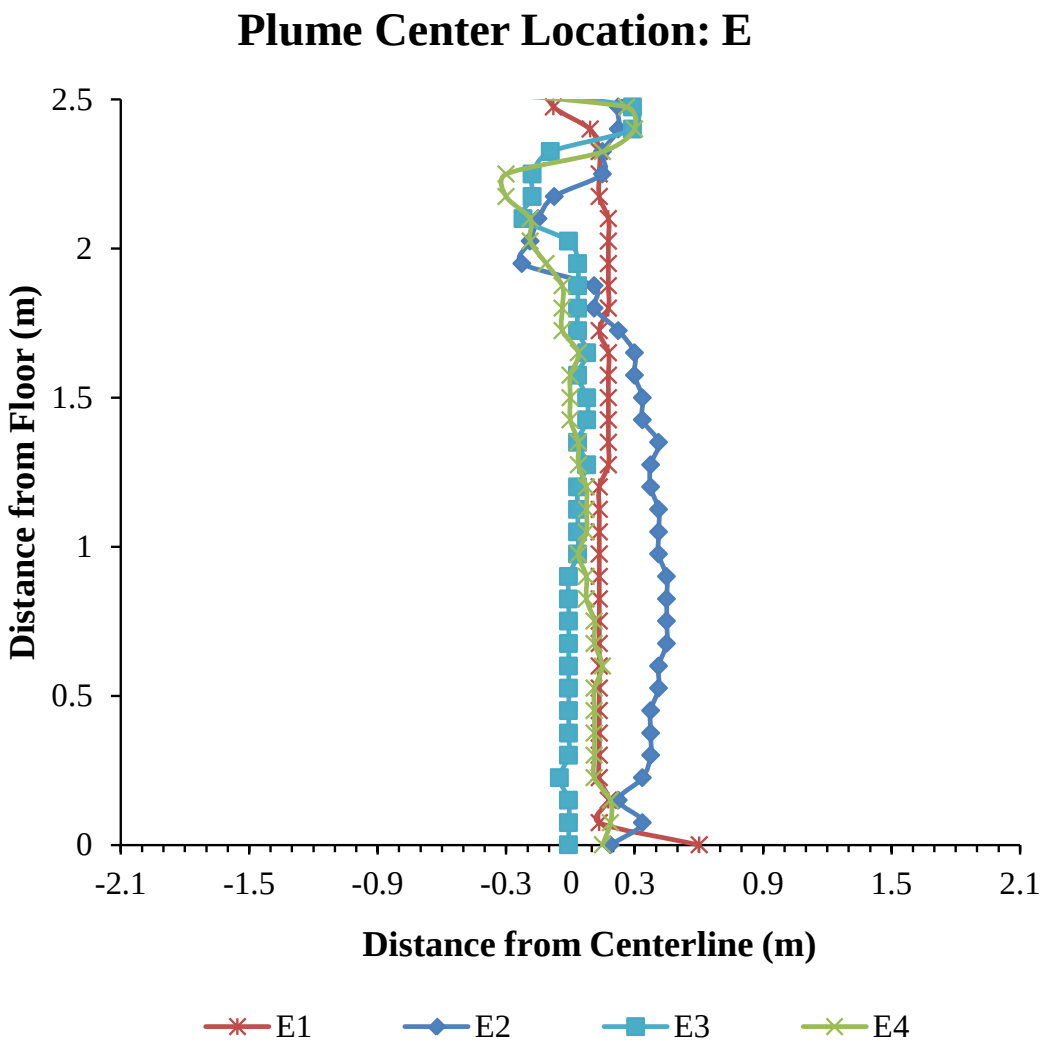

Figure 106. Plume center location for the E-configuration tests.

8.3.6 F-Configuration of Thermal Manikins

The temperature distributions, velocity profiles, and three-dimensional plumes for the thermal manikins in Configuration F are shown for the four beam positions in Figures 107-109, respectively. The results show symmetric airflow patterns for the

beam positions oriented in the center of the room, either perpendicular or parallel to the rows of thermal manikins. The airflow pattern created from Beam Position 2 was similar to the airflow pattern created by the thermal manikins in the asymmetric configuration, where the room air circulation was limited to the half of the room that contained the beam and the thermal manikins.

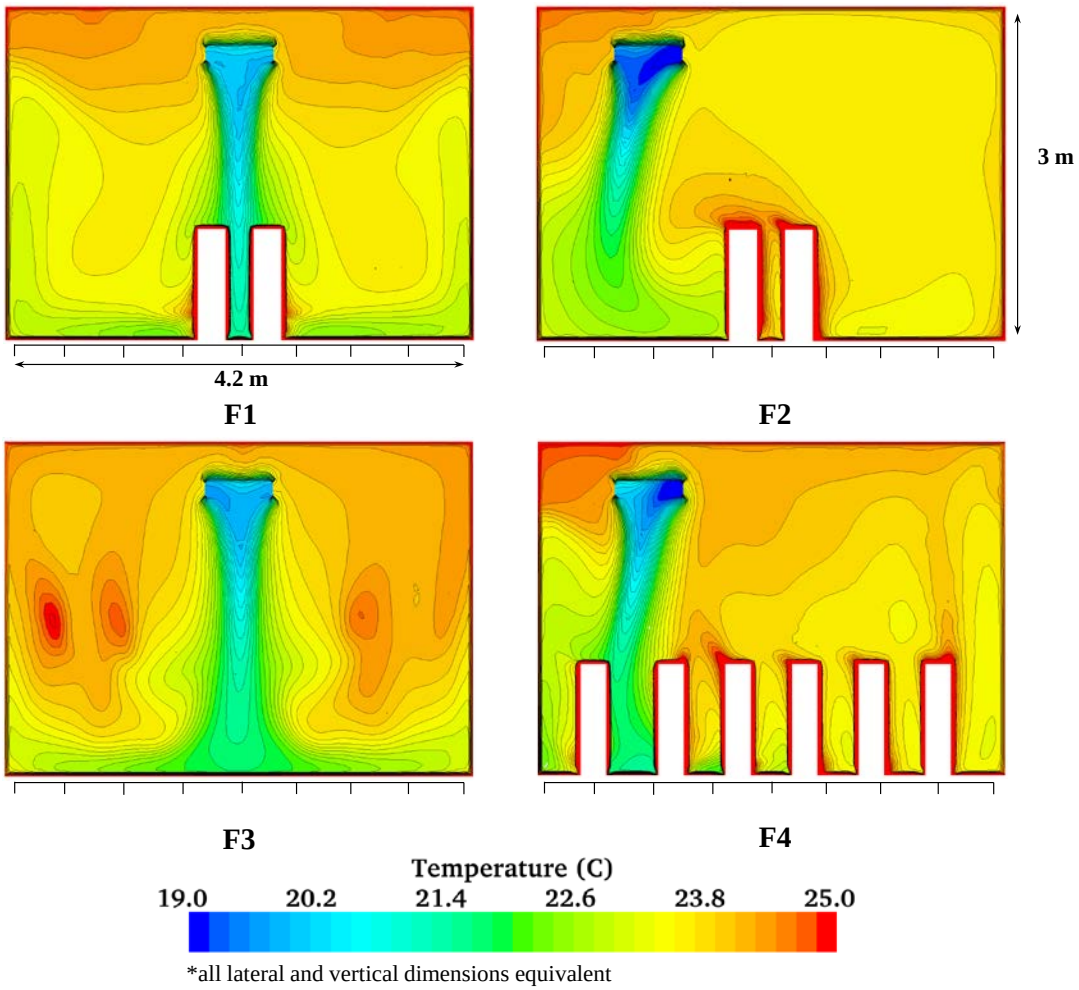

Figure 107. Temperature profiles for BPs 1-4 cooling the thermal manikins in the F-configuration.

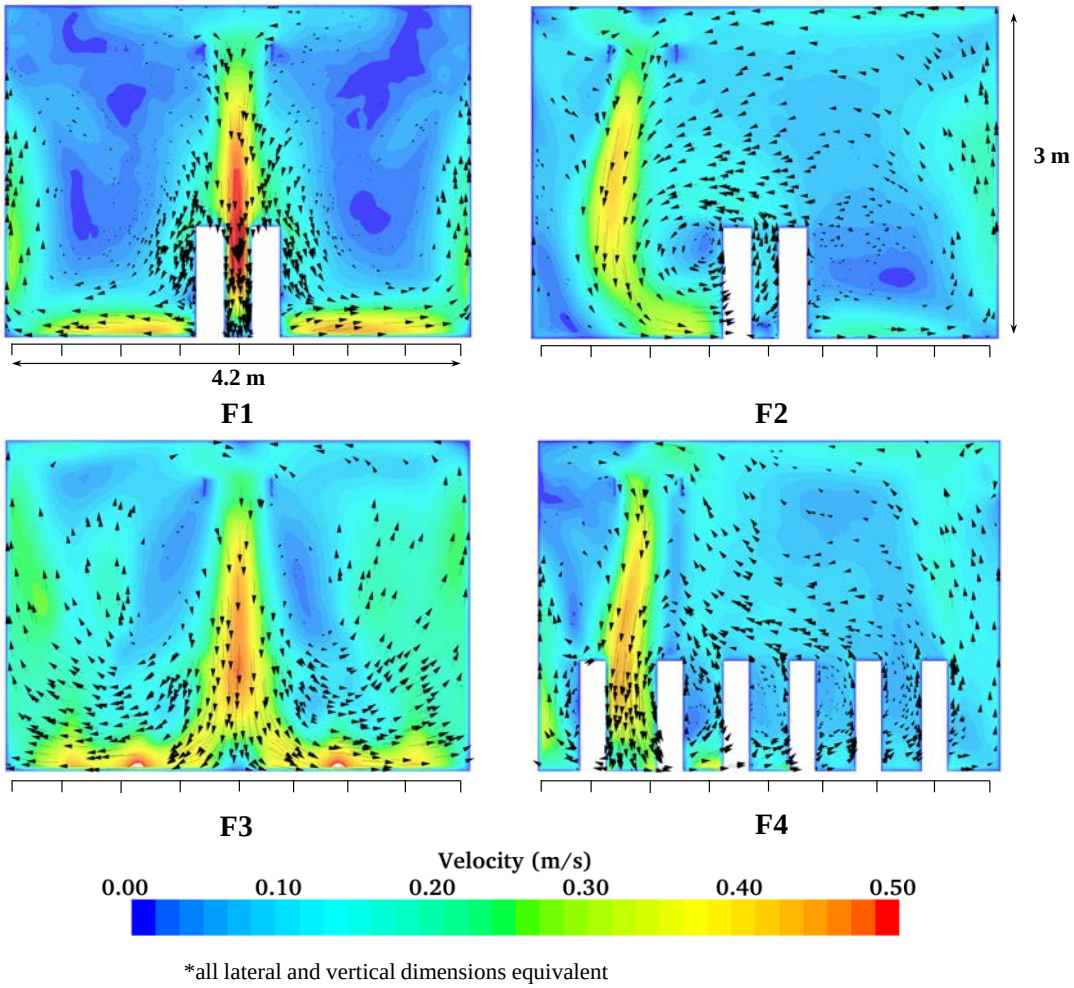

Figure 108. Velocity distributions for BPs 1-4 cooling the thermal manikins in the F-configuration.

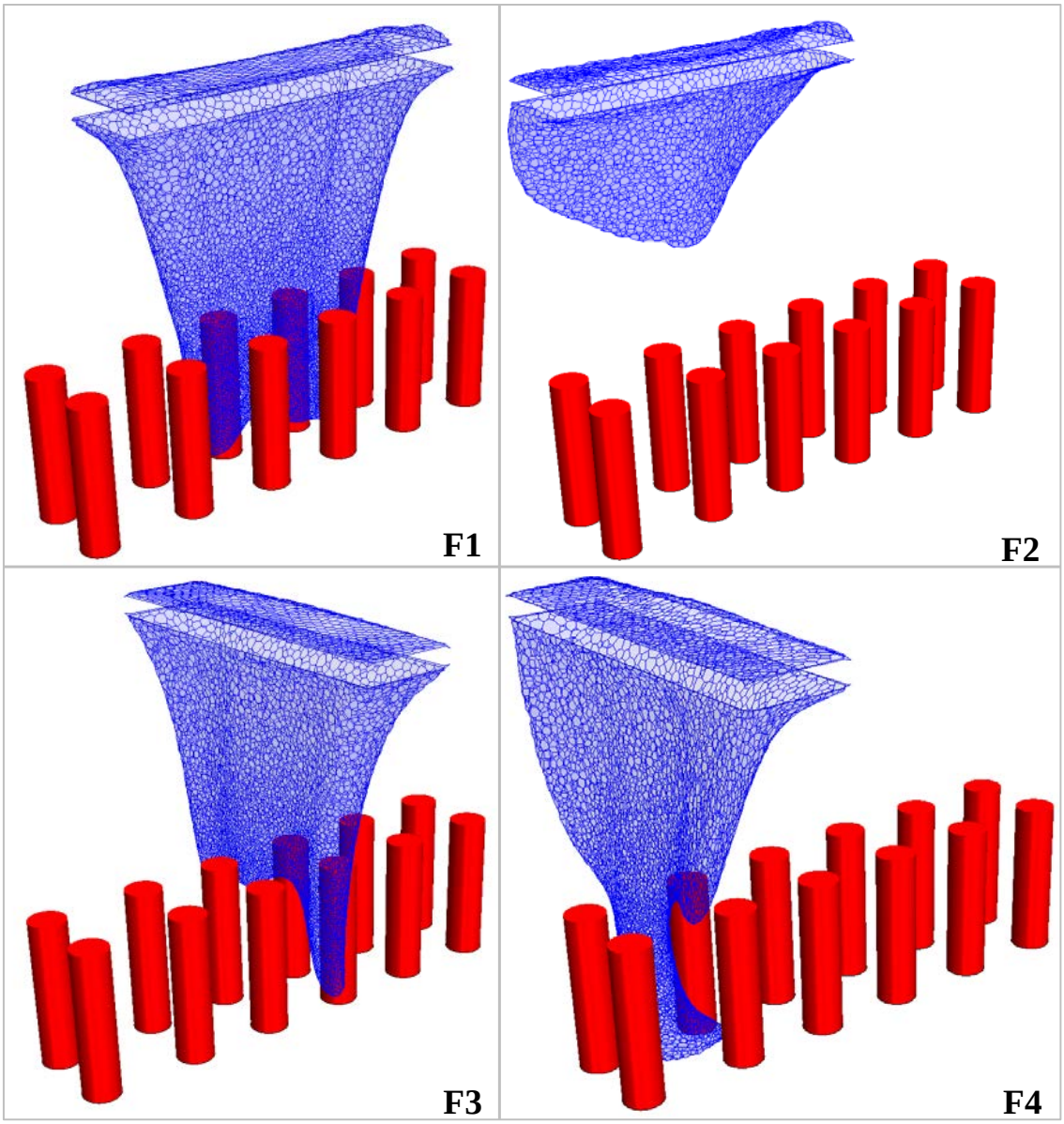

Figure 109. Three-dimensional plumes from the beam (21 °C) in BPs 1-4 cooling the thermal manikins in the F-configuration.

The airflow characteristics of the occupied zone, listed in Table 37, show that for all four beam orientations, the temperatures throughout the space were relatively uniform, with small maximum temperature differences of 5 °C or less as compared to the C, D and E configurations. The highest maximum velocities in the occupied zone were generated by the beam in Beam Positions 1 and 3, both located in the center of the room.

Table 37. Minimum temperature and maximum temperature and velocity for the Test F configuration.

	F1	*F2*	*F3*	*F4*
Minimum Temperature (°C)	20.2	21.2	20.5	21.6
Maximum Temperature (°C)	25.3	25.2	24.4	25.1
Maximum Velocity (m/s)	0.557	0.415	0.527	0.388
Maximum Temperature Difference (°C)	5.1	4.0	3.9	3.5

The minimum temperature location in relation to the beam centerline and vertical distance from the floor was plotted for each scenario of the F-configuration tests in Figure 110. The beam plume from the positions at the center of the room resulted in plume centers that followed the vertical centerline. Beam Positions 2 and 4 resulted in higher deviation from the vertical centerline.

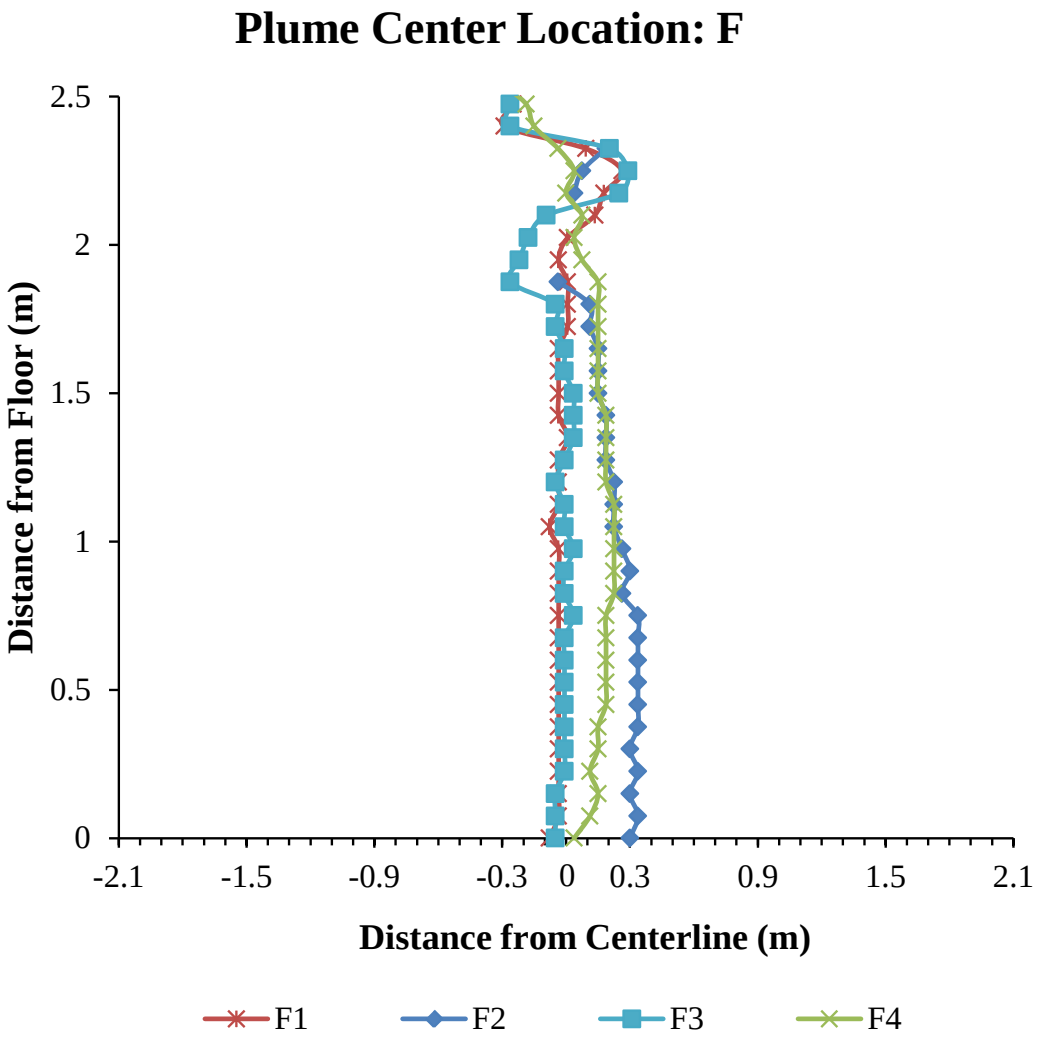

Figure 110. Plume center location for the F-configuration tests.

8.3.7 G-Configuration of Thermal Manikins

The temperature distributions, velocity profiles, and three-dimensional plumes for the thermal manikins in Configuration G are shown for the four beam positions in Figures 111-113, respectively. The results show symmetric airflow patterns for Beam

Positions 1 and 3 located in the center of the room either perpendicular or parallel to the rows of thermal manikins. For Beam Positions 2 and 4, the flow is highly varied. In Beam Position 4, a large area of air speed greater than 0.5 m/s was present for the region of the occupied zone nearest the thermal manikins and beam. The circulation of room air for Beam Position 2 was limited to the half of the room containing the beam and the thermal manikins, similar to the results in the asymmetric and F-configuration tests.

The airflow characteristics of the occupied zone, listed in Table 38, are similar to the F-configuration results and show that the beam orientation had an insignificant effect on the maximum temperature difference in the occupied zone. However, the maximum velocity in the occupied zone for Beam Position 3 was almost 50% higher than with Beam Position 2.

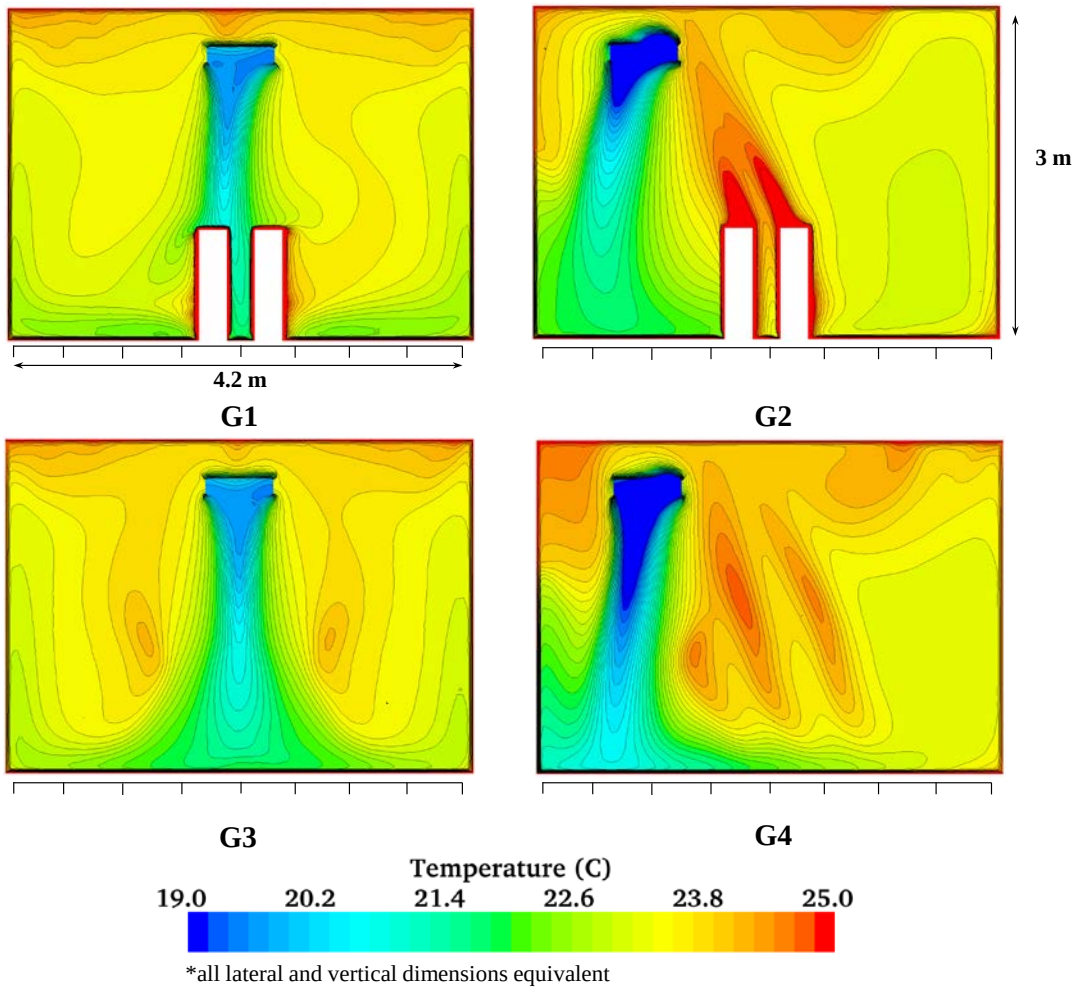

Figure 111. Temperature profiles for BPs 1-4 cooling the thermal manikins in the G-configuration.

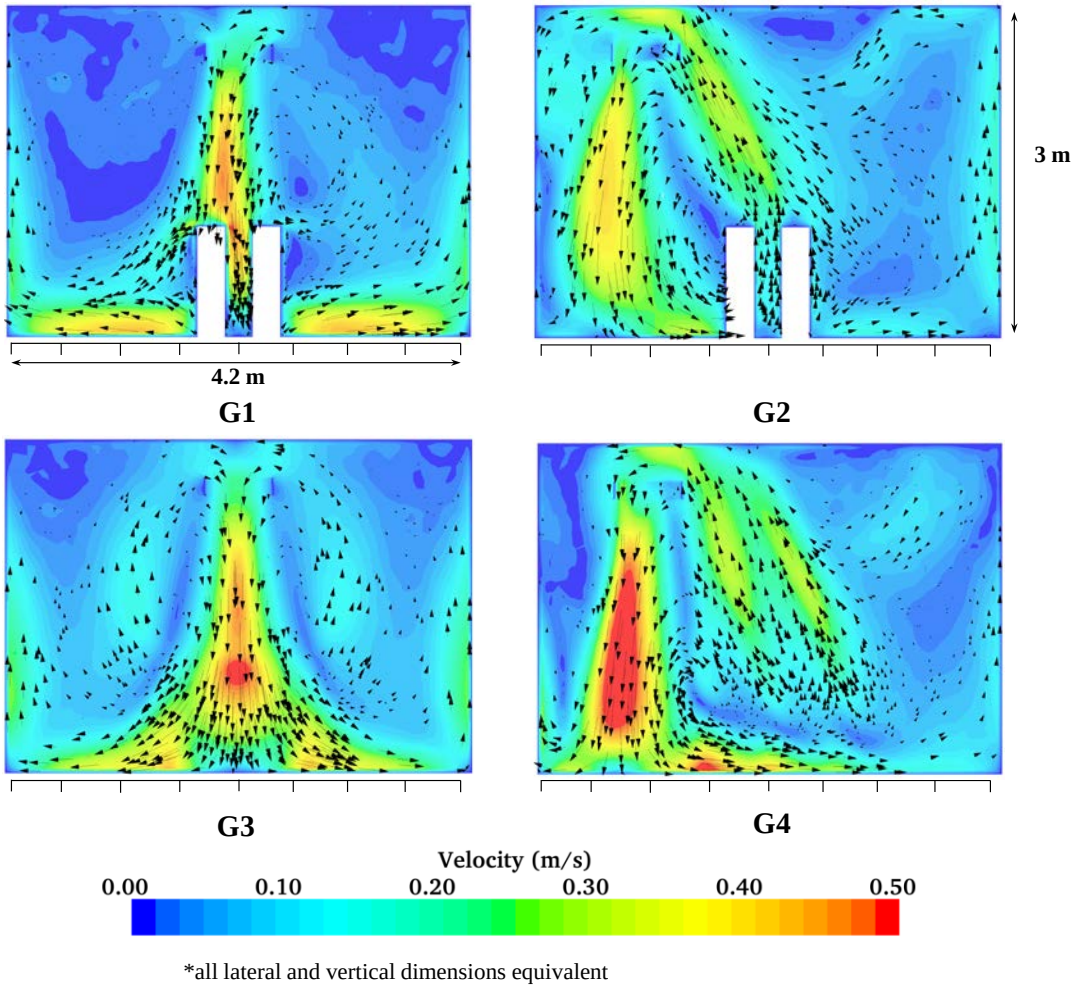

Figure 112. Velocity distributions for BPs 1-4 cooling the thermal manikins in the G-configuration.

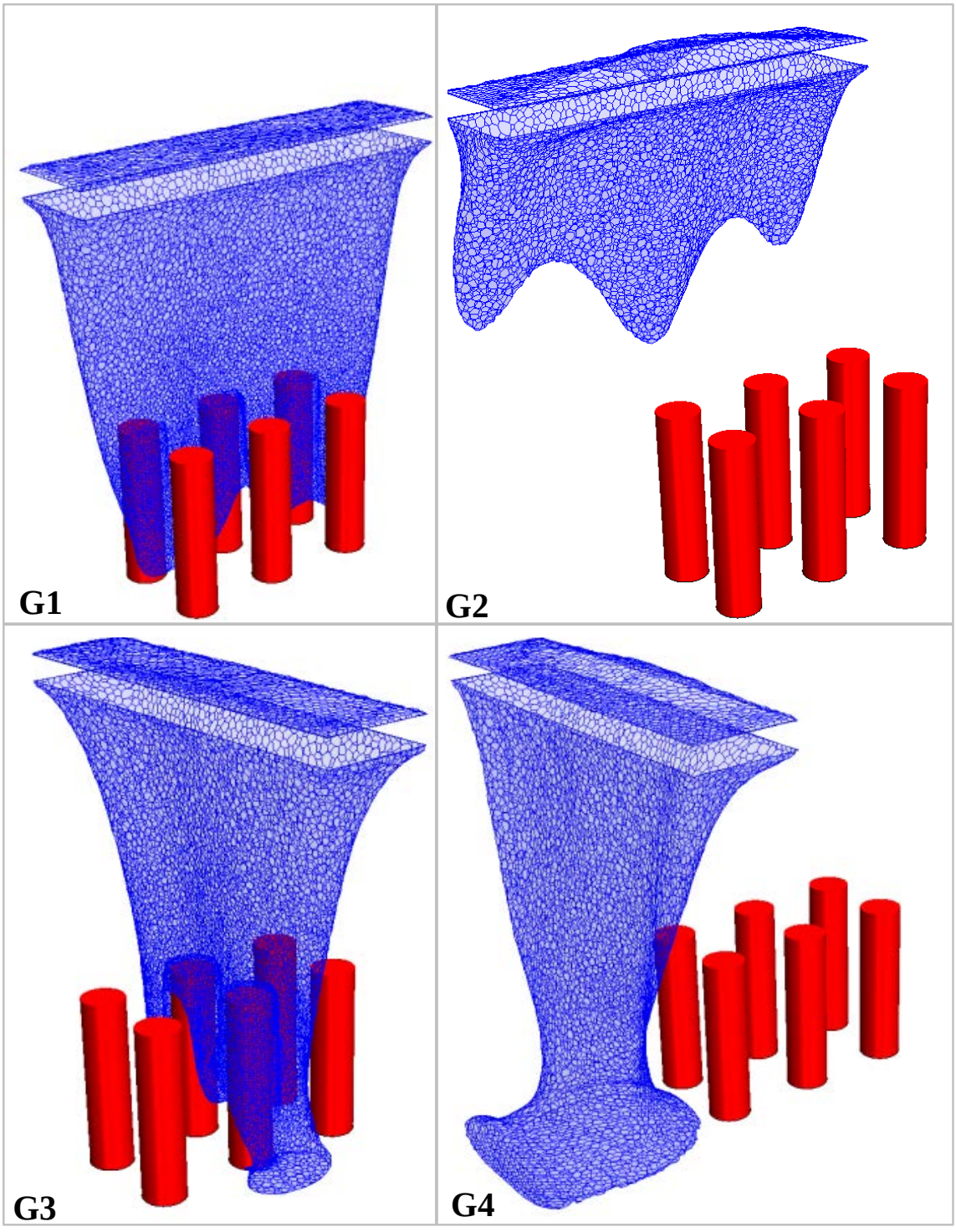

Figure 113. Three-dimensional plumes from the beam (21 °C) in BPs 1-4 cooling the thermal manikins in the G-configuration.

Table 38. Minimum temperature and maximum temperature and velocity for the Test G-configuration.

	G1	*G2*	*G3*	*G4*
Minimum Temperature (°C)	20.0	20.8	19.8	20.6
Maximum Temperature (°C)	25.1	25.0	24.0	24.7
Maximum Velocity (m/s)	0.512	0.409	0.592	0.485
Maximum Temperature Difference (°C)	5.1	4.2	4.2	4.1

The minimum temperature location in relation to the beam centerline and vertical distance from the floor was plotted for each scenario of the G-configuration tests in Figure 114. Of the four tests, only Beam Position 3 followed the vertical centerline. In the occupied zone, Beam Positions 1, 3, and 4 resulted in deviations of greater than 20 cm from the vertical centerline.

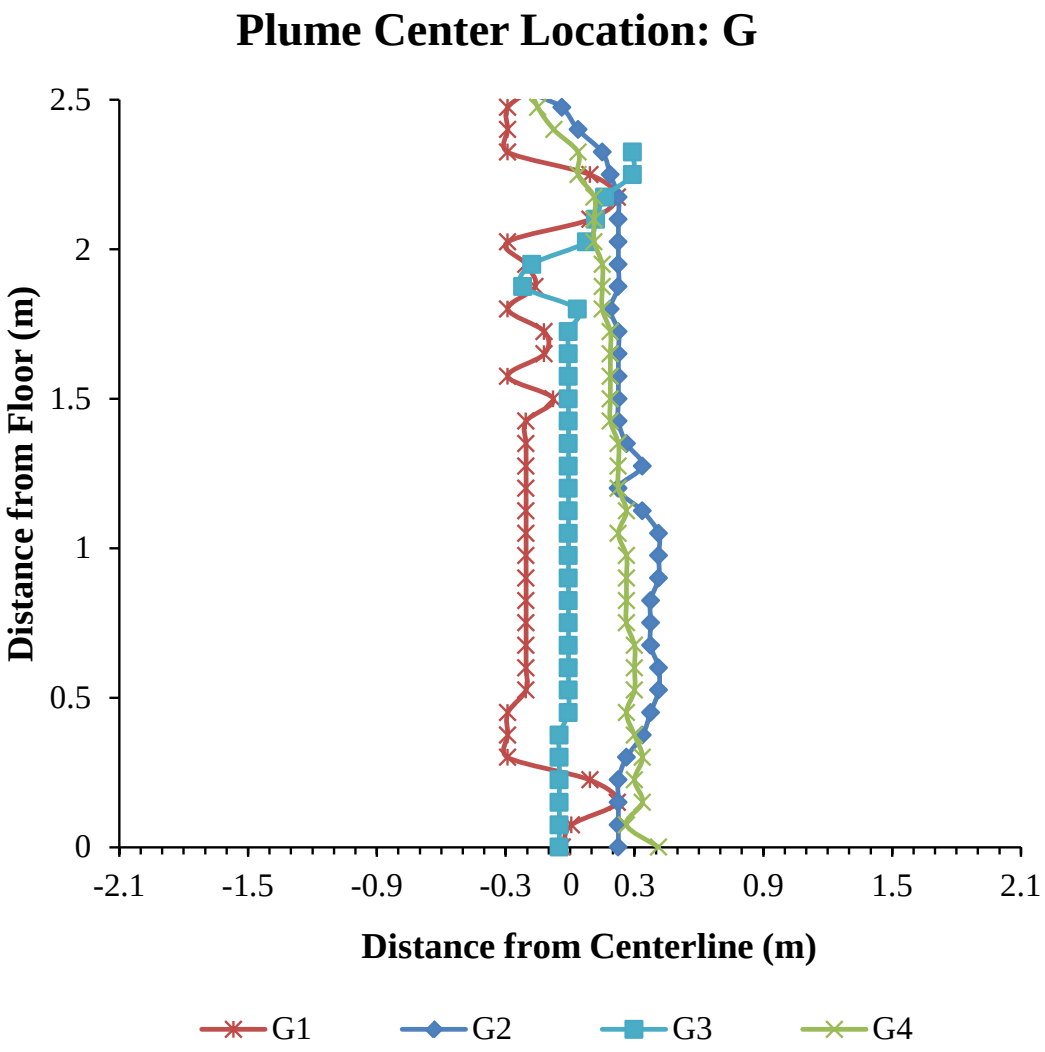

Figure 114. Plume center location for the G-configuration tests.

8.3.8 H-Configuration of Thermal Manikins

The temperature distributions, velocity profiles, and three-dimensional plumes for the thermal manikins in Configuration H are shown for the four beam positions in Figures 115-117, respectively. The results are similar to the Configuration G tests, with symmetric airflow patterns generated with Beam Position 1, and varied flow conditions for Beam Positions 2, 3 and 4. In Beam Position 1, the concentration of thermal manikins located beneath the beam, reduces the localized mass flow rate in the beam region directly above the thermal manikins. The shape of the plume reflected the reduced localized cooling rate and the displacement of the beam plume due to the proximity of the thermal manikins.

The airflow characteristics of the occupied zone for the H-configuration of thermal manikins, listed in Table 39, are similar to the G-configuration and show that the beam orientation had an insignificant effect on the maximum temperature difference in the occupied zone. Additionally, the maximum velocity in the occupied zone was relatively constant for each beam orientation.

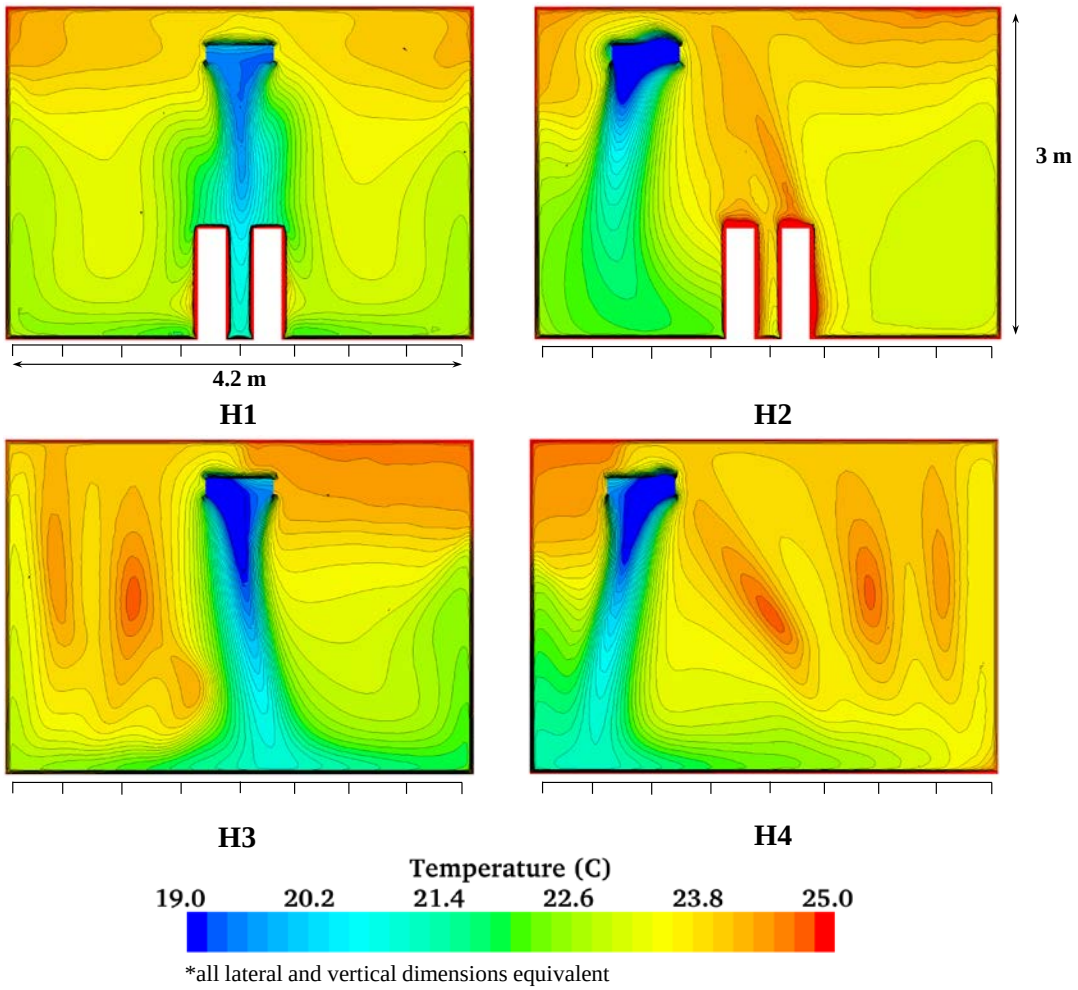

Figure 115. Temperature profiles for BPs 1-4 cooling the thermal manikins in the H-configuration.

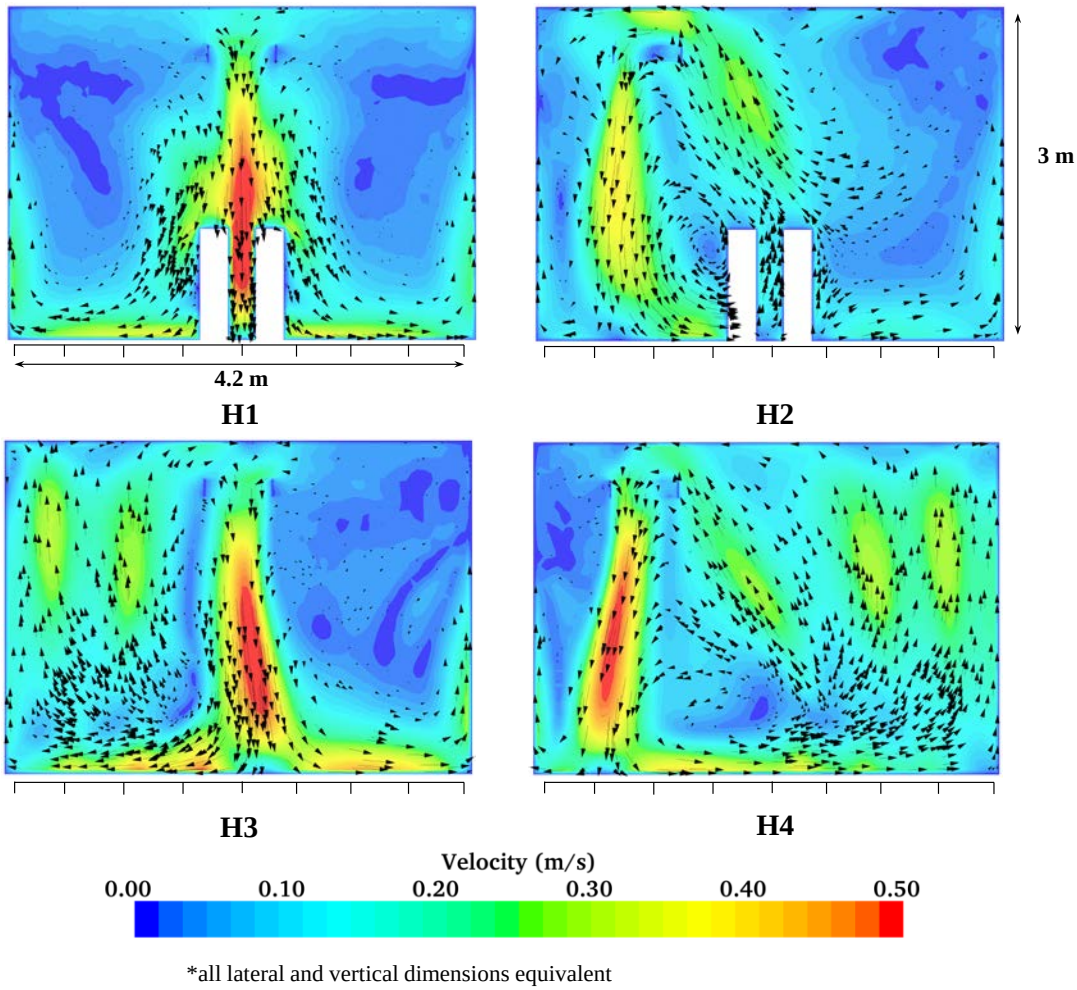

Figure 116. Velocity distributions for BPs 1-4 cooling the thermal manikins in the H-configuration.

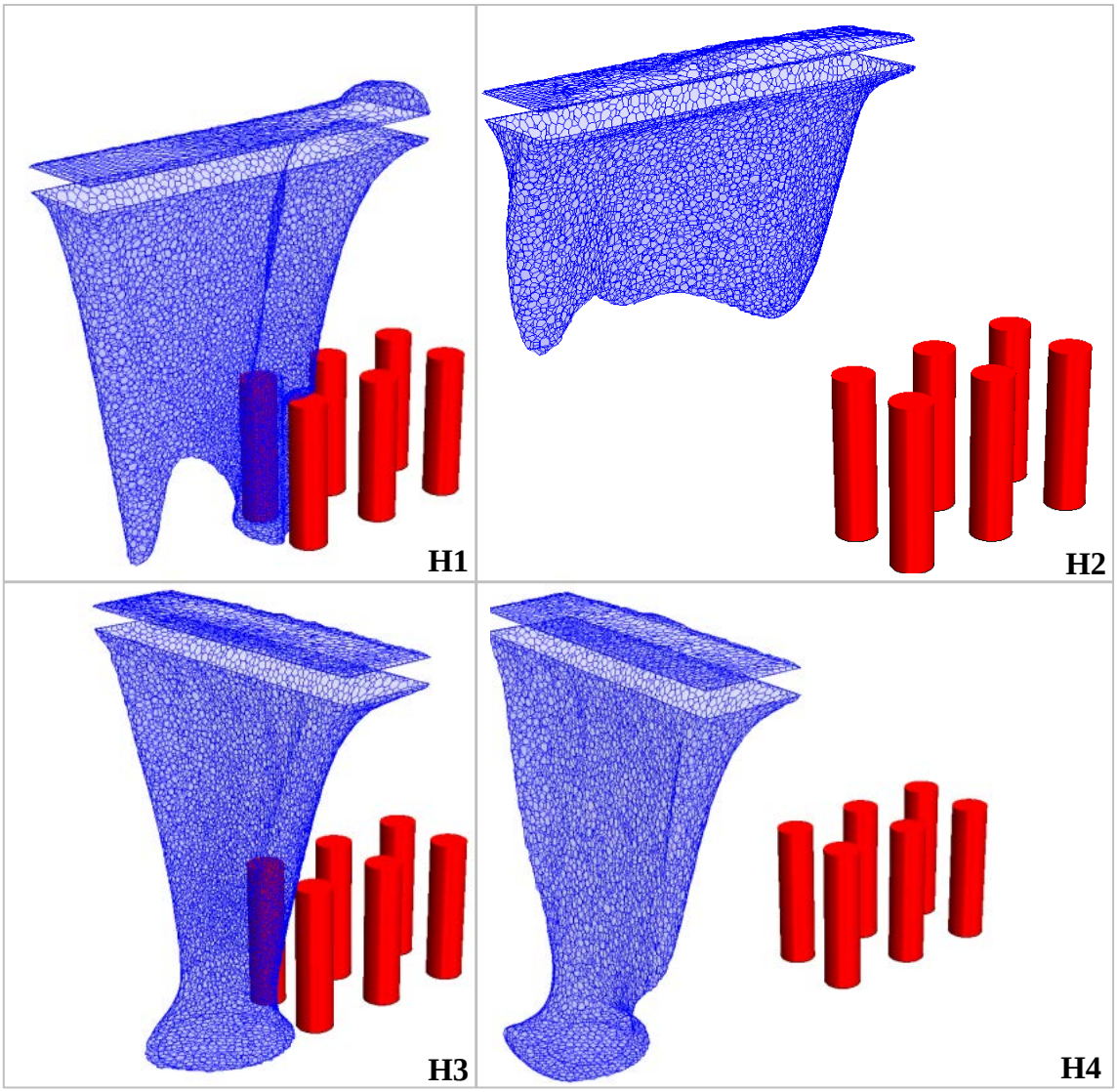

Figure 117. Three-dimensional plumes from the beam (21 °C) in BPs 1-4 cooling the thermal manikins in the H-configuration.

Table 39. Minimum temperature and maximum temperature and velocity for the Test H configuration.

	H1	*H2*	*H3*	*H4*
Minimum Temperature (°C)	20.3	20.7	19.6	20.7
Maximum Temperature (°C)	25.1	24.8	24.7	24.8
Maximum Velocity (m/s)	0.490	0.431	0.497	0.477
Maximum Temperature Difference (°C)	4.8	4.1	5.1	4.1

The minimum temperature location in relation to the beam centerline and vertical distance from the floor was plotted for each scenario of the G-configuration tests in Figure 118. Beam Position 1 resulted in a beam plume center that followed the vertical centerline. For Beam Positions 2, 3, and 4, the plume center deviated away from the heat sources by at least 20 cm for all three tests.

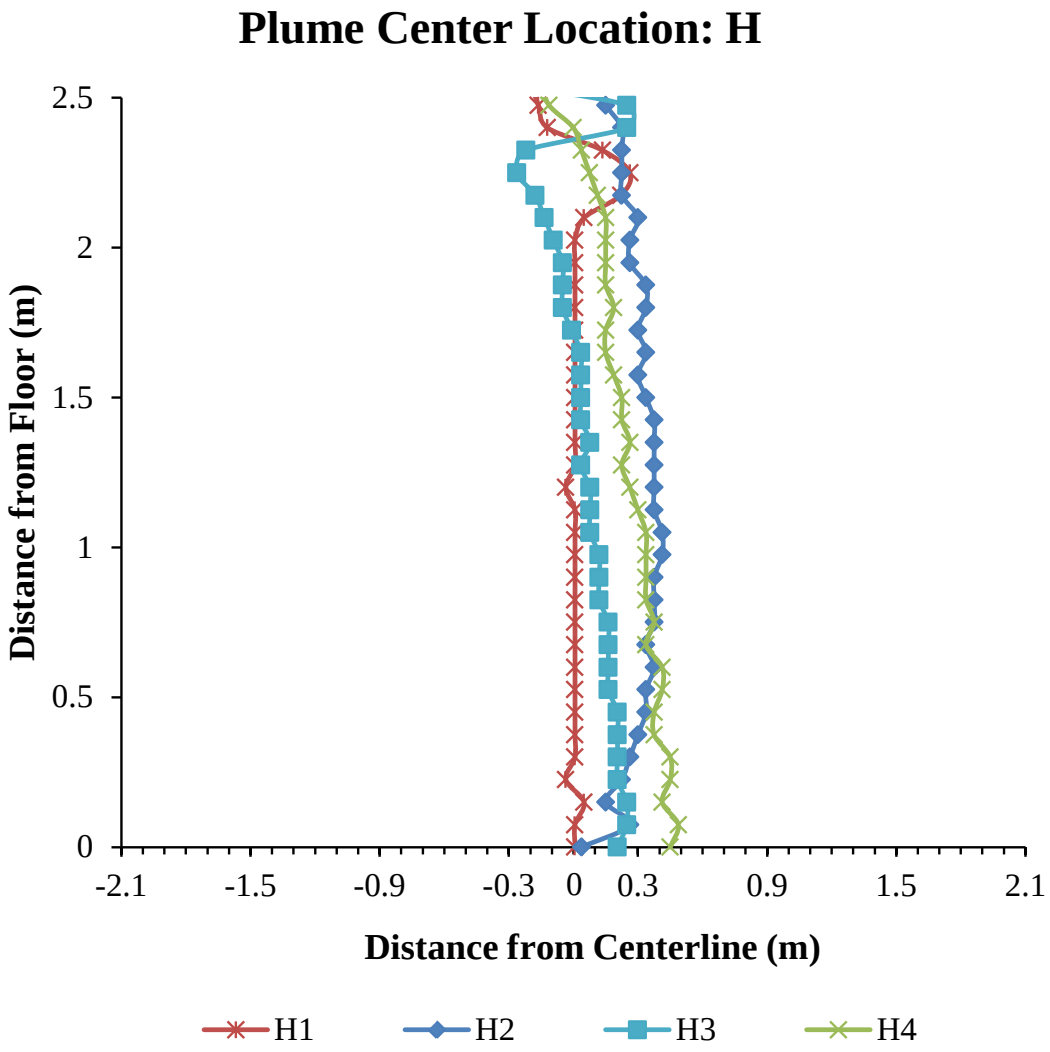

Figure 118. Plume center location for the H-configuration tests.

8.4 Summary

The objective of this chapter was to quantify effects on beam performance and room air characteristics for different beam positions, room dimensions, and heat source locations. The results of the beam capacity calculations showed that the beam orientation countered the reduced effect of an unbalanced heat source distribution. By rotating the beam to be perpendicular to the rows of thermal manikins, the calculated beam efficiency increased for the unbalanced heat sources. Additionally, the rotation of the beam resulted in a symmetric airflow pattern, mixing the entire occupied zone in contrast to the asymmetric flow pattern with mixing in only half of the room as a result of the unbalanced heat source distribution cooled by a beam with a parallel orientation.

However, a change in beam orientation that increases the efficiency of the beam performance can negatively impact the room air characteristics in the occupied zone. Higher maximum velocities and larger temperature differences in the occupied zone were shown for the beam oriented perpendicular to the heat sources in both the symmetric and asymmetric distributions. Similar results were found for additional configurations of diverse heat source distributions.

The beam thermal plume was not strongly influenced by the beam orientation, though the heat source locations changed the position and shape. For concentrated heat load distributions, the localized cooling capacity of the beam increased for the regions nearest to the heat sources if the beam was not near enough for the thermal plumes to interact. For beams positioned directly over the heat sources or in close proximity, the

heat source plumes were strong enough to displace the beam thermal plume away from the heat sources.

Finally, the results of testing the room dimensions were that little impact was calculated on the beam performance, thermal plume characteristics, or room air characteristics by increasing the volume of air cooled and the height of the beam. For room designs with passive chilled beams cooling symmetric heat load distributions, the flow pattern and thermal characteristics in the space will be unaffected with an increased ceiling height, beam height or wall length. Similarly, for designs with asymmetric or unbalanced heat source distributions, the adverse effects of reduced beam performance and variations in the room air characteristics throughout the occupied zone may not be compensated for by changing the room dimensions.

CHAPTER IX

CONCLUSIONS AND RECOMMENDATIONS

9.1 Summary

A numerical model was developed to calculate the performance and resultant airflow characteristics of a passive chilled beam. The methodology for the model development used a porous medium region to simulate the fin array of the passive chilled beam. Experiments were conducted in a thermal climate test chamber to measure the beam cooling capacity, air temperatures and velocities, and power input to heat sources. Symmetric and asymmetric arrangements of thermal manikins were tested and the data analysis showed a 15 % reduction in the passive beam cooling capacity for the asymmetric heat sources.

The measured data was used to validate the model predictions. Predictions of reference air temperatures above the passive chilled beam were within 5 % of the measured values. Similarly, air temperatures predicted below the passive chilled beam were within 10 % of the measured values. Coefficients used in the inertial resistance calculation throughout the porous medium region were adjusted to match the predicted passive chilled beam outlet velocities within 20 % of the measured values. Though, when the time-variance of the velocity was taken into account, the CFD calculation values fell within the range of variation.

The CFD model was used to further investigate the reduced cooling capacity of the beam with an asymmetric heat source distribution by comparing the calculated inlet

velocity field to the symmetric inlet velocity field. The results of the comparison revealed that the air velocities above the passive chilled beam of the asymmetric thermal manikin tests were higher than the symmetric thermal manikin tests. Additionally, the direction of the velocity field was parallel to the inlet of the passive chilled beam region, decreasing the mass flow rate of air through the beam.

A calculation for the beam cooling capacity was used to predict the passive chilled beam efficiency of additional geometric and spatial room arrangements. The results were increased beam efficiencies for spaces with the beam oriented perpendicular to the groupings of heat sources. However, increases in the beam efficiency also resulted in higher maximum velocities in the occupied zone. With unbalanced heat load configurations, the beam orientation affected the airflow in the space and, depending on the position in relation to the thermal manikins, created either well-mixed conditions or occupied zone conditions with a high degree of air temperature ranges that could negatively impact the thermal comfort of occupants.

9.2 Conclusions

From the investigative results presented in the dissertation, the following list of conclusions was drawn:

1. A passive chilled beam can be successfully modeled in CFD by using a porous medium model that acts as a heat sink and a source of momentum loss. The porous medium region requires a lower density of grid points for converged

solutions than modeling the surfaces of the beam fin array and can be used to calculate the resultant airflow in much larger spaces.

2. Arrangement of the heat sources in a space cooled by a passive chilled beam will affect the beam performance. The results of experimental tests were a 15 % reduction in the beam cooling capacity with heat sources grouped to only one side of the beam compared to a balanced load configuration. The combined strength of the thermal plumes from the grouped heat sources contributed to higher velocities at the inlet of the passive chilled beam directing the flow above and around the beam.

3. The calculation of the beam cooling capacity implemented in the CFD model was shown to be generalizable and could predict changes in beam performance based on heat source configurations.

4. The beam performance was increased for unbalanced heat source configurations by rotating the beam to be perpendicular in relation to the heat source locations. Unbalanced load configurations reduced the beam performance and contributed to asymmetric airflow in the space resulting in high variations of temperature throughout the occupied zone.

5. The basic features of the room geometry did not affect the beam performance and did not alter the reduction in beam performance for unbalanced loads.

9.3 Recommendations

Based on the results of this study, the passive chilled beam location should be designed with the expected heat load locations in consideration. For unbalanced heat sources, the position of the beam should be perpendicular to the grouping of heat sources for the maximum efficiency. Future studies of passive chilled beam performance should investigate effects from heat source configurations for a system that includes supply air distribution. The airflow through the space will be impacted not only by the passive chilled beam and the heat sources but also by the design of the supply air diffuser. The CFD model validated in this study can be used to calculate the cumulative effects of multiple sources of buoyancy and momentum in order to predict the thermal comfort of occupants.

REFERENCES

[1] H. Awbi, Ventilation of Buildings, Spon Press, London, England, 2003.

[2] D. Etheridge, M. Sandberg, Building Ventilation: Theory and Measurement, John Wiley and Sons Ltd, West Sussex, England, 1996.

[3] ASHRAE Standard 55, Thermal Environmental Conditions for Human Occupancy, ASHRAE Inc., 2004, Atlanta.

[4] Q. Chen, W. Xu, A Zero-equation Turbulence Model for Indoor Airflow Simulation, Energy and Buildings, 28 (1998) 137-144.

[5] J.D. Posner, C.R. Buchanan, D. Dunn-Rankin, Measurement and Prediction of Indoor Air Flow in a Model Room, Energy and Buildings, 35 (2003) 515-526.

[6] J. Srebric, V. Vukovic, G. He, X. Yang, CFD Boundary Conditions for Contaminant Dispersion, Heat Transfer and Airflow Simulations around Human Occupants in Indoor Environments, Building and Environment, 43 (2008) 294-303.

[7] J. Srebric, Q. Chen, Simplified Numerical Models for Complex Air Supply Diffusers, HVAC&R Research, 8 (3) (2002) 277-294.

[8] J. Srebric, Q. Chen, A Method of Test to Obtain Diffuser Data for CFD Modeling of Room Airflow, ASHRAE Transactions, 107 (2001) 108-116.

[9] H.E. Feustel, J. Dieris, A Survey on Air Flow Models for Multizone Structures, Energy and Buildings, 18 (1992) 79-100.

[10] Q. Chen, Z. Zhang, W. Zuo, Computational Fluid Dynamics for Indoor Environment Modeling: Past, Present and Future, Presented at The 6th International Indoor Air Quality, Ventilation and Energy Conservation in Buildings Conference (IAQVEC 2007), Sendai, Japan.

[11] F. Alamdari, Displacement Ventilation and Cooled Ceilings, Proceedings of ROOMVENT 1998, Ed: E. Mundt, T.-G. Malmstrom, 6 (1998), 197-204, Stockholm, Sweden.

[12] S.B. Riffat, X. Zhao, P.S. Doherty, Review of Research into and Application of Chilled Ceilings and Displacement Ventilation Systems in Europe, International Journal of Energy Research, 28 (2004) 257-286.

[13] D.N. Sorensen, P.V. Nielsen, Quality Control of Computational Fluid Dynamics in Indoor Environments, Indoor Air, 13 (2003) 2-17.

[14] Q. Chen, Prediction of Room Air Motion by Reynolds-Stress Models, Building and Environment, 31 (3) (1996) 233-244.

[15] N.B. Kaye, Y. Ji, M.J. Cook, Numerical Simulation of Transient Flow Development in a Naturally Ventilated Room, Building and Environment, 44 (2009) 889-897.

[16] M. Behne, Indoor Air Quality in Rooms with Cooled Ceilings. Mixing Ventilation or Rather Displacement Ventilation?, Energy and Buildings, 30 (1999) 155-166.

[17] V. Zboril, A. Melikov, B. Yordanova, L. Bozkhov, R. Kosonen, Airflow Distribution in Rooms with Active Chilled Beams, The 17th Air-conditioning and Ventilation Conference (2006), Prague, Czech Republic.

[18] R. Kosonen, M. Virta, A. Melikov, The Impact of Thermal Loads on Indoor Air Flow, Proceedings of Clima 2007 WellBeing Indoors (2007), Helsinki, Finland.

[19] A. Melikov, B. Yordanova, L. Bozhov, V. Zboril, R. Kosonen, Impact of the Airflow Interaction on Occupants' Thermal Comfort in Rooms with Active Chilled Beams, Presented at the 6th International Indoor Air Quality, Ventilation & Energy Conservation in Buildings Conference (IAQVEC 2007), Sendai, Japan.

[20] D.L. Loveday, K.C. Parsons, A.H. Take, S.Hodder, L.D. Jeal, Designing for Thermal Comfort in Combined Chilled Displacement Ventilation Environments, ASHRAE Transactions, 104 (1998) 901-911.

[21] D. Muller, I. Gores, R. Zielinski, Impact of the Thermal Load on the Room Airflow Pattern, The 9th International Conference on Air Distribution in Rooms (2004), Coimbra, Portugal.

[22] A. Melikov, B. Yordanova, L. Bozhov, V. Zboril, R. Kosonen, Human Response to Thermal Environment in Rooms with Chilled Beams, Proceedings of Clima 2007 WellBeing Indoors (2007), Helsinki, Finland.

[23] R. Kosonen, A. Melikov, B. Yordanova, L. Bozkhov, Impact of Heat Load Distribution and Strength on Airflow Pattern in Rooms with Exposed Chilled Beams, Proceedings of ROOMVENT 2007, Ed: O. Seppanen, J. Sateri, 1 (2007), 23-30, Helsinki, Finland.

[24] J. Fredriksson, M. Sandberg, B. Moshfegh, Experimental Investigation of the Velocity Field and Airflow Pattern Generated by Cooling Ceiling Beams, Building and Environment, 36 (2001) 891-899.

[25] R. Kosonen, P. Saarinen, H. Koskela, A. Hole, Impact of Heat Load Location and Strength on Air Flow Pattern with a Passive Chilled Beam System, Energy and Buildings, 42 (2010) 34-42.

[26] J. Fredriksson, M. Sandberg, The Effect of False Ceiling on the Cooling Capacity of Passive Chilled Beams, Building and Environment, 44 (2009) 1426-1430.

[27] J.S. Turner, Buoyant Plumes and Thermals, Annual Review of Fluid Mechanics, 1 (1969) 29-44.

[28] H. Rouse, C.S. Yih, H.W. Humphreys, Gravitational Convection from a Boundary Source, Tellus, 4 (1952) 201-210.

[29] B.R. Morton, G.I. Taylor, J.S. Turner, Turbulent Gravitational Convection from Maintained and Instantaneous Sources, Proceedings of the Royal Society of London A 234, (1956) 1-32.

[30] M.M. Scase, C.P. Caulfield, S.B. Dalziel, J.C.R. Hunt, Time-dependent Plumes and Jets with Decreasing Source Strengths, Journal of Fluid Mechanics, 563 (2006) 443-461.

[31] J.S. Turner, Model Experiments Relating to Thermals with Increasing Buoyancy, Quaterly Journal of the Royal Meteorological Society (1962) 62-74.

[32] W.D. Baines, J.S. Turner, Turbulent Buoyant Convection from a Source in a Confined Region, Journal of Fluid Mechanics, 37 (1969) 51-80.

[33] W.D. Baines, Entrainment by a Plume or Jet at a Density Interface, Journal of Fluid Mechanics, 68 (part 2) (1975) 309-320.

[34] B.R. Morton, J. Middleton, Scale Diagrams for Forced Plumes, Journal of Fluid Mechanics, 58 (1973) 165-176.

[35] B.R. Morton, Forced Plumes, Journal of Fluid Mechanics, 5 (1959) 151-163.

[36] C.P. Caulfield, Stratification and Buoyancy in Geophysical Flows (Ph.D. Thesis), University of Cambridge, 1991.

[37] G.R. Hunt, N.B. Kaye, Virtual Origin Correction for Lazy Turbulent Plumes, Journal of Fluid Mechanics, 435 (2001) 377-396.

[38] G.R. Hunt, N.B. Kaye, Lazy Plumes, Journal of Fluid Mechanics, 533 (2005) 329-338.

[39] M.M. Scase, C.P. Caulfield, S.B. Dalziel, Boussinesq Plumes and Jets with Decreasing Source Strengths in Stratified Environments, Journal of Fluid Mechanics, 563 (2006) 463-472.

[40] S. Kimura, A. Bejan, Mechanism for Transition to Turbulence in Buoyant Plume Flow, International Journal of Heat and Mass Transfer, 26 (10) (1983) 1515-1532.

[41] H.Q. Yang, Buckling of a Thermal Plume, International Journal of Heat and Mass Transfer, 35 (6) (1992) 1527-1532.

[42] J.D. Anderson, Computational Fluid Dynamics: The Basics with Applications, McGraw Hill, New York, New York 1995.

[43] Q. Chen, J. Srebric, A Procedure for Verification, Validation, and Reporting of Indoor Environment CFD Analyses, HVAC&R Research, 8 (2) (2002) 201-216.

[44] Z. Zhai, Z. Zhang, W. Zhang, Q. Chen, Evaluation of Various Turbulence Models in Predicting Airflow and Turbulence in Enclosed Environments by CFD: Part 1-Summary of Prevalent Turbulence Models, HVAC&R Research, 13 (6) (2007) 853-870.

[45] P.V. Nielsen, The Selection of Turbulence Models for Prediction of Room Airflow, ASHRAE Transactions, 104 (1998) 1119-1127.

[46] P.R. Spalart, S.R. Allmaras, A One-equation Turbulence Model for Aerodynamic Flows, La Recherce Aerospatiale, 1 (1994) 5-21.

[47] B.E. Launder, D.B. Spalding, The Numerical Computation of Turbulent Flows, Computer Methods in Applied Mechanics and Engineering, 3 (1974) 269-289.

[48] B.E. Launder, D.B.I. Sharma, Application of the Energy-dissipation Model of Turbulence to the Calculation of Flow Near a Spinning Disc, Letters in Heat and Mass Transfer, 1 (1974) 131-137.

[49] L. Davidson, Calculation of the Turbulent Buoyancy-driven Flow in a Rectangular Cavity using an Efficient Solver and Two Different Low Reynolds Number *k-e* Turbulence Models, Numerical Heat Transfer, Part A, 18 (1990) 129-147.

[50] W.P. Jones, B.E. Launder, The Calculation of Low-Reynolds-number Phenomena with a Two-equation Model of Turbulence, International Journal of Heat and Mass Transfer, 16 (1973) 1119-1130.

[51] F.B. Cheung, D.Y. Sohn, Numerical Study of Turbulent Natural Convection in an Innovative Air Cooling System, Numerical Heat Transfer, Part A, 16 (1989) 467-487.

[52] V. Yakhot, S.A. Orszag, Renormalization Group Analysis of Turbulence, Journal of Scientific Computing, 1 (1) (1986) 3-51.

[53] G. Gan, Prediction of Turbulent Buoyant Flow using an RNG k-e Model, Numerical Heat Transfer, Part A: Applications, 33 (2) (1998) 169-189.

[54] M. Cehlin, B. Moshfegh, Numerical and Experimental Investigations of Air Flow and Temperature Patterns of a Low Velocity Diffuser, Indoor Air 2002 - 9th International Conference on Indoor Air Quality and Climate, (2002), 765-770, Rotterdam, Netherlands.

[55] Y. Ji, M.J. Cook, V. Hanby, CFD Modelling of Natural Displacement Ventilation in an Enclosure Connected to an Atrium, Building and Environment, 42 (2007) 1158-1172.

[56] T. Zhang, K. Lee, Q. Chen, A Simplified Approach to Describe Complex Diffusers in Displacement Ventilation for CFD Simulations, Indoor Air, 19 (2009) 255-267.

[57] S. Teixeira, C.P. Leao, M. Neves, P. Arezes, A. Cunha, J.C. Teixeira, Thermal Comfort Evaluation using a CFD Study and a Transient Thermal Model of the Human Body, Proceedings of the European Conference on Computational Fluid Dynamics, Ed: J.C.F. Pereira, A. Sequeira, J.M.C. Pereira (2010), Lisbon, Portugal.

[58] S.A. Howell, I. Potts, On the Natural Displacement Flow Through a Full-scale Enclosure, and the Importance of the Radiative Participation of the Water Vapour Content of the Ambient Air, Building and Environment, 37 (2002) 817-823.

[59] C. Allocca, Q. Chen, L.R. Glicksman, Design Analysis of Single-sided Natural Ventilation, Energy and Buildings, 35 (2003) 785-795.

[60] Z. Lin, T.T. Chow, Q. Wang, K.F. Fong, L.S. Chan, Validation of CFD Model for Research into Displacement Ventilation, Architectural Science Review, 48 (2005) 305-316.

[61] A. Stamou, I. Katsiris, Verification of a CFD Model for Indoor Airflow and Heat Transfer, Building and Environment, 41 (2006) 1171-1181.

[62] B.A. Craven, G.S. Settles, A Computational and Experimental Investigation of the Human Thermal Plume, Journal of Fluids Engineering, 128 (2006) 1251-1258.

[63] J. Gao, X. Zhang, J.N. Zhao, Numerical Determination of Convection Coefficients for Internal Surfaces in Buildings Dominated by Thermally Stratified Flows, Journal of Building Physics, 31 (3) (2008) 213-223.

[64] P. Emvin, L. Davidson, A Numerical Comparison of Three Inlet Approximations of the Diffuser in Case E1 Annex 20, Proceedings of ROOMVENT 1996, Ed: S. Murakami, 1 (1996), 219-226, Yokohama, Japan.

[65] Q. Chen, Z. Jiang, Simulation of a Complex Air Diffuser with CFD Technique, Proceedings of ROOMVENT 1996, Ed: S. Murakami, 1 (1996), 227-234, Yokohama, Japan.

[66] P.V. Nielsen, The Box Method - a Practical Procedure for Introduction of an Air Terminal Device in CFD Calculation, Institute for Bygningsteknik, Aalborg Universite, Denmark.

[67] Y. Huo, J. Zhang, C. Shaw, F. Haghighat, A New Method to Describe the Diffuser Boundary Conditions in CFD Simulation, Proceedings of ROOMVENT 1996, Ed: S. Murakami, 2 (1996), 233-240, Yokohama, Japan.

[68] B. Zhao, X. Li, Q. Yan, A Simplified System for Indoor Airflow Simulation, Building and Environment, 38 (2003) 543-552.

[69] E. Djunaedy, K.W.D. Cheong, Development of a Simplified Technique of Modelling Four-way Ceiling Air Supply Diffuser, Building and Environment, 37 (2002) 393-403.

[70] M.C. Soteriou, Y. Dong, B.M. Cetegen, Lagrangian Simulation of the Unsteady Near Field Dynamics of Planar Buoyant Plumes, Physics of Fluids, 14 (9) (2002) 3118-3140.

[71] Guozhong, Zheng, Y. Jing, H. Huang, L. Shi, Airflow Distribution and Microenvironment Evaluation of MP Task Conditioning System, American Society of Mechanical Engineers Energy Sustainability 2007 Conference Proceedings (2007), 797-806, Long Beach, California.

[72] G. Cammarata, G. Petrone, A Numerical Investigation on Active Chilled Beams for Indoor Air Conditioning, Proceedings of the COMSOL Conference, Ed: B. Nilsson (2008) Hannover, Germany.

[73] H. Tomita, K. Abe, Numerical Simulation of the Rayleigh-Benard Convection of Air in a Box of a Large Aspect Ratio, Physics of Fluids, 11 (3) (1999) 743-745.

[74] M.J. Cook, T. Zitzmann, P. Pfrommer, Dynamic Thermal Building Analysis with CFD - Modelling Radiation, Journal of Building Performance Simulation, 1 (2) (2008) 117-131.

[75] M. Deevy, Y. Sinai, P. Everitt, L. Voigt, N. Gobeau, Modelling the Effect of an Occupant on Displacement Ventilation with Computational Fluid Dynamics, Energy and Buildings, 40 (2008) 255-264.

[76] H.-J. Park, D. Holland, The Effect of Location of a Convective Heat Source on Displacement Ventilation: CFD study, Building and Environment, 36 (2001) 883-889.

[77] T. Kim, S. Kato, S. Murakami, J. Rho, Study on Indoor Thermal Environment of Office Space Controlled by Cooling Panel System using Field Measurement and the Numerical Simulation, Building and Environment, 40 (2005) 301-310.

[78] E.C.f. Standardization, Ventilation for Buildings: Testing and Rating of Passive Chilled Beams, in, Brussels, Belgium, 2005.

[79] E.J. LeFevre, Laminar Free Convection from a Vertical Plane Surface, Proceedings of the Ninth International Congress for Applied Mechanics, 4 (1956) 168-174.

[80] A. Ugursal, C.H. Culp, An Empirical Thermal Comfort Model for Transient Metabolic Conditions, ASHRAE Transactions, 118 (1) (2012) 742-750.

APPENDIX A

THEORETICAL BACKGROUND OF CFD

A.1 CFD Basis

The fundamental equations of continuity, momentum and energy are based on the three physical principles that: 1) mass is conserved, 2) force is equal to the product of mass and acceleration, and 3) energy is conserved [42]. These physical principles are applied to the flow model to develop the partial differential equations that govern the flow equations. In CFD, numbers are used to replace the partial differential equations and are advanced through space or time to solve the mathematical relationships. The end result is a numerical description of the flow field.

A.2 Governing Equations

The continuity equation can be derived based on an integral analysis of a fixed volume in space of the fluid based on the physical principle that mass is conserved. The flow of mass into or out of the control volume can be described by the surface integral:

$$\oiint_S \rho\vec{V} \cdot \mathrm{d}\vec{S} \tag{A.1}$$

The mass contained within the volume can be described with the volume integral:

$$\oiiint_{\mathcal{V}} \rho \mathrm{d}\mathcal{V} \tag{A.2}$$

and the time rate of change of the total mass is then:

$$\frac{\partial}{\partial t}\iiint_{\mathcal{V}} \rho \mathrm{d}\mathcal{V} \tag{A.3}$$

Setting the time rate of change of total mass within the control volume equal to the mass flow into and out of the control volume, results in the following:

$$\frac{\partial}{\partial t}\iiint_{\mathcal{V}} \rho \mathrm{d}\mathcal{V} + \iint_{S} \rho \vec{V} \cdot \mathrm{d}\vec{S} = 0 \tag{A.4}$$

which is the integral form of the continuity equation for a fixed volume in space. In order to transform the integral equation into a differential form, the divergence theorem is applied. The surface integral can then be written as:

$$\iint_{S} \rho \vec{V} \cdot \mathrm{d}\vec{S} = \iiint_{\mathcal{V}} \nabla \cdot (\rho \vec{V}) \mathrm{d}\mathcal{V} \tag{A.5}$$

Substituting this result into the integral form of the continuity equation:

$$\iiint_{\mathcal{V}} \frac{\partial \rho}{\partial t} \mathrm{d}\mathcal{V} + \iiint_{\mathcal{V}} \nabla \cdot (\rho \vec{V}) \mathrm{d}\mathcal{V} = 0 \tag{A.6}$$

where the time differential was placed inside the volume integral. This can be re-written as:

$$\iiint_{\mathcal{V}} \left[\frac{\partial \rho}{\partial t} + \nabla \cdot (\rho \vec{V}) \right] \mathrm{d}\mathcal{V} = 0 \tag{A.7}$$

In order for the volume integral to equal zero, the integrand must also equal zero. As a result the differential form of the continuity equation for a fixed infinitesimal volume in space is:

$$\frac{\partial \rho}{\partial t} + \nabla \cdot (\rho \vec{V}) = 0 \tag{A.8}$$

The second physical principle applied to the flow leads to the momentum equation. The forces acting on an infinitesimal fluid particle are set equal to the product of the mass

and acceleration of the particle. The forces that act on a fluid particle are categorized as either a body or surface force. Gravity and electrical and magnetic fields are examples of body forces, while surface forces are either shear or normal. In the *x*-direction of the flow in three dimensional Cartesian space, the forces can be described by:

$$F_x = \left(-\frac{\partial p}{\partial x} + \frac{\partial \tau_{xx}}{\partial x} + \frac{\partial \tau_{yx}}{\partial y} + \frac{\partial \tau_{zx}}{\partial z}\right)\mathrm{d}x\mathrm{d}y\mathrm{d}z + \rho f_x \mathrm{d}x\mathrm{d}y\mathrm{d}z \qquad \text{A.9}$$

The mass of fluid can be written as:

$$m = \rho \mathrm{d}x\mathrm{d}y\mathrm{d}z \qquad \text{A.10}$$

and the acceleration as the substantial derivative of the fluid velocity:

$$a_x = \frac{\mathrm{D}u}{\mathrm{D}t} \qquad \text{A.11}$$

Substituting Equations A.10 and A.11 into A.9:

$$\rho \frac{\mathrm{D}u}{\mathrm{D}t} = -\frac{\partial p}{\partial x} + \frac{\partial \tau_{xx}}{\partial x} + \frac{\partial \tau_{yx}}{\partial y} + \frac{\partial \tau_{zx}}{\partial z} + \rho f_x \qquad \text{A.12}$$

By expanding the substantial derivative of *u* and applying the divergence theorem, this becomes:

$$\frac{\partial(\rho u)}{\partial t} + \nabla \cdot \left(\rho u \vec{V}\right) = -\frac{\partial p}{\partial x} + \frac{\partial \tau_{xx}}{\partial x} + \frac{\partial \tau_{yx}}{\partial y} + \frac{\partial \tau_{zx}}{\partial z} + \rho f_x \qquad \text{A.13}$$

which is the *x*-direction momentum equation. Along with the *y*-direction and *z*-direction equations, this group of three equations are named the Navier-Stokes equations:

$$\frac{\partial(\rho v)}{\partial t} + \nabla \cdot \left(\rho v \vec{V}\right) = -\frac{\partial p}{\partial y} + \frac{\partial \tau_{xy}}{\partial x} + \frac{\partial \tau_{yy}}{\partial y} + \frac{\partial \tau_{zy}}{\partial z} + \rho f_y \qquad \text{A.14}$$

$$\frac{\partial(\rho w)}{\partial t} + \nabla \cdot \left(\rho w \vec{V}\right) = -\frac{\partial p}{\partial z} + \frac{\partial \tau_{xz}}{\partial x} + \frac{\partial \tau_{yz}}{\partial y} + \frac{\partial \tau_{zz}}{\partial z} + \rho f_z \qquad \text{A.15}$$

For Newtonian fluids the shear stresses can be written as:

$$\tau_{xx} = \lambda \nabla \cdot \vec{V} + 2\mu \frac{\partial u}{\partial x} \quad \text{A.16}$$

$$\tau_{yy} = \lambda \nabla \cdot \vec{V} + 2\mu \frac{\partial v}{\partial y} \quad \text{A.17}$$

$$\tau_{zz} = \lambda \nabla \cdot \vec{V} + 2\mu \frac{\partial w}{\partial z} \quad \text{A.18}$$

$$\tau_{xy} = \tau_{yx} = \mu \left(\frac{\partial v}{\partial x} + \frac{\partial u}{\partial y} \right) \quad \text{A.19}$$

$$\tau_{xz} = \tau_{zx} = \mu \left(\frac{\partial u}{\partial z} + \frac{\partial w}{\partial x} \right) \quad \text{A.20}$$

$$\tau_{yz} = \tau_{zy} = \mu \left(\frac{\partial w}{\partial y} + \frac{\partial v}{\partial z} \right) \quad \text{A.21}$$

with the Stokes hypothesis for the bulk viscosity coefficient:

$$\lambda = -\frac{2}{3}\mu \quad \text{A.22}$$

and substituting in are the Navier-Stokes equations in conservation form:

$$\begin{aligned} &\frac{\partial(\rho u)}{\partial t} + \frac{\partial(\rho u^2)}{\partial x} + \frac{\partial(\rho uv)}{\partial y} + \frac{\partial(\rho uw)}{\partial z} \\ &= -\frac{\partial p}{\partial x} + \frac{\partial}{\partial x}\left(\lambda \nabla \cdot \vec{V} + 2\mu \frac{\partial u}{\partial x} \right) \\ &+ \frac{\partial}{\partial y}\left[\mu \left(\frac{\partial v}{\partial x} + \frac{\partial u}{\partial y} \right) \right] + \frac{\partial}{\partial z}\left[\mu \left(\frac{\partial u}{\partial z} + \frac{\partial w}{\partial x} \right) \right] \\ &+ \rho f_x \end{aligned} \quad \text{A.23}$$

$$\frac{\partial(\rho v)}{\partial t}+\frac{\partial(\rho uv)}{\partial x}+\frac{\partial(\rho v^2)}{\partial y}+\frac{\partial(\rho vw)}{\partial z}$$
$$= -\frac{\partial p}{\partial y}+\frac{\partial}{\partial x}\left[\mu\left(\frac{\partial v}{\partial x}+\frac{\partial u}{\partial y}\right)\right]$$
$$+\frac{\partial}{\partial y}\left(\lambda\nabla\cdot\vec{V}+2\mu\frac{\partial z}{\partial y}\right)+\frac{\partial}{\partial z}\left[\mu\left(\frac{\partial w}{\partial y}+\frac{\partial v}{\partial z}\right)\right] \quad \text{A.24}$$
$$+\rho f_y$$

$$\frac{\partial(\rho w)}{\partial t}+\frac{\partial(\rho uw)}{\partial x}+\frac{\partial(\rho vw)}{\partial y}+\frac{\partial(\rho w^2)}{\partial z}$$
$$= -\frac{\partial p}{\partial z}+\frac{\partial}{\partial x}\left[\mu\left(\frac{\partial u}{\partial z}+\frac{\partial w}{\partial x}\right)\right]$$
$$+\frac{\partial}{\partial y}\left[\mu\left(\frac{\partial w}{\partial y}+\frac{\partial v}{\partial z}\right)\right]+\frac{\partial}{\partial z}\left(\lambda\nabla\cdot\vec{V}+2\mu\frac{\partial w}{\partial z}\right) \quad \text{A.25}$$
$$+\rho f_z$$

The third principle applied to the flow is the conservation of energy and results in the energy equation. The rate of change of energy inside the fluid element is equal to the sum of the heat flux into the element and the rate of work done on the element due to surface and body forces. The rate of energy within the fluid element may be written as:

$$\rho\frac{\mathrm{D}\left(e+\frac{V^2}{2}\right)}{\mathrm{D}t}\mathrm{d}x\mathrm{d}y\mathrm{d}z \quad \text{A.26}$$

The heat flux into the fluid element is the sum of the volumetric heating of the element and the heating due to thermal conduction:

$$\left[\rho\dot{q} - \left(\frac{\partial \dot{q}_x}{\partial x} + \frac{\partial \dot{q}_y}{\partial y} + \frac{\partial \dot{q}_z}{\partial z}\right)\right] \mathrm{d}x\mathrm{d}y\mathrm{d}z \tag{A.27}$$

The conduction can be related to the product of the thermal conductivity and the temperature gradient and substituting into Equation A.27 becomes:

$$\left[\rho\dot{q} + \frac{\partial}{\partial x}\left(k\frac{\partial T}{\partial x}\right) + \frac{\partial}{\partial y}\left(k\frac{\partial T}{\partial y}\right) + \frac{\partial}{\partial z}\left(k\frac{\partial T}{\partial z}\right)\right] \mathrm{d}x\mathrm{d}y\mathrm{d}z \tag{A.28}$$

The rate of work done on the element due to body force is the product of the force and the velocity component in the direction of the force:

$$\rho\vec{f}\cdot\vec{V}(\mathrm{d}x\mathrm{d}y\mathrm{d}z) \tag{A.29}$$

The rate of work done on the element due to surface forces is a result of pressure and shear forces. For the *x*-direction rate of work for the pressure forces is:

$$\left[up - \left(up + \frac{\partial(up)}{\partial x}\mathrm{d}x\right)\right] \mathrm{d}y\mathrm{d}z = -\frac{\partial(up)}{\partial x}\mathrm{d}x\mathrm{d}y\mathrm{d}z \tag{A.30}$$

The *x*-direction rate of work for the shear forces is:

$$\left[\left(u\tau_{yx} + \frac{\partial\left(u\tau_{yx}\right)}{\partial x}\mathrm{d}y\right) - u\tau_{yx}\right] \mathrm{d}x\mathrm{d}z = \frac{\partial\left(u\tau_{yx}\right)}{\partial x}\mathrm{d}x\mathrm{d}y\mathrm{d}z \tag{A.31}$$

Combining the body and surface forces:

$$\left[-\frac{\partial(up)}{\partial x} + \frac{\partial(u\tau_{xx})}{\partial x} + \frac{\partial\left(u\tau_{yx}\right)}{\partial y} + \frac{\partial(u\tau_{zx})}{\partial z}\right] \mathrm{d}x\mathrm{d}y\mathrm{d}z \tag{A.32}$$

With the addition of the *y*-direction and *z*-direction terms, the combined body and surface force expression becomes:

$$\left[\left(-\frac{\partial(up)}{\partial x}+\frac{\partial(vp)}{\partial y}+\frac{\partial(wp)}{\partial z}\right)+\frac{\partial(u\tau_{xx})}{\partial x}+\frac{\partial\left(u\tau_{yx}\right)}{\partial y}\right.$$
$$+\frac{\partial(u\tau_{zx})}{\partial z}+\frac{\partial\left(v\tau_{xy}\right)}{\partial x}+\frac{\partial\left(v\tau_{yy}\right)}{\partial y}+\frac{\partial\left(v\tau_{zy}\right)}{\partial z}$$
$$\left.+\frac{\partial(w\tau_{xz})}{\partial x}+\frac{\partial\left(w\tau_{yz}\right)}{\partial y}+\frac{\partial(w\tau_{zz})}{\partial z}\right]\mathrm{d}x\mathrm{d}y\mathrm{d}z \qquad \text{A.33}$$
$$+\rho\vec{f}\cdot\vec{V}(\mathrm{d}x\mathrm{d}y\mathrm{d}z)$$

By combining equations A.28, A.29, and A.33 the energy equation is defined as:

$$\rho\frac{\mathrm{D}\left(e+\frac{V^2}{2}\right)}{\mathrm{D}t}=\rho\dot{q}\ +\ \frac{\partial}{\partial x}\left(k\frac{\partial T}{\partial x}\right)+\ \frac{\partial}{\partial y}\left(k\frac{\partial T}{\partial y}\right)+\ \frac{\partial}{\partial z}\left(k\frac{\partial T}{\partial z}\right)$$
$$-\frac{\partial(up)}{\partial x}+\frac{\partial(vp)}{\partial y}+\frac{\partial(wp)}{\partial z}+\frac{\partial(u\tau_{xx})}{\partial x}$$
$$+\frac{\partial\left(u\tau_{yx}\right)}{\partial y}+\frac{\partial(u\tau_{zx})}{\partial z}+\frac{\partial\left(v\tau_{xy}\right)}{\partial x}+\frac{\partial\left(v\tau_{yy}\right)}{\partial y} \qquad \text{A.34}$$
$$+\frac{\partial\left(v\tau_{zy}\right)}{\partial z}+\frac{\partial(w\tau_{xz})}{\partial x}+\frac{\partial\left(w\tau_{yz}\right)}{\partial y}$$
$$+\frac{\partial(w\tau_{zz})}{\partial z}\mathrm{d}x\mathrm{d}y\mathrm{d}z+\rho\vec{f}\cdot\vec{V}$$

Based on the definition for the substantial derivative, the left-hand side of Equation A.34 can be written as:

$$\rho\frac{\mathrm{D}\left(e+\frac{V^2}{2}\right)}{\mathrm{D}t}=\rho\frac{\partial\left(e+\frac{V^2}{2}\right)}{\partial t}+\rho\vec{V}\cdot\nabla\left(e+\frac{V^2}{2}\right) \qquad \text{A.35}$$

considering that:

$$\rho\frac{\partial\left(e+\frac{V^2}{2}\right)}{\partial t}=\frac{\partial\left[\rho\left(e+\frac{V^2}{2}\right)\right]}{\partial t}-\left(e+\frac{V^2}{2}\right)\frac{\partial\rho}{\partial t} \tag{A.36}$$

and,

$$\rho\vec{V}\cdot\nabla\left(e+\frac{V^2}{2}\right)=\nabla\cdot\left[\rho\left(e+\frac{V^2}{2}\right)\vec{V}\right]-\left(e+\frac{V^2}{2}\right)\nabla\cdot\left(\rho\vec{V}\right) \tag{A.37}$$

Then substitute Equation A.36 and A.37 into A.35:

$$\begin{aligned}\rho\frac{\mathrm{D}}{\mathrm{D}t}\left(e+\frac{V^2}{2}\right)=&\frac{\partial\left[\rho\left(e+\frac{V^2}{2}\right)\right]}{\partial t}\\&-\left(e+\frac{V^2}{2}\right)\left[\frac{\partial\rho}{\partial t}+\nabla\cdot\left(\rho\vec{V}\right)\right]+\nabla\\&\cdot\left[\rho\left(e+\frac{V^2}{2}\right)\vec{V}\right]\end{aligned} \tag{A.38}$$

Using the continuity equation, the second term on the right-hand side is zero, and simplifying:

$$\rho\frac{\mathrm{D}\left(e+\frac{V^2}{2}\right)}{\mathrm{D}t}=\frac{\partial}{\partial t}\left[\rho\left(e+\frac{V^2}{2}\right)\right]+\nabla\cdot\left[\rho\left(e+\frac{V^2}{2}\right)\vec{V}\right] \tag{A.39}$$

Substituting Equation A.39 into A.34 the conservation form of the energy equation is obtained:

$$\rho\frac{\partial}{\partial t}\left[\rho\left(e+\frac{V^2}{2}\right)\right]+\nabla\cdot\left[\rho\left(e+\frac{V^2}{2}\right)\vec{V}\right]$$

$$=\rho\dot{q}+\frac{\partial}{\partial x}\left(k\frac{\partial T}{\partial x}\right)+\frac{\partial}{\partial y}\left(k\frac{\partial T}{\partial y}\right)$$

$$+\frac{\partial}{\partial z}\left(k\frac{\partial T}{\partial z}\right)-\frac{\partial(up)}{\partial x}+\frac{\partial(vp)}{\partial y}+\frac{\partial(wp)}{\partial z}$$

$$+\frac{\partial(u\tau_{xx})}{\partial x}+\frac{\partial\left(u\tau_{yx}\right)}{\partial y}+\frac{\partial(u\tau_{zx})}{\partial z}+\frac{\partial\left(v\tau_{xy}\right)}{\partial x}$$

$$+\frac{\partial\left(v\tau_{yy}\right)}{\partial y}+\frac{\partial\left(v\tau_{zy}\right)}{\partial z}+\frac{\partial(w\tau_{xz})}{\partial x}+\frac{\partial\left(w\tau_{yz}\right)}{\partial y}$$

$$+\frac{\partial(w\tau_{zz})}{\partial z}\mathrm{d}x\mathrm{d}y\mathrm{d}z+\rho\vec{f}\cdot\vec{V}$$

A.40

APPENDIX B

TENSOR NOTATION

The following is an overview of the tensor notation used throughout this text. Cartesian tensors were used to transcribe the fluid equations. Tensors are made up of tensor components and basis vectors and the number of independent basis vectors defines the dimension of the tensor. Tensors of order zero are scalars and do not need to be described with a basis vector. Vectors are tensors of order one and can be written as:

$$\vec{x} = \sum_{i=1}^{3} x_i \vec{e}_i = x_i \vec{e}_i \qquad \text{B.1}$$

For example, the first order tensor for velocity, u_i, is written as:

$$u_i = (u_1, u_2, u_3) = (u, v, w) \qquad \text{B.2}$$

A second order tensor, formed by the product of two order one tensors can be written as:

$$\boldsymbol{T} = \vec{a}\vec{b} = \sum_{i=1}^{3}\sum_{j=1}^{3} a_i b_j \vec{e}_i \vec{e}_j = a_i b_j \vec{e}_i \vec{e}_j \qquad \text{B.3}$$

For example, the second order tensor of stress, is written as

$$\tau_{ij} \; (i, j = 1, 2, 3) \qquad \text{B.4}$$

and in the form of a matrix:

$$\tau_{ij} = \begin{bmatrix} \tau_{11} & \tau_{21} & \tau_{31} \\ \tau_{12} & \tau_{22} & \tau_{32} \\ \tau_{13} & \tau_{23} & \tau_{33} \end{bmatrix} = \begin{bmatrix} \tau_{xx} & \tau_{yx} & \tau_{zx} \\ \tau_{xy} & \tau_{yy} & \tau_{zy} \\ \tau_{xz} & \tau_{yz} & \tau_{zz} \end{bmatrix} \qquad \text{B.5}$$

For a scalar product such as:

$$\vec{a} \cdot \vec{b} = (a_i \vec{e}_i) \cdot \left(b_j \vec{e}_j\right) = a_i b_j \left(\vec{e}_i \vec{e}_j\right) \quad \text{B.6}$$

By using the Kroneker delta, δ_{ij}, the scalar product can be written in Cartesian index notation as:

$$\vec{a} \cdot \vec{b} = \ a_i b_j \delta_{ij} = a_i b_i \quad \text{B.7}$$

where the Kroneker delta is defined as:

$$\delta_{ij} = \ \vec{e}_i \cdot \vec{e}_j = \begin{cases} 1 & for\ i = j \\ 0 & for\ i \neq j \end{cases} \quad \text{B.8}$$